UNIVERSITY OF CALIFORNIA SAN DIEGO

Development of Low Seismic Damage Structural Systems

A dissertation submitted in partial satisfaction of the
requirements for the degree of Doctor of Philosophy

in

Structural Engineering

by

Arpit Nema

Committee in charge:

Professor José I. Restrepo, Chair
Professor Joel P. Conte
Professor Kenneth Loh
Professor Bhaskar Rao
Professor Chia-Ming Uang

2018

The Dissertation of Arpit Nema is approved, and it is acceptable in quality and form for publication on microfilm and electronically:

Chair

University of California San Diego

2018

DEDICATION

To my friends, Koorosh and Rodrigo,

whose support made this journey possible.

TABLE OF CONTENTS

LIST OF SYMBOLS

A_{ch}	Cross-sectional area of a member measured to the outside edges of transverse reinforcement
A_g	Gross area of concrete member section
A_P, A_m	Areas in the prototype and model scale structures respectively
A_{sED}	Total area of energy dissipator reinforcement
A_{sh}	Total cross-sectional area of transverse reinforcement, including crossties, within spacing s and perpendicular to dimension b_c
A_{st}	Total area of non-prestressed longitudinal reinforcement including bars or steel shapes, and excluding prestressing reinforcement
A_{sPT}	Total area of prestressing reinforcement
C_d	Deflection amplification factor
D	The effect of dead load
D_o	Outer diameter of column steel shell
E	Material Young's modulus
E_c	Concrete Young's modulus
$F_{ED,o}$	Total force capacity of hysteretic dissipators
F_P, F_m	Forces in the prototype and model scale structures respectively
$F_{PT,i}$	Initial force in the prestressing reinforcement in a hybrid re-centering member
F_{PP}	Design force capacity of total prestressing reinforcement in a hybrid re-centering member
F_y	Total yielding force of hysteretic dissipators

H_r	Height of specimen roof above foundation level.
H_s	Inter-story height in the structure
K_P, K_m	Stiffness in the prototype and model scale structures respectively
K_{tr}	Transverse reinforcement index
L	The effect of live load
L_c	Clear span of column
M_o	Nominal moment capacity of beams at column-beam joint surface
M_P, M_m	Masses in the prototype and model scale structures respectively
$M'_m, \Delta M_m$	Target and required additional mass in the model scale structure
M_W	Moment magnitude scale for earthquake size
P_u	Factored axial force; to be taken as positive for compression and negative for tension
R	Response modification coefficient
S	The effect of seismic load
S_A	Area scale factor
S_F	Force scale factor
S_K	Stiffness scale factor
S_M	Mass scale factor
S_{DS}	Design, 5 percent damped, spectral response acceleration parameter at short periods as defined in ASCE 7-10 (ASCE 2010) Section 11.4.1
S_{D1}	Design, 5 percent damped, spectral response acceleration parameter at a period of 1 s as defined in ASCE 7-10 (ASCE 2010) Section 11.4.1
S_S	Mapped MCE_R, 5 percent damped, spectral response acceleration

	parameter at short periods as defined in ASCE 7-10 (ASCE 2010) Section 11.4.1
S_T'	Target period scale factor
S_V	Volume scale factor
S_a	Acceleration scale factor
S_l	Length scale factor
S_σ, S_σ'	Stress scale factor, based on S_l and Target respectively
S_1	Mapped MCE_R, 5 percent damped, spectral response acceleration parameter at a period of 1 s as defined in ASCE 7-10 (ASCE 2010) Section 11.4.1
T	Structural undamped period of vibration
T_L	Long-period transition period as defined in in ASCE 7-10 (ASCE 2010) Section 11.4.5
V_c	Nominal shear strength provided by concrete
V_e	Design shear force for load combinations including earthquake effects
V_P, V_m	Volumes in the prototype and model scale structures respectively
W	Specimen seismic weight
b_c	Cross-sectional dimension of member core measured to the outside edges of the transverse reinforcement composing area A_{sh}
c_b	Lesser of: (a) the distance from center of a bar or wire to nearest concrete surface, and (b) one-half the center-to-center spacing of bars or wires being developed
d	Distance from extreme compression fiber to centroid of longitudinal tension reinforcement
d_b	Nominal diameter of bar, wire, or prestressing strand

f_c'	Specified strength of concrete in compression
f_{pu}	Specified tensile strength or Guaranteed Ultimate Tensile Strength (GUTS) of prestressing reinforcement
f_y	Yield strength of steel reinforcement
f_{yt}	Yield strength of transverse steel reinforcement
$f_{y,exp}$	Expected yield strength of steel reinforcement
$f_{u,exp}$	Expected tensile strength of steel reinforcement
g	Acceleration due to gravity
h_x	Maximum center-to-center spacing of longitudinal bars laterally supported by corners of crossties or hoop legs around the perimeter of the column
$j_{d,PP}$	Level arm between compression resultant and tensile force in prestressing reinforcement
k_f	Concrete strength factor
k_n	Confinement effectiveness factor
l	The weighted length corresponding to each integration point in the force-based beam-column element (FBE)
l_R	Reference length considered for accounting for mesh-size effects when using beam-column element. Taken to be 300 mm, based on the length of the cylindrical molds used for measuring f_c'
l_d	Development length in tension of deformed bar, deformed wire, plain and deformed welded wire reinforcement, or pretensioned strand
l_{dc}	Development length in compression of deformed bars and deformed wire
l_o	Length, measured from joint face along axis of member, over which special transverse reinforcement must be provided
l_P, l_m	Lengths in prototype and model scale structures respectively

l_{sc}	Compression lap splice length
l_{st}	Tension lap splice length
s	Center-to-center spacing of items, such as longitudinal reinforcement, transverse reinforcement, tendons, or anchors
s_o	Center-to-center spacing of transverse reinforcement within the length l_o
t_o	Thickness of column steel shell
Λ	Factor that considers the effect of unloading on the concrete fracture energy in compression
Λ_C	Re-centering coefficient
Λ_D	Energy dissipation coefficient
Ω_o	Overstrength factor
α	Ratio between hysteretic element moment contribution and nominal beam moment capacity
β	Ratio $2F_y/W$
ε_o	Concrete strain at f_c'
ε_u	Concrete strain at failure i.e. zero stress
λ	Modification factor to reflect the reduced mechanical properties of lightweight concrete relative to normal weight concrete of the same compressive strength
ξ	Total equivalent viscous damping of an oscillating system
ρ	Mass density
ρ_l	Ratio of area of longitudinal reinforcement to gross area of concrete section
ρ_l'	Ratio of area of longitudinal reinforcement to area of confined boundary element for walls or confined core for columns

ρ_s	Ratio of volume of spiral reinforcement to total volume of core confined by the spiral, measured out-to-out of spirals
σ_P, σ_m	Stresses in the prototype and model scale structures respectively
ψ_e	Factor used to modify development length based on reinforcement coating
ψ_r	Factor used to modify development length based on confining reinforcement
ψ_s	Factor used to modify development length based on reinforcement size
ψ_t	Factor used to modify development length for casting location in tension

LIST OF FIGURES

LIST OF TABLES

ACKNOWLEDGEMENTS

I would like to thank my advisor, Professor José I. Restrepo whose support and advice has helped me improve my abilities as an engineer and researcher.

I would like to thank my fellow researchers and friends: Koorosh Lotfizadeh, Rodrigo Carreño, Gabriele Guerrini, Michelle Chen and David Duck for their support and friendship over the years.

For their collaboration on the testing of the four-story structure, I would like to thank the research team from University of Arizona, Tucson: Dr. Robert B. Fleischman, Dr. Dichuan Zhang, Dr. Zhi Zhang, Dr. Ulina Shakya and Dr. Anshul Agarwal; and the research team from Lehigh University: Dr. Richard Sause and Dr. Georgios Tsampras.

I would like to thank the staff at the Large High-Performance Outdoor Shake Table (LHPOST) at UC San Diego: Dan Radulescu, Paul Greco, Alex Sherman, Hector Vicencio and Robert Beckley for their invaluable help during the testing of the four-story structure studied in this work.

I would like to thank Dr. Khalid Mosalam, Dr. Selim Gunay and Yingjie Wu from University of California, Berkeley for their valuable insights into the specimen design and numerical model development for the study of the low-damage bridge specimen.

I would like to thank the technical staff at the PEER Earthquake Shaking Table at the Richmond Field Station academic facilities of the University of California, Berkeley: Clement Barthes, Robert Cerney, Lobsang Garcia and Nathaniel Knight for their

enthusiasm and invaluable assistance during the testing of the low-damage bridge specimen studied in this work.

I would like to thank Dr Andre R. Barbosa Associate Professor, Oregon State University, for sharing the base analytical model of the 13-story structure developed upon as a part of this work. I would also like to thank Frank Beckwith, Doctoral student at UC San Diego for sharing the analytical model of a 4-bent bridge which served as the baseline for studying low-damage bridge systems as part of this work.

The experimental study of the four-story structure was supported financially by the National Science Foundation (NSF) under Grant CMMI-1135033, Network for Earthquake Engineering Simulation Research (NEESR). Additional support was provided by "Fund of Social Development" grant (No.КФ-14/03) at Nazarbayev University. Industry practitioners contributed significantly to the experimental test program. I am thankful to the following industry partners for their contributions of time, materials, monetary donations and expertise: the Prestressed/Precast Concrete Institute (PCI), PCI West, the Charles Pankow Foundation, T.B. Penick & Sons, Inc., Star Seismic, MMFX, Midstate Precast, Davis Wire, DYMAT, Brewer Crane and Rigging, JVI Inc., Pleiger Inc., BASF Inc., Gerdau Inc., HRC Inc., Core Slab, Dura Fiber, Triton Structural Concrete, Atlas Construction Supply, Inc., Western Concrete pumping, Steel City Scaffold, Clark Pacific, Wire Reinforcement Institute, Fyfe Co., LLC.

The experimental and analytical work on the low-damage bridge specimen, was supported by funding from the Pacific Earthquake Engineering Research Center (PEER),

University of California Berkeley. I am thankful for their contributions of time, financial support and expertise.

Finally, I want to thank the members of my committee for their time and valuable contribution to define the objectives for this dissertation.

Chapter 3, in part, references material presented in *Shake‐table test performance of an inertial force‐limiting floor anchorage system*, Earthquake Engineering & Structural Dynamics. 2018 Aug; 47(10), pp.1987-2011, Zhang, Zhi; Fleischman, Robert B.; Restrepo, José I.; Guerrini, Gabriele; Nema, Arpit; Zhang, Dichuan; Shakya, Ulina; Tsampras, Georgios and Sause, Richard. Chapter 3, in part, is a reprint of the material as it appears in *Seismic response of precast concrete gravity columns in a building system* Nema, Arpit and Restrepo, José I. The dissertation author co-authored the material in both publications.

Chapter 5, in part, is a reprint of the material presented in *Low-damage Columns for Accelerated Bridge Construction,* PEER Research Report (in-preparation) Nema, Arpit and Restrepo, José I. The dissertation author is the principal author on the report.

Chapter 6, in part, is a reprint of the material presented in *Low-damage Columns for Accelerated Bridge Construction,* PEER Research Report (in-preparation) Nema, Arpit and Restrepo, José I. The dissertation author is the principal author on the report.

VITA

2011	Bachelor of Technology, Civil Engineering.
	Indian Institute of Technology - Kanpur
2015	Master of Science in Structural Engineering
	University of California San Diego
2018	Doctor of Philosophy in Structural Engineering
	University of California San Diego

PUBLICATIONS

Fleischman, R., Restrepo J. I., **Nema A.**, Zhang D., Shakya U., Zhang Z., Sause R., Tsampras G., and Monti G. (2015) "Inertial force-limiting anchorage system for seismic resistant building structures" *Structures Congress*, pp. 1302-1313. 2015.

Zhang, Z., Fleischman, R.B., Restrepo, J.I., Guerrini, G., **Nema, A.**, Zhang, D., Shakya, U., Tsampras, G. and Sause, R., 2018. "Shake‐table test performance of an inertial force‐limiting floor anchorage system". *Earthquake Engineering & Structural Dynamics*, 47(10), pp.1987-2011.

Saunders, J.K., Goldberg, D.E., Haase, J.S., Bock, Y., Offield, D.G., Melgar, D., Restrepo, J., Fleischman, R.B., **Nema, A**., Geng, J. and Walls, C., 2016. "Seismogeodesy using GPS and low‐cost MEMS accelerometers: Perspectives for earthquake early warning and rapid response". *Bulletin of the Seismological Society of America*, 106(6), pp.2469-2489.

Nema A., Restrepo J. I., Conte J.P., Kelly, D.J. (in-preparation) "Improved three-dimensional modeling of structural walls and floor diaphragms"

Nema A. and Restrepo J. I. (in-preparation) "Seismic response of precast concrete gravity columns in a building system"

Nema A. and Restrepo J.I. (in-preparation) "Low-damage Columns for Accelerated Bridge Construction" *PEER Research Report*

Nema A. and Restrepo J.I. (in-preparation) "Shake table test and numerical simulation of a low-damage two column bridge bent"

ABSTRACT OF THE DISSERTATION

Development of Low Seismic Damage Structural Systems

by

Arpit Nema

Doctor of Philosophy in Structural Engineering

University of California San Diego, 2018

Professor José I. Restrepo, Chair

Modern society requires enhanced seismic performance from its structures that is beyond simple life-safety requirements, which has been the main design objective in the 20th and early 21st centuries. Multiple approaches to low-damage seismic structures have

been developed towards the end of the last century, one of which is the hybrid re-centering element approach studied experimentally and analytically in this work.

The first half of this dissertation focuses on the application of re-centering behavior to structural walls in multi-story structures. A four story, half scale structure with an eccentric arrangement of structural walls was tested dynamically at the UC San Diego Large High-Performance Outdoor Shake Table (LHPOST). The test also incorporated a new low damage gravity column concept. Results from the test provided valuable information about the two-dimensional seismic behavior of multi-story structures incorporating hybrid-re-centering structural walls.

An analytical model was developed for modeling the behavior of re-centering structural walls and calibrated as a part of a full three-dimensional model of the test specimen analyzed under a sequential application of the measured excitation history. An analytical model for a re-centering system applicable to moment frames was also developed and calibrated against experimental results from a previous study undertaken at UC San Diego. As a conclusion, the two models were incorporated into an analytical model of a thirteen-story structure with different lateral force resisting systems in orthogonal directions which was then studied using seven historic ground motions following the guidelines of ASCE/SEI 7-10 (2010).

The second half of the dissertation focuses on re-centering systems in bridge structures. A 35% scale, bridge bent with two hybrid re-centering columns was tested dynamically at the UC Berkeley PEER Shaking table. The specimen was constructed using a new socket connection based Accelerated Bridge Construction technique. Precast

construction was utilized for the three major bent components: the columns, the bent-cap and the foundation, which were then assembled at the test facility. Results from the test were used to calibrate the dynamic behavior of a computational model developed for the analysis of re-centering bridge columns. The proposed model improves upon earlier models resulting in significantly faster analysis speeds, allowing for the modeling of complete bridge systems in reasonable time-frames. Finally, the multi-column bridge bent model was incorporated into a comprehensive three-dimensional model of an existing bridge and used for studying the bridge response under different configurations of prestress force capacities and energy dissipation capacities.

Chapter 1

INTRODUCTION

1.1. Low-damage multi-story buildings

The short- and long-term recovery of a community in the aftermath of a seismic event is greatly affected by the damage experienced in some key structures, which are involved in either the immediate relief efforts, e.g. hospitals (Hall et al. 1994) or affect the long-term economy of the community, e.g. damage to high-rise apartments, buildings supporting local tourism, trade-ports or other industry (Chang 2000). Sustenance of our modern society has prompted the shifting of the performance objectives of these structures away from mere life-safety to the ability to return to full operation in a short time in the aftermath of significant earthquakes.

While the high importance structures like hospitals are adopting technologies like base-isolation to ensure continuous operation, such technologies are not seen as economically viable for other structures which impact the community in the long-term. Re-centering structural systems, including hybrid re-centering structural walls and hybrid re-centering moment frames, constitute a viable alternative for improving the

performance of importance structures. These systems concentrate deformation demands that arise during seismic events at specially designed rocking interfaces, resulting in low to no damage away from these interfaces and thus minimizing disruption of operation. At the same time, these systems are well suited for utilizing precast construction techniques, thus providing affordable and high-quality construction of structures with high seismic performance which can be erected in a shorter period as compared to more conventional monolithic structures.

In part, this work explores the bi-directional experimental performance of precast hybrid re-centering, low-damage structural walls under dynamic seismic excitations. The experimental work also evaluates the performance of a new low-damage gravity column concept, developed to provide supplemental vertical load bearing capacity while accommodating the bi-directional lateral deformations arising in a structure. Additionally, an analytical model is developed for predicting the response of low-damage walls which is then calibrated to the results from the experiment. A numerical model for predicting the response of low-damage moment frames is also developed and calibrated to test results from published experiments. As a culmination of this analytical work, the models for the two low-damage systems are incorporated into a 13-story building which is then analyzed dynamically under an ensemble of seven ground motions to verify the desired low-damage behavior at the structure level.

1.2. Low-damage bridge systems

As reported by the U.S. Geological Survey (2014), at least 40 percent of the United States of America can expect to experience earthquakes with the potential to

damage highway bridges within their lifetime. This problem is compounded by the fact that 54,560 bridges across the country are already considered structurally deficient as of 2017. These bridges often serve as key links in the local and national transportation networks, and any closures have a severe cost associated with them beyond merely the costs of repair or replacement, in the form of economic losses related to medium- and long-term interruption of local businesses and disruption of local communities (Palermo and Pampanin 2008). Additionally, the aftermath of any seismic event sees the importance of these bridges increase significantly, in terms of relief work access.

Considering the importance of these structures, the associated design philosophy is shifting from collapse prevention to the ability to return to full operation in a short time in the aftermath of moderate to strong earthquakes. In addition to performance, the associated construction philosophy is also being modernized with the utilization of Accelerated Bridge Construction (ABC) techniques to reduce impacts of construction work on traffic, society, economy and on-site safety during construction.

The latter half of this work presents the key features and seismic performance of a structural bridge subsystem designed and constructed around the aforementioned philosophies of low-damage structures and Accelerated Bridge Construction. Accelerated construction is achieved by utilizing precast columns and precast foundations/cap beams connected using an innovative dry-socket connection; while the concept of low-damage is incorporated in the form of hybrid re-centering behavior of the columns (Guerrini and Restrepo 2011; Restrepo et al. 2011). Re-centering columns are designed to display only minor damage localized at the interface between the column and foundation/bent cap,

under the same seismic demands that would cause extensive damage in conventional columns; and to return to their original position after the event, induced by unbonded post-tensioned elements. This results in a significant reduction in the repair costs and downtime. The work presented here is an enhancement to an earlier research (Guerrini et al. 2015), with a different outlook.

The bridge specimen presented in this work represents a 35% scale, two-column bent cap based on an existing bridge located in a high seismicity region. The specimen was tested under two component shaking table excitation dynamic excitations. The specimen showed a flag-shaped non-linear response typical of hybrid re-centering systems, with rocking behavior occurring at the interface between the columns and the foundation / bent-cap. The specimen was subjected to a total of twelve earthquakes at the University of California, Berkeley's Shaking table located at Richmond Field Station off-campus academic facilities. A numerical model of the test specimen was developed and verified using the dynamic test results. Finally, the dynamic model developed for re-centering bridge columns was incorporated into a three-dimensional model of an existing bridge, which was then used to study the bridge response under an ensemble of seven historic ground motion when outfitted with different configurations of re-centering bridge columns.

1.3. Outline

This dissertation is split into the following seven chapters:

- Chapter 1 Introduction

This chapter details the motivations, objective and scope of this research work and an outline of the content presented in the dissertation.

- Chapter 2 Literature Review

  Details of the research efforts on the experimental and analytical study of re-centering behavior in buildings and bridges, and on the development and testing of Accelerated Bridge Construction techniques as they apply to socket-based connections between bridge columns and bridge foundations / bent-caps.

- Chapter 3 Shake Table Testing of Low-damage Walls

  This chapter presents details and results of the shake table testing of a four-story, half scale specimen with hybrid-recentering walls and ductile gravity columns.

- Chapter 4 Analytical Simulation of a 13-Story Building

  The analytical modeling and verification of re-centering walls and re-centering moment frames is presented in this chapter, followed by an analytical study of re-centering behavior in a 13-story building.

- Chapter 5 Shake Table Testing of Low-Damage Bridge Bents

  Details and results from a dynamic, bi-directional shake table test of a bridge bent with two re-centering columns are presented in this chapter.

- Chapter 6 Analytical Simulation of 4-bent Prototype Low-Damage Bridge

  This chapter presents the development of an analytical model of hybrid re-centering bridge columns. The analytical model was used for making

decisions relating to the dynamic test presented in Chapter 5. After the completion of testing, the model was further calibrated to the experimental results. Finally, an analytical study of an existing bridge redesigned using different configurations of re-centering columns is presented.

- Chapter 7 Conclusions

  The main findings of this research work and proposed future work.

Chapter 2

LITERATURE REVIEW

Low-damage, re-centering structural systems, particularly those based on hybrid rocking behavior, have been the subject of significant research efforts in the past few decades. Given their excellent seismic performance demonstrated by the low damage observed in subassembly tests and their suitability for fast and high-quality construction using pre-fabricated components, re-centering systems are prime candidates for mitigating the issues of extensive damage, costly repairs and associated downtimes to critical services seen in recent earthquakes.

2.1. Low-damage structural systems in buildings

The earliest reported implementation of re-centering systems was in an industrial chimney at the Christchurch, New Zealand airport (Sharpe and Skinner 1983). Built in 1977, the chimney employed a passive rocking mechanism combined with hysteretic dampers to meet architectural and engineering requirements.

The PREcast Seismic Structural Systems (PRESSS) project was one of the earliest works to explore, both experimentally and analytically, the performance of hybrid

rocking systems. The project started as a study into the seismic performance of precast systems (Priestley 1991). The analytical work by Priestley and Tao (1993) studied the behavior of partially unbonded prestressing tendons in precast moment frame connections for preserving prestressing forces under large ductilities. The experimental behavior of re-centering frames was studied experimentally by MacRae and Priestley (1994) and then improved in the works of Stone et al. (1995) in terms of energy dissipation by incorporating mild steel reinforcement across joints.

The promising results from these studies led to further analytical investigations into hybrid self-centering systems (El-Sheikh et al. 1999; Kurama et al. 1999) and culminated in the simulated seismic test of a 60% scale, five story structure (Nakaki et al. 1999; Priestley et al. 1999) incorporating a hybrid coupled wall in one direction, and hybrid and precast moment frames emulating precast connections in the other direction as lateral force resisting systems. The excellent results observed for reinforced concrete systems resulted in the extension of hybrid re-centering systems to steel moment frames (Christopoulos et al. 2002), masonry walls (Toranzo-Dianderas 2002), and testing of several precast concrete configurations (Holden et al. 2003; Perez et al. 2003).

Multiple Energy dissipation solutions to improve the performance in re-centering systems have been explored by different authors, including milled bars in grouted ducts (Restrepo and Rahman 2007), viscous and mild steel external dissipators (Marriott et al. 2009), flexural external dissipators (Toranzo et al. 2009) and steel plate fuses (Eatherton and Hajjar 2014), while the behavior and effect of hybrid components has been explored experimentally by Belleri et al. (2014).

2.2. Low-damage bridge columns

The first rocking bridge columns were inspired by the rocking chimney described by Sharpe and Skinner (1983), implemented in the "stepping" railway bridge over the South Rangitikei River, Zealand (Cormack 1988) and included torsional hysteric energy dissipators for controlling drifts.

A pioneering study on the application of rocking systems to bridges was carried out by Mander and Cheng (1997), which included both theoretical development and experimental validation of hybrid bridge columns. Their work was followed by multiple analytical and experimental studies on hybrid bridge columns, exploring construction methods, energy dissipation solutions and numerical simulation options. Hewes and Priestley (2002) studied the experimental and analytical performance of segmented rocking bridge columns with unbonded prestressing steel and without additional elements for energy dissipation, under different levels of initial prestress and varying thickness steel jackets confining the columns' plastic end regions. Kwan and Billington (2003a; b) and Ou et al. (2006) performed analytical studies on re-centering columns using Finite Element Analysis (FEA). Sakai and Mahin (2004) and Hieber et al. (2005) studied the behavior of hybrid bridge columns using fiber-based elements, with the former followed by shaking table tests (Jeong et al. 2008). Palermo and Pampanin (2008) conducted analytical studies using lumped plasticity to model a prototype bridge, with supporting data from experiments comparing the performance of cantilevered monolithic and hybrid columns under monotonic and cyclic loading (Palermo et al. 2007). Mariott et al. (2009, 2011) developed analytical models utilizing multiple springs to model the rocking

interface, and conducted uni- and bi-directional quasi-static cyclic tests on monolithic and hybrid columns, exploring different energy dissipation solutions. Guerrini et al. (2013; 2015) tested dual shell hybrid bridge columns under cyclic loading and shaking table excitation; their work explored options for external and internal energy dissipation, and the improvement of prestressing (PT) bar deformability through the addition of polyurethane pads. Thonstad et al. (2016) tested a two-column, three-bent system with precast elements under shaking table excitation.

2.3. Bridge pier socket connections

The use of precast concrete elements offers an excellent mean for reducing on-site construction work, and has been implemented for some time in the construction of bridge girders, columns and cap beams in low seismic regions. However, the construction of the bridge substructure in seismically active regions is done mostly using conventional cast-in-place methods. This trend primarily stems from limited research into the seismic performance of precast connections. Considering the significant advantages precast systems display, increased research efforts are underway exploring various methods for emulating cast-in-place, fixed-end connections, in addition to the development of precast element connections similar to those used for re-centering systems where a localized gap is allowed to develop.

Precast columns, either hybrid or emulating a fixed-base connection, can be connected to the precast or cast-in-place foundations and bent caps through reinforcing bar couplers, grouted ducts, pockets or sockets. The use of grouted ducts or reinforcing bar couplers typically involves prefabrication of the column over its clear height, with

either the duct or the coupler embedded inside. Grouted duct connections are commonly used in hybrid bridge column studies and have been explored by Pang et al. (2010), Restrepo et al. (2011) and Tazarav and Saiidi (2015). The performance of couplers with grouted splices has been studied by Ameli et al. (2016; 2015), while mechanical splices were explored in Haber et al. (2014). For both connection types, the bedding mortar at the interface requires careful attention to develop the full potential of the column, more so for hybrid systems.

Pocket connections typically involve rebars extending out from the connecting precast members, which need to be carefully meshed together before they are surrounded by either grout or concrete. This connection type has been explored in Restrepo et al. (2011). Socketed connections allow the entire precast column to be embedded inside the end beam, which may be precast with a socket or cast on site by placing its reinforcing cage around the precast column. When used with precast cap beams or foundations, socket connections result in very easy to assemble systems. A conservative design treatment of this connection type is included in some design codes (AIJ,1988, DIN 1045), and both theoretical and experimental results for improved capacity calculation have been presented in Osanai et al. (1996), Blandon and Rodriguez (2005) and Fernandes Canha et al. (2007). The application of this connection to hybrid bridge columns has been explored by Haraldsson et al. (2013a), Mashal et al. (2012; 2013), Belleri and Riva (2012) and Thonstad et al. (2016).

Chapter 3

SHAKE TABLE TESTING OF LOW-DAMAGE WALLS

3.1. Introduction

This chapter presents the design, construction and results from a four-story precast concrete structure tested at the University of California San Diego Large High-Performance Outdoor Shake Table (LHPOST). The shake table test was a part of a three-year long joint research project involving the University of Arizona (UoA), University of California San Diego (UC San Diego) and Lehigh University (LU), with the primary objective of the project being the development and testing of Force-Limiting Self Centering (FL-SC) floor anchorage systems. In addition to the study of the FL-SC connection, the experiment also provided an opportunity for the testing of precast hybrid rocking walls, ductile precast gravity columns and the use of high strength steel reinforcement in reinforced concrete construction. Data obtained from the test was invaluable for the assessment of the performance of FL-SC systems, and for the verification and enhancement of analytical models developed for predicting the response of buildings utilizing the various structural systems tested.

The structure consisted of cast-in-place rigid floor diaphragms supported vertically by ductile precast gravity columns and laterally by precast, post-tensioned structural walls. The test specimen was purposely built with an eccentric wall layout to develop a coupled longitudinal-torsional response on a unidirectional shake table, to better represent the behavior of buildings under multi-directional ground shaking. Additionally, the structure layout and connections allowed for the modification of response from a force-limiting configuration to full-lateral restraint structural configurations with hybrid rocking walls and emulative monolithic walls. The configurations tested were (a) rocking walls with force-limiting lateral connections (Phase I) (b) rocking walls fully resisting inertial forces (Phase II) and (c) conventional fixed-base walls resisting inertial forces (Phase III). The multi-phase testing provided a unique opportunity to test and compare the performance of different lateral resistance systems for the same structure.

3.2. Design

The prototype structure for the test is a 4-story Seismic Design Category E residential building designed for a Site Class C location in downtown Berkeley. The site-specific ground motion parameters obtained from ASCE7-05 were S_S=2.08, S_1=0.92 and T_L=6 seconds and the design live load on the structure was 1.92 kPa (40 psf). The prototype has a footprint of 46.3 m x 28.0 m (152-ft x 92-ft), with a 203 mm (8-inch) thick floor slab supported by 356 mm (7-inch) square columns spaced at 7 m (23') in the transverse direction and 7.7 m (25'-4") in the longitudinal direction. Lateral force resistance is provided by reinforced concrete structural walls 406 mm (16-inch) thick,

with four walls 4.27 m (14-ft) long in the longitudinal direction and eight walls 3.45 (11-ft 4-inch) long in the transverse direction. The typical story height is 3.2 m (10-ft 6-inch). The floor plan of the prototype is shown in Figure 3.1.

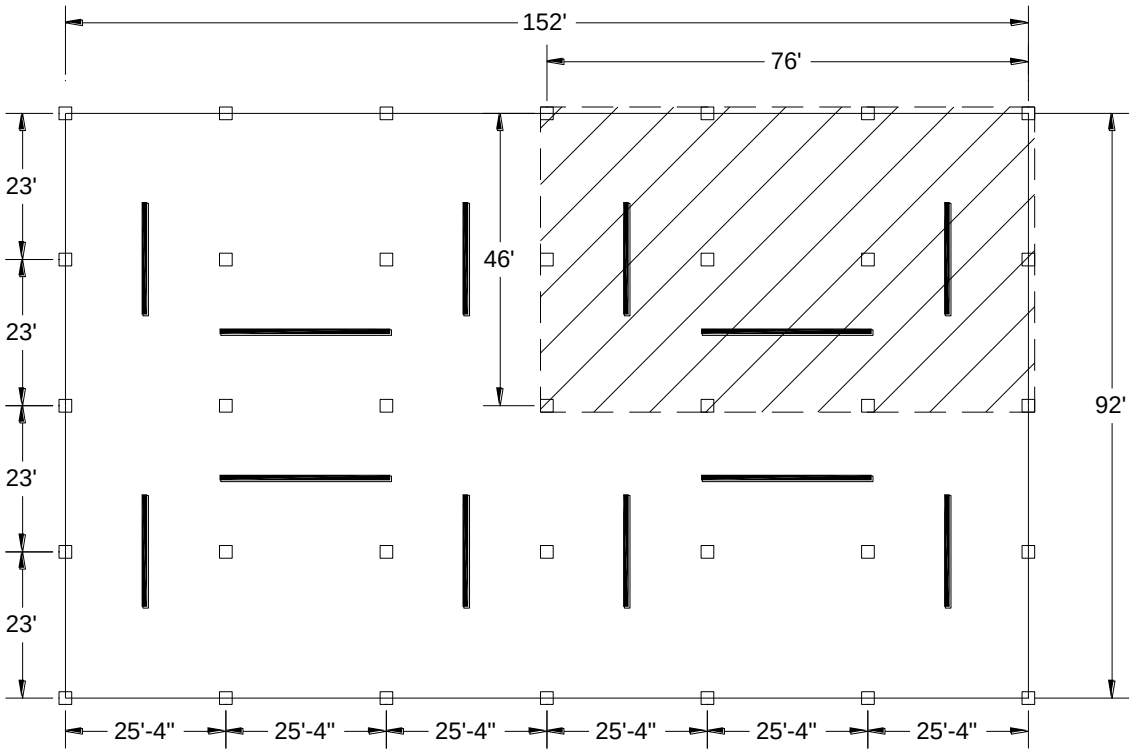

Figure 3.1 Prototype structure floor plan

The test specimen was extracted from one quadrant of a four-story structure, as highlighted in Figure 3.1. Only a single quadrant of the structure was selected to take advantage of the eccentric layout of the walls. This eccentricity ensured a coupled lateral-torsional response, which allowed for the evaluation of different FL-SC devices and lead to the development of realistic deformations in the low-damage columns.

The shake table dimensions of 12.2 m x 7.6 m (40-ft x 25-ft) required that the specimen dimensions be scaled down 50% in addition to representing a single quadrant of the prototype. However, the scaling of the inter-story heights was limited to 66% to

ensure ease of access for construction and inspection. Additional scaling was required for the mass of the structure with the objective of maintaining similar stresses between the prototype and the specimen, which resulted in thicker floor slabs than required based on dimensional scaling. The test specimen and its floor plan are shown in Figure 3.2, Figure 3.3 and Figure 3.4.

Details of the specimen scaling and the design of the specimen components are presented in the following sections.

Figure 3.2 Test specimen

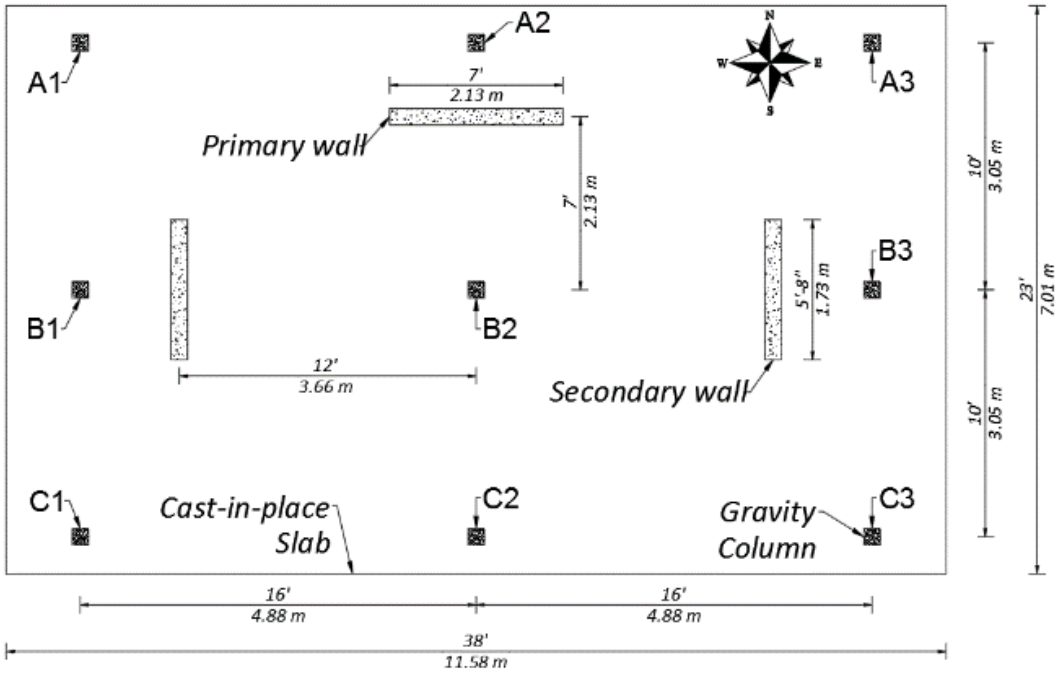

Figure 3.3 Test specimen plan

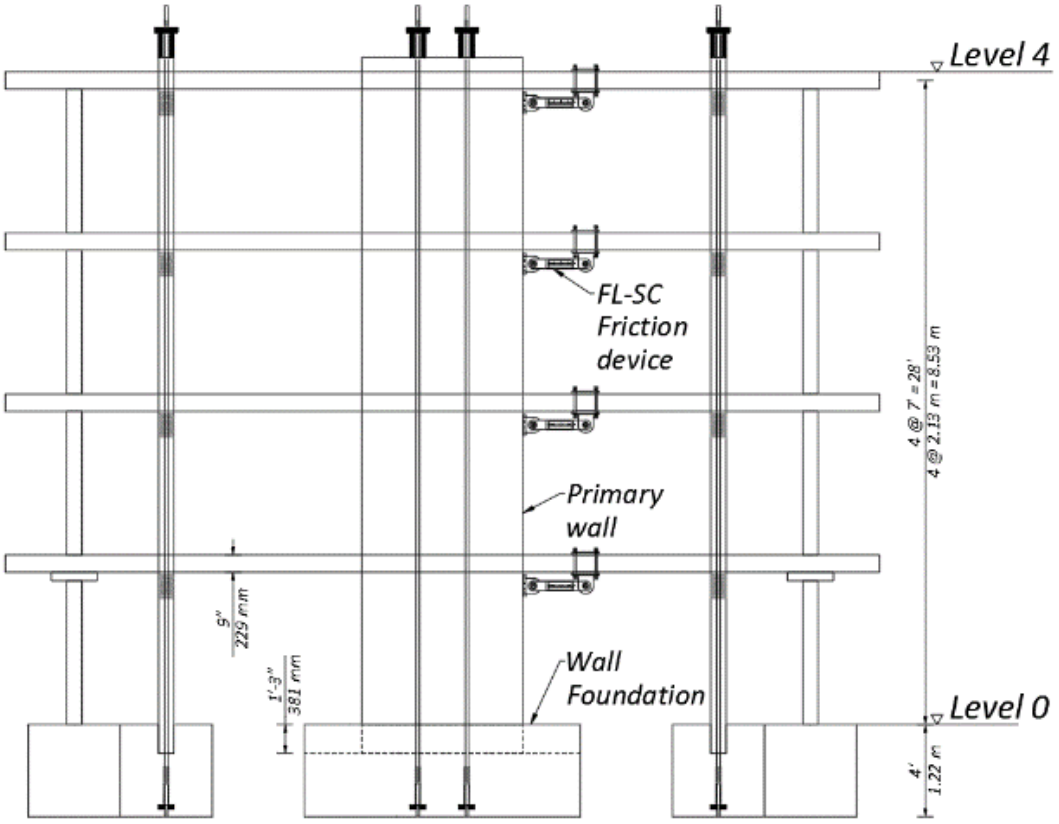

Figure 3.4 Test specimen elevation

3.2.1. Scaling

The specimen scaling procedure involved mass substitution in addition to geometrical scaling. The additional mass was required for similitude between stresses in the specimen and the prototype.

Scaling in the model space without mass substitution is derived from the length scale, defined as the ratio of the model unit length to the prototype unit length, as defined by equation 3.1(a). The remaining scale factors are derived from the length scale factor assuming consistent mass density and mass material modulus between the prototype and the specimen and are listed in equations 3.1(b) to (g).

Length $$S_l = \frac{l_m}{l_p} = 50\% \quad (3.1(a))$$

Area $$S_A = \frac{A_m}{A_p} = \frac{l_m^2}{l_p^2} = S_l^2 \quad (3.1(b))$$

Volume $$S_V = \frac{V_m}{V_p} = \frac{l_m^3}{l_p^3} = S_l^3 \quad (3.1(c))$$

Mass $$S_M = \frac{M_m}{M_p} = \frac{\rho V_m}{\rho V_p} = S_l^3 \quad (3.1(d))$$

Force $$S_F = \frac{F_m}{F_p} = \frac{M_m g}{M_p g} = S_l^3 \quad (3.1(e))$$

Stress $$S_\sigma = \frac{\sigma_m}{\sigma_p} = \frac{F_m/A_m}{F_p/A_p} = S_l \quad (3.1(f))$$

Stiffness $$S_K = \frac{K_m}{K_p} = \frac{EA_m/l_m}{EA_p/l_p} = S_l \quad (3.1(g))$$

As can be noted from equation 3.1(f), the stresses in the model space are scaled by the factor S_l. To impose similitude in terms of stresses, additional mass is added to the

system such that equation 3.1(f) with the total modified mass results in a scale factor of 1. The additional mass required can then be obtained from the total model space mass necessary for stress similitude. This relation is expressed in equation 3.2(a). Finally, the scale time scale factor can be obtained using the masses and stiffnesses in the model and prototype space (equation 3.2(b)).

$$S'_{\sigma} = 1 = \frac{M'_m g/A_m}{M_p g/A_p} \Rightarrow M'_m = M_p S_l^2 = \frac{M_m}{S_l} \qquad \Delta \mathrm{M_m} = M'_m - M_m = M_m \frac{(1 - S_l)}{S_l} \qquad 3.2(a)$$

Time $$S'_T = \frac{T_m^2}{T_P^2} = \frac{\sqrt{M'_m/K_m}}{\sqrt{M_p/K_p}} = \sqrt{S_l} \qquad 3.2(b)$$

Acceleration $$S'_a = \frac{l_m/T_m^2}{l_m/T_P^2} = 1 \qquad 3.2(c)$$

3.2.2. Floor Slabs

The slabs were intended to function as rigid diaphragms connecting together the lateral force resisting system and the gravity load resisting system and were also the primary source of inertial mass. All slabs measured 7 m (23-ft) wide x 11.5 m (38-ft) long, with openings for walls, and were cast-in-place. The slab thickness at 229 mm (9-inches) was greater than the required by 50%-dimensional scaling. This was done to provide the additional inertial mass as required by the scaling target of maintaining equivalent stresses between the prototype and the specimen.

ASTM A52 steel plates were embedded in the slabs at various locations to facilitate the installation of different lateral-force transmitting components:

- force-limiting devices for the first phase of testing, bolted through holes provided

in the slabs at one end and bolted to plates embedded in the structural walls at the other end.

- elastomeric bearings between walls and slabs to provide limited re-centering.
- slotted shear connectors, welded to plates embedded in the slabs and connected to the structural walls through a vertical slotted connection. These connectors provided full lateral force transmission for Phase II of testing without restraining relative vertical movement.
- bumpers bolted to the slabs to control contact forces in the event of large slab-wall relative movement. The mechanical response of the bumpers was tested in Zhang (2017), and is shown in Figure 3.7.

The slabs were designed using grillage analysis. The design forces were calculated from the load combination of $1.6\,D + 1.2\,L$. Primary reinforcement was provided by 4-in x 4-in W6.7/W6.7, ASTM A185 Grade 80 welded-wire reinforcement (WWR) mesh at the top and bottom of the slabs. The mesh was doubled in locations of high stresses, typically around gravity columns and the locations of lateral force transmitting connections. Additional reinforcement was provided by #4 ASTM A706 Grade 60 rebars around the wall openings. The sites of column-slab connections were also additionally reinforced against punching shear failure using bent up stirrups. The layout of reinforcement in the slab, excluding the wire mesh, is shown in Figure 3.5.

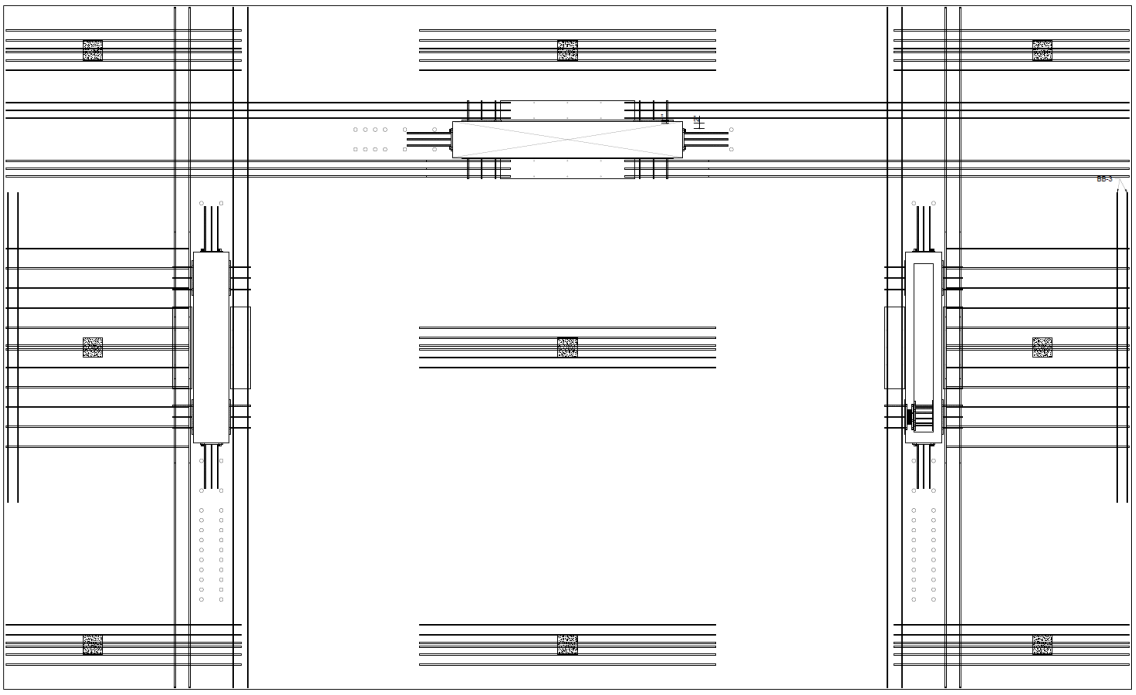

Figure 3.5 Typical slab reinforcement

Figure 3.6 Bumper elements

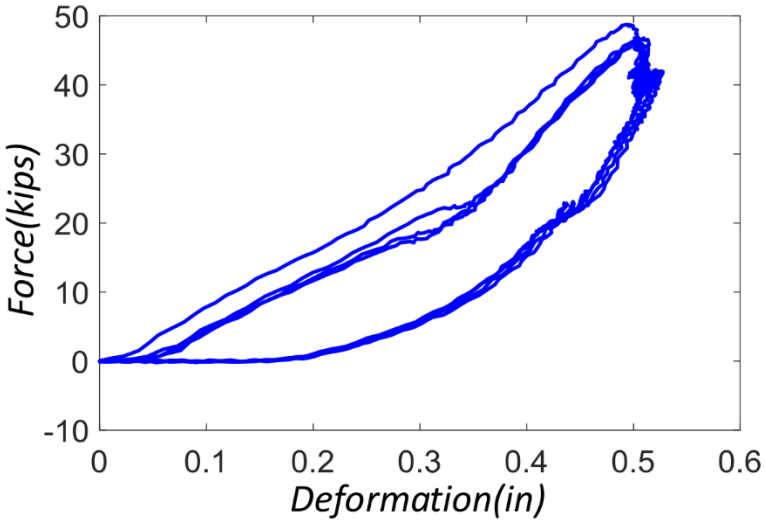

Figure 3.7 Bumper response

3.2.3. Low-damage gravity columns

A new gravity column concept was employed in the test structure to ensure satisfactory performance over the course of testing. The structure was expected to undergo multiple cycles of significant inter-story drifts, requiring highly ductile behavior from the gravity columns. The desired behavior was achieved by concentrating the longitudinal reinforcement in the ends at the center of the column section, with all the perimeter reinforcement being continuous only over the clear story height. The proposed arrangement of longitudinal reinforcement results in a smaller flexural stiffness due to a reduced moment arm in the section, and at the same time provides ductile behavior by reducing the strains in the central longitudinal rebar and the concrete. The reduction in strains and heavy confinement by the concrete at the column center provides improved protection against column failure resulting from buckling and fracture.

The columns were designed to meet the axial demands calculated as a part of the grillage analysis done for the design of slabs. The columns were designed following

Section 21.13.14.1 of ACI 318-11, which pertains to the design of members not designated as part of the seismic force-resisting system. The applicable ACI 318-11 provisions for the column design and the compatibility of the final columns with the provisions is listed in Table 3.2.

All the columns were 203 mm (8-inch) square, precast over the story clear height of 1.9 m (75-inch). Each column was reinforced with 8 #3 ASTM A1035 Grade 100 bars around the core perimeter and designed to bear the largest axial load given by the grillage analysis, which was the axial load in the center column at the foundation level. The design axial loads for the columns are given in Table 3.1. The 8 #3 bars were terminated within the column and a single #7 ASTM A1035 Grade 100 bar, which was similar in strength to the perimeter bars, provided continuity with the columns and slabs of adjacent levels. The connection to adjacent levels was facilitated by the provision of a corrugated sleeve in one half of the column, and a near 3ft length of #7 rebar protruding out of the other half. The slabs were cast around a 9in length of the protruding rebar, and the remaining length was grouted inside the sleeves in the upper columns. Each column was heavily confined using doubled #2 reinforcement hoops over the end 635 mm (25-inch) and single #2 reinforcement hoops over the column middle, which also acted as shear reinforcement in the column. The column reinforcement layout and the connection details are shown in Figure 3.8. Some pictures of the columns during the precast construction process are presented in Figure 3.9

Column installation began with leveling using four L-shaped steel feet bolted to the column bottom, while leaving a 0.5-inch gap underneath to be filled with grout for

improving the contact area with the foundation, as shown in Figure 3.10. After leveling all the columns, the gaps were sealed, and the connection was grouted with non-shrink, non-metallic high strength grout poured at fluid consistency.

Table 3.1 Column axial load ratio, listed as a percent of design f'_cA_g

Column	A1	A2	A3	B1	B2	B3	C1	C2	C3
Design gravity loads	10.6	20.9	10.7	21.2	45.4	19.3	10.6	20.9	10.7
Expected axial loads	8.94	12.9	8.94	11.1	15.4	11.1	8.94	12.9	8.94

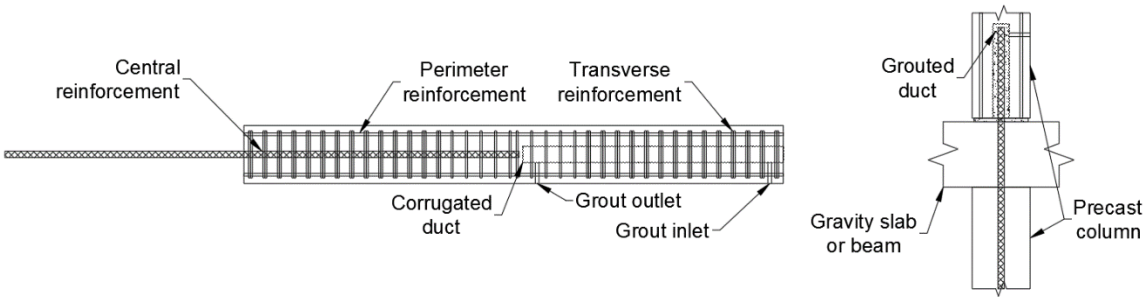

Figure 3.8 Gravity column reinforcement and connection details

3.2.4. Low-damage walls

Three walls, each 9.22 m (30-ft 3-inch) tall and 203 mm (8-inch) wide, composed the vertical elements of the Lateral Force Resisting System (LFRS). The primary wall, which provided resistance in the direction of shaking, was 7ft wide, while the two secondary walls, which provided resistance to the twisting induced due to the eccentric wall layout, were 1.73 m (5-ft 8-inch) wide. The walls were seated on high strength grout beds at the bottom of 381 mm (15-inch) deep grooves in their corresponding foundations; the grooves provided a means to convert the walls from low-damage walls to emulative monolithic walls. The walls were designed for rocking behavior in Phases I and II of the test, and monolithic behavior for Phase III of the test. The reinforcement layout for the

walls are shown in Figure 3.11 and Figure 3.12. The flexural energy dissipators installed on the walls are shown in Figure 3.15.

(a) Gravity column perimeter reinforcement cage

(b) Columns with fresh poured concrete

(c) Finished columns ready for transport

Figure 3.9 Column construction at the precast plant

(a) Central bar pre-installed in foundation

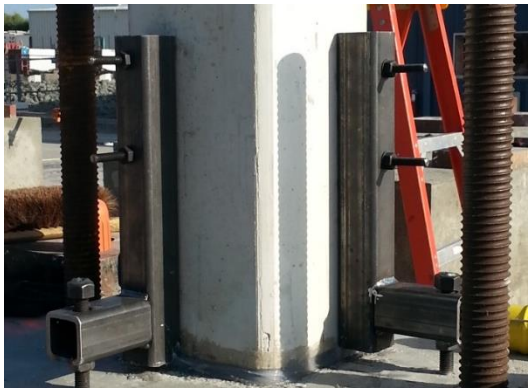

(b) Column ready for grouting

Figure 3.10 Column assembly

Table 3.2 Applicable ACI 318-14 provisions for the design of low-damage gravity columns

Section	Design requirement
18.14.2	Design gravity load: 1.2D + 1.0L + 0.2S or 0.9D
18.2.5	Concrete strength limits • $f_c' \geq 3\ ksi$ • $f_c' \leq 5\ ksi$, if using lightweight concrete

18.2.6	Reinforcement strength and ductility requirements
	• Longitudinal steel: deformed bars limited to Gr 60 A706 steel
	• Transverse steel: limits on yield strength for design purposes:
	  ○ Confining reinforcement: $f_y \leq 100\ ksi$
	  ○ Shear reinforcement: $f_y \leq 60\ ksi$

18.7.4	Longitudinal reinforcement requirements • Bounds on area of longitudinal reinforcement. $0.01\ A_g \leq A_{st} \leq 0.06 A_g$ • At least six longitudinal bars in columns with circular hoops

18.7.5	• Confinement reinforcement requirements
	  ○ Extent of confinement, l_o, shall be at least the greatest of:
	  ○ Depth of column at the joint face, d
	  ○ One sixth of the clear span of the column, L_c
	  ○ 18 in.
	• Maximum spacing of transverse reinforcement, s shall be less than:
	  ○ One-fourth the minimum column dimension
	  ○ Six times the diameter of the smallest longitudinal bar
	  ○ $s_o = 4 + \frac{14 - h_x}{3} \leq 6\ in.$
	• Amount of transverse reinforcement, Table 18.7.5.4
	  ○ For rectilinear hoops:
	  ▪ $\frac{A_{sh}}{s\ b_c} \geq Max\left\{0.3\ \left(\frac{A_g}{A_{ch}} - 1\right)\ \frac{f_c'}{f_{yt}}\ , 0.09\frac{f_c'}{f_{yt}}\right\}$
	  ▪ $\frac{A_{sh}}{s\ b_c} \geq 0.2\ k_f k_n \frac{P_u}{f_{yt} A_{ch}}$, if $P_u > 0.3 A_g f_c'\ \ OR\ f_c' > 10{,}000\ psi$
	  ○ For spiral or circular hoops:
	  ▪ $\rho_s \geq Max\left\{0.45\ \left(\frac{A_g}{A_{ch}} - 1\right)\ \frac{f_c'}{f_{yt}}\ , 0.12\frac{f_c'}{f_{yt}}\right\}$
	  ▪ $\rho_s \geq 0.35\ k_f k_n \frac{P_u}{f_{yt} A_{ch}}$, *if* $P_u > 0.3 A_g f_c'\ \ OR\ f_c' > 10{,}000\ psi$
	• For transverse reinforcement outside of length l_o, maximum spacing, s, shall be less than:
	  ○ Six times the diameter of the smallest longitudinal bar
	  ○ 6 in.

Table 3.2 Applicable ACI 318-14 provisions for the design of low-damage gravity columns (continued)

Section	Design requirement
18.7.6	Shear reinforcement requirements • Design force, V_e, to be calculated considering maximum forces that can be generated at the face of the joints at each end of the column • Concrete shear capacity, $V_c = 0$, if both of the following conditions occur: ○ Earthquake-induced shear force is at least one-half of the maximum required shear strength within l_o ○ Factored axial compressive force P_u including earthquakes is less than $A_g f_c'/20$
25.4	Development length, central reinforcement • Tension: $l_d = \left(\frac{3}{40} \frac{f_y}{\lambda\sqrt{f_c'}} \frac{\psi_t \psi_e \psi_s}{\left(\frac{c_b + K_{tr}}{d_b}\right)} \right) d_b$ • Compression: $l_{dc} = Max \left\{ \frac{f_y \psi_r}{50\lambda\sqrt{f_c'}} \ , 0.0003 f_y \psi_r \right\} d_b$
25.5	Non-contact splice length between central and perimeter reinforcement • Lap splice not permitted for bars larger than No. 11 • Tension: ○ $l_{st} = Max\{1.3\ l_d, 12\ in.\}$ ○ Different sized bars being spliced, l_{st} is greater of l_d of the larger bar and l_{st} of the smaller bar • Compression: ○ For $f_y \leq 60\ ksi$, $l_{sc} = Max\{0.0005 f_y d_b, 12\ in.\}$ ○ For $f_y > 60\ ksi$, $l_{sc} = Max\{(0.0009 f_y - 24) d_b, 12\ in.\}$ ○ Different sized bars being spliced, l_{sc} is greater of l_{dc} of the larger bar and l_{sc} of the smaller bar

Wall design for rocking behavior was based on Displacement Based Design principles (Belleri 2009) and followed the guidelines given in Restrepo and Rahman (2007). Each secondary wall was designed to have half the strength of the primary wall. For improved re-centering, the walls were provided with high-strength unbonded post-tensioning bars. Two ASTM A722 46 mm (1.75-inch) diameter bars with a Guaranteed

Ultimate Tensile Strength (GUTS) of 1030 MPa (150 ksi) were installed through 80 mm (3 1/8 -inch) Inner Diameter (ID) ducts in the primary wall and two 36 mm (1.375-inch) bars with 1030 MPa GUTS were installed through 51 mm (2-inch) ID ducts in each of the secondary walls. The wall post-tensioning provides an easy method for regulating the wall strength, which was utilized to test the specimen behavior under low-strength, moderate-ductility and high-strength, low ductility configurations of the primary wall. The bars were post-tensioned using anchor plates mounted on hollow-core plunger jacks resting on top of the wall. The seating areas for the plunger jacks were locally reinforced to prevent crushing of concrete in the walls. To prevent early PT bar yielding, elastic polyurethane pads were installed between the plunger jack and the wall for each bar. With these pads, bar tensile requirements are partially transformed into compressive deformation in the pads.

Energy dissipation in the walls, to help control lateral displacement and acceleration demands, was provided by external flexural energy dissipators at the base of the walls. These dissipators, developed by Toranzo (2002), have a variable cross section designed to ensure that yielding and energy dissipation occurs over their entire length. Eight dissipators were installed in the primary walls and four dissipators were installed in each of the secondary walls. The attachment of the dissipators involved a welded connection to the wall face at one end and a hinged connection to the foundation at the other. The external installation allowed for easy inspection and replacement of the dissipators over the course of testing.

Under rocking behavior, the wall flexural openings are concentrated at the rocking interface unlike monolithic walls where flexural deformations are distributed over a plastic hinge length. This results in large compressive stresses in the wall toes, which are further magnified due to impacts actions during wall rocking. To ensure elastic performance of the walls under these stresses, each wall of the test specimen was heavily confined at the base using a 203 mm (8-inch) wide ASTM A572 Gr 50 steel channel at the base and two 9.5 mm (3/8-inch) thick ASTM A572 Gr 50 steel plates over a 305 mm (12-inch) height at each toe surface. Since shear force transfer at the base of rocking walls happens primarily through friction, weld beads were provided in the toes of the steel channels to improve the force transfer and prevent sliding behavior in the walls. Some pictures of the North wall during precast and installation are shown in Figure 3.13 and Figure 3.14.

For Phase III of testing, the walls were designed for monolithic behavior, following the guidelines of ASCE7-10 and ACI 318-11. The walls were designed as Special RC Walls with $R = 6, \Omega_o = 2.5$ and $C_d = 1$. Longitudinal reinforcement in the walls was provided by ASTM A1035 Grade 100 #4 rebars, with the number of rebars reduced above the 2nd level, and shear reinforcement was provided by two ASTM A1035 Grade 100 #3 bars spaced at 254 mm (10-inch) on center. Each wall was provided with heavily confined boundary elements in the plastic hinge region, extending over the lower 3.5 m (12-ft) of the wall. These regions, spanning a length of 508 mm (20-inch) in the primary wall and 355 mm (14-inch) in each secondary wall, were confined using ASTM A1035 Grade 100 #2 plain bars spaced at 50.8 mm (2-inch) on center. The locations of

the lap splices in the longitudinal bars between the 2nd and 3rd levels were also heavily confined. Slab gravity loads in the walls for Phase III were simulated by wall post-tensioning stresses.

Transfer of forces from the slabs to the walls was through the force limiting devices in the first phase of testing. The devices were connected to plates embedded in the wall during construction. For the second and third phase of testing, the force-limiting devices were replaced by slotted shear connectors, as shown in Figure 3.16 to ensure the full transfer of lateral forces between the slabs and the walls. This detail allowed for relative vertical and rotational movement between the walls and the slabs and was designed to accommodate the vertical uplift in the walls arising due to rocking in Phase II and plastic hinge elongation in Phase III. These connectors required the installation of vertical slots in the walls during their construction. Anchor straps were screwed into the slots before the beginning of the second phase, and the other end of the straps were then welded to the plates embedded in the slabs. This detail precluded the walls from bearing the gravity load of the slabs, and the transfer of vertical uplift forces in the slabs and the columns. To further stiffen the connection provided by the PSA connectors, roller bearings were also installed in the gap between the edge of the wall and the floor slab.

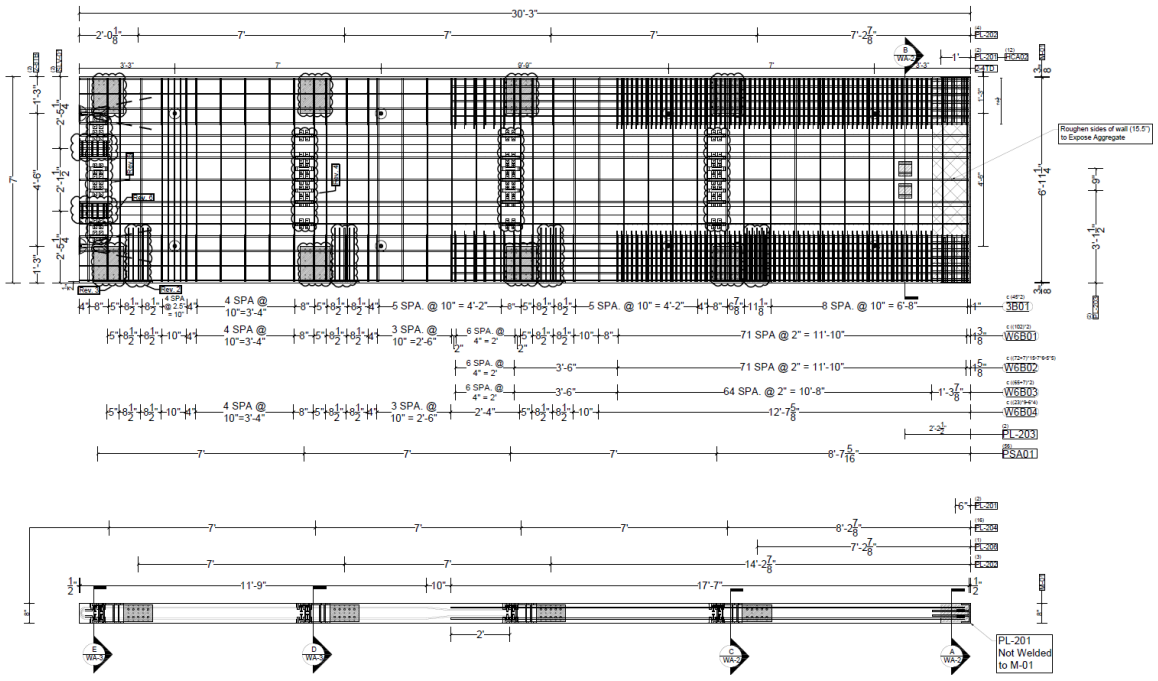

Figure 3.11 North wall reinforcement layout

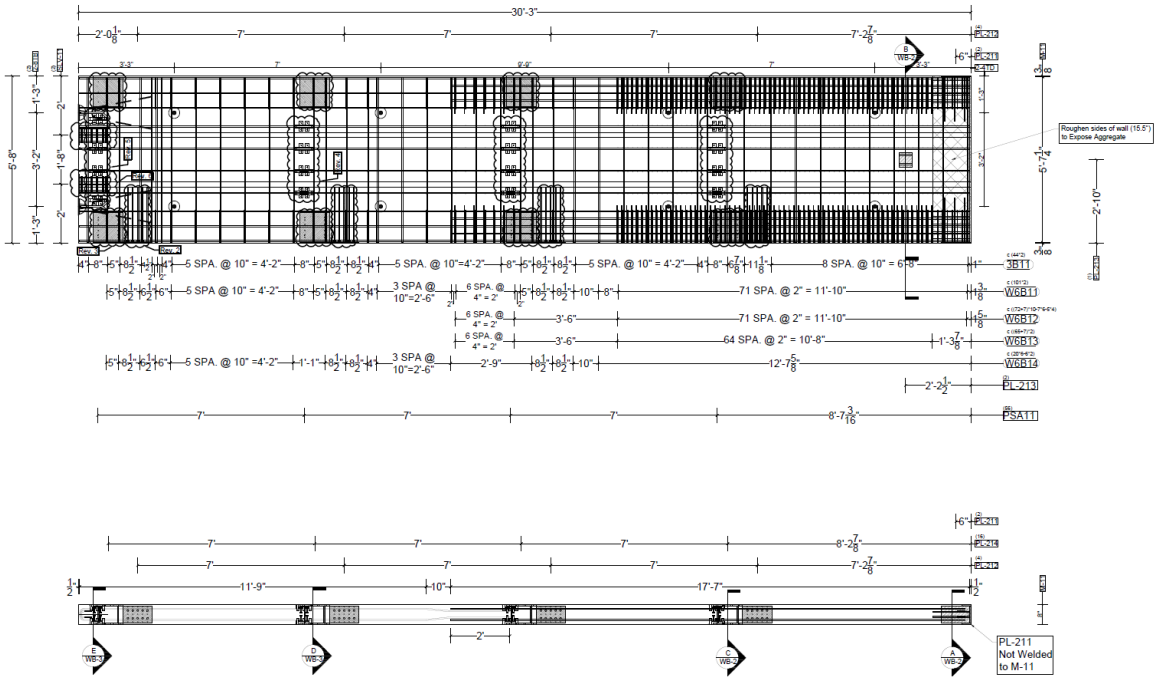

Figure 3.12 East/West wall reinforcement layout

(a) North wall reinforcement cage

(b) North wall end channel with beads

Figure 3.13 North wall construction at the precast plant

(a) North wall being lifted

(b) North wall being guided using PT bars

(c) Polypropylene fibers for wall bed grout

(d) Wall bed preparation

Figure 3.14 North wall installation

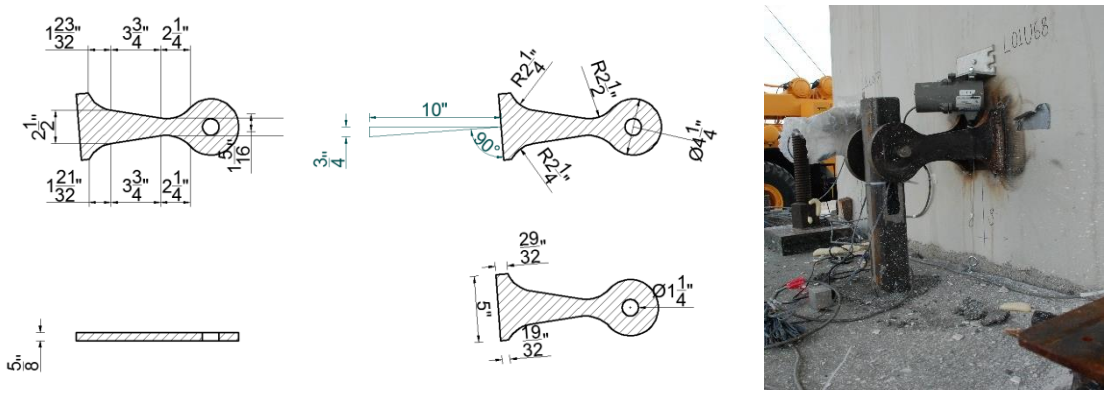

Figure 3.15 Wall flexural energy dissipators

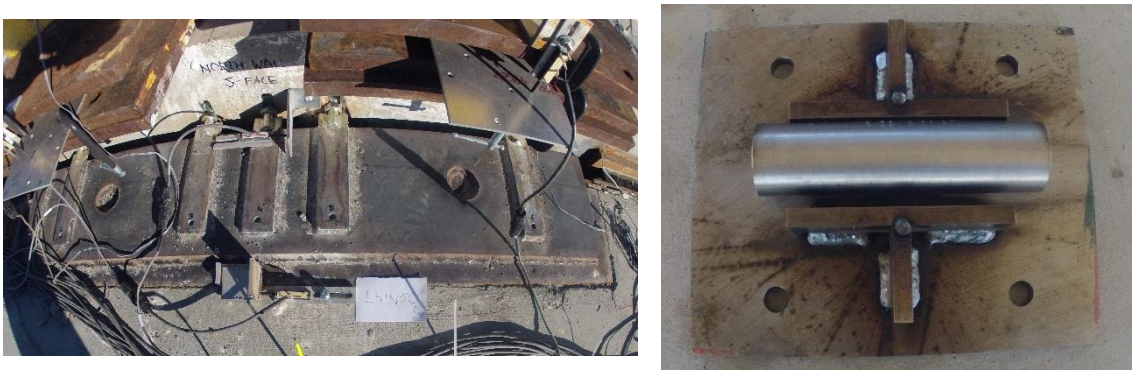

Figure 3.16 Slotted shear connector (primary wall) and roller bearing

3.2.5. Force-Limiting Self-Centering (FL-SC) connections

Two prototype force-limiting devices were tested during this experiment. For the primary wall, force-limiting behavior was provided by a device designed and produced at the Lehigh University which utilizes friction to limit the force that can be transmitted. The friction damper (FD) device, as shown in Figure 3.17(a), consists of two fiberglass-brass shims sliding on either side of a steel plate with slotted holes. The normal force, and hence the slip force, between the shims and the steel plate can be easily and precisely controlled by tightening the bolts going through the shims and the steel plate. In the aftermath of an earthquake, the force can be reduced by loosening the bolts and the slabs can then be easily moved to undo any relative displacement.

An alternative force-limiting device for use with the secondary walls was developed at UC San Diego and utilizes steel yielding to achieve the desired effect. The buckling restrained dissipator (BRD) device, illustrated in Figure 3.17(b), consists of a 25.4 mm (1-inch) diameter ASTM A576-1018 Grade 40, hot-rolled round stock with portions milled down to a smaller diameter of 12.7 mm (0.5-inch). The milled down portions, which are limited to lengths of 50.8 mm (2-inch) to avoid buckling during compression, yield in compression and tension to limit the forces that can be transferred. The milled bar is encased inside a steel pipe with the inner diameter close to that of the round stock, and this assembly is then placed inside a larger diameter outer pipe with the space between filled with grout. This setup ensures that there is no global buckling in the device.

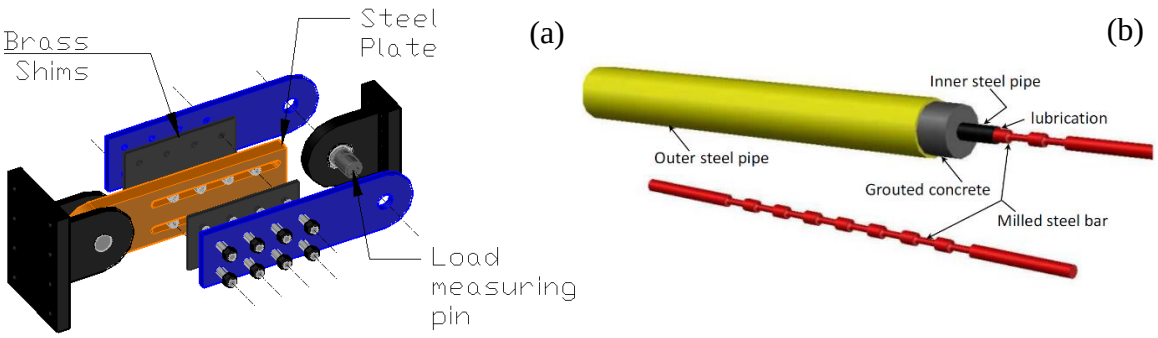

Figure 3.17 Force limiting devices: (a) Friction Damper (b) Buckling Restrained Dissipator

Both the friction and buckling-restrained force-limiting devices were connected to the walls and slabs through spherical bearings installed on pinned clevises to reduce transfer of moments and shears. In addition to the force-limiting devices, elastomeric bearings also connected the slabs and the walls, with four bearings per wall at each floor. Each bearing was 51 mm (2 inch) thick and was formed from carbon fibers sandwiched

between eight square layers of rubber. The bearing geometric and material properties are listed in Table 3.3. These bearings with a soft response in the transverse direction and a stiff response in the axial direction, provided limited re-centering forces along the wall longitudinal direction, while keeping the wall centered in the slot in the slabs in the wall transverse direction.

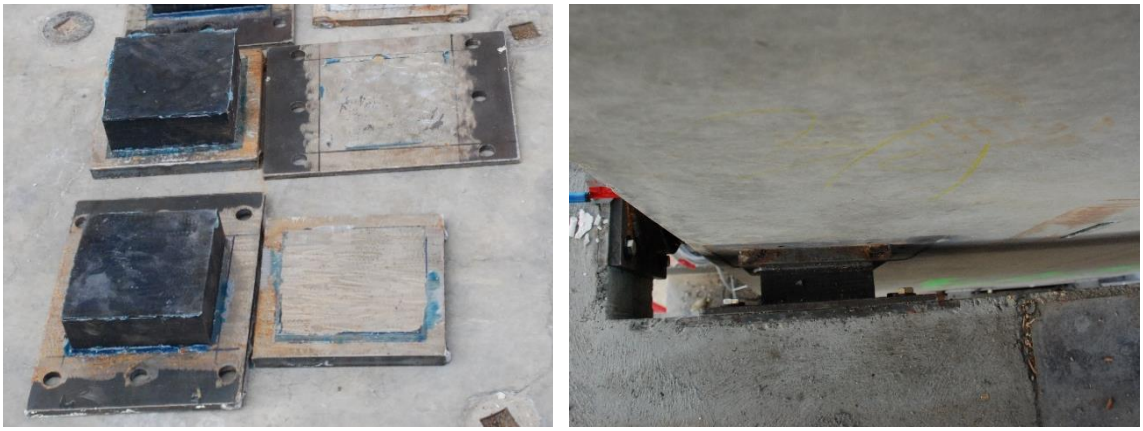

Figure 3.18 Elastomeric bearings

Table 3.3 Elastomeric bearing properties

Location	Shear modulus		Length		Shear stiffness		Compression stiffness		Tension stiffness	
	MPa	ksi	mm	in	N/mm	kip/in	N/mm	kip/in	N/mm	kip/in
East-West wall	0.655	0.095	178	7	21.2	45.4	19.3	10.6	20.9	10.7
North-South wall			152	6	11.1	15.4	11.1	8.94	12.9	8.94

3.2.6. Foundations

The primary function of the foundation structure was to transfer the table motion to the base of the building. This required special provisions to accommodate the unique nature of the columns and the walls. To provide a stiff connection between the shake table and the test structure, all the foundations were 1.22 m (4-ft) thick and clamped to

the table using post-tensioning bars installed through tie-down holes present in the shake table platen at 0.61 m (2-ft) intervals.

The nine column foundations measured 1.22 m (4-ft) tall x 1.22 m (4-ft) long x 0.61 m (2-ft) wide and were tied down with a total force of 1.3 MN (300 kip) for each foundation. ASTM A1035 Grade 100 #4 staple shaped reinforcing bars formed the longitudinal and transverse reinforcement. Additionally, each of the column foundations had a 0.91 m (3-ft) length of ASTM A1035 Grade 100 #7 rebar protruding out vertically to provide the starting central reinforcing bars required by the gravity columns. The reinforcement layout for a typical column foundation is shown in Figure 3.19.

The three wall foundations were 1.22m (4-ft) wide and 1.22 m (4-ft) tall, with a length of 3.6 m (12-ft) for the primary wall and 3.0 m (10-ft) for each of the two secondary walls. The tie down force was provided by bars post tensioned to 890 kN (200 kip) per bar for a total of 10.7 MN (2400 kip) in the primary wall foundation (12 bars) and 7.1 MN (1600 kip) in each of the two secondary wall foundations (8 bars). The anchorage system for wall post-tensioning was embedded in the foundations during construction. Additionally, HSS 2 ½ posts were embedded in the foundations to facilitate the installation of the wall energy dissipation devices.

For converting the walls from rocking behavior to monolithic, fixed-base configuration, the wall foundations had a 304 mm (15-inch) deep by 229 mm (9-inch) wide socket in the center for wall placement. The filling of this groove with high strength grout achieved the conversion to fixed-end configuration for the walls. The bottom of each groove was embedded with T-headed bars near the wall toes to prevent damage due

to impact forces during wall rocking in the first two phases of testing. The longitudinal reinforcement in the wall foundations was provided by 12 #4 rebars at the top and 8 #4 rebars at the bottom, split evenly on each side of the groove. Transverse reinforcement was provided by 2 #4 hoops and 2 #4 ties, with greater concentration near the wall toes to assist in transferring the uplift forces in the fixed-base configuration. The reinforcement layout for the wall foundations is presented in Figure 3.20.

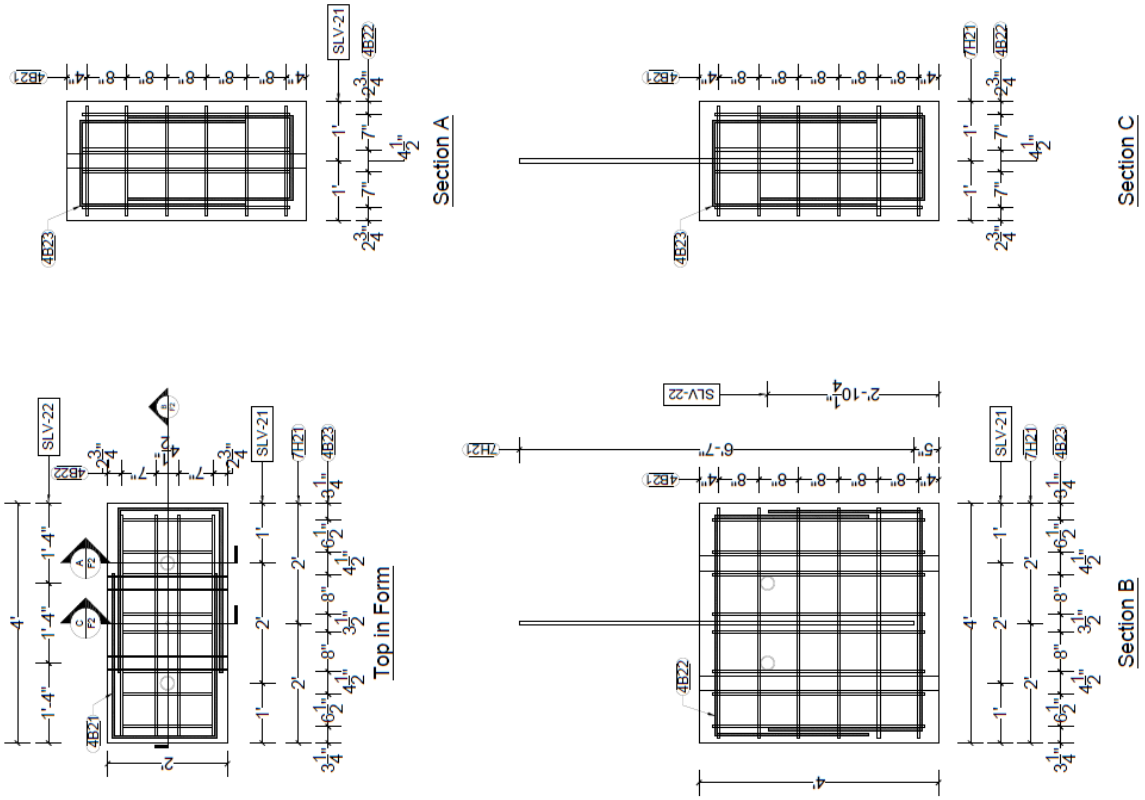

Figure 3.19 Column foundation

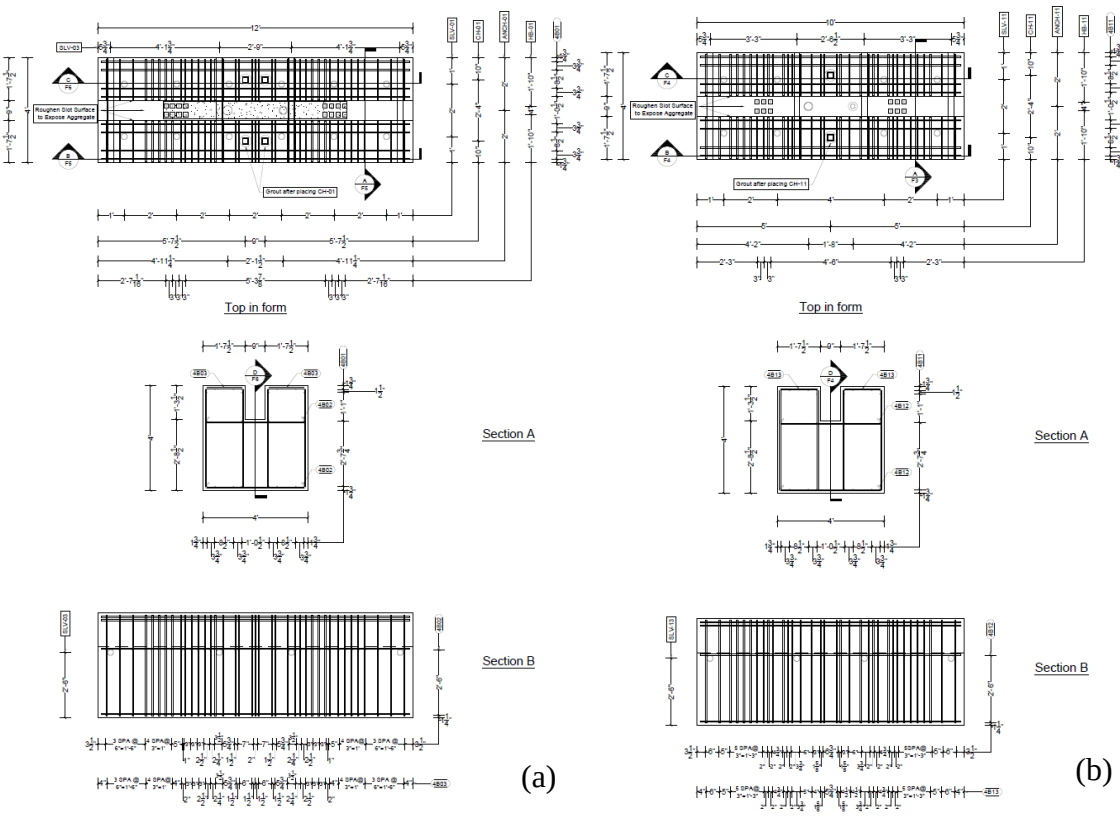

(a) (b)

(a) North wall **(b) East / West wall**

Figure 3.20 Wall foundation reinforcement layout

3.3. Material properties

3.3.1. Concrete

The specified strength of concrete was 48 MPa (7 ksi) for the precast elements, 41.4 MPa (6 ksi) for the foundations and 34.5 MPa (5 ksi) for the gravity slabs. The compressive strength was measured using 152 mm (6-inch) diameter and 305 mm (12-inch) high standard concrete cylinders. Sample cylinders were tested for strength 28-days after concrete casting and before the beginning of each phase of the experiment. The sample cylinders from the slabs were also tested for their 3-day strength to ensure sufficient strength for the installation of the next level of gravity columns. The average

strengths measured on each day of testing are listed in Table 3.4. For the cylinders tested before the beginning of each test phase, stress-strain data was also obtained using a compressometer. Typical compressometer stress-strain responses of the concrete cylinders before the start of Phase II are shown in Figure 3.21(a).

3.3.2. Grout

High strength, non-shrink grout was used in the column connections, to form the base of the rocking walls and to create the emulative-monolithic connection between the walls and foundations. Reinforcing polypropylene fibers were added, in a proportion of 0.04% by weight, to the mortar bed under the rocking walls to improve the strength and toughness. Compressive strengths of the grouts were measured using 50.4 mm (2-inch) diameter and 101 mm (4-inch) high standard cylinders at 28-days, and at the beginning of each phase of testing. The average of the strength measured from three sample cylinders is listed in Table 3.4.

3.3.3. Structural steel

ASTM A1035 Grade 100 steel was specified for the reinforcement used in the walls, columns and the foundations, while ASTM A706 Grade 60 steel was used for the reinforcing bars in the slabs in addition to the ASTM A185 Grade 80 Welded Wire Reinforcement. The milled steel bars used in the BRD devices were obtained from ASTM A576-1018 Grade 40 round bars. The unbonded prestressing steel bars used in the walls were specified as ASTM A722 Grade 150 steel. Finally, the wall energy dissipators were obtained by water-jet cutting from ASTM A572 Grade 50 steel plates.

Table 3.4 Measured strengths of cementitious materials

Member (Casting Date)	Age (Days)	28	DOT-1 (12-Dec-13)	DOT-2 (18-Dec-13)	DOT-3 (16-Jan-14)
Foundation (18-Sep-2013)	MPa	43.6	50.4	-	-
	ksi	6.32	7.31	-	-
Column (12-Sep-2013)	MPa	38.5	41.4	43.9	45.9
	ksi	5.58	6.0	6.36	6.65
North wall (19-Sep-2013)	MPa	53.6	51.7	58.7	61.5
	ksi	7.78	7.5	8.51	8.92
East/West wall (24-Sep-13)	MPa	61.2	65.8	64.7	65.4
	ksi	8.87	9.54	9.39	9.48
Slabs	MPa	46.5	54.1	58.5	58.7
	ksi	6.74	7.85	8.48	8.51
Column grout	MPa	66.3	71.3	62.6	58.5
	ksi	9.61	10.3	9.08	8.49
Rocking interface grout	MPa	80.9	84.2	80.4	-
	ksi	11.7	12.2	11.6	-
Phase III grout 5-Day strength	MPa			59.8	
	ksi			8.67	

Samples from the ASTM A1035 Grade 100 and ASTM A706 Grade 60 reinforcement bars used in the walls, columns, slabs and foundations were tested under monotonic loading, and the ASTM A576-1018 Grade 40 bars used in the BRD devices were tested under monotonic and cyclic loading. Table 3.5 lists the measures stress-strain properties from these tests. Also included in the table are the properties for the ASTM A572 Grade 50 steel plates used in the wall dissipators as obtained from the mill-certificates. The average stress strain response for the deformed ASTM A1035 Grade 100 reinforcement is shown in Figure 3.21(b).

Table 3.5 Structural steel mechanical properties

Material	Elastic modulus		Yield stress		Yield Strain	Onset of strain hardening	Ultimate stress		Uniform Strain
	GPa	ksi	MPa	ksi	(%)	(%)	MPa	ksi	(%)
A706	182	26400	617	75	0.47	0.88	770	112	11.2
A1035	182	26400	914	133	0.70	n/a	1167	169	5.5
A50	n/a	n/a	440	64	n/a	n/a	573	83	n/a
A576	201	29100	352	47	0.36	2.55	450	65.3	19

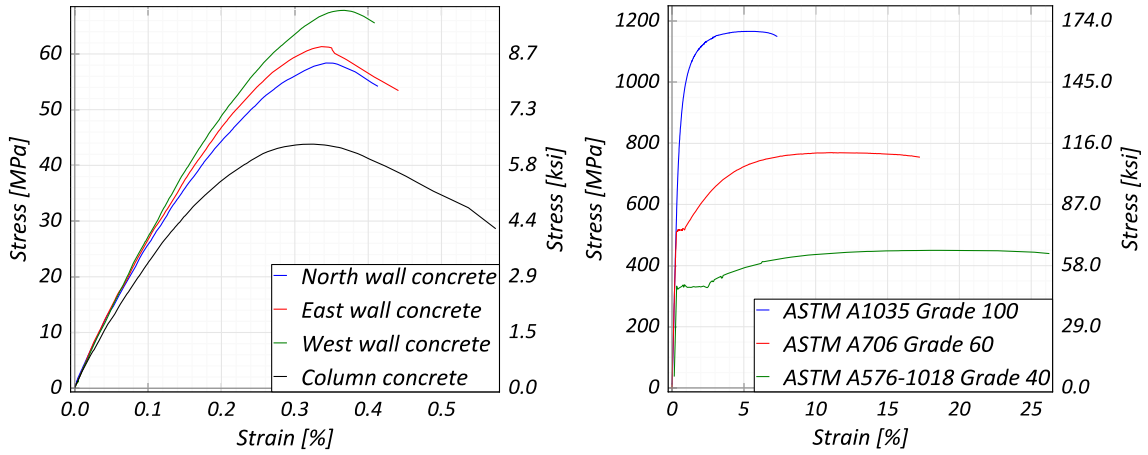

(a) Concrete **(b) Steel**

Figure 3.21 Material stress-strain response

3.4. Test program

3.4.1. Instrumentation

Over 250 sensors were used to capture the response of the structure in each of the test phases. A summary of the installed sensors is presented in Table 3.6. Due to differences in the lateral force resisting system in each phase, slightly different sensor setups were used in each phase of testing. Different types of sensors were installed to measure accelerations, displacements, strains, pressures, wall rotations and forces. These sensors were recorded at six Data Acquisition (DAQ) Systems, with 64 channels per

module. Sensor data was sampled at a synchronized rate of 240 samples per second. These sensors were in addition to and synchronized with 32 sensors present on the shake table platen to provide actuator feedback information. The platen sensors were recorded at a dedicated DAQ at 256 samples per second and the data from these sensors was resampled at 240 Hz to match the sampling rate of the other six DAQs. The typical sensor layout is shown in the plan and elevation view in Figure 3.22.

Table 3.6 List of sensors installed on the four story test specimen

Sensor type	Count	Sensor type	
String pots	32	Strain gauges	83
LVDT	58	Load cells	4
Pressure Transducers	6	Spring loaded linear pots	12
Accelerometers	63	GPS	6

At least four accelerometers were installed on each floor to measure the accelerations in the East-West direction and the North-South direction, with additional accelerometers on the roof. The 1st and 3rd floors were also fitted with accelerometers measuring vertical accelerations. Accelerometers measuring the input ground motion acceleration were installed on both the shake table platen and the structure foundations. Finally, accelerometers for measuring impacts in the North wall were installed on the wall South face.

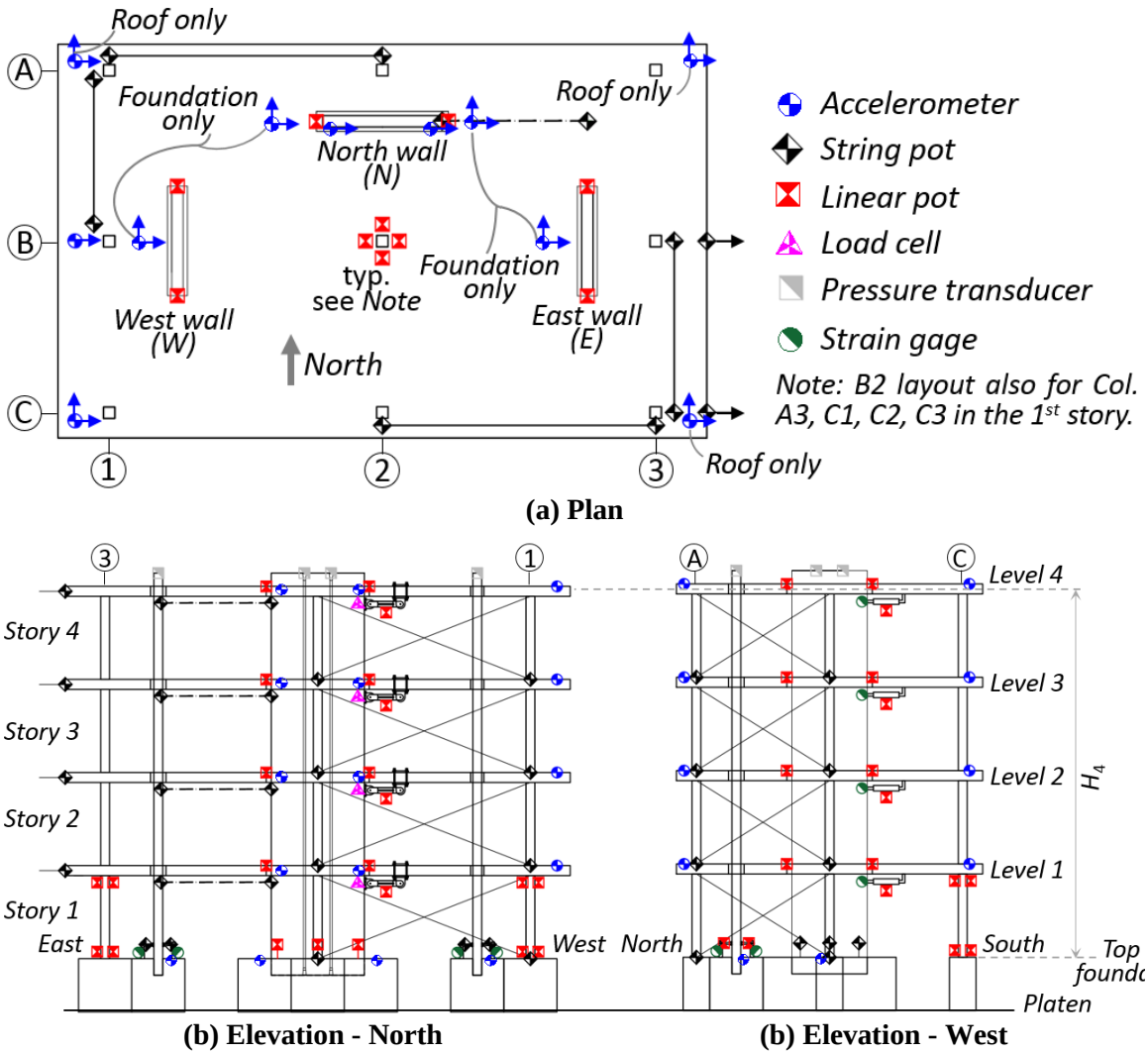

(a) Plan

(b) Elevation - North **(b) Elevation - West**

Figure 3.22 Typical instrumentation, four-story test specimen

String potentiometers, used where large displacements were expected, were installed in X-shape configurations as shown in Figure 3.22(b) and (c) on lines AB-West, 23-South, 12-North and BC-East at each level to measure the relative displacements between the floors. Two string potentiometers per floor were also connected between the East perimeter and a rigid tower anchored outside the shake table platen to measure the absolute displacement of the test specimen. A string potentiometer was installed at each

floor between the East-West wall and the slab at a sufficient distance from the wall to measure wall-floor relative displacement with minimal effects from wall uplift.

Linear Voltage Displacement Transducers (LVDT) with strokes smaller than 127 mm (5 inch) were used for finer, localized deformations. 6 LVDTs per wall were used at the wall bases for measuring the wall uplift and base rotations. LVDTs were also used to measure the uplift and horizontal relative displacement between the walls and floor slabs, to measure the column end rotations at the bottom and top regions of select first level columns and to measure the deformation of the FD and BRD devices.

Spring loaded linear pots, with a measurement range smaller than 50.8 mm (25.4 inch) were used for measuring the deformation of the bumpers at the roof level and for measuring the lateral deformation of the PSA connectors. For Phase III of testing, spring loaded linear pots were used to measure the wall local deformation at the foundation level.

5mm electrical foil strain gauges were installed on select reinforcing bars in the boundary elements of the North wall, in the first level precast gravity columns with attached LVDTs and in the PT bars to measure their longitudinal deformations. Strain gauges were also installed on the BRD devices and on the wall energy dissipators to gauge the forces developed in these elements.

Pressure transducers were installed on the wall post-tensioning bars to dynamically measure the applied axial forces on the walls. Forces in the FD devices were measured using commercial load sensing clevis pins which connected the devices to the North wall. Electronic gyroscopes were installed on top of the North wall to measure the

wall rotation at the roof level. Six GPS instruments, five at the roof and one at connected to the foundation on line A1, were installed as a part of a payload project (Saunders et al. 2016).

Sixteen GoPro cameras were used to record some key responses during shaking at a high resolution, to help with the visualization and interpretation of data, and capture crack openings in the walls and columns. Two additional cameras placed off the platen were used to record the overall structural response.

3.4.2. Test sequence

The test structure was subjected to ground motions selected and scaled to match the target response spectra at 5% damping from two sites with moderate (Seattle, Washington) and high (Berkeley, California) levels of seismic hazard. The selected ground motions came from the 1979 Imperial Valley event for the Seattle site, and from the 1989 Loma Prieta event for the Berkeley site. Details of the ground motions are given in Table 3.7, and the scaled time histories are shown in Figure 3.23(a) and Figure 3.23(b). The target response spectra and the response spectrum of the matching ground motion are shown in Figure 3.23(c).

Table 3.7 Earthquake records

Record Name	Earthquake	M_w	Station	Site location	Scale factor, DE	Scaled PGA
BE05	Loma Prieta	7.0	Los Gatos Pres. Center / 000	Berkeley	0.723	0.41
SE05	Imperial Valley	6.5	El Centro Array #5 / 140	Seattle	1.140	0.59

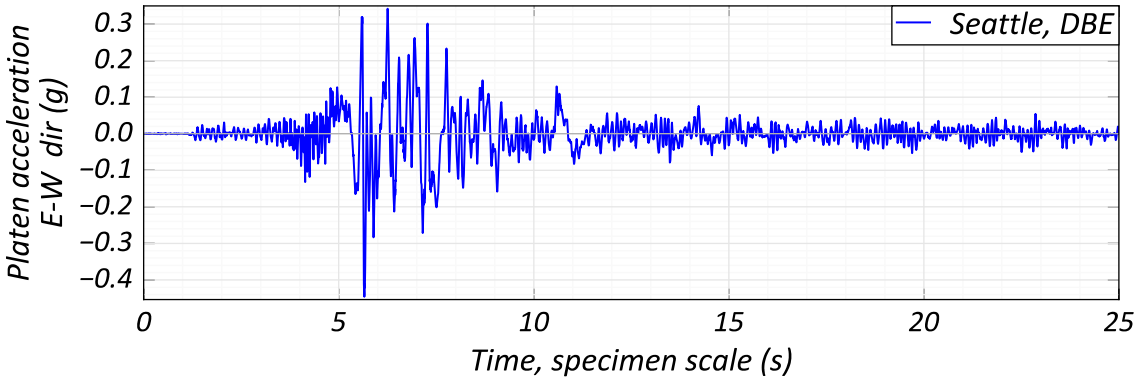

(a) Seattle record time history

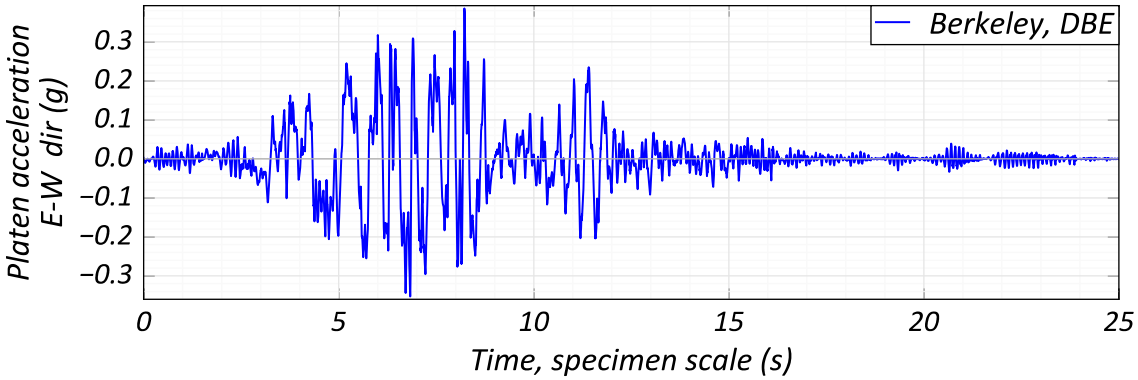

(b) Berkeley record time history

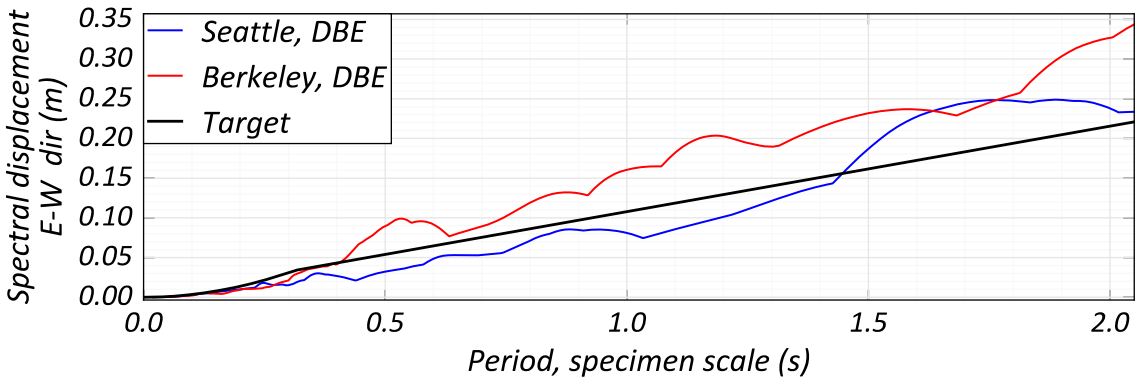

(c) Spectral displacement

Figure 3.23 Input acceleration record details

The experiment was executed in three phases, with a different configuration of the LFRS tested in each phase. Phase I tested the hybrid rocking walls and the FL-SC system. Since this phase covered the primary objective of the test, multiple configurations

were tested, with different combinations of limiting force and post-tensioning forces in the walls. The FL-SC system was replaced with stiff horizontal links in Phase II, in order to provide comparison data for the FL-SC performance. Finally, the walls were rigidly connected to the foundation for Phase III, modeling a more conventional structure. The rigid connection was created by filling a socket surrounding the walls, provided in the respective foundations for this purpose, with high strength non-shrink grout. The floor diaphragms and gravity columns remained unchanged, providing an excellent test for the cyclic load capacity of the columns.

Table 3.8 Shake table test sequence

Phase	EQ#	Record x Scale	Initial PT (% f_{pu})		FD Slip Force (kip)	Phase	EQ#	Record x Scale	Initial PT (% f_{pu})		FD Slip Force (kip)
			N	E/W					N	E/W	
	EQ01	BE05 x 0.67	61.4	54	11.5		EQ12	BE05 x 1.5	58.8	63.3	25.1
	EQ02	BE05 x 0.67	61.2	54	20.8	I	EQ13	BE05 x 1.0	58.8	65.8	19.9
	EQ03	SE05 x 1.0	61.2	54	20.8		EQ14	BE05 x 1.5	58.8	65.8	19.9
	EQ04	BE05 x 1.0	61.2	54	20.8		EQ15	SE05 x 1.00	62.5	70.5	N/A
	EQ05	BE05 x 0.67	49.3	54	28.5		EQ16	BE05 x 0.67	62.5	70.5	N/A
I	EQ06	SE05 x 1.0	49.3	54	28.5	II	EQ17	BE05 x 1.0	62.5	70.5	N/A
	EQ07	BE05 x 1.0	49.3	54	28.5		EQ18	BE05 x 1.0	60.0	62.5	N/A
	EQ08	BE05 x 1.0	49.7	54	19.2		EQ19	BE05 x 1.5	60.0	62.5	N/A
	EQ09	SE05 x 1.5	49.7	54	19.2		EQ20	BE05 x 1.0	45.3	70	N/A
	EQ10	BE05 x 1.5	49.7	54	19.2	III	EQ21	BE05 x 1.5	45.3	70	N/A
	EQ11	BE05 x 1.0	58.8	63.3	25.1		EQ22	BE05 x 1.5	45.3	70	N/A

For each configuration, the structure was subjected to multiple motions with increasing intensities. A typical test sequence consisted of a design basis earthquake (DBE) for the Seattle site, followed by a DBE for the Berkeley and a maximum considered earthquake (MCE_R) for the Berkeley site. Additionally, the structure was also subjected to white noise ground motions at the beginning and end of each test sequence

to characterize its dynamic properties. These motions were synthesized with the aim of exciting the structure with a consistent amount of energy, distributed evenly in a wide band of frequencies. A complete list of the excitations (except the white noises) imposed on the structure is presented in Table 3.8.

3.5. Test results

In the test results presented below, global lateral displacements have been normalized by height of the roof (9.22 m / 363 inch) and are expressed as drift ratios. Base shears have been normalized by the structure weight, 2024 kN (455 kip) and overturning moments have been normalized by the product of the structural weight and the roof height (18.7 MN-m / 13800 kip-ft). Post tensioning forces have been normalized by the ultimate force capacity of the respective bars as calculated from the nominal bar area and the Guaranteed Ultimate Tensile Strength, GUTS (1034 MPa / 150 ksi). Any non-normalized values have been scaled back to prototype space, unless otherwise stated. Positive transverse drifts and accelerations are defined to be towards the North and the East directions while positive rotations are defined along the North axis. All the results have been filtered through a 5-point Butterworth low-pass filter with a cut-off frequency of 25 Hz.

3.5.1. Global performance

The peak and residual drifts observed at the floor geometric center during the test are shown in Figure 3.24. Note that the grouped results indicate responses in the structure in response to a continuous set of excitations, during which properties like the FD slip force and PT bar prestress were not modified externally. The re-centering nature of the

structure can be inferred from the negligible residual drifts seen during Phase I and Phase II. The specimen showed significant residual drifts under the MCE_R level ground motions during Phase III of testing. Under EQ21 (Phase III), in addition to damage in the structural walls, failure was also observed in the emulative fixed-base connection between the foundation and the primary wall. Figure 3.25 shows the peak and residual twisting seen in the roof level slab. The effect of the FL-SC system is clearly visible here in the form of smaller twisting in the slab, due to the limited inertia forces transferred to the structural walls.

Figure 3.26 shows the peak accelerations measured at the geometrical center of the floors. From this figure, a preliminary conclusion would be smaller accelerations in the structure when the lateral force transfer is not limited between the floor and the walls. However, when accounting for the torsional response of the floors, the accelerations in Phase II become equal if not greater than those in Phase I, as shown in Figure 3.27. Thus, the results in Figure 3.26 and Figure 3.27 demonstrate the importance of two-dimensional testing for structural systems. Phase III has larger floor accelerations than both Phase I and Phase II which is a result of the greater stiffness of the structural walls under fixed base condition.

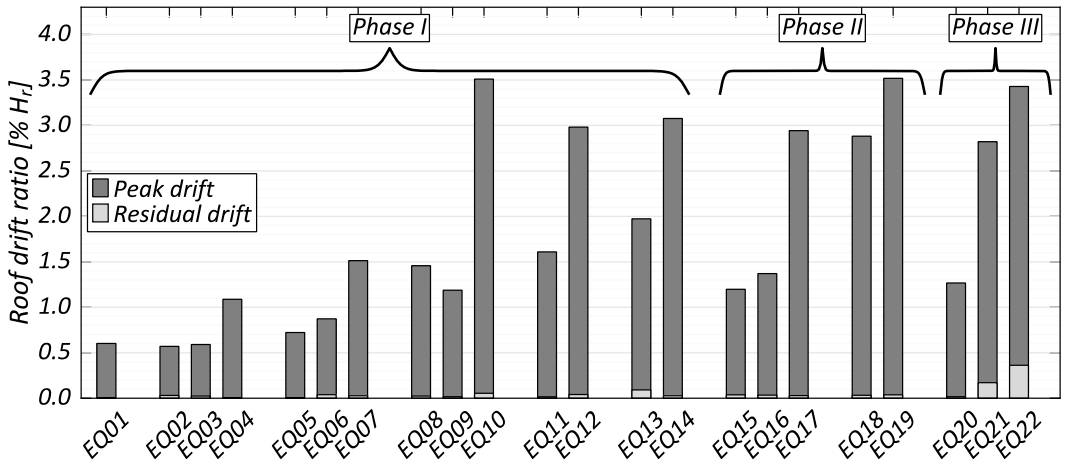

Figure 3.24 Peak and residual roof drift ratios at floor center

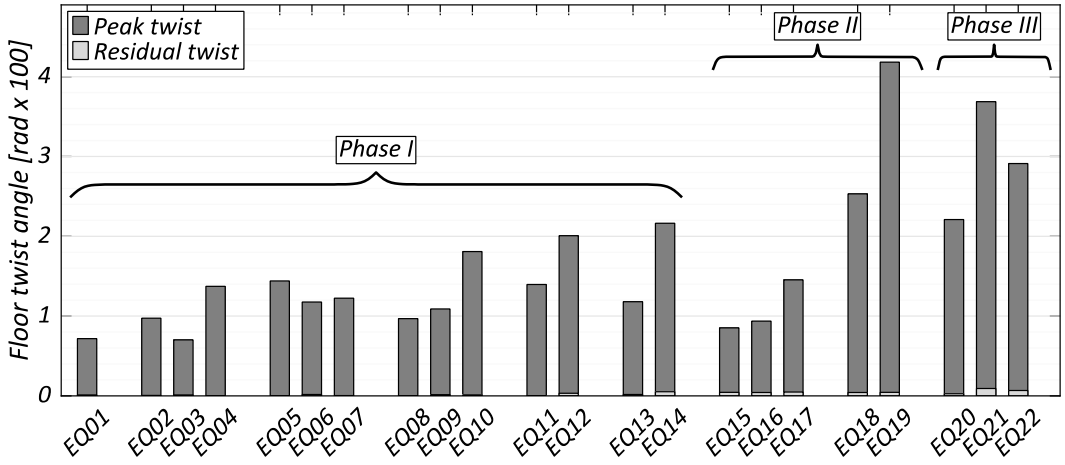

Figure 3.25 Peak and residual roof twist angles

Figure 3.28 shows the moment-drift hysteresis at the structural level for some MCE_R level earthquakes. Under EQ10, the energy dissipators in the North wall came loose, which is seen in the sudden drop in the moment capacity at a drift greater than +2% and a subsequent softening of the hysteretic response. To counter the slipping of the flexural energy dissipators, locking nuts were installed at the ends of the pin connection between the devices and the foundation for subsequent testing.

Comparing the response under EQ12, EQ14 and EQ19, which have similar configurations of PT stresses in the structural walls, shows the effect of the FL-SC system. A sudden increase in stiffness around zero drifts arises due to gap closing at the base of the rocking wall. This increase in stiffness is not apparent in EQ19 as a result of cumulative damage to the mortar bed at the rocking interface but can be clearly observed in EQ17. The bulge seen around zero-drift in the hysteretic response in Phase I is a result of energy dissipation in the FL-SC system. Comparing the responses of EQ12 and EQ14 indicates that lower slip forces in the FL-SC system result in lower energy dissipated in this region. From the structural response under EQ21, it can be inferred that the emulative fixed-base wall has a stiffer response. The failure of the emulative connection occurs at a drift of -2%, where a sudden drop in the system moment is observed, followed by a softer structural response.

Typical responses of the two FL-SC devices are shown in Figure 3.29, without any scaling of the forces and deformations to prototype level. The FD devices have a well-defined elastic-perfectly plastic response. The slip force of these devices was well defined and easily controlled through the applied normal forces between the brass shims and the steel plates. The response of the BRD device is also well-defined and resembles the hysteretic response of the constitutive steel material, with no buckling under compression. The relative displacement between the floor and the primary wall is shown in Figure 3.30. Studying the relative displacements under Phase II and Phase III shows that while the PSA connection significantly reduced the relative displacements, it was not completely rigid resulting in finite relative movement between the wall and the floors.

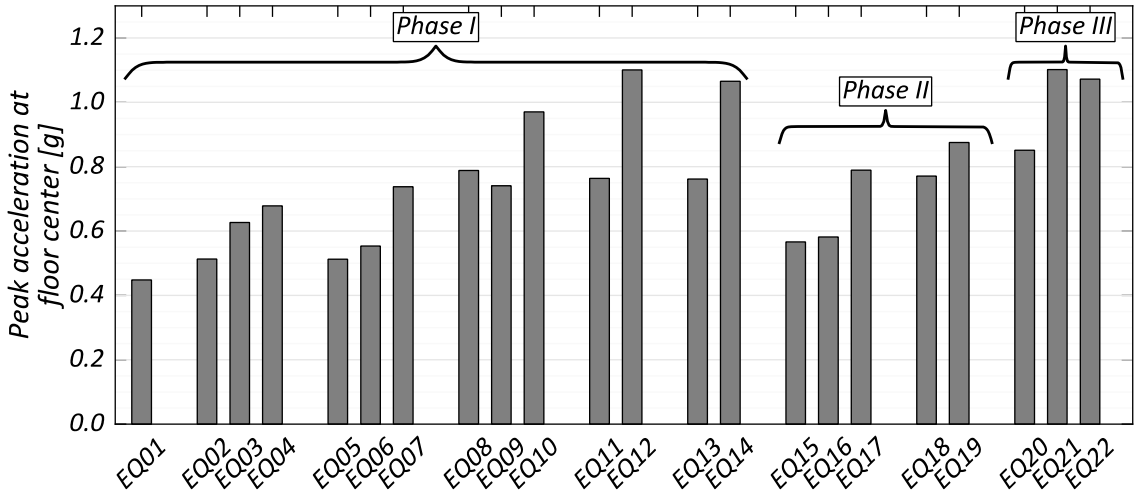

Figure 3.26 Peak accelerations at floor center

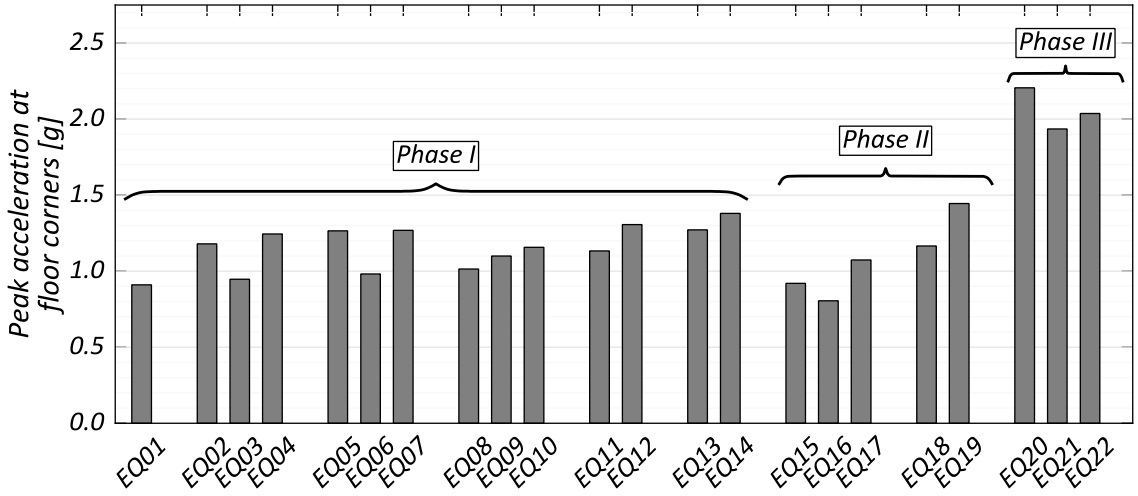

Figure 3.27 Peak accelerations at floor corners

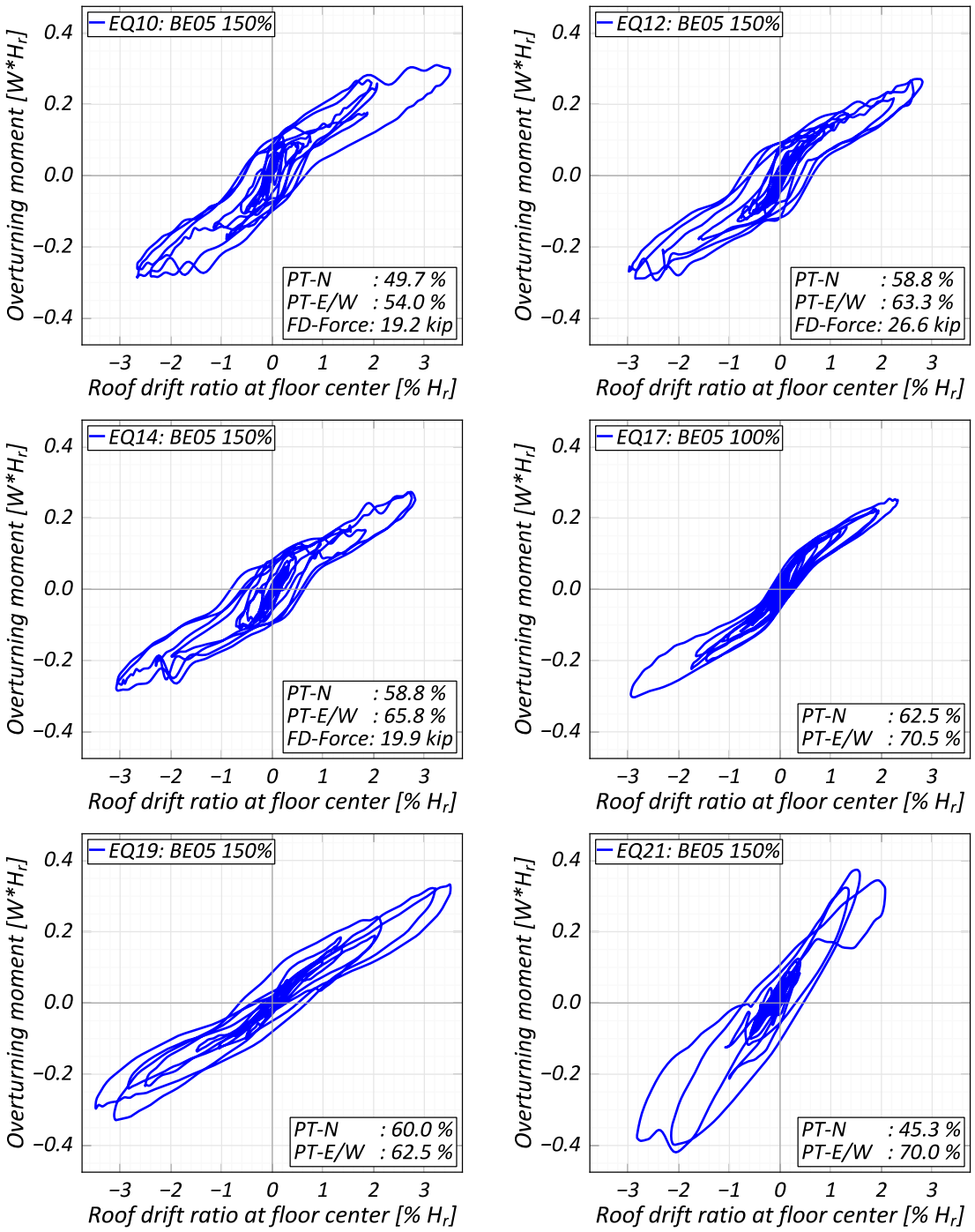

Figure 3.28 Comparison of global hysteresis, MCE$_R$ level earthquakes

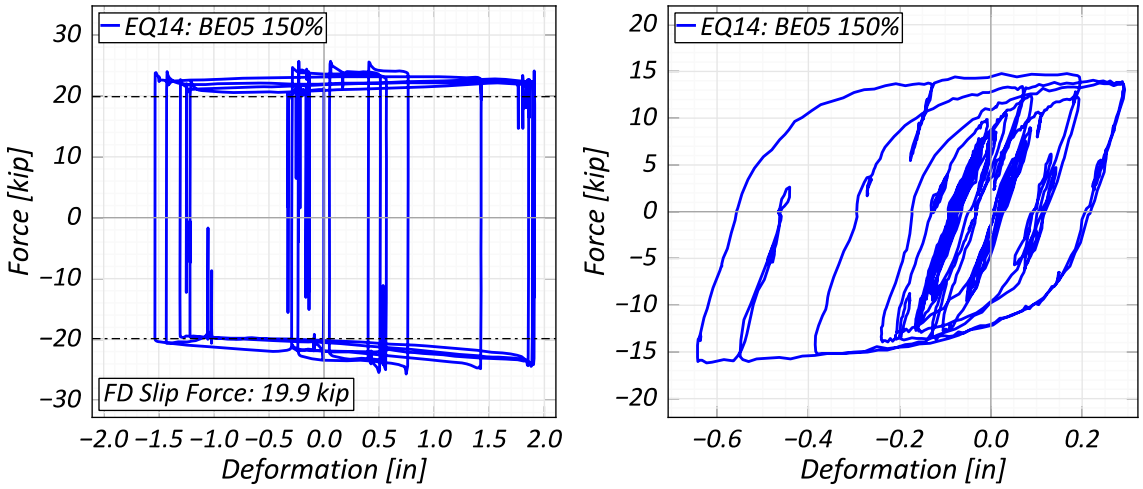

Figure 3.29 Typical FD and BRD responses

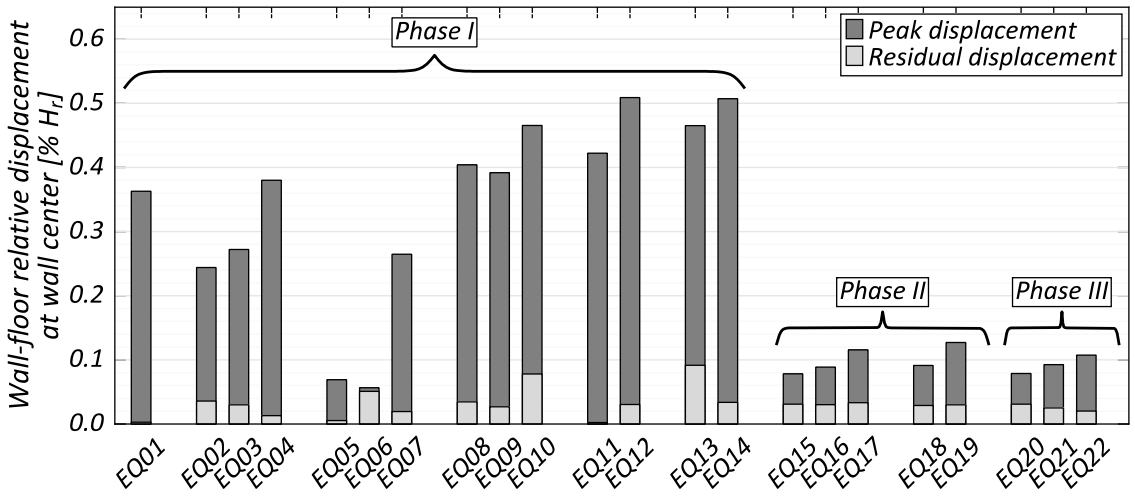

Figure 3.30 Floor-wall relative displacement at roof level

3.5.2. Performance of structural walls

Figure 3.31 shows the global overturning moment vs the rotation in the North wall. For Phase I and Phase II, the rotation is measured at the top of the foundation, while for Phase III, the rotation is the total rotation seen in the wall over the first story. The wall re-centering behavior is clearly seen in the hysteretic responses during Phase I and Phase II. Comparing the responses under EQ17 and EQ19 to EQ10, EQ12 and EQ14 shows a gradual widening of the hysteretic loops around zero rotation. This widening is

accompanied by minor softening of the response and is indicative of crushing in the mortar under the wall edges. The response under EQ21, Phase III clearly shows the development of permanent deformations in the wall.

Figure 3.32 and Figure 3.33 show the peak and residual levels of roof drift and wall base rotation observed in the North wall, where the re-centering behavior is again clearly observed. Figure 3.34 shows the peak and residual stresses seen in the two PT bars in the North wall. While the PT bars underwent inelastic deformations in all the MCE_R level earthquakes during Phase I and Phase II, this did not negatively affect the re-centering capacity of the system. The stress strain response of these PT bars during the MCE_R level excitations is shown in Figure 3.35, where the inelastic deformations can be observed. It should be noted that the pressure transducers used for measuring the stresses reached their load capacity which is seen in the form of constant stresses at peak strains in the stress-strain response. This effect is also visible in Figure 3.34 in the form of stress loss under peak stresses smaller than 90% GUTS, which is the approximate yield stress for the A1035 Grade 150 bars.

Figure 3.36 shows the measured response, in the specimen space, of the energy dissipators in the North wall. It can be observed that as the wall undergoes rocking, a state of residual compressive force, with a corresponding uplift force in the walls, develops in the dissipators. The slipping of the dissipators during EQ10 can also be seen in the form of loss of strength and stiffness in the corresponding graph.

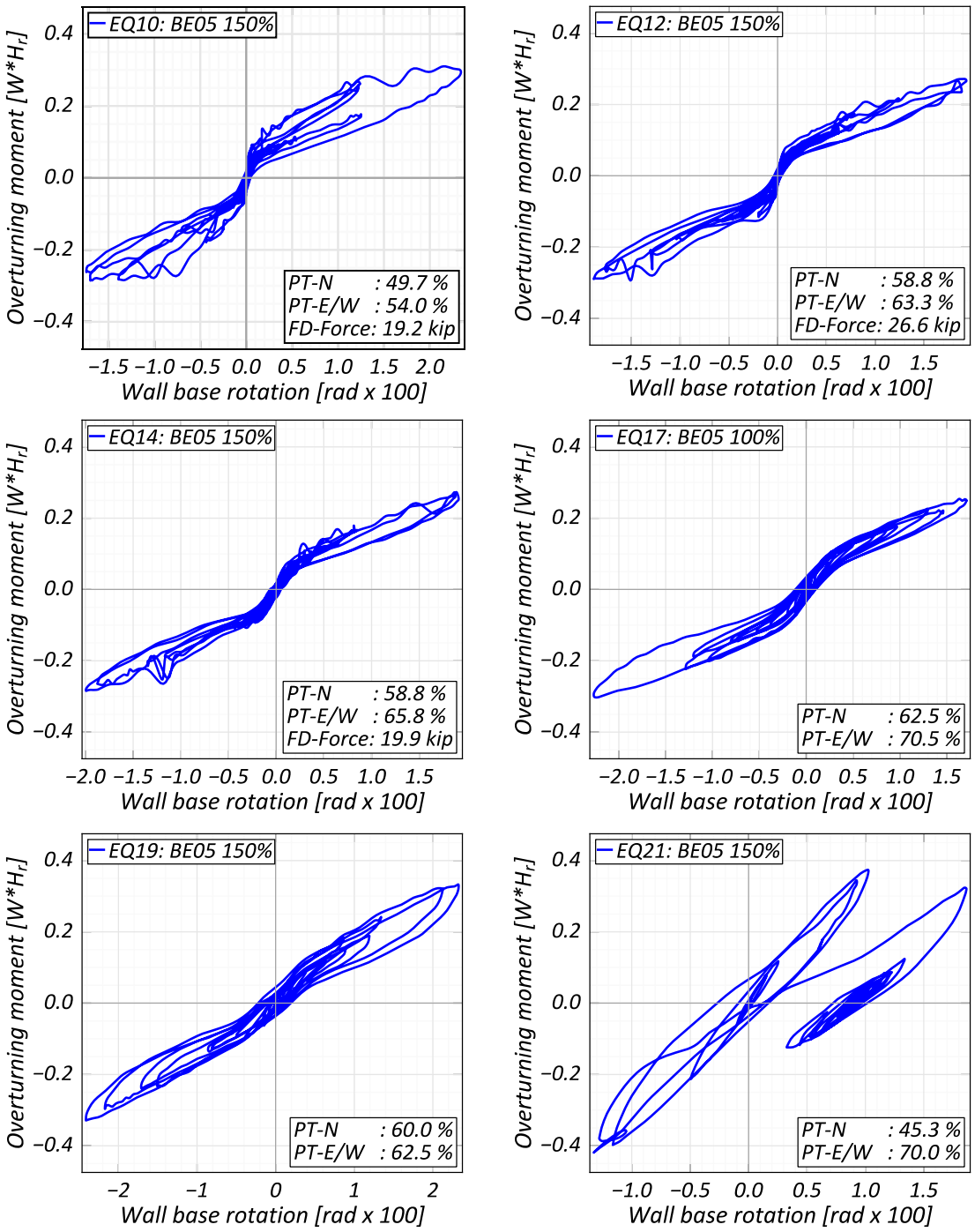

Figure 3.31 North wall moment vs base rotation, MCE$_R$ level earthquakes

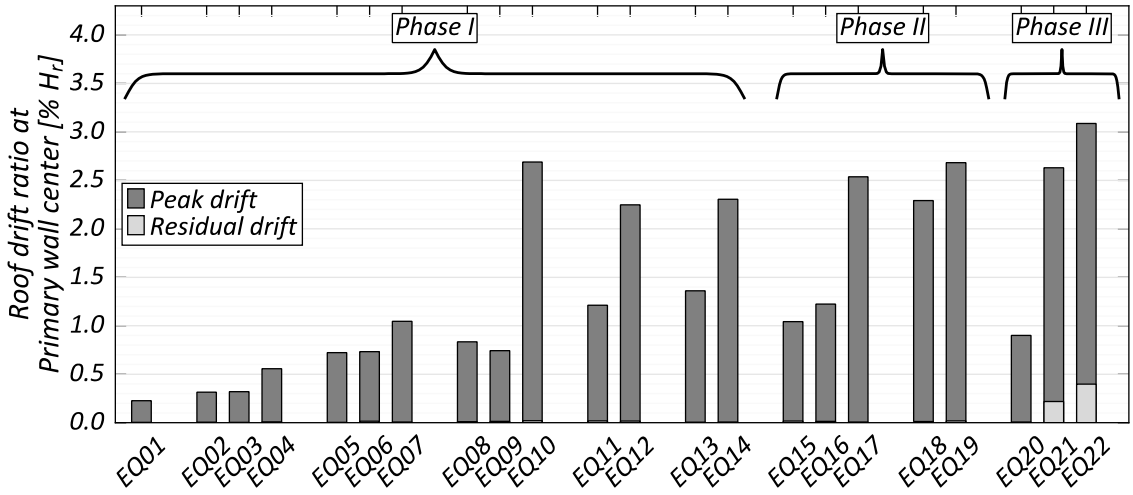

Figure 3.32 Peak and residual North wall drifts at roof level

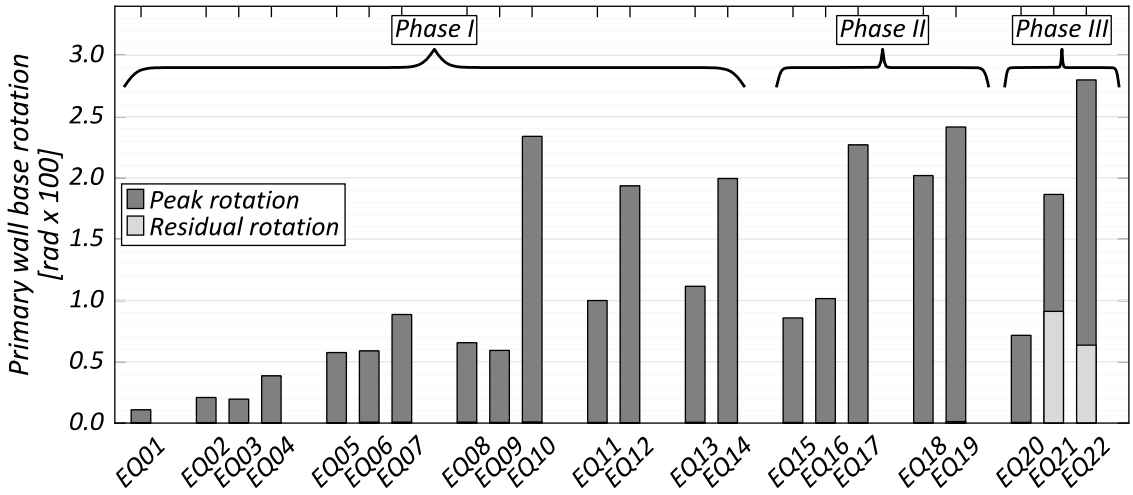

Figure 3.33 Peak and residual North wall base rotation

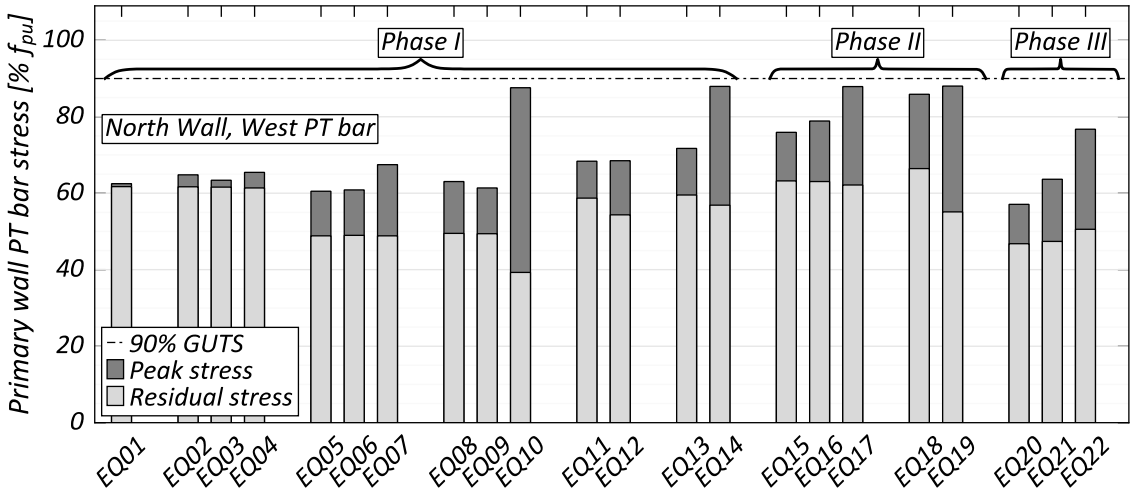

(a) West PT bar

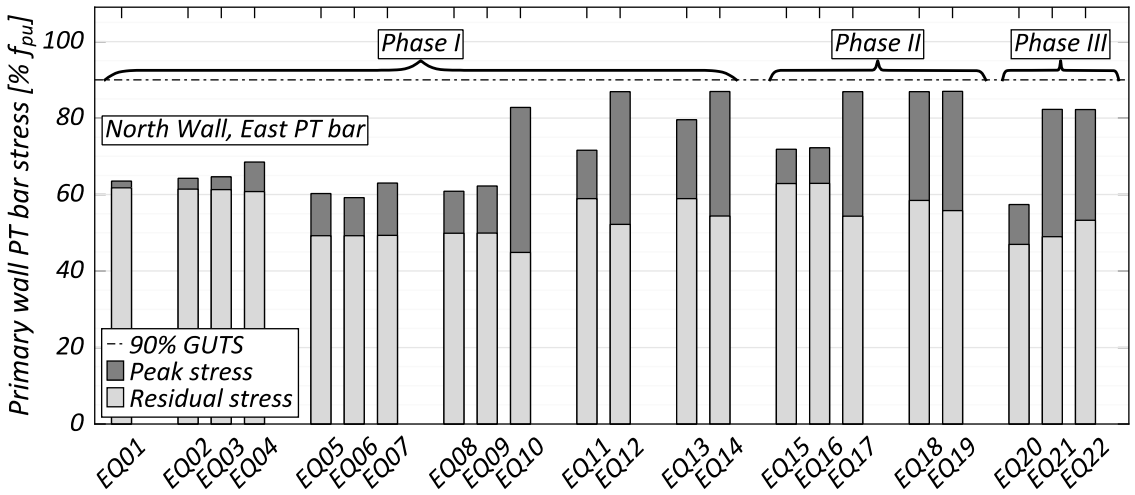

(b) East PT bar

Figure 3.34 Peak and residual stresses in North wall PT bars

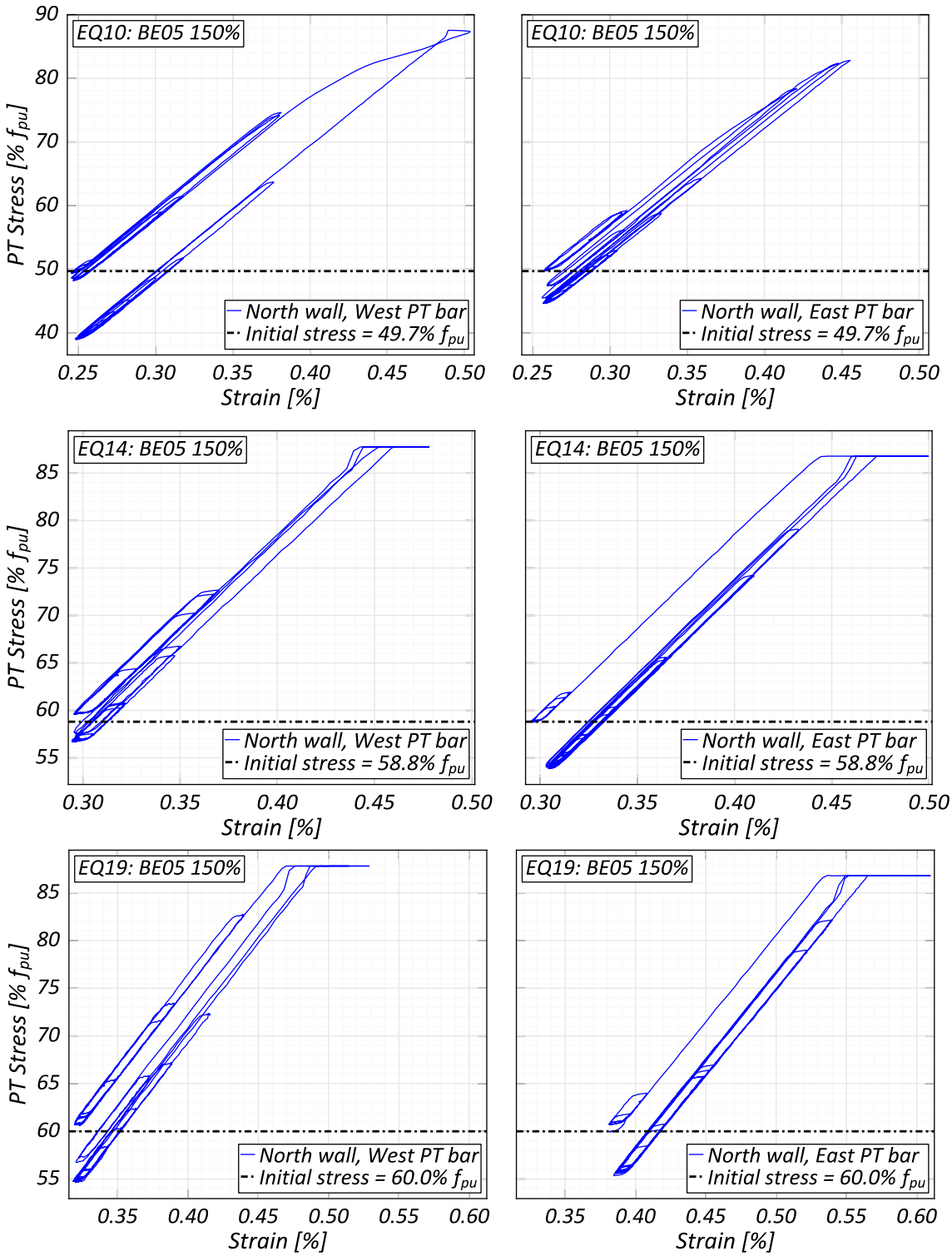

Figure 3.35 Stress-strain responses in North wall PT bars

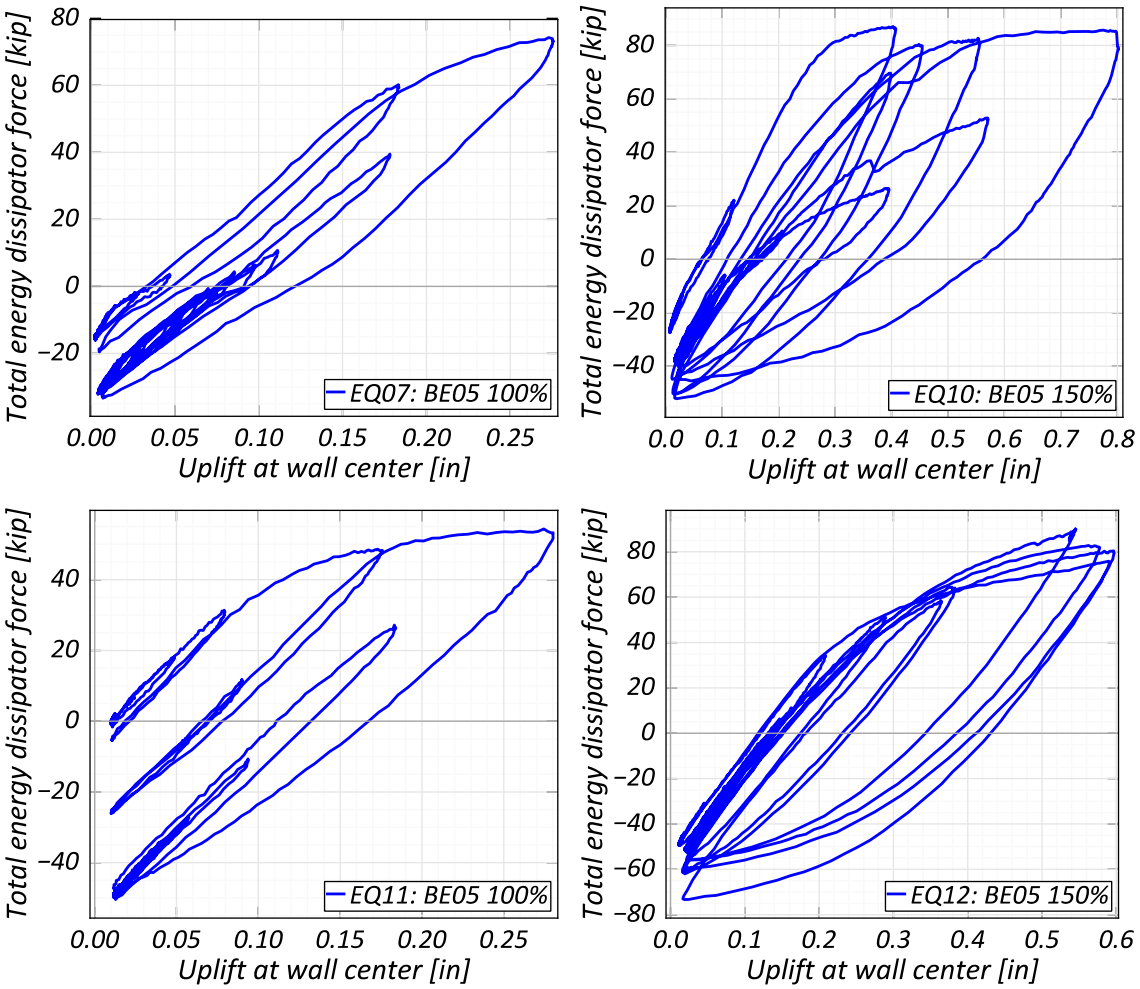

Figure 3.36 North wall energy dissipator force vs deformation response

Figure 3.37 North wall damage during Phase I

Figure 3.38 North wall damage during Phase II

Figure 3.39 North wall damage during Phase III

3.5.3. Performance of low-damage precast gravity columns

Results for columns B2, the column with the largest axial load, and column C3, a corner column with large expected drifts, are presented below. A summary of the peak inter-story drift, column rotations and central bar strain as measured at the first level is presented in Figure 3.40, Figure 3.41 and Figure 3.42 respectively. Both columns underwent large peak drifts during the MCE_R level earthquakes. Column C3 had larger deformations, as a consequence of torsion in the structure. The time histories of the drifts and strains measured in column C3 during the last MCE_R level excitation of each phase of testing are shown in Figure 3.43 and Figure 3.44.

The effect of the structure's eccentricity can be seen in the magnification of the East-West and North-South peak drifts in column C3 compared to column B2. The column rotations behave identically to the column drifts, indicating no significant localized rotations at the column ends except at the column-foundation / column-slab interface. Comparing the reinforcement bar strains to the yield strain, the peak strains measured in the central bar only marginally exceed the yield point, signifying an elastic response even during MCE_R level events. It should be noted that this slight yielding is only seen in the corner columns, due to a combination of higher axial loads and lower rotations.

From the drift time histories, it can be inferred that the GLRS's period remained largely unchanged until the end of the test, even though drifts exceeding 3% were registered multiple times over each MCE_R level event during Phase I and Phase II. In Phase III, the response is stiffer than the earlier phases largely due to the stiffness of the

emulative fixed-base walls. Photographs of the damage in the two columns in the first level are presented in Figure 3.45 and Figure 3.46. From the pictures, it can be seen that column damage is limited to a distance of one column depth from the end. The visible damage is limited to spalling of the concrete surface, with the confining reinforcement exposed at a few locations. It should be kept in mind that this level of damage is seen after multiple cycles of DBE and MCE_R level events, demonstrating the effectiveness of the proposed gravity column design.

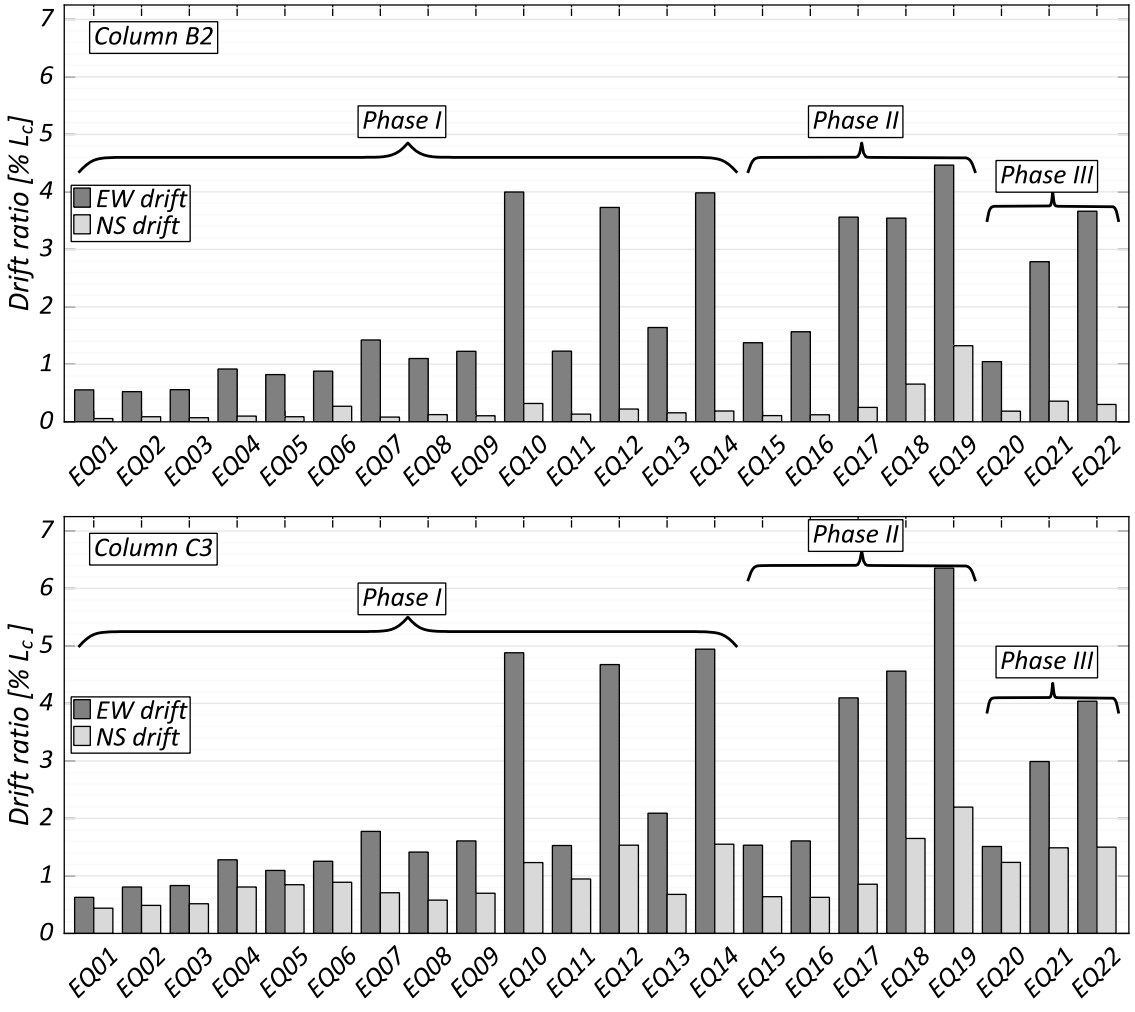

Figure 3.40 Column peak drift ratios at ground level

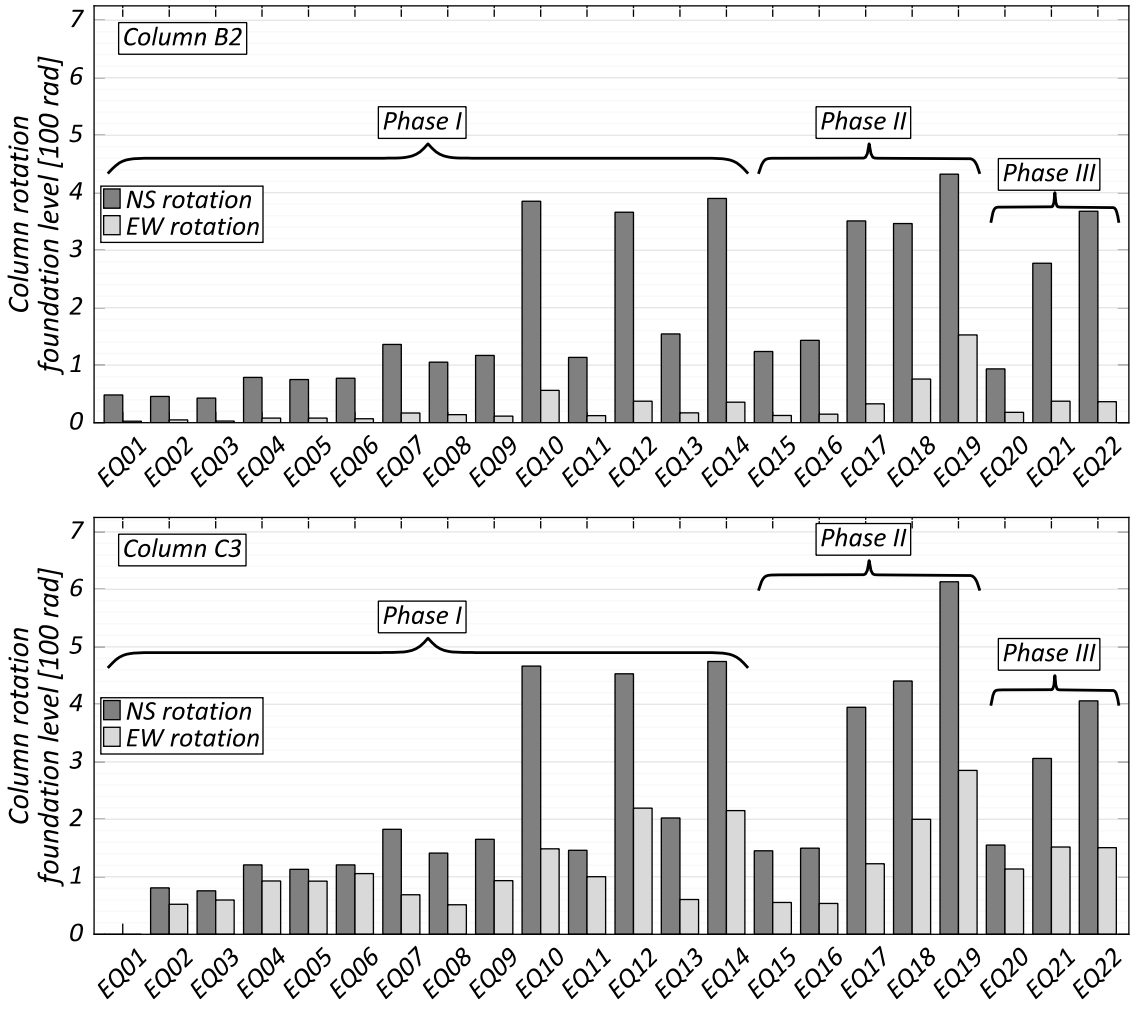

Figure 3.41 Column peak rotations at ground level

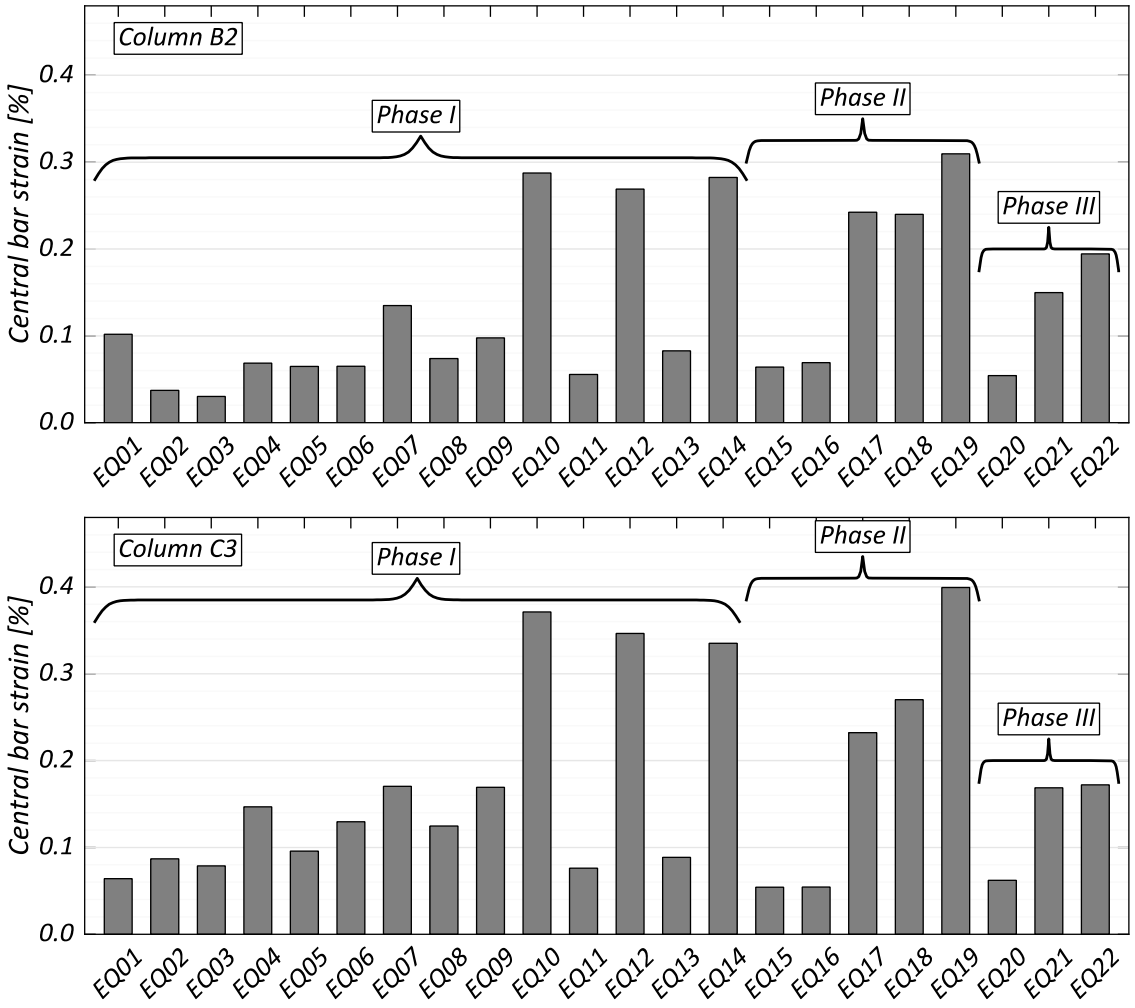

Figure 3.42 Peak strains in central reinforcement in gravity columns at ground level

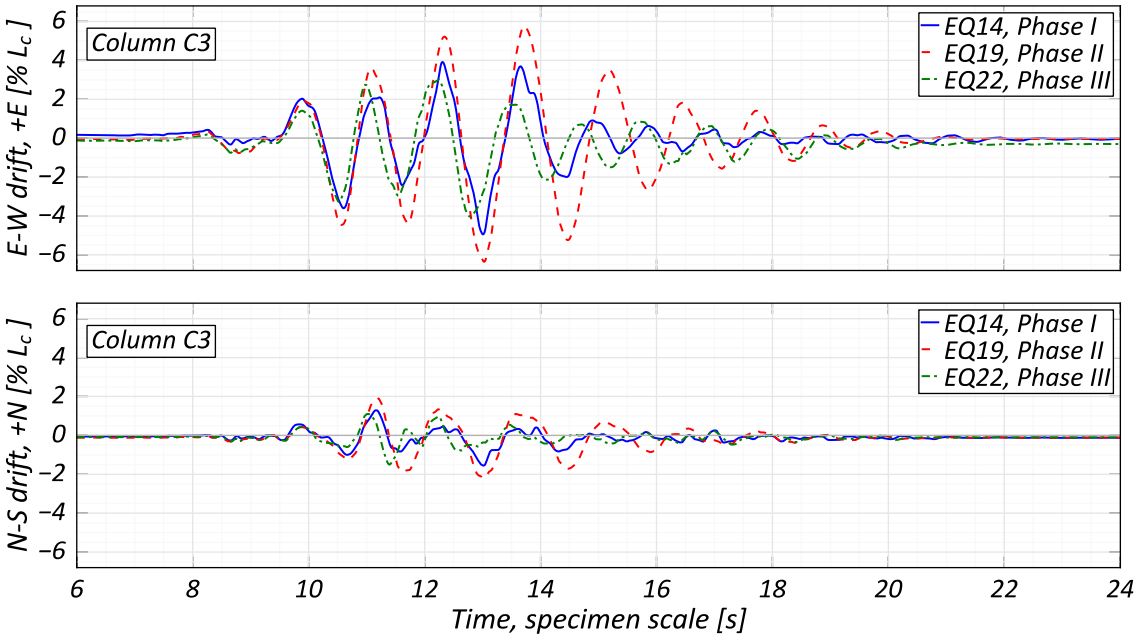

Figure 3.43 Drift time histories during MCE$_R$ level earthquakes in Column C3

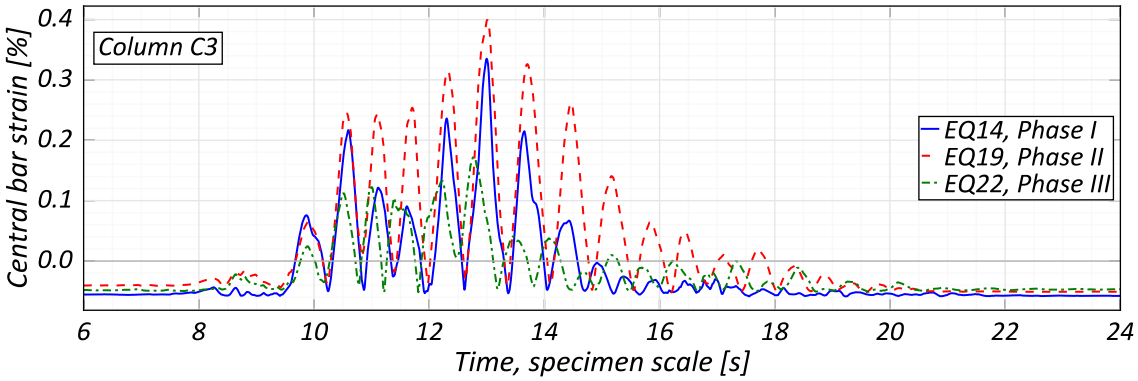

Figure 3.44 Central reinforcement strain time histories during MCE$_R$ level earthquakes in Column C3

(a) Initial condition **(b) Damage at the bottom** **(c) Damage at the top**

Figure 3.45 Damage propagation in column B2

(a) Initial condition **(b) Damage at the bottom** **(c) Damage at the top**

Figure 3.46 Damage propagation in column C3

3.6. Acknowledgments

For their collaboration on the testing of the four-story structure, I would like to thank the research team from University of Arizona, Tucson: Dr. Robert B. Fleischman, Dr. Dichuan Zhang, Dr. Zhi Zhang, Dr. Ulina Shakya and Dr. Anshul Agarwal; and the research team from Lehigh University: Dr. Richard Sause and Dr. Georgios Tsampras.

I would like to thank the staff at the Large High-Performance Outdoor Shake Table (LHPOST) at UC San Diego: Dan Radulescu, Paul Greco, Alex Sherman, Hector Vicencio and Robert Beckley for their invaluable help during the testing of the four-story structure studied in this work.

The experimental study of the four-story structure was supported financially by the National Science Foundation (NSF) under Grant CMMI-1135033, Network for

Earthquake Engineering Simulation Research (NEESR). Additional support was provided by “Fund of Social Development” grant (No.КФ-14/03) at Nazarbayev University. Industry practitioners contributed significantly to the experimental test program. I am thankful to the following industry partners for their contributions of time, materials, monetary donations and expertise: the Prestressed/Precast Concrete Institute (PCI), PCI West, the Charles Pankow Foundation, T.B. Penick & Sons, Inc., Star Seismic, MMFX, Midstate Precast, Davis Wire, DYMAT, Brewer Crane and Rigging, JVI Inc., Pleiger Inc., BASF Inc., Gerdau Inc., HRC Inc., Core Slab, Dura Fiber, Triton Structural Concrete, Atlas Construction Supply, Inc., Western Concrete pumping, Steel City Scaffold, Clark Pacific, Wire Reinforcement Institute, Fyfe Co., LLC.

Chapter 3, in part, references material presented in *Shake‐table test performance of an inertial force‐limiting floor anchorage system*, Earthquake Engineering & Structural Dynamics, 47(10), pp.1987-2011, 2018, Zhang, Zhi; Fleischman, Robert B.; Restrepo, José I.; Guerrini, Gabriele; Nema, Arpit; Zhang, Dichuan; Shakya, Ulina; Tsampras, Georgios and Sause, Richard. Chapter 3, in part, is a reprint of the material as it appears in *Seismic response of precast concrete gravity columns in a building system* Nema, Arpit and Restrepo, José I. The dissertation author co-authored the material in both publications.

Chapter 4

ANALYTICAL SIMULATION OF A 13-STORY BUILDING

4.1. Introduction

This chapter presents the analytical work done on buildings with low-damage structural components, with a focus on hybrid re-centering beam-column joints and rocking structural walls. The analytical work was performed with the analysis program OpenSees (Mazzoni et al. 2007; McKenna et al. 2010), developed by the Pacific Earthquake Engineering Research (PEER) Center. The analytical work included the model development and verification for re-centering structural walls based on the experimental results presented in Chapter 3, and the model development and verification for hybrid re-centering frame systems using experimental results from Stanton et al. (1995). The two models were then incorporated into the analytical model of a 13-story building, with the resulting models used for an analytical study comparing the response of the different re-centering systems and the fixed-base design of the building under an ensemble of seven historic ground motions.

4.2. Modeling of low-damage walls

4.2.1. Wall analytical model

The Non-linear Beam-Truss Model (NL-BTM), derived from the work of Lu and Panagiotou (2014), was utilized for the modeling of low-damage structural walls. The beam-truss formulation evolved from the Strut-and-Tie model developed to obtain a discrete representation of stress fields in a reinforced concrete structure. Using this formulation, the response of structural walls including flexure-shear interaction can be easily incorporated into simple lumped plasticity or fiber-based element models, resulting in reduced computation complexity when compared to Finite Element Models utilizing shell or solid elements. The adopted beam-truss model for a conventional fixed-base wall, as shown in Figure 4.1, builds upon the truss-based model presented in Panagiotou and Restrepo (2006) by incorporating the wall non-linear section response for out-of-plane behavior, and has four main components:

- Non-linear fiber-based Euler-Bernoulli frame elements in the vertical direction representing the wall boundary regions, which are typically well-confined.
- Beam-column elements in the vertical direction representing concrete and longitudinal reinforcement in the wall web.
- Beam-column elements in the horizontal direction representing the effective areas of transverse reinforcing steel.
- Non-linear truss elements in the diagonal of the panels formed by the horizontal and vertical elements representing the diagonal concrete struts.

The diagonal truss elements account for the effect of biaxial strain field on concrete compressive behavior by employing the four-node *Truss2* element and the associated concrete model, *ConcretewBeta*, developed by Lu and Panagiotou. The horizontal and vertical frame elements modeling the wall interior account of out-of-plane non-linear behavior through fiber-based beam-column representation but have flexural releases for truss-like in-plane behavior following the strut-and-tie modeling approach. Bar-buckling and fracture are not included in the model.

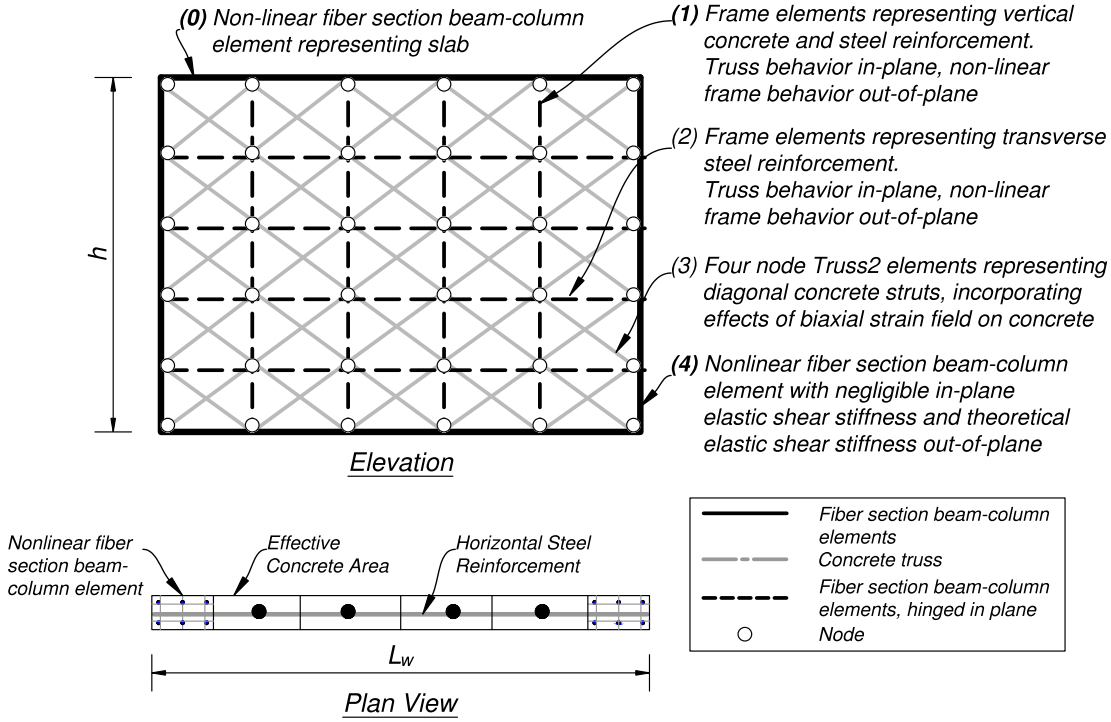

Figure 4.1 Structural wall Non-linear Beam Truss Model

The above model represents the structural wall above the rocking interface. Complete modeling of rocking behavior requires additional elements to represent the rocking interface, the energy dissipators and the post-tensioning elements. A common approach to the modeling of the rocking interface involves multiple springs connected

rigidly to the wall central node. This approach imposes the Euler-Bernoulli constraint of plane-sections remaining plane on the rocking interface. For a more accurate model of the wall rocking interface which accounts for a violation of Euler-Bernoulli assumption, displacement-based beam-column elements with no tensile resistance are added between each line of wall vertical elements and the foundation. The *Concrete02* constitutive rule with zero tensile strength is used for modeling the fiber-sections in these elements. The peak strength for the constitutive rule can be obtained from a suitable mortar bedding layer, however the initial stiffness needs to be calibrated to account for the spread of inelastic behavior within the structural wall toe, assumed to extend uniformly for a length equal to the neutral axis depth (Restrepo and Rahman 2007).

The energy dissipators are modeled using *Truss* elements and are connected to the structural wall at a suitable height and fixed to the ground at a suitable depth below the foundation level to account for the actual wall geometry. The post-tensioning elements can be represented using either fiber-based or truss elements. For short walls, the fiber-based elements are recommended to account for any localized yielding occurring in these elements at the rocking interface. *Steel02* material model is utilized for the post-tensioning elements with an appropriate initial stress applied using the *InitStrainMaterial* rule. The anchorage locations in the foundation and on top of the wall are selected on the basis of the actual wall geometry. A representation of this model for the wall at the ground level is shown in Figure 4.2.

For dynamic modeling of a rocking wall, special care needs to be taken in assigning damping to the rocking interface. During rocking behavior, there is no element

connecting the uplifted wall nodes to the foundation nodes which should result in zero damping forces between the two sets of nodes. However, under Rayleigh damping derived from initial stiffness, large damping forces can arise at these locations as a result of large relative velocities. To avoid these artificial damping forces and energy dissipation, it is recommended to either assign zero damping to all the nodes and elements forming the rocking interface or more appropriately use a damping matrix derived from the current or committed stiffness matrix of the model (Charney 2008).

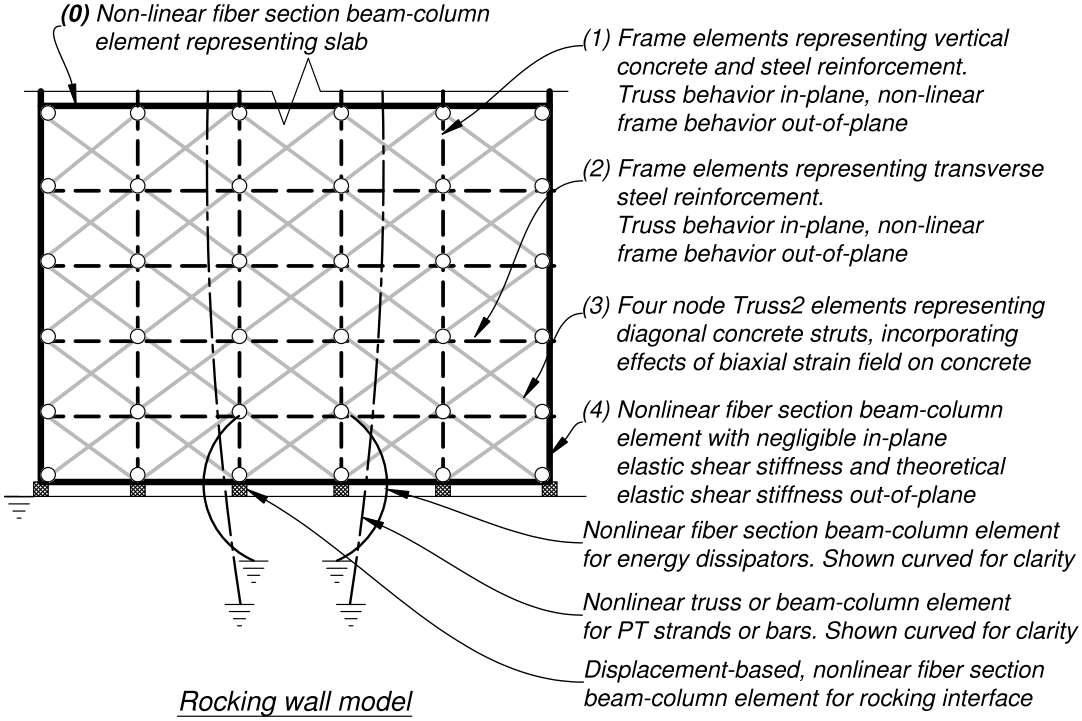

Figure 4.2 Non-linear Beam Truss Model for Rocking walls, ground level

4.2.2. Model verification: modeling of 4-story shake table test structure

The numerical model for hybrid re-centering walls presented above was verified using the test results from the 4-story specimen presented in Chapter 3. Details of the model are presented below. A rendering of the analytical model is presented in Figure 4.3.

4.2.2.1. Wall Model

The wall model presented in Section 4.2.1 was utilized for modeling the three structural walls in the test specimen, with one modification: each wall boundary region was represented using two non-linear fiber-based elements due to the significant depth compared to wall length. The wall webs were represented by six (6) vertical elements in the primary wall and five (5) vertical elements in the secondary walls. Along the wall height, two (2) rows of horizontal elements were utilized for the socketed depth of the wall and eight (8) rows of horizontal elements were utilized over the story clear height. The height of the elements forming the rocking interface was set equal to the actual thickness of the mortar bed i.e. 50.8 mm (2 inch).

In the boundary elements, the confined concrete core and the unconfined cover was modeled below floor 2, and the element section for the remaining wall height was modeled only with unconfined concrete. Confined concrete properties were assigned to the diagonal elements in the socketed wall depth and in the wall boundary elements below floor 2, while unconfined concrete properties were assigned to the remaining diagonal struts. The *ConcretewBeta* material rule modeled the concrete behavior in the structural wall elements to independently model the concrete unconfined and confined

parameters and the initial stiffness. The reinforcing steel in the vertical and horizontal elements was modeled using *Steel02* material hysteretic rule.

The *Concrete02* material rule for the rocking interface utilized the measured mortar strength (82.7 MPa / 12 ksi) and a theoretical initial stiffness of 42.8 GPa (6244 ksi), with the strains in the stress-strain relationship amplified by the ratio of the theoretical neutral axis depth to the actual element height to account for the spread of inelastic behavior within the structural wall. Additionally, the residual strength of the interface needed to be calibrated for accurate modeling of the accumulated damage in the mortar bed during the test. Calibrated residual strengths of 45.5 MPa (6.6 ksi) and 66.2 MPa (9.6 ksi) were set for the primary (North) and the secondary (East/West) walls respectively.

The energy dissipator behavior was modeled using the *Steel02* material rule and calibrated to the measured force-displacement response during the test, with different dissipator properties for the primary and the secondary wall. The dissipators were connected to the walls at the mid depth, with the vertical connection location determined from the actual wall geometry and the total length for the fixed ground anchor location determined from the calibrated behavior. Replacement of the primary wall dissipators was accounted for by a replacement of the corresponding truss with a virgin element in the model.

Each post-tensioning bar was modeled using a force-based beam column element with three integration points, and a circular grid of fibers representing the bar area. Each element was fixed at the bottom at a node representing the bar anchor location in the

foundation and connected to the top of the wall by stiff elastic elements representing the pressure transducers. The primary wall had additional elements in series between the stiff connectors and the post-tensioning elements to represent the elastomeric bearing pads. Updates to the wall post-tensioning forces were carried out at the beginning of each new day of testing and required replacement of the post-tensioning bars with new elements incorporating the updated initial stresses.

For modeling the walls during Phase III of testing, the nodes representing the top of the wall socket were updated to have a fixed base constraint and the energy dissipator elements were removed.

4.2.2.2. Column Model

The gravity columns were modeled using force-based beam-column elements to account for the difference in column section properties at the ends. One force-based element with four-integration points was implemented per column, per floor over the story clear height. The column fiber-sections away from the ends modeled the perimeter #3 bars, the confined and unconfined concrete and the central #7 bar. The column end sections modeled the central #7 bar using a circular grid of fibers and the confined concrete using a rectangular fiber grid to account for the reduced stiffness at these locations. Properties of the confined concrete were calculated from the transverse reinforcement and the measured unconfined concrete properties following the recommendations of Chang and Mander (1994). The confined and unconfined concrete was modeled using the *ConcretewBeta* material rule to independently model the concrete unconfined and confined parameters and the initial stiffness.

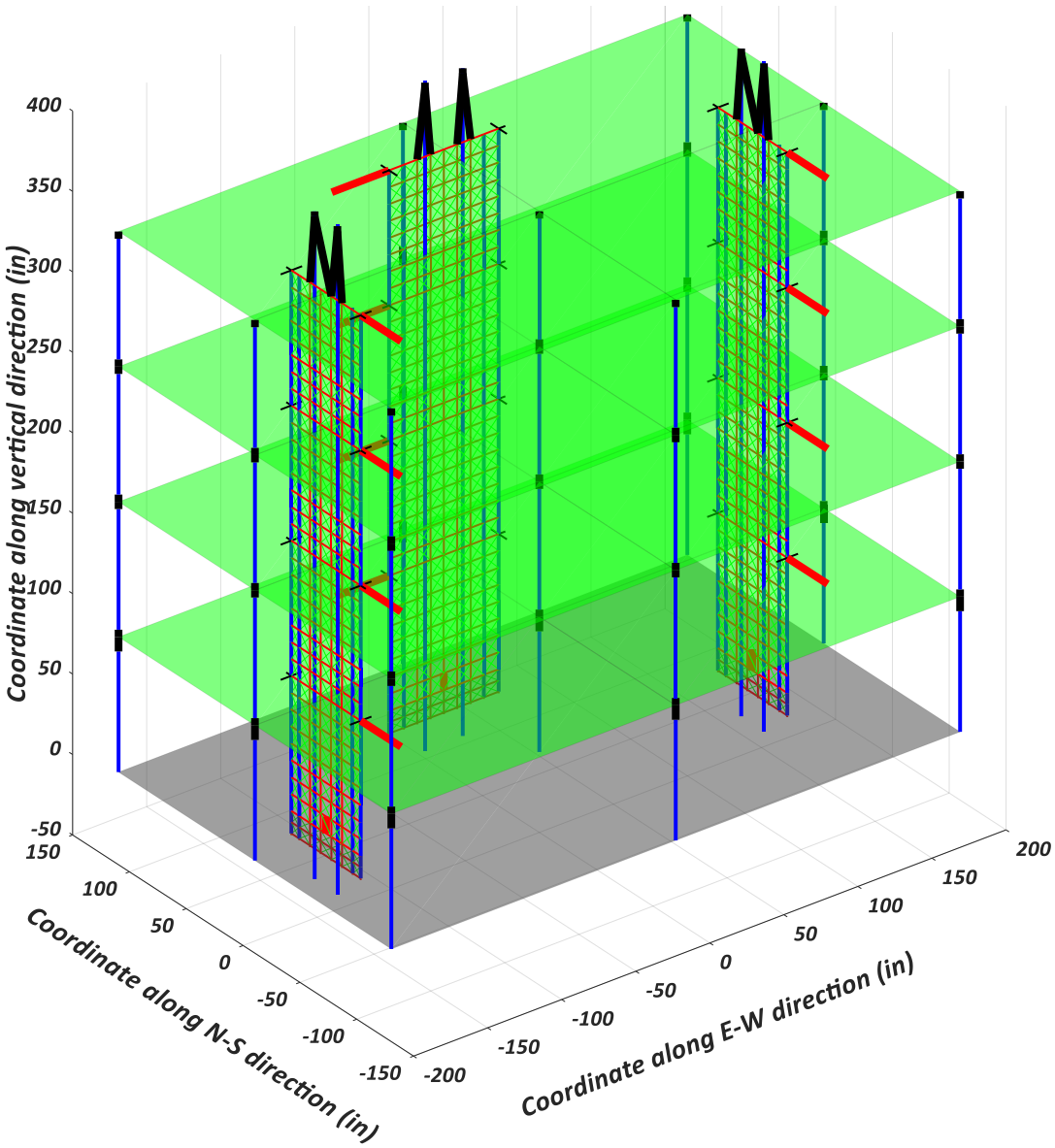

Figure 4.3 Rendering of the finite element model of the 4-story test structure

4.2.2.3. Slab Model

The concrete slabs were modeled at their mid-depth using the four-node *ShellMITC4* formulation for shell elements. Four elements, with the nodes centered in line with the gravity columns, were modeled for each floor. An elastic membrane-plate section was assigned to each element with a stiffness calculated using empirical equations

for the Young's Modulus of concrete. The gravity columns, modeled over the story clear height, were connected to the slab elements using elastic beam-column elements with section properties (area and the moments of inertia) calculated from the columns' gross section and the Young's and Shear modulus defined by the slab concrete properties.

4.2.2.4. Lateral Force Transfer Connections

Lateral force transfer between the gravity system and the walls was primarily through the force limiting devices in Phase I and through a combination of the slotted shear connectors and the roller bearings for Phase II and Phase III. Additionally, a small amount of force was also transferred through the elastomeric bearings, and through the bumper elements in the event of large relative displacements between the walls and the floors during Phase I.

For Phase I of the test, the force-limiting devices were modeled using truss elements. The truss representing a FD device was modeled to have elastoplastic hysteretic behavior with a large initial stiffness of 2768 MN/mm (24500 kip/in) approximated from the test data, a length of 794 mm (31.25 in) derived from the device geometry and a slip force defined by the measured kinetic friction force. The truss representing the BRD device was modeled using the *SteelDRC* hysteretic rule, with geometric properties calibrated to match the device response with cyclic test response measured outside of the dynamic test. One end of these devices was connected to the corresponding wall and the other end connected to the floor center using stiff elastic elements. The trusses representing these two force-limiting devices were removed at the beginning of the second day of test for Phase II in accordance with the experiment.

The elastomeric bearings were modeled using four two-node link elements for each wall and floor, with one element at each corner of the wall. Elastic material response was specified in the axial and the two shear directions of the elements, with stiffness values for Phase I provided in Zhang (2017). These two-node link elements were updated at the start of Phase II to reflect the larger horizontal shear stiffness provided by the slotted-shear connectors and the roller bearings during Phase II and Phase III. The bumpers were also modeled using two-node link elements with a multi-linear elastic response specified in the axial direction. The multi-linear material response includes an initial gap corresponding to the actual bumper-wall arrangement and has two stiffness levels corresponding to the bumper behavior as characterized in Zhang (2017).

4.2.2.5. Analysis Procedure

The numerical model of the 4-story test structure presented in the preceding sections was analyzed under a sequential application of the measured shake-table platen ground motions during the dynamic testing. Updates to the model, corresponding to changes during the test, were incorporated at the beginning of the day-of-testing. Past non-linear response of the post-tensioning bars could not be incorporated and the elements representing the bar were reset to their undamaged state when updating the initial prestress.

The analysis started with application of mass, rotational inertia and gravity loads corresponding to the structure weight measured during different stages of construction. The applied rotational inertia accounted for the wall openings was applied for the floor slabs and required that the floor mass be lumped at column B2. Mass for the columns and

the walls was applied level with the slab mass. Gravity loads for the columns and walls coincided with the masses and the slab loads were applied at the column locations based on the tributary areas. Following gravity load application, the initial prestress corresponding to day 1 of test was applied to the wall post-tensioning bars and the FD and BRD elements were added to the model.

Eigenvalue analysis was performed on the model with the initial wall prestress and the force-limiting devices to compute the structural modal properties. The calculated modal properties were used to assign damping properties to the structure following the Rayleigh damping formulation for the damping matrix. The Rayleigh coefficients were calculated by assigning 0.75% damping to Mode 1 ($T = 0.45\ s$) and Mode 13 ($T = 0.154\ s$), and were found to be 0.154 for mass-proportional damping and 2.84 x 10^{-4} for stiffness proportional damping. As an important note, the damping matrix was updated at each time step of the analysis using the stiffness at the end of the previous time step i.e. using the committed model stiffness. This damping formulation ensures that any fictional damping forces arising during the non-linear rocking behavior are eliminated and spurious damping is not added to the numerical model as the structure fundamental period elongates during the sequential analysis (Charney 2008). The initially assigned damping ratios are shown in Figure 4.4.

The assignment of damping was followed by Non-Linear Time History Analysis (NL-THA) of the model. An integration time step of 1/480 seconds, equal to half the data sampling rate for the test, was used for the Newmark constant average acceleration method. For the analysis time range of 5 seconds to 10 seconds, which was the period

with non-linear rocking behavior in the structure, a reduced time step of 1/1920 seconds was used to ensure convergence of results. P-Delta formulation was considered in all analyses to include geometric effects arising due to large drifts in the structure.

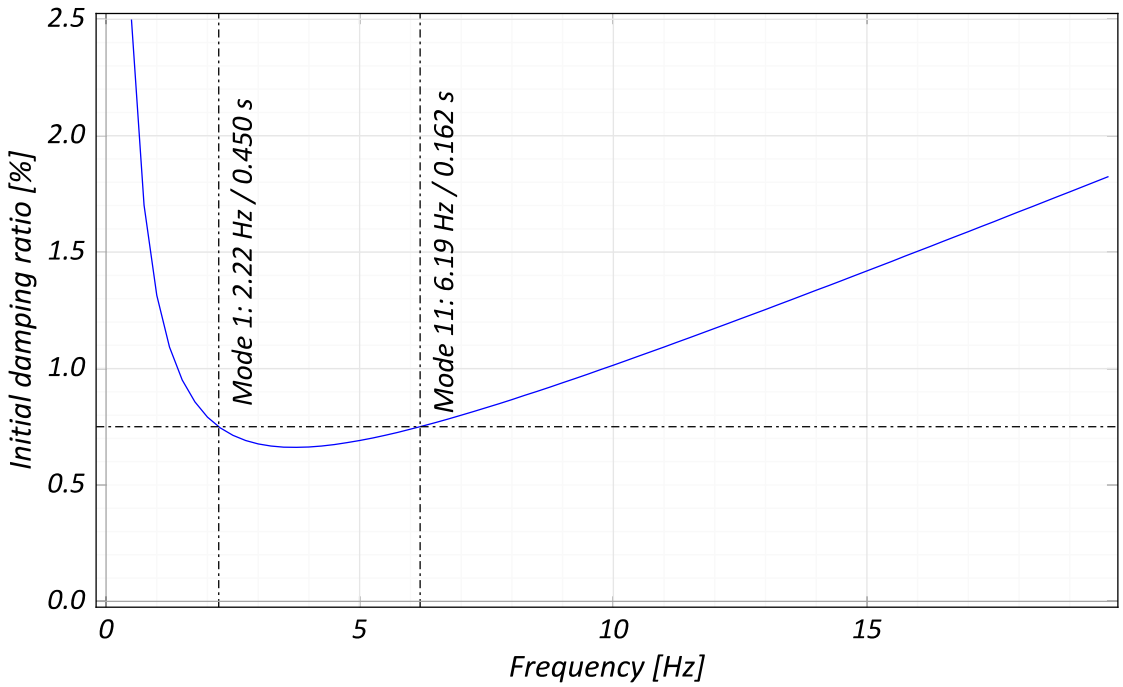

Figure 4.4 Rayleigh damping model used for the analysis of the four-story specimen

4.2.2.6. Analysis Results

A comparison between some analytical and experimental results is presented in Figure 4.5 through Figure 4.15. In general, the analytical results show a good match with the experimental results for Phase I and Phase II. For Phase III, the match is poor after the first excitation due to the foundation failure not being modeled.

Figure 4.5 and Figure 4.6 compare the peak roof drifts and twisting at the floor center. The results for the drift and floor twist indicate prediction of larger deformation responses, particularly in the transverse direction of the structure.

Figure 4.5 compares the results for the global hysteretic response of the structure. For Phase I, the response is well captured, although with smaller energy dissipation in the model at larger drifts. This could be a result of the contribution of non-structural components like the safety railings to the structural response. For EQ10, the failure of the primary wall energy dissipators is not captured, resulting in smaller drifts in the 3rd quadrant. The energy dissipation in the FL-SC devices is captured reasonably well, as indicated by a wider loop around zero drifts. For Phase II, the response on the first sequence is captured well, however the second sequence shows smaller stiffness and forces after gap opening at the wall base. Additionally, the analytical response around zero drift is more pinched. For Phase III, the model shows similar levels of stiffness until the failure of the emulative connection.

Figure 4.8 compares the FD and BRD response at the end of Phase I. The FD response shows a good match in terms of the deformations and forces. The BRD response shows skewed and larger deformations, but the shape of the hysteretic loops shows a good calibration between the model and the experiment. Figure 4.9 shows a comparison between the floor-primary wall relative displacement at the roof level. As a general trend the results show a good match in Phase I, however the results for Phase II and Phase III are significantly smaller, indicating larger stiffnesses of the lateral force transferring connection in the model.

Figure 4.10 shows a comparison between the model and experiment results for the wall moment-rotation hysteretic response. These results are similar to the global hysteresis in their accuracy: good match for Phase I, lower post gap-opening stiffness

during the second ground motion sequence in Phase II and similar initial stiffness in Phase III until the failure of the emulative connection. Figure 4.11 and Figure 4.12 compare the primary wall peak drifts and base rotations and show a good match for Phase I except for EQ11, and for the first sequence of Phase II. The excitations in Phase I and Phase III with significant differences show larger deformations in the model.

Figure 4.13 compares the peak stresses in the PT bars in the primary walls. While there are significant differences for the excitations with large peak PT stresses, it should be noted that these load measurements were clipped due to the pressure jacks reaching maximum capacity. In these cases, it can be safely assumed that the predictions from the model are closer to the actual stress during the experiment. Figure 4.14 shows a comparison between the primary wall PT bar stress-strain responses for some MCE_R level excitations during Phase I and Phase II, where it can be seen that the stress loss is greater in the model during the later stages of Phase II. This is likely due to the modeling limitation requiring pristine PT bars at the beginning of each sequence of excitations with updated initial PT stresses, which results in lack of damage memory in the PT bar model.

Figure 4.15 shows a comparison between the model and experimental force-deformation in the primary wall energy dissipators. The results show a stiffer dissipator response before EQ10, this is a result of the energy dissipator response being calibrated to results from EQ12. Additionally, the failure of the dissipators in EQ10 is not captured. Finally, while EQ12 shows good match between the model and the experiment, the forces in EQ11 are significantly larger, which could be a contributing factor to the errors seen for this excitation in the previous results.

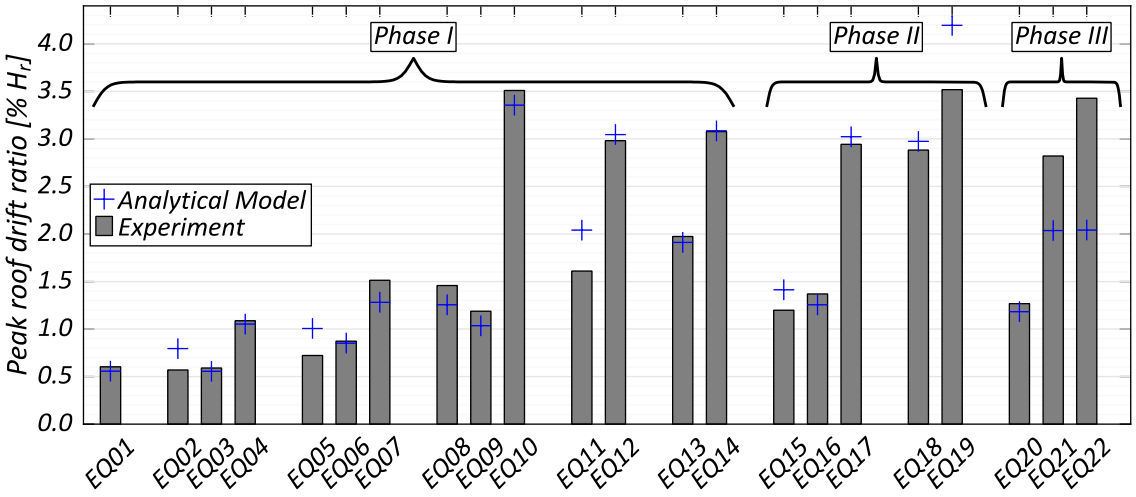

Figure 4.5 Peak roof drift ratios at floor center

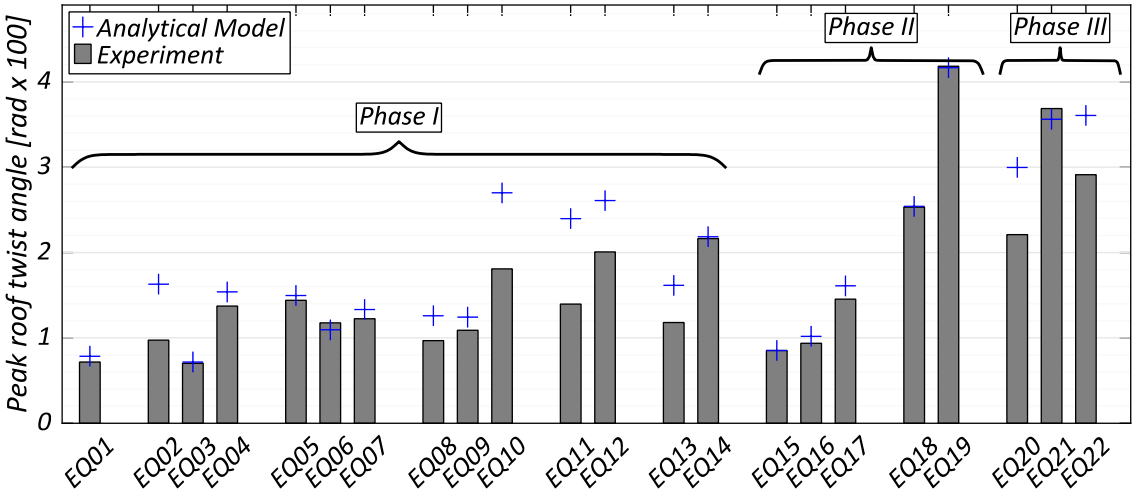

Figure 4.6 Peak floor twist angle

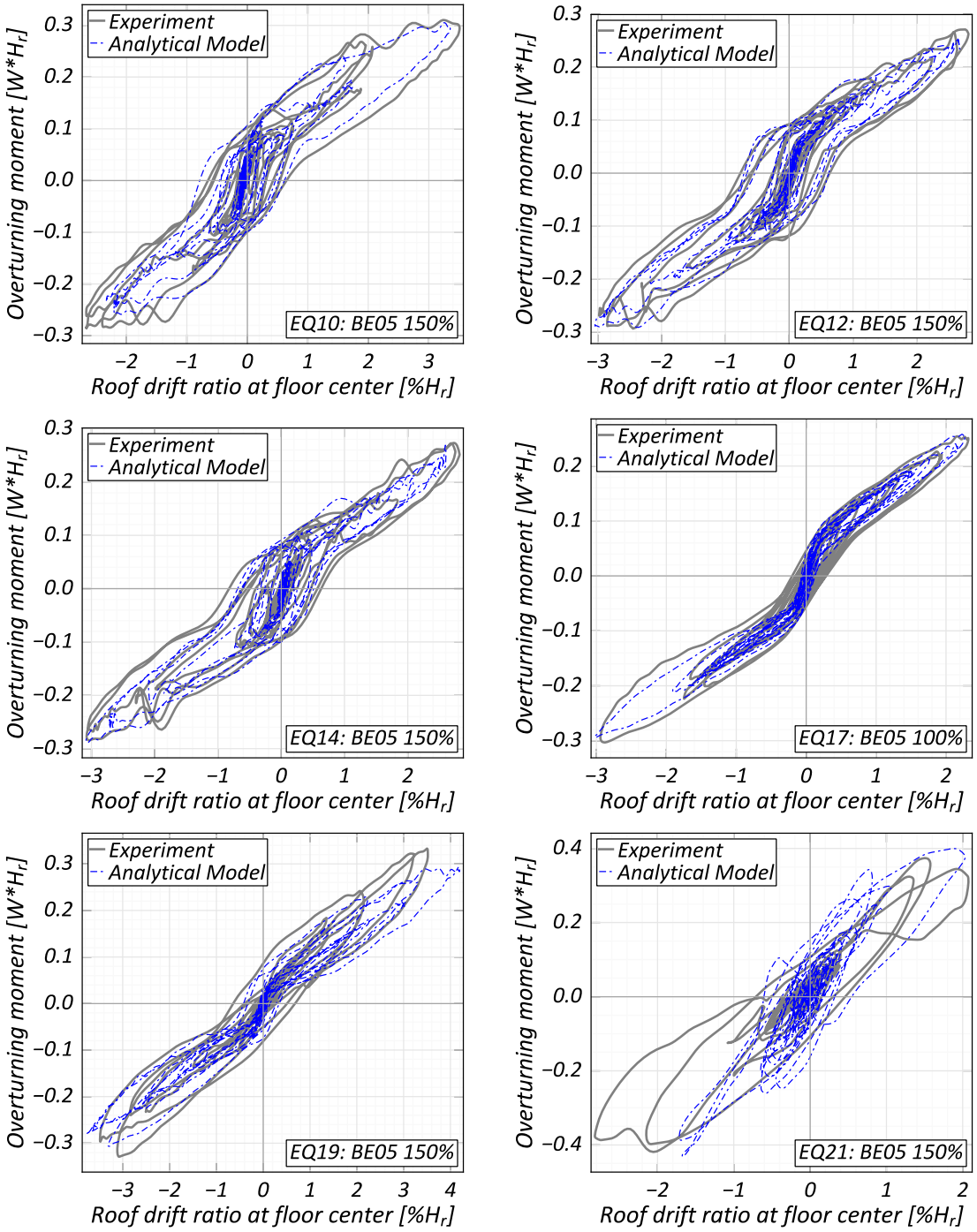

Figure 4.7 Comparison of global hysteresis, MCE$_R$ level earthquakes

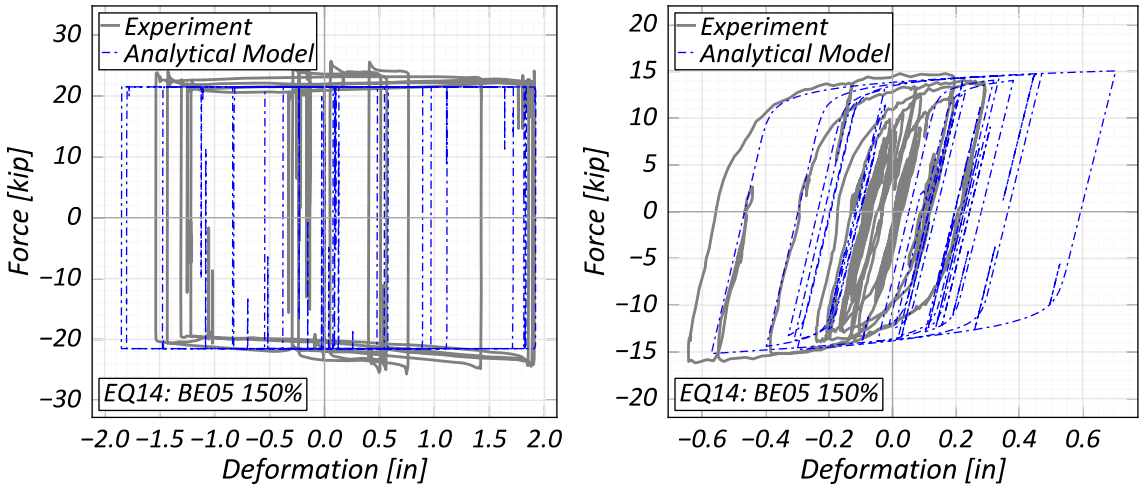

Figure 4.8 Typical FD and BRD response

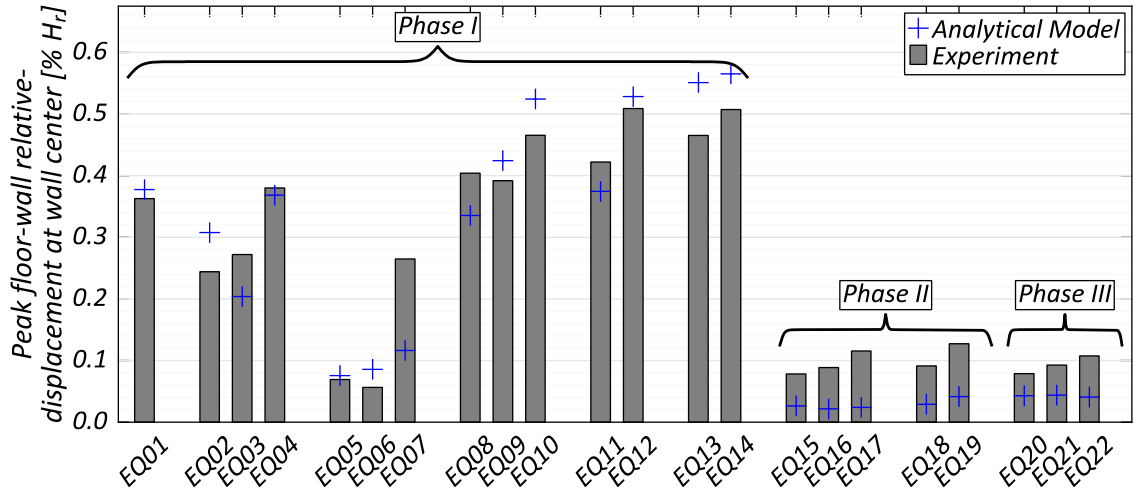

Figure 4.9 Peak floor-wall relative displacement at roof level

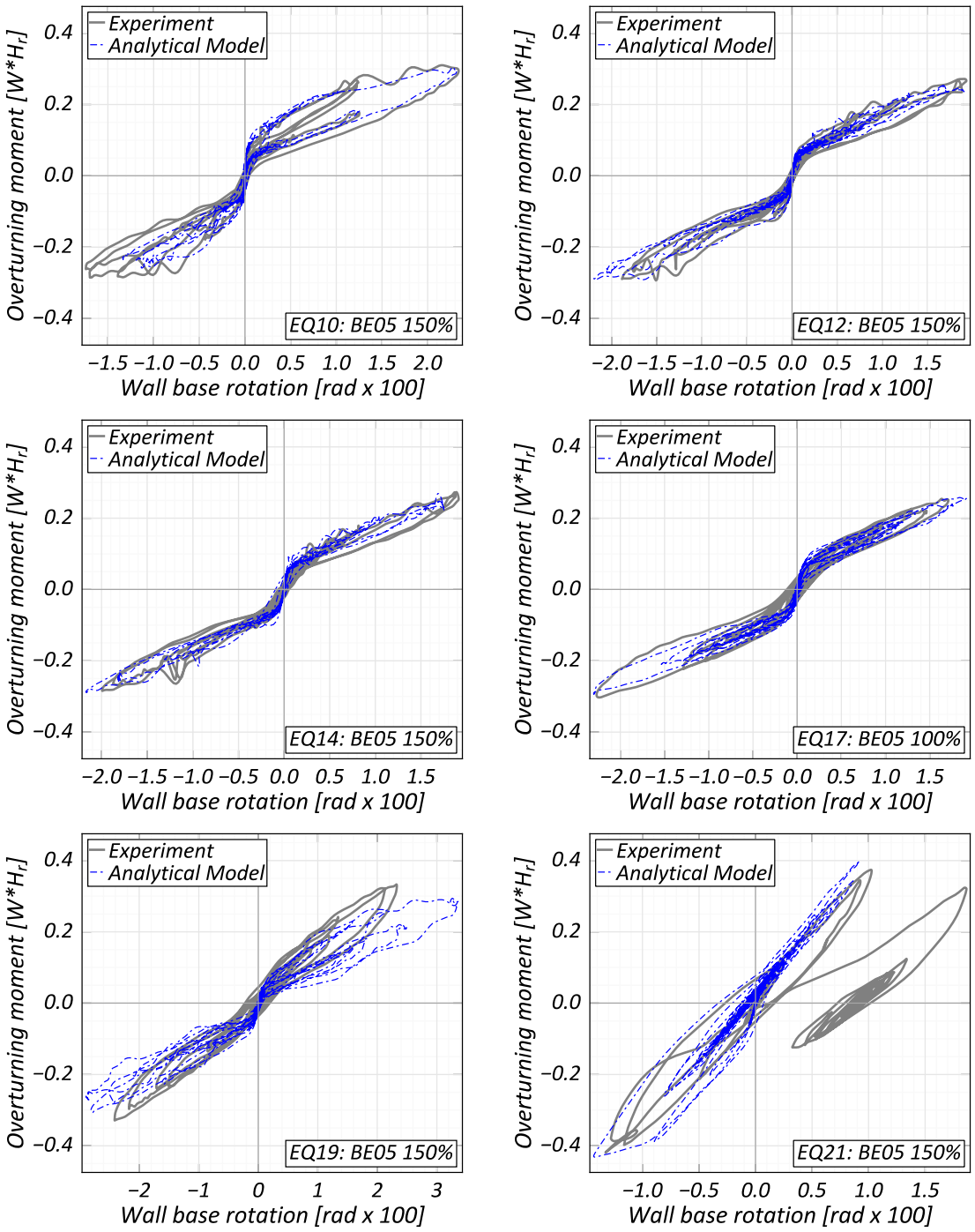

Figure 4.10 E-W wall moment vs base rotation, MCE$_R$ level earthquakes

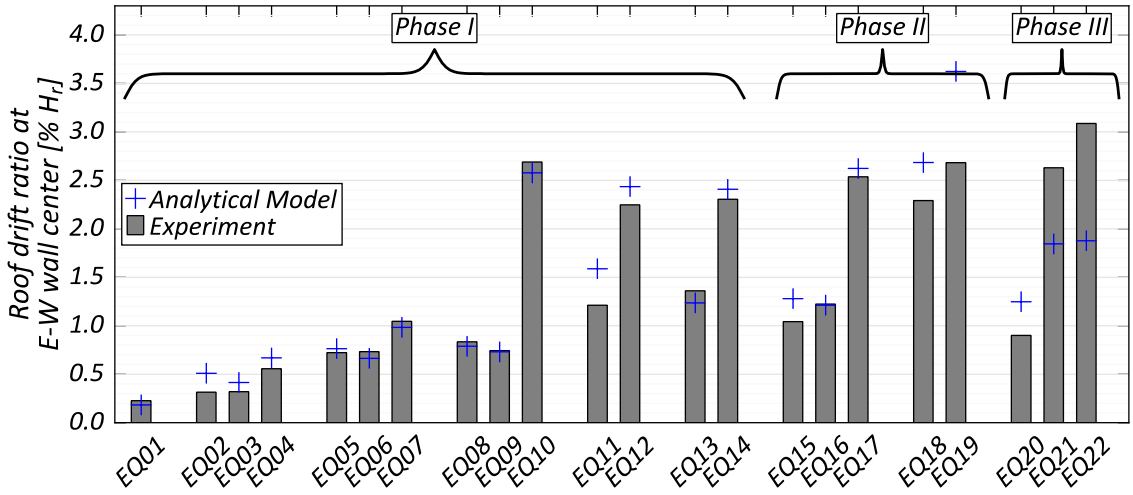

Figure 4.11 Peak roof drifts in the E-W wall

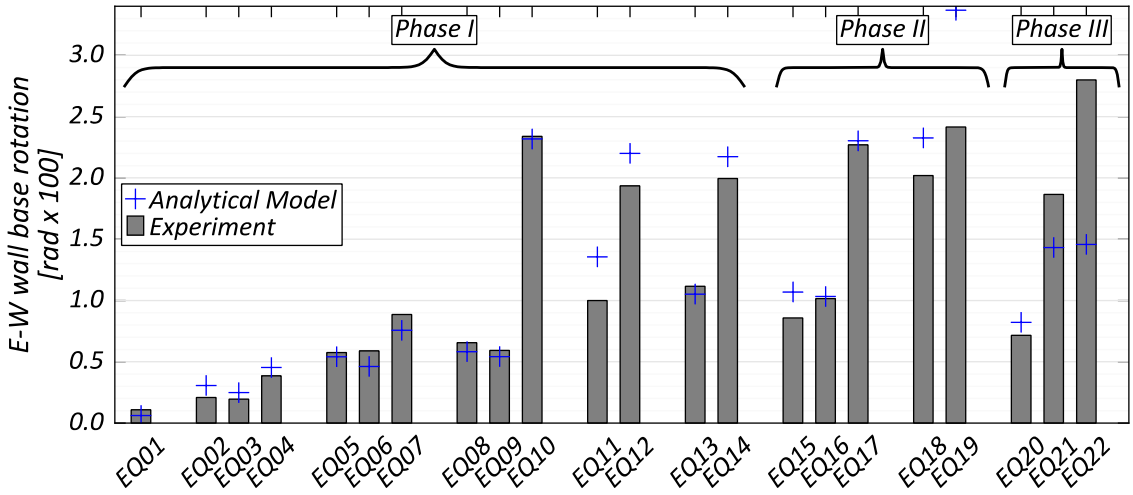

Figure 4.12 Peak base rotations in E-W wall

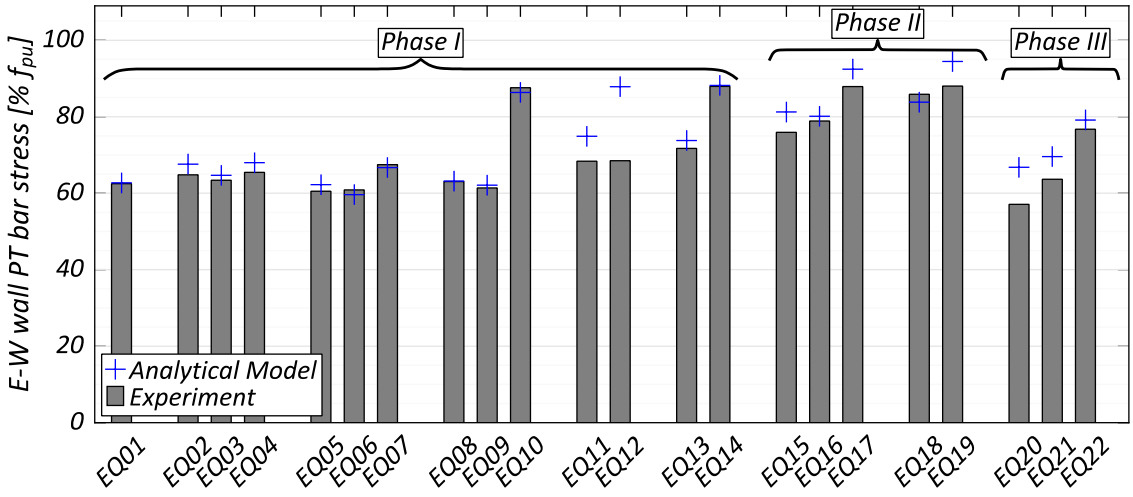

(a) West PT bar

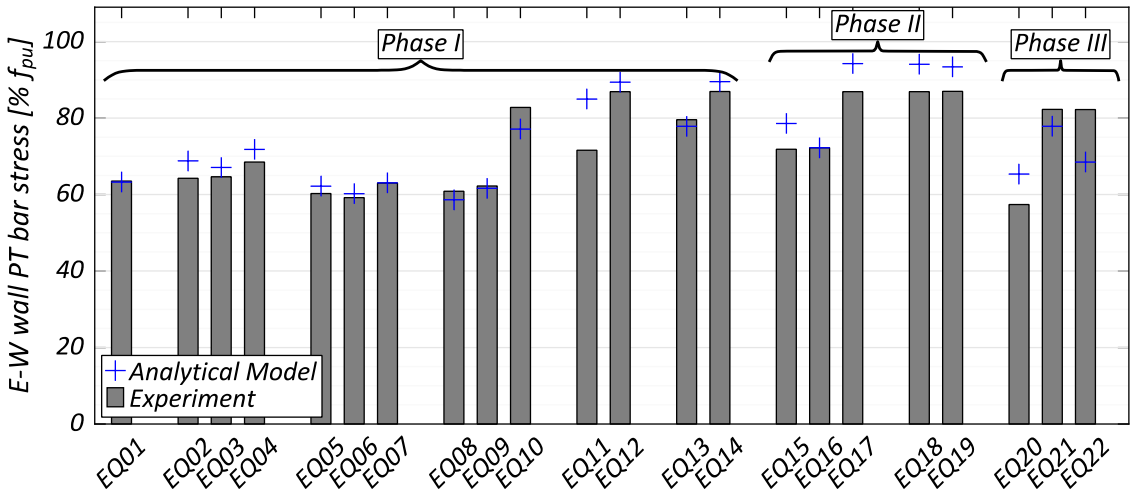

(a) East PT bar

Figure 4.13 Peak stresses in E-W wall PT bars

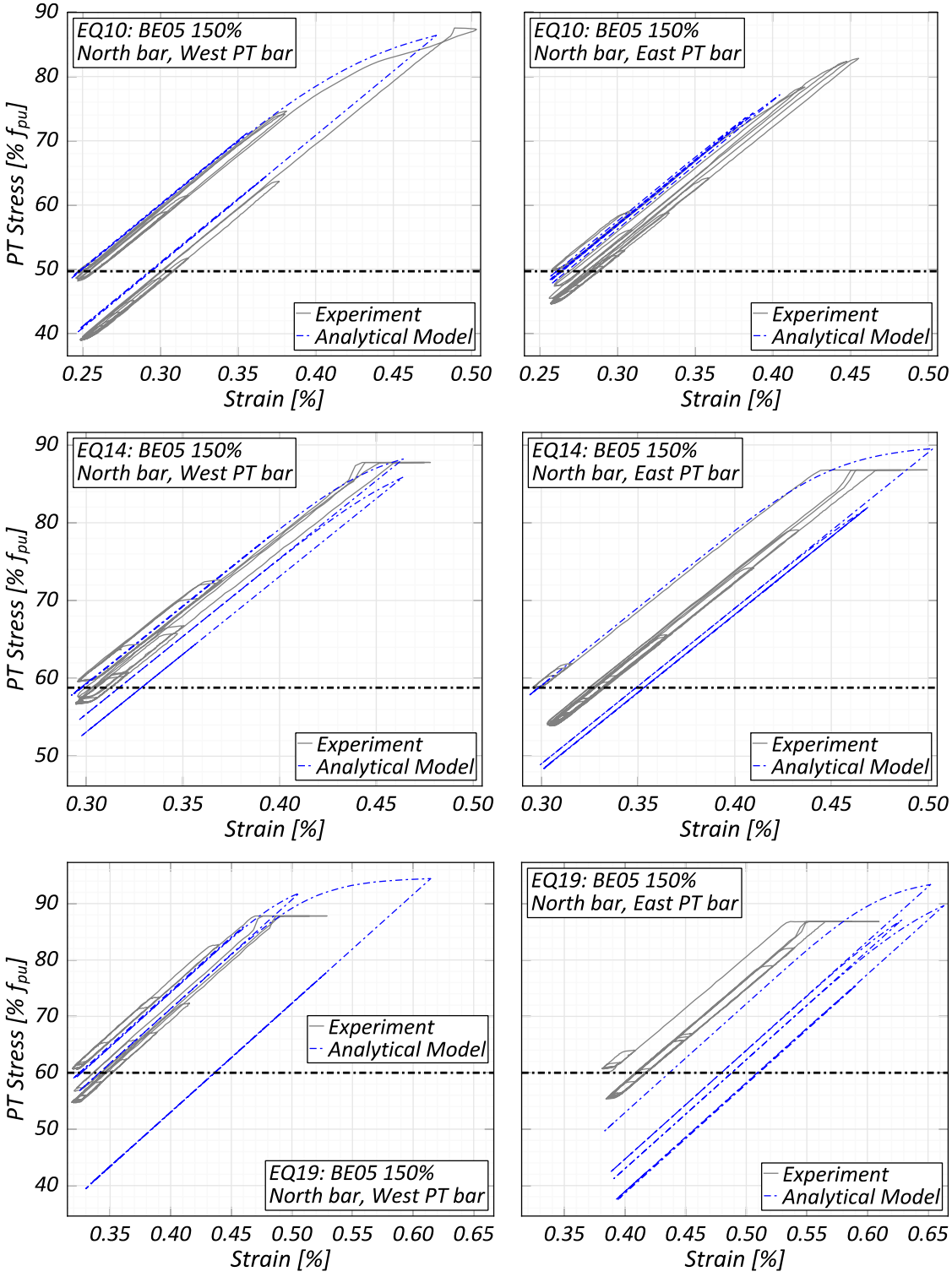

Figure 4.14 Stress-strain responses in E-W wall PT bars

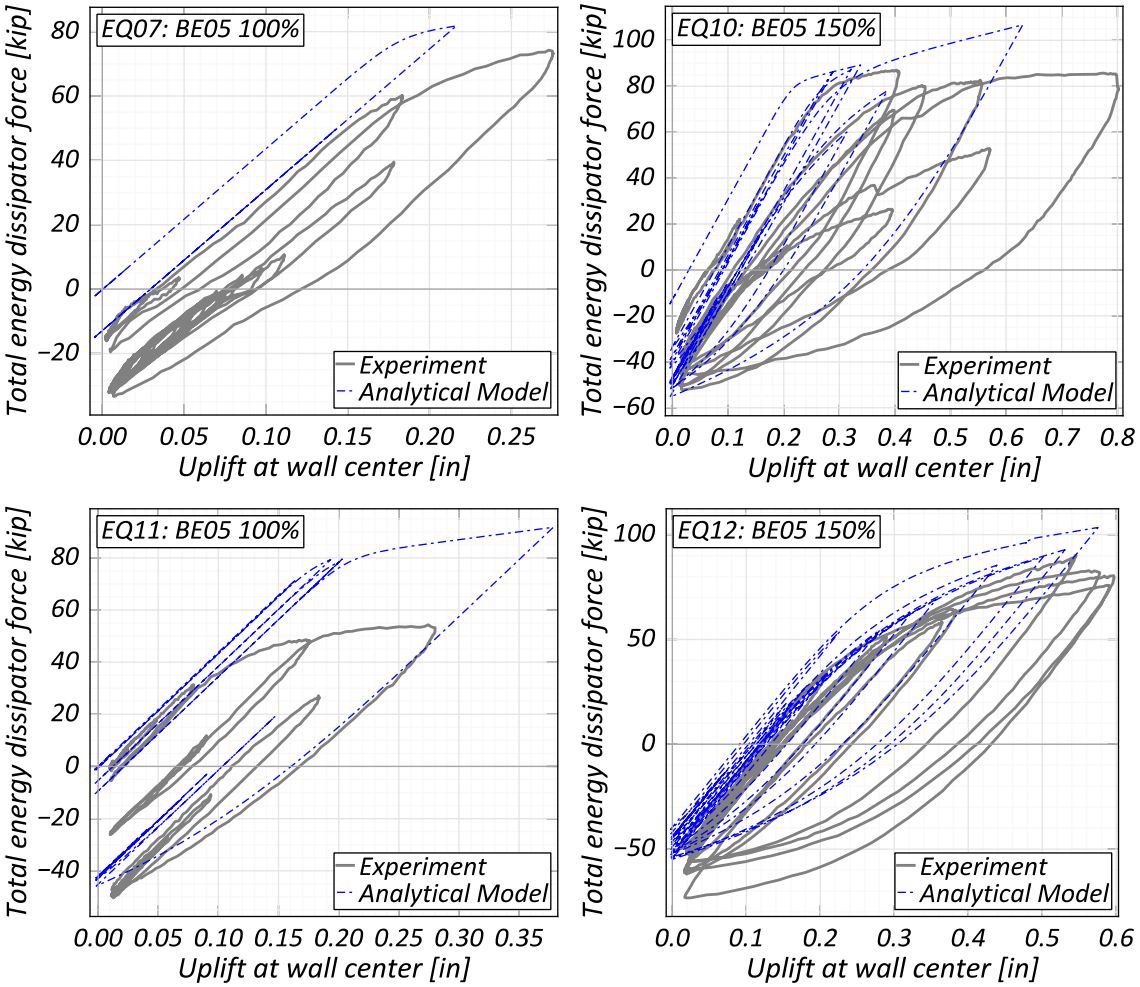

Figure 4.15 E-W wall energy dissipator force vs deformation response

4.3. Low-damage frame systems

4.3.1. Analytical model

The low-damage frame system considered in this work primarily consists of gravity beams capable of rocking at the beam-column joints. The beams can be considered to be formed from four main components:

- A beam segment connecting two adjacent beam-column joints. The beam ends are well confined to maintain a damage free state under large concentration of

compressive stresses which arise during rocking.

- A rocking interface between the beam segment and the joint. The interface is formed from a high strength layer of cementitious material.
- Energy dissipator elements connected between the joint and the beam segment for controlling the system deformations and accelerations. For hysteretic behavior arising from material yielding (for e.g. steel), special care must be taken to limit tensile strains, achieved by debonding a suitable length of the dissipator across the beam-column joint.
- Unbonded post-tensioning elements to maintain the connection between the beam and the column, and to ensure re-centering behavior following non-linear behavior.

The analytical model for the re-centering frame system closely follows the functional components. The rocking interface is modeled using a single displacement-based beam-column element (DBE) with two integration points. Compression-only material rules are used to model the behavior of fibers constituting the element section to simulate the contact behavior at the rocking interface. The energy dissipators are modeled using a single DBE with two integration points, with one end connected to the beam-column joint and the other representing the anchorage location inside the beam. The beam segment is modeled using two beam-column elements separated at the anchorage location of the energy dissipators within the beam which is obtained from the debonded length and the bond-development length. The unbonded post-tensioning bars are modeled using a single truss element connecting the ends of the frame with an applied initial strain

corresponding to the prestress in the bars. Finally, the joint itself is modeled using elastic beam-column elements extending between the joint center and the face of the beams or the columns. A representation of the proposed model is shown in Figure 4.16.

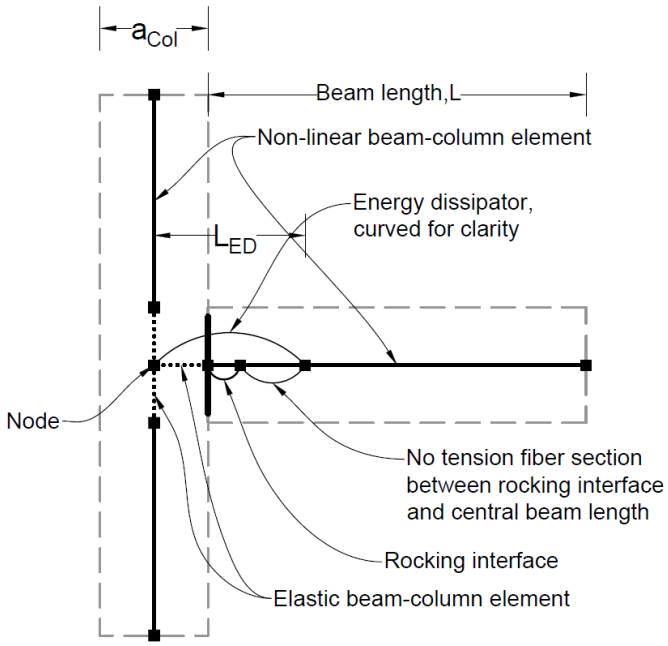

Figure 4.16 Rocking beam model illustration

4.3.2. Model verification: modeling of precast Reinforced Concrete (RC) frame

To verify the accuracy of the re-centering frame model presented above, it is tested against experimental results from Stanton et al. (1995). The experiment tested the performance of a hybrid reinforced precast frame slice consisting of two rocking beams connected at mid height of a gravity column as show in Figure 4.17, with cyclic displacement applied at the column top. 3 x 12.7 mm (0.5 inch), Grade 270 ($f_{pu} = 1862\ MPa = 270\ ksi$) post-tensioning strands prestressed to $0.44\ f_{pu}$ located at the beam centroid provided the re-centering force. Mild steel reinforcement was provided near the top and bottom of the beams to provide energy dissipation. Multiple

configurations of energy dissipators were tested as indicated in Table 4.1. A short debond length of 25.4 mm (1 inch) was provided on both sides of the beam-column interface to avoid bond failure observed in earlier phases of testing. In specimen P-P-Z4, the energy dissipator bars were fully bonded to maximize bond length to prevent bond failure observed in specimen N-P-Z4.

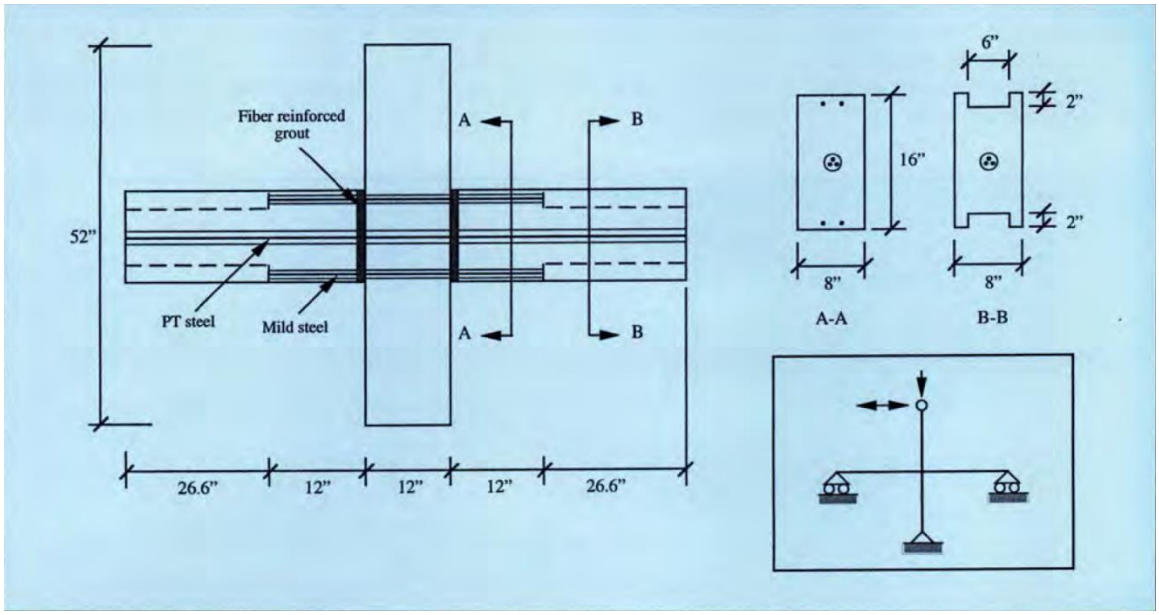

Figure 4.17 Test specimen for calibrating rocking beam model (Stanton et al. 1997)

Axial load of 0.4 $f_c' A_g$, with a design concrete strength of 41.4 MPa (6 ksi), was applied to the top of the gravity column tops and 20-kip vertical loads were applied at 89 mm (3.5 inch) on the beams on either side of the column face. Enough confinement was provided to prevent a brittle compressive failure of the beams during rocking. After application of the initial stress, the post-tensioning strands were grouted at one end (grouted length of 676 mm / 26.6 inch) to model the partial grouting envisioned in the full prototype structure. The partial grouting of unbonded PT tendons is to reduce risk of complete loss of prestress along one side of the building should an end anchorage fail.

Under partial grouting, the tendons are to be unbonded through the column and for a distance on either side of the column and bonded at the mid span of each bay. The length of the unbonded distance is calculated from the required development length of the tendons.

Table 4.1 Energy dissipator reinforcement details for test specimens (Stanton et al. 1997)

Specimen	Mild Steel	$f_{y,exp}$(ksi)	$f_{u,exp}$(ksi)
M-P-Z4	2 #3 Grade 60	61	98
N-P-Z4	2 SS 304	75	100
O-P-Z4	3 #3 Grade 60	61	98
P-P-Z4	3 SS 304	75	100

In the analytical model of the frame slice, the beam segments are modeled using fiber-based beam-column elements, while the columns are modeled using elastic beam-column elements for simplicity. The rocking interface is modeled using DBE and extends from the column face to the location of the 20-kip vertical load. The energy dissipators are assumed to have an unbonded length accounting for bond development, assumed to be 10 bar diameters on each end, in addition to the length debonded intentionally. The dissipators at the top and bottom of a beam are modeled using a single DBE starting at the column face. Their other end connects to a DBE starting at the rocking interface and representing only the concrete in the beam segment. The remaining length of the beam is modeled using an FBE extending to the ends. The post-tensioning tendons are modeled using truss element anchored at the ends of the beams, and for simplicity, the grouted end on one side of the frame slice is modeled symmetrically in the form of a reduction of 338 mm (13.3 inch) in beam length on both sides.

The results from the analytical model are compared to the test results in Figure 4.18. The comparison shows very good match when mild-steel reinforcement is used. For the specimen with stainless steel 304 reinforcement (SS 304), the load is over predicted. This could be attributed to the steel model used – the same Menegotto-Pinto steel model is used for both types of steel.

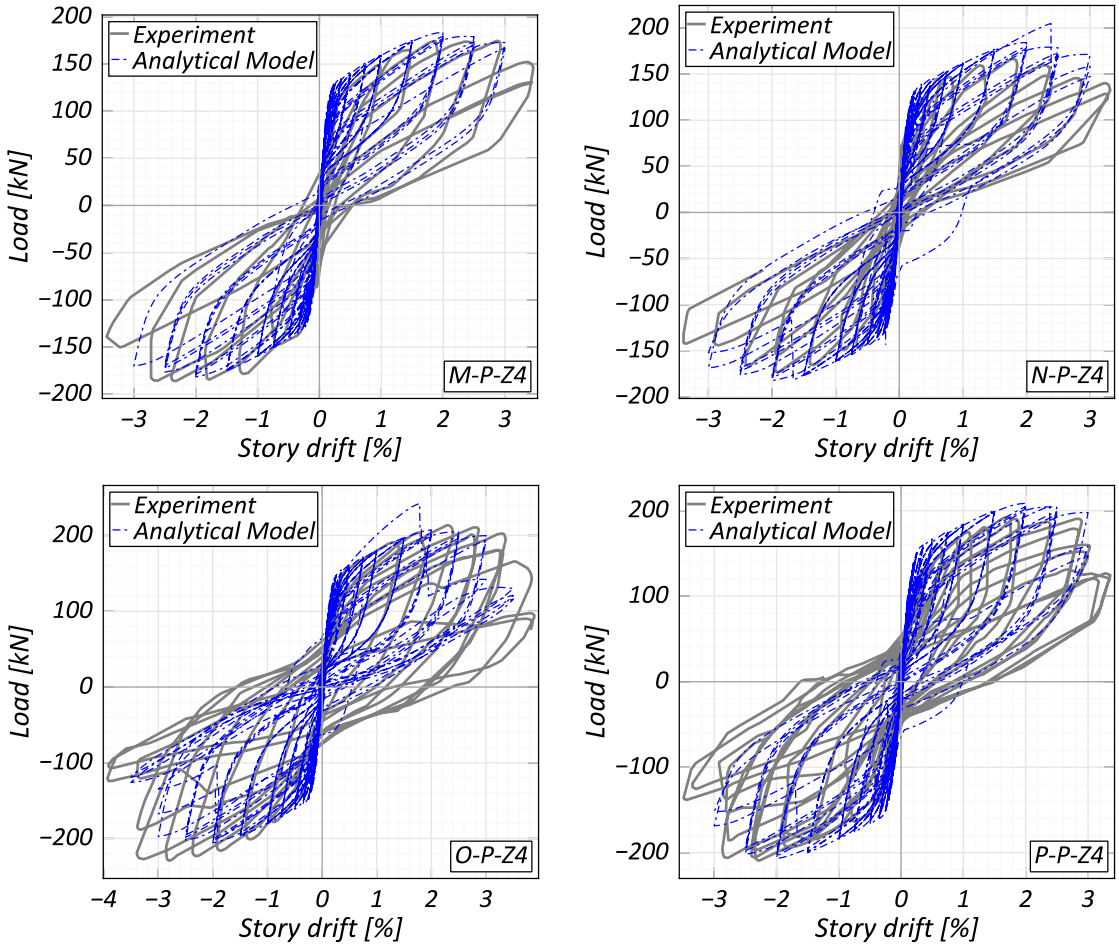

Figure 4.18 Experiment vs analytical results, re-centering beam model

4.4. Analytical study: 13-story building

4.4.1. Building details

The thirteen-story building studied in this analytical study is based on the NEHRP reinforced concrete frame-wall building design example in FEMA-451 (2006). The complete details of the building design using fixed-end members are presented in Barbosa et al. (2009). The building is assumed to be located in Berkeley, California, with an office occupancy. The site is on Soil Class C, with site-specific spectral values, S_{DS} and S_{D1}, of 1.12 and 0.53 respectively, as defined in ASCE/SEI 7-10 (2010) in conjunction with the USGS Java Ground Motion Calculator (2008). The building has one basement level and twelve stories above grade, as shown in Figure 4.19 and Figure 4.20. Typical bays are 9.144 m (30 feet) long in the North-South direction and either 12.192 m (40 feet) or 6.096 m (20 feet) long in the East-West direction.

The floor consists of a two-way, 203 mm (8 inch) thick cast-in-place slab. In the East-West direction, along grid lines 2 through 7, slabs are supported by beams spanning 12.192 m (40 feet) in the exterior bays and 6.096 m (20 feet) in the interior bays. On exterior grid lines 1 and 8, the larger spans have been subdivided into two equal parts and therefore these frames have a total of five 6.096 m (20 feet) spans. In the North-South direction, the slabs are supported by beams spanning 9.144 m (30 feet) on grid lines A, B, C and D. The beams in both directions are 813 mm (32 inch) deep and 572 mm (22.5 inch) wide.

The lateral force-resisting system in the North-South direction consists of four 7-bay Special Moment-resisting Frames, while in the East-West direction, the lateral force-

resistance is provided by a dual system composed of four Special Moment Frames (SMF) and four Special Structural Walls with outrigger beams on gridlines 3, 4, 5, and 6. All columns are 762 mm (30 inch) square; the structural walls are 6.858 m (22.5 feet) long with 762 mm (30 inch) square boundary elements at both ends and a 305 mm (12 inch) thick web.

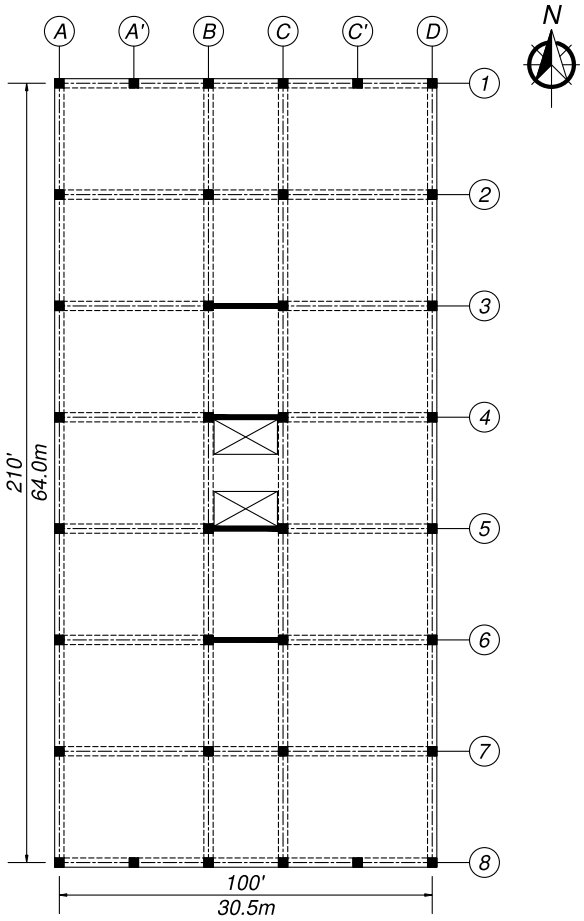

Figure 4.19 Plan view of analytical study building (Barbosa 2011)

To determine the member sections, the building was designed according to ACI 318-11 (2011) and ASCE/SEI 7-10 (2010) requirements using Grade 60 reinforcement throughout and a specified concrete strength (f'_c) of 5 ksi. According to ASCE/SEI 7-10,

the building was classified as Seismic Design Category D, with an importance factor (*I*) of 1 and response modification coefficients (*R*) of 8 for the Special Reinforced Concrete Moment Frame system in the North-South direction and 7 for the dual system composed of the Special Reinforced Concrete Structural walls and the Special Moment Frames in the East-West direction. The design base shear coefficients were 4.1% in the North-South (Special Moment Frames) direction and 7.6% in the East-West direction (dual system). The drift requirements in ASCE/SEI 7-10 (2010) were verified to be fulfilled using a 3D elastic SAP2000 model.

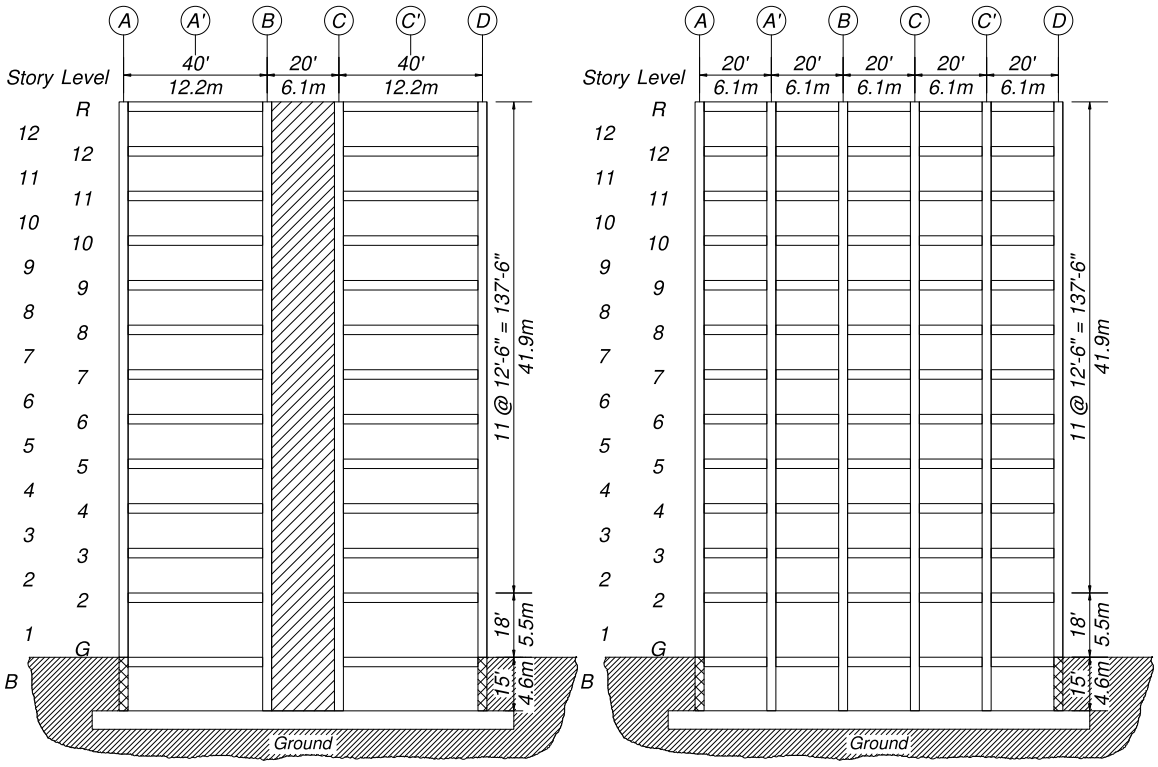

Figure 4.20 Elevation of analytical study building through grid lines 3 and 8 (Barbosa 2011)

Typical reinforcement ratios in key column, beam, and wall elements are listed in Table 4.2, Table 4.3 and Table 4.4 respectively. The unfactored gravity axial load in the

perimeter columns ranged approximately from 0.15 f'_cA_g to 0.35 $f'_c\ A_g$, while the gravity load on the walls was 0.12 f'_cA_g.

Table 4.2 Column reinforcement ratios in selected columns in Story 1

Location	Ratio, ρ_l
Corners	1.7%
Line B/C; Line 1/8	2.1%
Line A/D; Line 2/7	2.1%
Line A'/C'; Line 1/8	2.1%
Line B/C; Line 2/7	2.8%

Table 4.3 Beam reinforcement ratios in selected beams on Level 1

Location	Ratio, ρ_l'	Ratio, ρ_l
Outrigger beam lines 3-6	1.5%	0.7%
Lines B8-C8	0.77%	0.55%
Lines A8-A7 and A5-A4	0.64%	0.55%

Table 4.4 Wall reinforcement ratios in Story 1,

Location	Ratio, ρ_l
Boundary elements	1.3%
Web	0.2%
Total web and boundary elements	0.73%

For this analytical study, the Grade 60 reinforcement was replaced by high strength Grade 100 reinforcement. The replacement was achieved by reducing the area of the longitudinal reinforcement detailed for the Grade 60 design by the ratio of the nominal yield strengths of the two reinforcement grades, i.e. a factor of 0.6. This modification results in a slight reduction in structural stiffness and hence increased deformations, which give a provide a more suitable structure for demonstrating the effect

of re-centering structural components on the building behavior. The high strength reinforcement was assumed to be adequately developed under the same layout as Grade 60 reinforcement through the use of mechanical couplers to offset the increased development length requirements.

4.4.2. Low-damage wall system

The re-centering wall behavior in the building was designed following the recommendations of Rahman and Restrepo (2007). The design requires the selection of post-tensioning forces, energy dissipator elements and controlling the neutral axis depth to ensure stable hysteretic and geometric behavior. The wall foot-print was assumed to be unchanged for the re-centering system.

Post-tensioning force in each wall was provided by 15 mm (0.6 inch) Grade 270 tendons ($f_{pu} = 1862\ MPa = 270\ ksi$) debonded over the wall height. In each wall, two groups of tendons, each with a steel area of 77 cm^2 (11.94 $inch^2$) and a prestress of 60% f_{pu}, spanned the wall height at an offset of 1.524 m (60 inch) from the wall center.

Preliminary design for energy dissipators was done using Grade 60 steel. Twelve (12) #11 Grade 60 reinforcing bars distributed over a 3.05 m (120 inch) length of the wall around the wall center-line provided the energy dissipation. An effective debonded length of 40 bar diameters (d_b) including the bond development was assumed for each bar. The total energy dissipator area was selected for an equivalent viscous damping ratio of approximately 20% as given by equation 4.1 developed in Toranzo (2002). For the final analytical model, the reinforcement was replaced with Grade 100 steel with a cross section area reduced by a factor of 0.6 to maintain similar levels of strength between the

Grade 60 and Grade 100 designs. Additionally, the dissipator debond length as calculated for the Grade 60 building was scaled up by a factor of 1.29 ($\sqrt{100/60}$) to counter the increased deformation demands expected in the Grade 100 building and the reduced ductility capacity of the Grade 100 reinforcement.

$$\xi = \frac{2}{\pi}\frac{\beta}{1+\beta}100\%$$
$$\beta = \frac{2F_y}{W} \qquad 4.1$$

An important change between the fixed-end building and the rocking wall building is in the connection between the floor slabs and the walls. In the fixed-base building, the walls carry the gravity loads in their respective tributary areas in addition to resisting the lateral loads. This gravity load constraints wall uplift and rotation and adds uncontrolled re-centering behavior through variable axial loads from the floor vertical accelerations. For full utilization of wall re-centering behavior, the vertical motion between the walls and the floors was decoupled using PSA connectors, with supplementary gravity load bearing members provided in lieu of the structural walls for supporting the floor beams. These columns were designed to have low flexural stiffness, following the gravity column concept presented in Chapter 3 With these gravity columns, the axial load in the walls was limited to their self-weight, and the neutral-axis depth at the displacement capacity was determined to be approximately 0.813 m (32 inch), which is under the limit recommended by Rahman and Restrepo (2007).

4.4.3. Low-damage frame system

As a part of the analytical study, the building perimeter frames above the ground level were replaced with a re-centering frame system. In the re-centering frame design, some of the longitudinal reinforcement in the fixed-end beams was replaced by post-tensioning steel. For determining the amounts of post-tensioning steel and the energy dissipating mild steel, the moment capacity of the beams in the fixed-end and re-centering frame system was maintained at the same level, with a pre-selected portion of the moment capacity assigned to the mild-steel ($\alpha = 30\%$) and the remaining capacity obtained from the post-tensioning steel at the allowed maximum stress, which is selected as a part of the design. This concept is presented in equation 4.2. The preliminary design of the re-centering frame system was completed using Grade 60 steel for the energy dissipators and Grade 270 post-tensioning tendons with an allowed peak stress of 65% f_{pu}, expected to be reached at 3% rotation at the beam-column joint.

$$M_o = \alpha M_o + F_{PP} j_{d,PP} \qquad 4.2$$

The beams in the perimeter frame along the North-South face of the building were designed with 3 #9 and 2 #8 Grade 60 reinforcement bars at the top and 5 #8 Grade 60 reinforcement bars at the bottom. The corresponding beams in the re-centering frame were reinforced with 2 #8 Grade 60 bars at the top and bottom with a debond length of 254 mm (10 inch) at the beam-column joint. The post-tensioning was provided by 10 x 15 mm strands with an initial stress of 45% f_{pu} and unbonded over the length of the entire frame with anchorage at the frame ends.

The beams forming the perimeter frame in the East-West direction were reinforced with 2 #10 and 3 #9 Grade 60 bars at the top and 5 #8 Grade 60 bars at the bottom. These larger moment capacity beams were replaced with re-centering beams reinforced with 3 #7 Grade 60 bars at the top and the bottom with the same debond length of 254 mm (10 inch), and with additional post-tensioning reinforcement provided by 12 x 15 mm (0.6 inch) diameter strands with an initial stress of 45 % f_{pu}.

For the final analytical model with Grade 100 mild steel reinforcement, the bar cross section area was reduced by a factor of 0.6 (60/100) to maintain similar strength to the Grade 60 design. The effective debond length for the energy dissipator mild steel bars was assumed to be the debond length and an additional 10 bar diameter length on each end to account for the bar development.

4.4.4. Analytical model

The nonlinear dynamic response of the building to seismic base excitation was analyzed using the Open System for Earthquake Engineering Simulations (OpenSees 2013). The finite element model of the fixed-end building was developed in Barbosa (2011) using OpenSees and a representation of the model is shown in Figure 4.21.

Beams and columns were modeled using force-based, discrete-fiber elements. Barbosa (2011) presents a parametric study to determine the correct number of integration points and the section discretization to reduce localization issues and optimize computation times. The parametric study was calibrated against test data from Soesianawati (1986), specimen No.1. Based on the study, each section was divided into 105 fibers (49 fibers in the core and 14 fibers in each of the four cover regions). Three

integration points were used for the beams, wall non-linear fiber elements and at the column elements at the bottom of the basement level, while four integration points were used for the remaining columns.

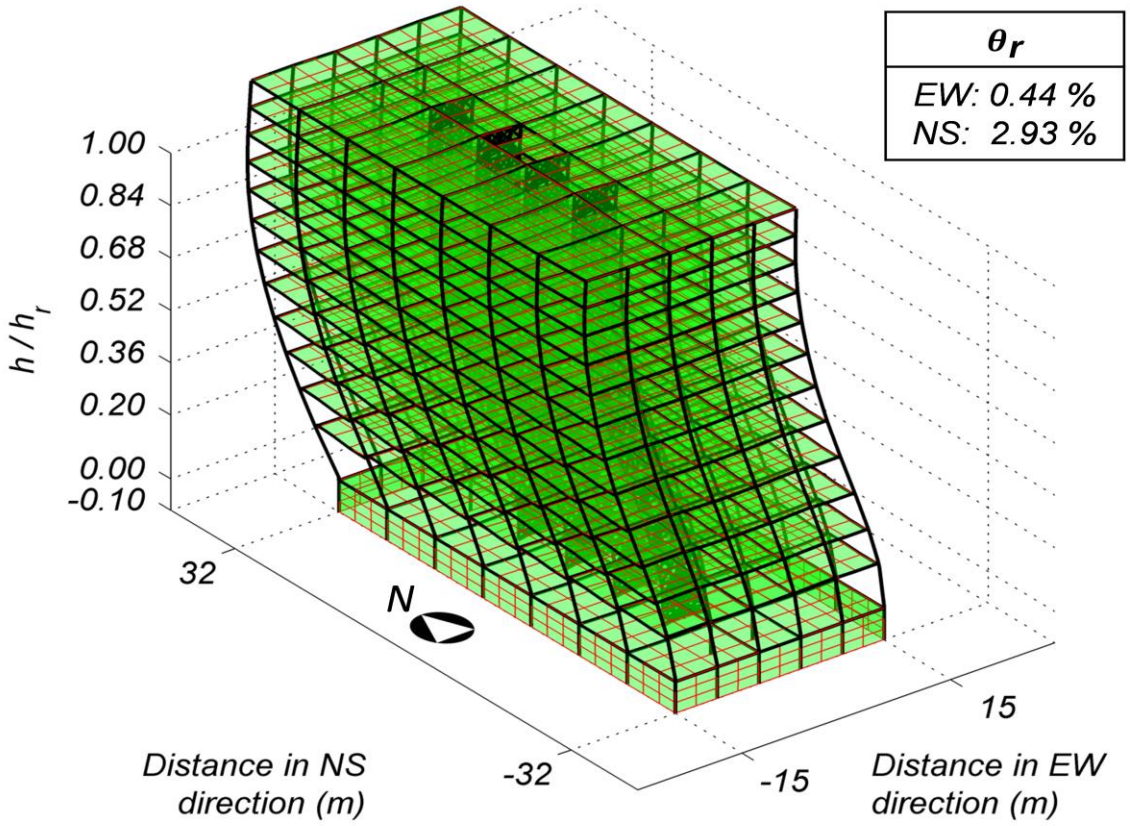

Figure 4.21 Rendering of the finite element model of the analytical study building

All analyses were performed assuming expected material properties. The Concrete02 model with the linear tension stiffening material was used to model unconfined and confined regions in the structure. The expected unconfined concrete strength was assumed to be 6.8 ksi, that is 1.36 times the specified strength. The expected strength for the core concrete, well confined by hoops in columns and boundary elements of walls, was calculated at 9.4 ksi. Additionally, to further control localization the

concrete material behavior was modified based on the notion of concrete fracture energy, as per the suggestion of Lu and Panagiotou (2014). For this, the crushing strain (ε_u) was modified for the end integration points using equations 4.3 and 4.4.

$$\varepsilon_u = (1 - \Lambda)\varepsilon_o + \frac{l_R}{l}(0.2\% + \Lambda\varepsilon_o) \quad 4.3$$

$$\Lambda = \frac{f_c'}{0.5(E_c'\varepsilon_o + f_c')} \quad 4.4$$

The reinforcement was modeled using an advanced material model based on the works of Dodd, Restrepo and Carreño, which is an enhancement to the material rule presented in Dodd and Restrepo-Posada (1995). The parameters used for the steel model are listed in table 4, and the monotonic backbone curve is shown in Figure 4. The steel model is not included in the current official release of OpenSees and required a custom build from source code. A complete description of the material models, except the steel model, and their parameters is given in the OpenSees Command Language Manual (Mazzoni et al. 2007). The model developed here did not capture bond slip of the beam longitudinal reinforcement anchored in the beam-column joints, or of the wall longitudinal bars anchored below the critical region of the walls where plasticity developed. Under this limitation, the model is unable to capture any bond failure of longitudinal bars anchored in beam-column joints. However, under the assumption of reinforcement anchorage through mechanical devices, bond slip was expected to play a minor role in the response. The effect of transverse tensile strain on compressive stresses could also not be captured using the concrete model used.

A phenomenological model was adopted for the slabs, based on the experimental observations by McBride et al. (1996) and Lau and Fenwick (2002). Both studies reported that: (a) presence of slab influences the lateral behavior of frames by increasing both story shear capacity and stiffness and (b) beam plastic hinge elongation is observed regardless of the presence of slabs, and, according to McBride et al., not influenced by the presence of slabs. The beam plastic hinge elongation was also observed in the aftermath of the February 2011 earthquake in Christchurch, New Zealand (Barbosa 2011). Further details of the floor diaphragm model can be found in Barbosa (2011).

The structural walls were modeled using the Non-linear Beam Truss model presented in Section 4.2.2.1. The boundary regions at the wall toes were modeled using one force-base beam column element for each toe, and the wall web was divided into three segments for modeling using the beam-column element with flexural releases in plane. Along the wall height, four subdivisions were used in the basement and in the first story, with the remaining stories divided into two subdivisions vertically. For the rocking wall implementation, the rocking interface was modeled using 50.8 mm (2 inch) thick beam-column element, the PT strands were modeled using truss elements anchored at the ground level and the energy dissipators were modeled using beam-column elements. Both the PT elements and the energy dissipator elements were located colinear with the outer elements representing the web. Finally, the frames with rocking behavior were modeled as presented in Section 4.3, using a 25.4 mm (1 inch) thick rocking interface and with the PT strands anchored at the frame ends.

4.4.5. Input ground motions and analysis strategy

In order to perform the nonlinear time-history analyses, seven historical ground motion pairs were selected for the analyses from the 2010 PEER Strong Motion Database (2011). All seven ground motions are listed in Table 4.5 and had near-fault characteristics. Figure 4.22 shows the spectra for ground motions in the Fault Normal and Fault Parallel directions, respectively. A comparison of the arithmetic mean spectra for the Fault Normal and Fault Parallel ground motions reveals that the Fault Normal components of the ground motions have stronger intensity than the Fault Parallel components over the entire period range. The ground motion records were scaled to ensure that the arithmetic mean spectra calculated for 5% damping of the square root sum of the squares of the Fault Normal and Fault Parallel components were greater than the response spectra determined from ASCE/SEI 7-10 for the maximum considered earthquake. This objective was attained up to a period of 5.8 seconds, except for a small range at around a period of 0.6 seconds, as shown in Figure 4.22(c). Figure 4.22(a) shows that, beyond a period of 0.75 seconds, the mean spectrum corresponds very closely to the ASCE/SEI 7-10 spectrum.

The non-linear analysis using OpenSees was done in three stages. In the first stage, non-linear static analysis was performed with gravity loads applied to the structural model. This led to the development of cracking in some members, and small changes in the modal properties of the structure. Modal analysis is performed on the cracked structure in the second stage and Rayleigh damping is defined based on the mass and the initial stiffness matrix, with the matrix coefficients determined on the basis of the cracked

structure frequencies. Damping coefficients of 2% were set at the first mode (1.77 seconds, 0.56 Hz) and the tenth mode (0.16 seconds, 6.25 Hz), meaning that all the higher modes of significance were under-damped. The Rayleigh coefficients were calculated to be 0.129 for mass-proportional damping and 9.45 x 10^{-4} for stiffness proportional damping. The damping formulation used for the 13-story building is shown in Figure 4.23. At the highest frequency of 6.25 Hz, the cumulative modal mass was calculated to be nearly 100% of the total mass in the direction of the frames and 95% in the direction of the walls. In the third stage, non-linear dynamic time-history analyses were performed, with an integration time step no larger than 0.005 seconds.

During the dynamic analysis, the damping matrix for the re-centering systems is recalculated at each step using the structural stiffness matrix updated to reflect the most current stiffness at the rocking interfaces. This damping formulation ensures that any fictional damping forces arising during the non-linear rocking behavior are eliminated and spurious damping is not added to the numerical model as the structure fundamental period elongates during the dynamic analysis (Charney 2008).

Table 4.5 Details of ground motions used for 13-story building parametric study

Record ID	Earthquake	M_w	Station	MCE_R Scale Factor	Scaled PGA (g), Fault Normal
NZ002	Christchurch, NZ, 2011	6.3	PRPC	1.55	0.88
P0179	Imperial Valley, 1979	6.5	El Centro Array #7	1.5	0.69
P0082	San Fernando, 1971	6.6	Pacoima Dam	1.2	1.72
P0990	Northridge, 1994	6.7	Newhall -W. Pico Canyon Road	1.0	0.43
P1024	Northridge, 1994	6.7	Sylmar – Converter Station East	1.2	1.01
P0144	Tabas, Iran, 1978	7.4	Tabas	1.0	0.85
C4816	Wenchauan, China, 2008	7.1	Mianzuqingping	1.0	0.93

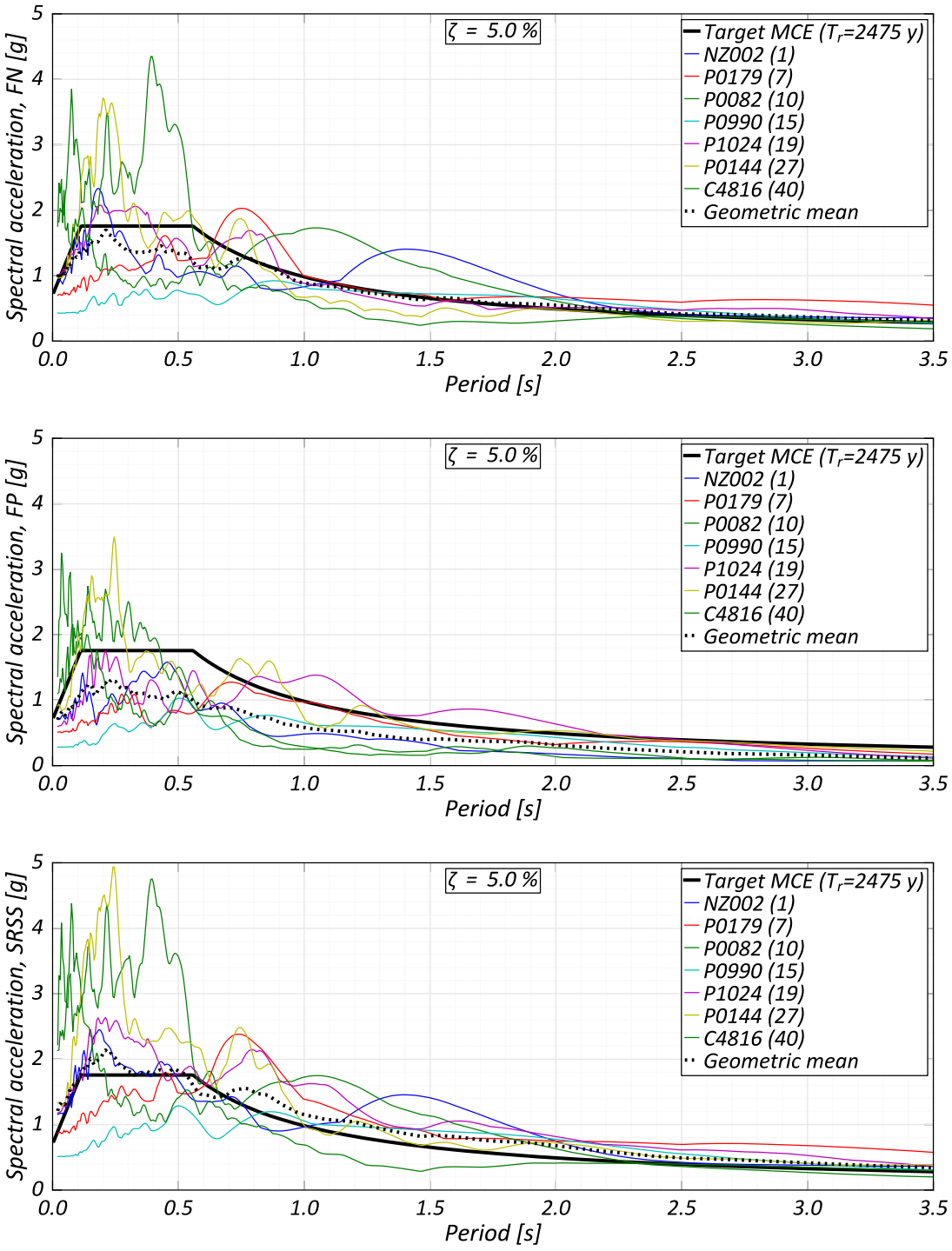

Figure 4.22 Response spectra for 5% damping of records scaled at MCE_R (maximum considered earthquake), mean and target spectra

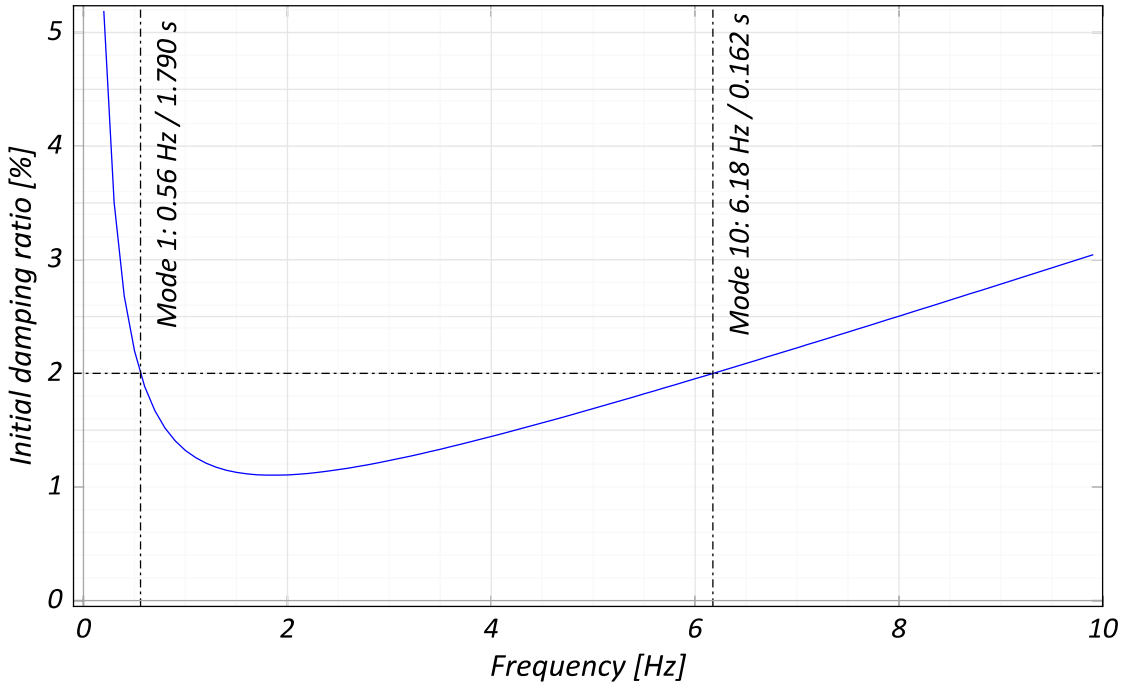

Figure 4.23 Rayleigh damping model used for the analysis of the 13-story building

All the nonlinear analyses were carried out accounting for non-linear geometry (P-Delta effects). The Newton Raphson algorithm is used to solve the equilibrium equations in all stages. Load control is used to formulate the equilibrium equations during Stage I, while the Newmark constant average acceleration method is used to integrate the equations of motion during Stage III.

Convergence is decided on the basis of the energy unbalance in the system for Stage I, with convergence criteria of energy unbalance less than 10^{-12} kip-in. For Stage III, convergence is decided using the increment in the norm of the displacement vector, with a tolerance of 10^{-5} inches. Should the analysis fail to converge during the transient stage, the integration time step size and the tolerances are successively changed (time step size reduced to a minimum of 0.00025 s, and tolerances increased to a maximum of

0.1 inches) until convergence is reached again, at which point these values are reverted to the originals and the analysis restarted.

4.4.6. Results

In the results from the analytical study of the 13-story building presented next, the floor drifts have been normalized by the height of the roof above the ground level, while the inter-story heights have been normalized by the story height and presented as a percent. The floor acceleration envelopes have been calculated from the geometric mean of the acceleration envelopes under individual ground motions, normalized by the ground motion's PGA. The overturning moments have been normalized by the structure total weight 227.4 MN (51134 kips) and the roof height above the ground level. The results have been presented for the structure orientation parallel to the fault normal component of the ground motion i.e. if the fault normal component is applied along the North-South direction, the corresponding results presented are also in the North-South direction and vice-versa. For all results, applied fault normal and fault parallel components of the individual ground motions have been oriented such that the structure peak roof drift responses along the dual system and the SMF occur along the positive X (East) and positive Y (North) direction respectively, to remove the effect of structure orientation.

Figure 4.24 and Figure 4.25 show the geometric mean of the floor story drift and the floor inter-story drift envelopes over the structure height. The envelopes along the East-West direction, i.e. parallel to the structural walls, are very clearly separated into two groups on the basis of the structural wall configuration, indicating that the wall configuration controls the response in the dual system. The greatest inter-story drift is

seen at the ground level for the low-damage wall configuration, and at mid-structure height for the conventional wall configuration. For the East-West direction, the low-damage wall configuration has greater drift envelopes than the conventional, fixed end wall configuration.

For case when the fault-normal component of the ground motion is applied along the North-South direction i.e. orthogonal to the plane of the wall, the configurations of both the walls and frames have an effect on the global structure response. The general response is skewed towards the East direction, indicating permanent deformations under peak drifts. For the peak drift direction, all configurations show similar levels of peak inter-story drifts, which occur between floors 3 and 4. At levels below floor 3, the conventional structure shows the smallest floor and inter-story drifts, followed by the configuration with only low-damage walls. The remaining two configurations show very similar levels of drifts. This trend is reversed above floor 4, with largest drifts in the conventional configuration, followed by the low-damage wall configuration, with the remaining two configurations showing similar and smallest levels of drifts. Along the West direction, the envelopes show a consistent trend with lowest drifts in the low-damage wall configuration, followed by the conventional configuration, the low-damage wall & frame configuration and lastly the low-damage frame configuration with largest drifts.

Figure 4.26 shows the geometric mean of the overturning moment envelope in the structure. For the case when the fault normal component oriented in the East-West direction, the moment demands are smaller by roughly 10% in the structure with the low-

damage walls as compared to the conventional, fixed-base walls. The response along the direction of the dual-system is again controlled by the wall configuration. For the case with fault normal component oriented orthogonal to the walls, the smallest moment demand is observed in the configuration with the low-damage walls, followed by the conventional, fixed-end system, the configuration with low-damage frames and low-damage walls, and finally the low-damage frame configuration.

Figure 4.27 shows the geometric mean of the acceleration envelope along the wall height. Along the East-West direction, the configurations with low-damage walls show larger accelerations below floor 7, however above floor 7, all configurations show similar levels of peak accelerations. A sharp decrease in peak accelerations is seen at floor 10, followed by global peak accelerations at the roof level. Along the North-South direction, the configuration of the lateral force resisting system does not exert any significant effect on the acceleration envelope, with all accelerations significantly reduced above the basement level.

Figure 4.28 shows the geometric means of the peak drift ratios seen at the geometric center of the floors in the structure. The peak drifts in the East-West direction, where the response is governed by the wall response, show a significant increase of roughly 25% for the low-damage wall configuration compared to the conventional wall configuration. The peak drifts in the North-South direction however show minimal effect of the configuration of the SMF or the structural walls.

Figure 4.29 shows the geometric means of residual floor and inter-story drifts seen at the geometric center of the floor. The advantage of the low-damage systems is

apparent from these results. A significant reduction in residual drifts is typically observed in the low-damage configurations. A 75% reduction in the North-South direction inter-story drifts is observed due to the low-damage frame, while a 43% reduction is observed in the East-West direction inter-story drifts due to the low-damage wall system. The incorporation of low-damage frames results in the reduction of residual drifts for all cases. However, for the scenario where the low-damage wall configuration is excited with the fault normal ground motion component in the out-of-plane direction to the walls, an increase in residual drifts is observed. A possible explanation for this behavior is damage to the rocking interface layer due to a shallow neutral axis and large compressive stresses.

Figure 4.30 compares with the conventional, fixed-end structure the response of the structure with the low-damage wall configuration. For the low-damage wall system, the flag shaped hysteresis can be clearly seen in the moment-rotation response. The wall base moments are noticeably smaller for the low-damage wall system, this is a result of the vertical direction disconnect introduced to allow rocking in this system. The disconnect results in significant reduction of the axial load which can be transferred from the floors to the walls, which results in smaller base moment in the low-damage walls. The flag shape hysteresis of the low-damage walls shows only a minor effect on the global moment-drift response, which is visible in the form of a small amount of pinching and increased drifts in the East-West direction. One contributing factor for this behavior is the low percent (less than 50%) of the global moment being carried by the structural walls.

Figure 4.31 shows a comparison between the global and local responses between the conventional, fixed-end frame structure and the low-damage frame structure. Compared to the low-damage wall system, the energy dissipated in the low-damage frame system is significantly larger. The reduction in residual drifts can be clearly seen in the global structure response under the low-damage frame configuration. The increased axial loads in the beams also result in larger moments at the local and global level.

Figure 4.32 and Figure 4.33 demonstrate the effect of the damping scheme employed at the rocking interface on the response of the structure with the low-damage frame and the low-damage wall configuration respectively. The global response is seen to be largely unaffected by the damping formulation, with slightly larger drifts and smaller overturning moments under the updated stiffness damping formulation. A significantly larger difference is seen for the element local response i.e. for the wall-moment vs wall-rotation and beam-moment vs inter-story drift response. For both configurations, the initial stiffness damping formulation shows significantly larger energy dissipation as compared to the updated stiffness damping formulation.

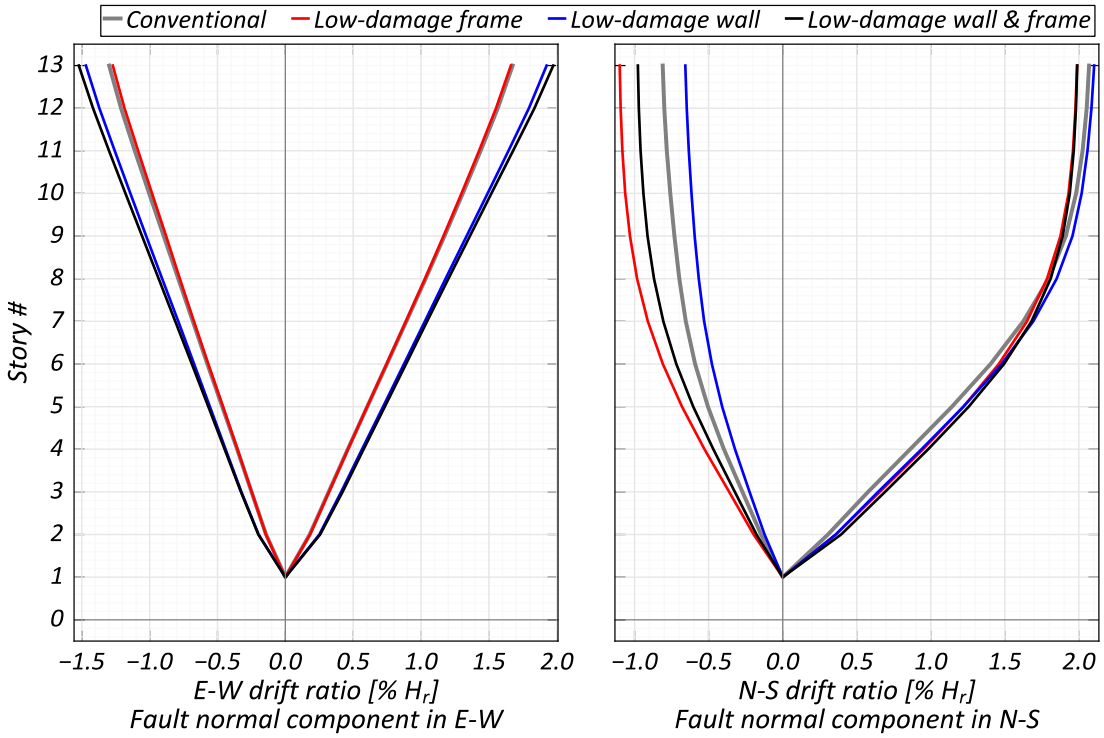

Figure 4.24 Story drift envelope, MCE$_R$ level earthquake

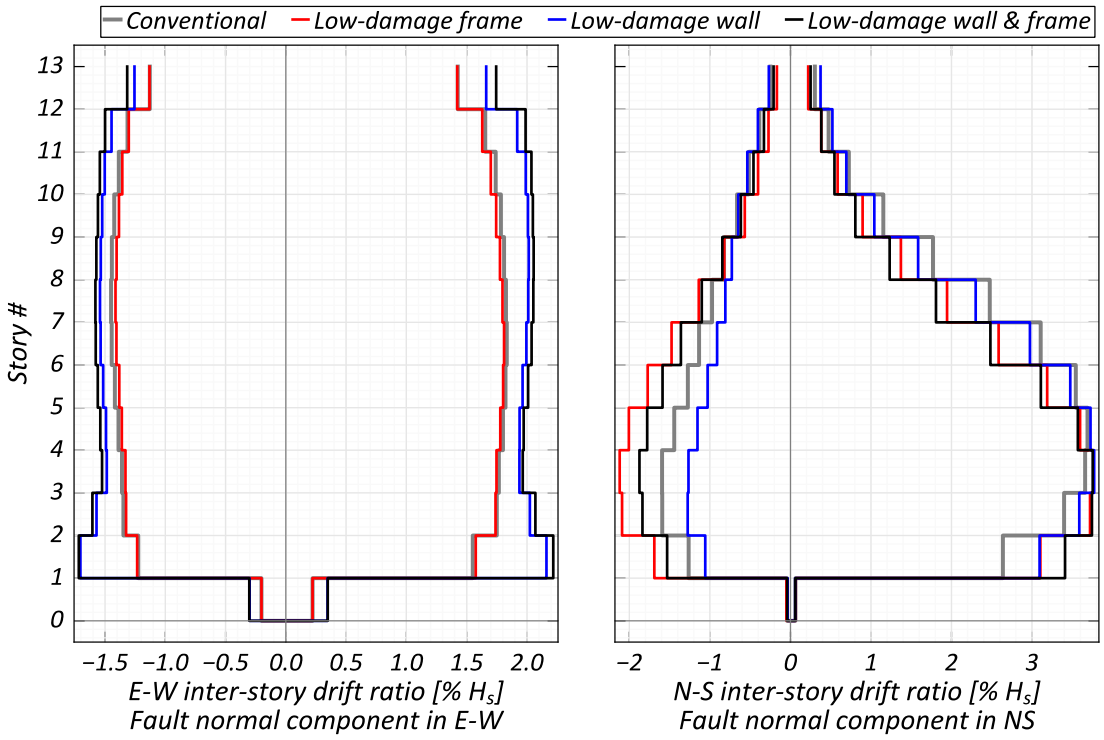

Figure 4.25 Inter-story drift envelope, MCE$_R$ level earthquake

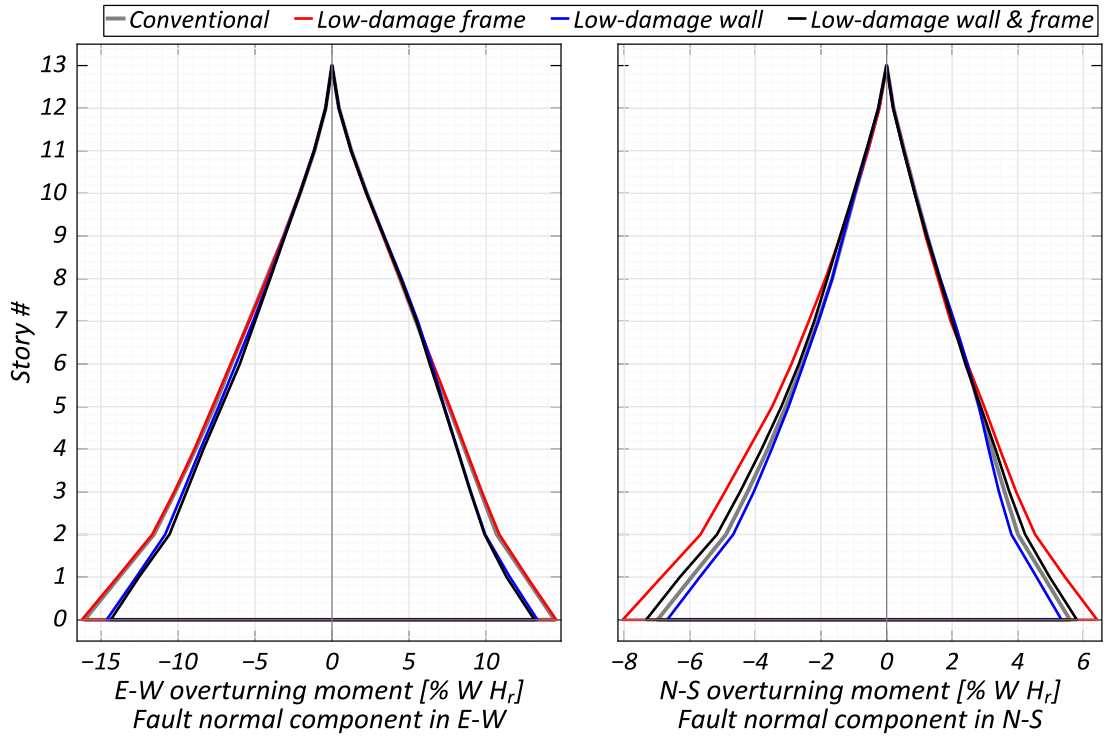

Figure 4.26 Overturning moment envelope, MCE$_R$ level earthquake

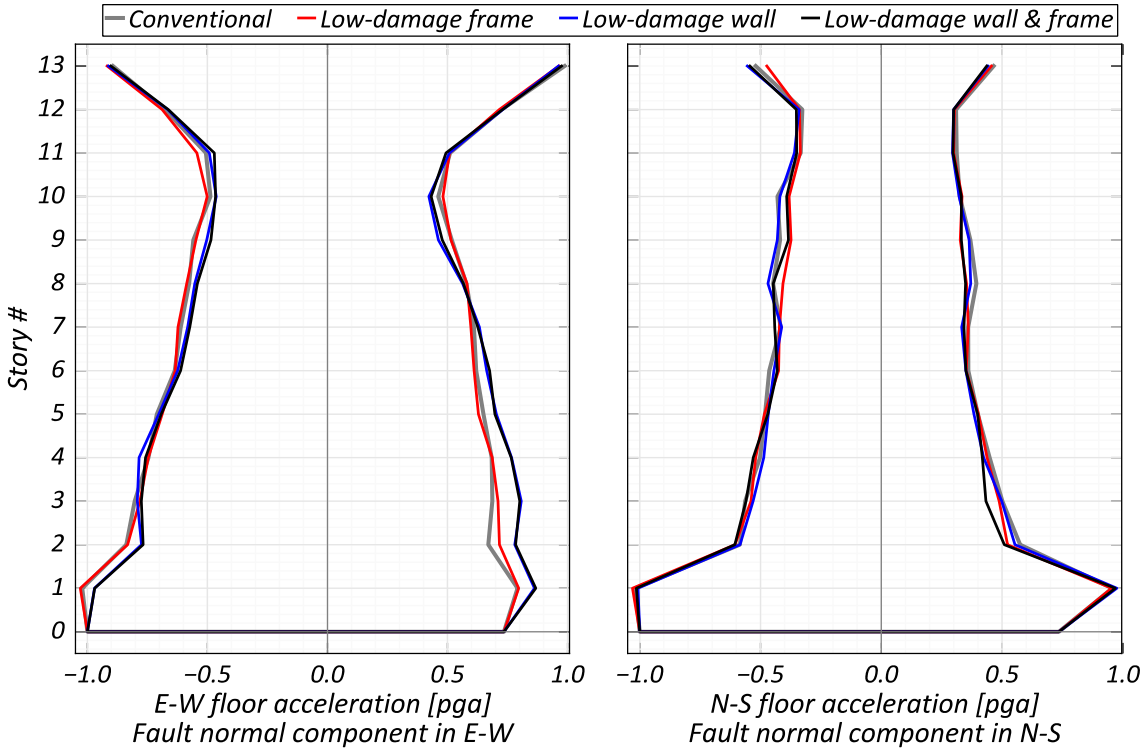

Figure 4.27 Floor acceleration envelope, MCE$_R$ level earthquake

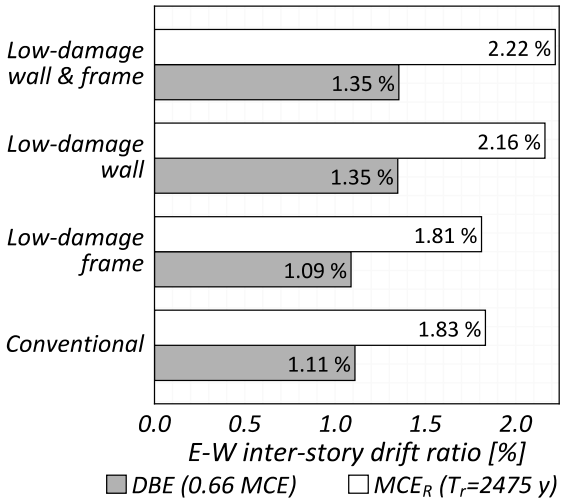

(a) Inter-story drifts in dual system (fault normal component in the E-W direction)

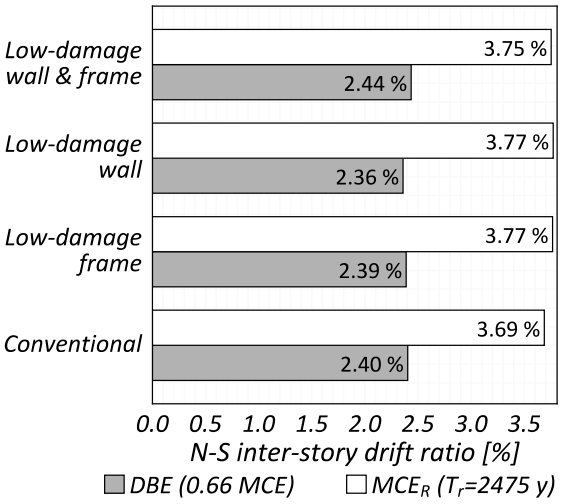

(b) Inter-story drifts in SMF (fault normal component in the N-S direction)

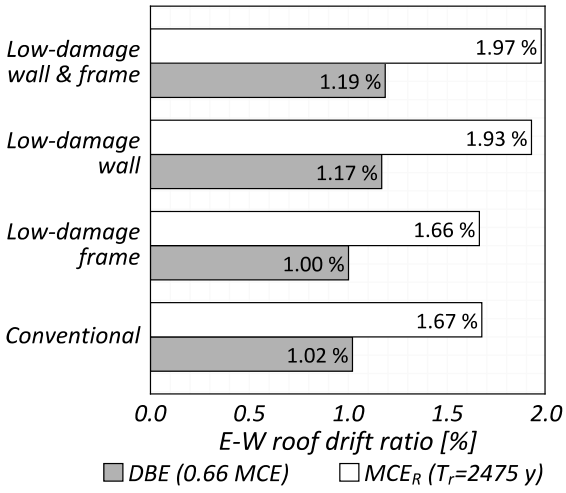

(c) Roof drifts in dual system (fault normal component in the E-W direction)

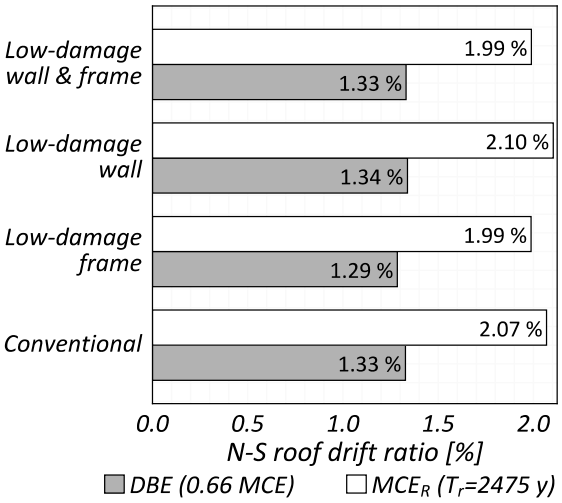

(d) Roof drifts in SMF (fault normal component in the N-S direction)

Figure 4.28 Peak drift ratios

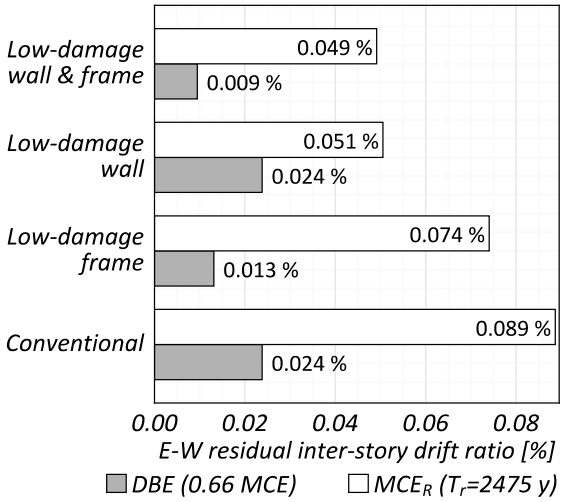

(a) Residual inter-story drifts in dual system (fault normal component in the E-W direction)

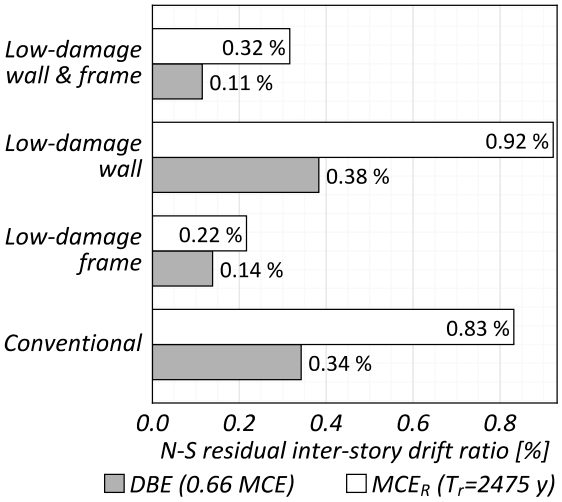

(b) Residual inter-story drifts in SMF (fault normal component in the N-S direction)

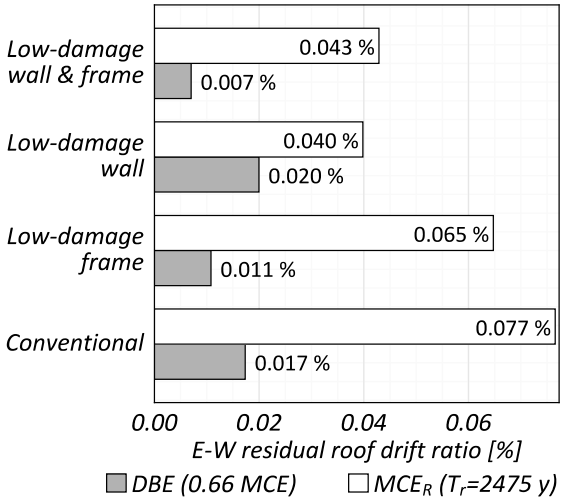

(c) Residual roof drifts in dual system (fault normal component in the E-W direction)

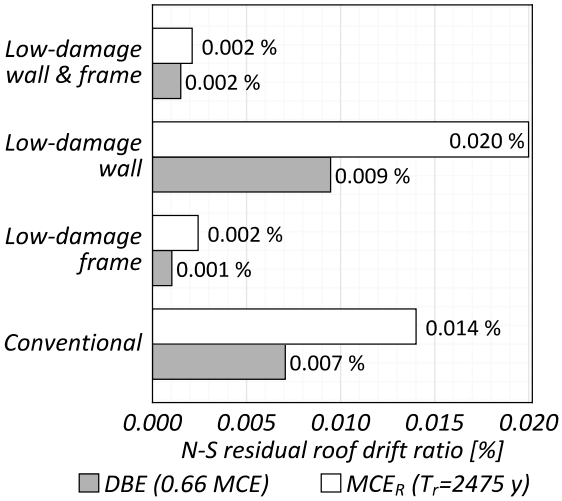

(d) Residual roof drifts in SMF (fault normal component in the N-S direction)

Figure 4.29 Residual drift ratios

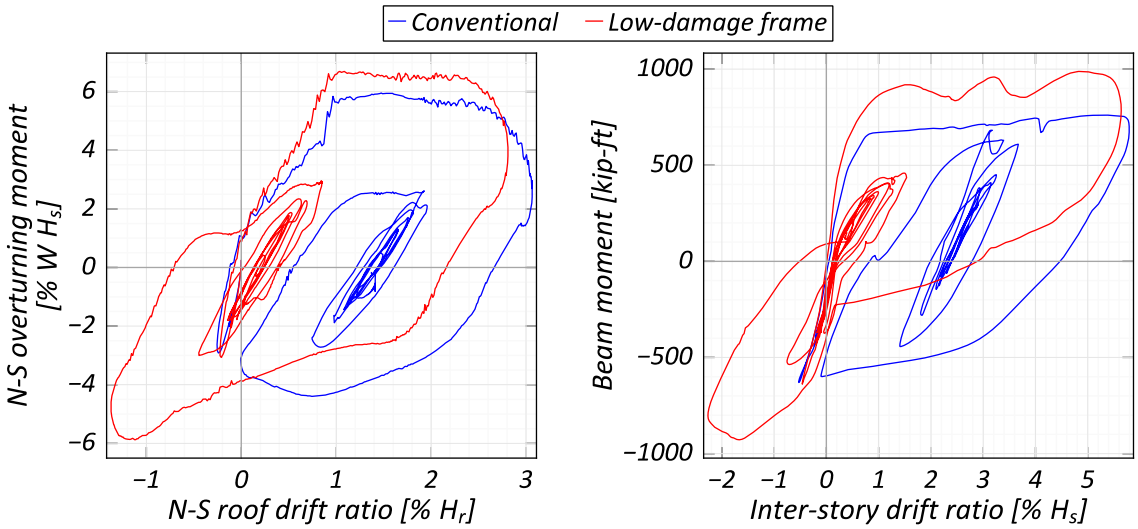

Figure 4.30 Structure response under different frame configurations, fault normal component along N-S direction

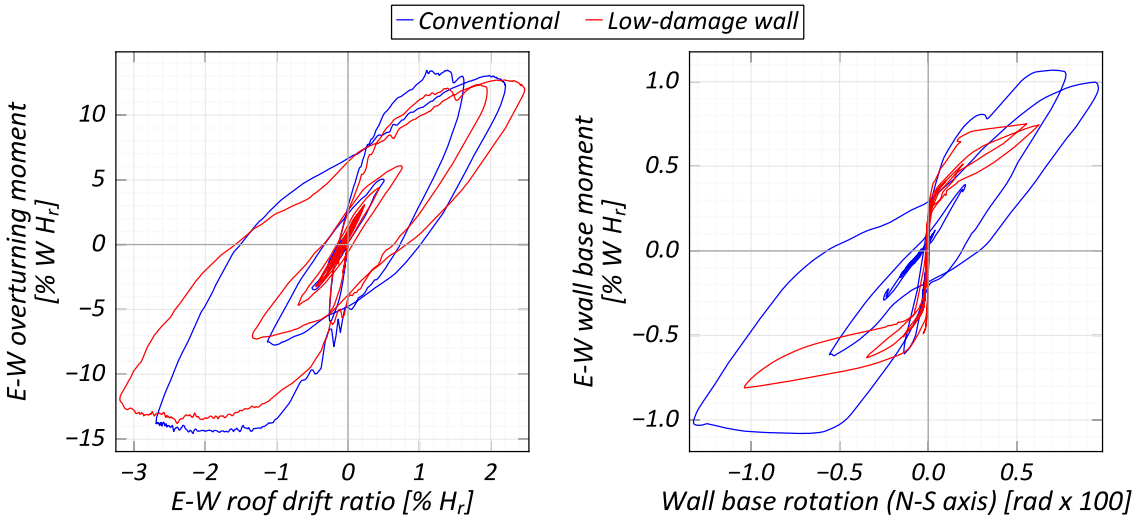

Figure 4.31 Structure response under different wall configurations, fault normal component along E-W direction

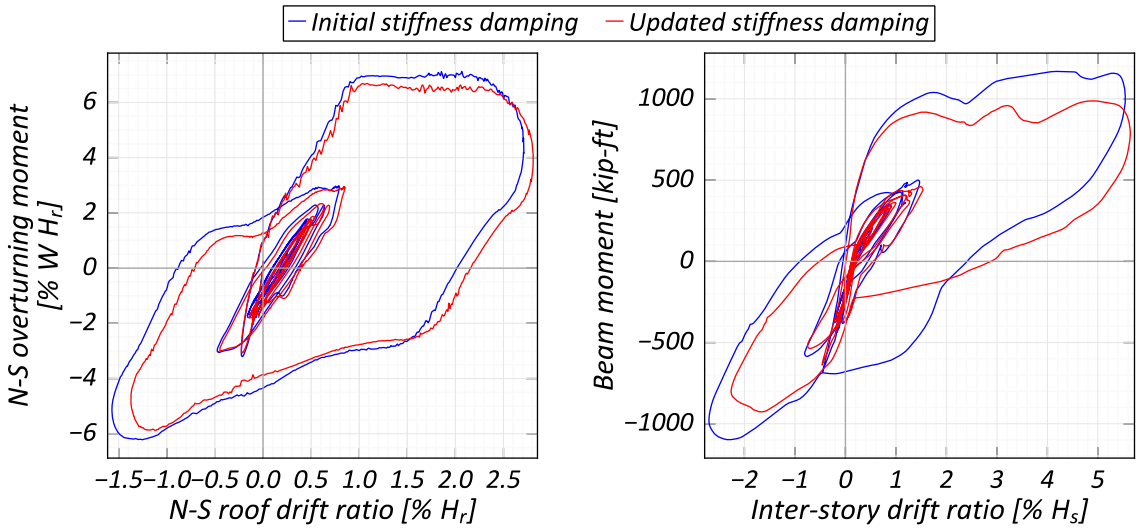

Figure 4.32 Effect of Rayleigh damping stiffness type on re-centering frame response, fault normal component along N-S direction

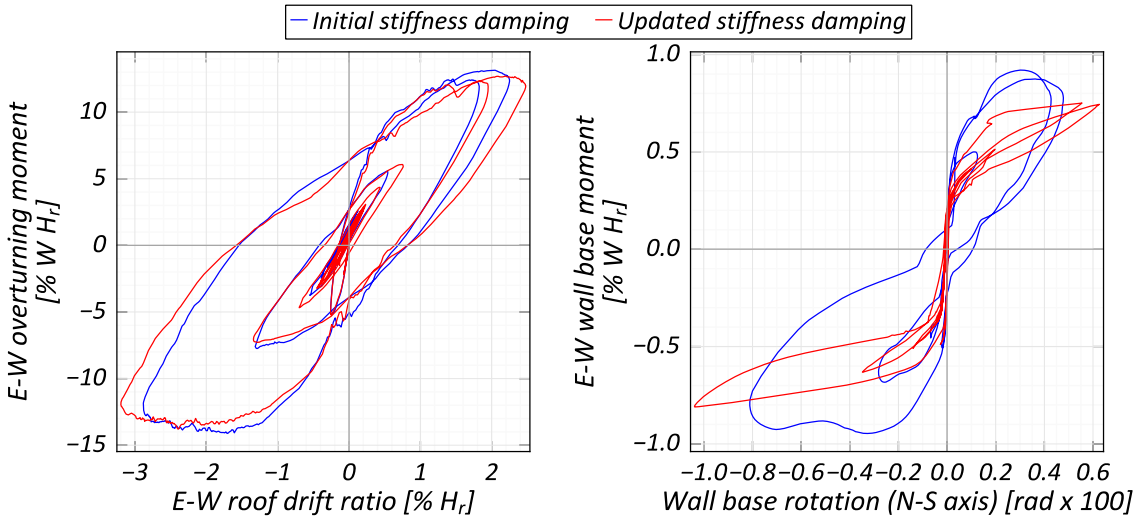

Figure 4.33 Effect of Rayleigh damping stiffness type on re-centering wall response, fault normal component along E-W direction

4.5. Acknowledgements

I would like to thank Dr Andre R. Barbosa, Associate Professor, Oregon State University, for sharing the base analytical model of the 13-story structure developed upon as a part of this work.

Chapter 5

SHAKE TABLE TESTING OF LOW-DAMAGE BRIDGE BENTS

5.1. Introduction

This chapter presents the design, construction and results from a two-column bridge bent, with hybrid re-centering behavior, tested dynamically at the PEER Shaking Table located in the UC Berkeley Richmond Field Station campus. This study continues the research done under the PEER Transportation Systems Research Program (TSRP) by Guerrini et al. (2013; 2015) where single column bents were tested under cyclic and dynamic loading. In addition to testing a multiple column configuration, this study also involved the development of an alternate and more robust precast construction technique for Accelerated Bridge Construction (ABC).

5.2. Design and construction

The prototype bent for the experiment was derived from Bent-3 of the Massachusetts Avenue Over Crossing (MAOC) bridge, located in close proximity (5.8 km / 3.6 mi) to the San Andreas Fault. The existing bridge consists of four bents, each

with four cast-in-place, fixed-end columns spaced at 3.067 m (120.5-in) on-center and reinforced with 22 No. 36 (Imperial size #11) Gr 60 bars, for a reinforcement ratio (ρ_l) of 1.9%. Bent-3 of the bridge has a clear height of 9.6 m (378-in), with a foundation size of 13 m x 3.45 m x 1.22 m (512-in x 136-in x 48-in) and a bent cap size of 14.85 m x 1.83 m x 1.37 m (585-in x 72-in x 54-in). Complete details of the bridge are presented in Chapter 6 as part of the analytical study of the bridge.

For the hybrid column design of the prototype re-centering bent, a portion of the longitudinal steel in the MAOC bridge columns was replaced with unbonded post-tensioning steel. This replacement was done while maintaining equal levels of steel strength between the two columns, following equation 5.2. Additional criteria for the replacement of mild steel with post-tensioning steel are given in equations 5.2 (a) and (b), developed in Guerrini et al. (2015). The limit on the re-centering coefficient (Λ_C) ensures the closure of the opening in the rocking interface to complete the re-centering of the system, while the limit on the energy dissipation coefficient (Λ_D) ensures sufficient energy dissipation capacity in the system to avoid the development of large lateral displacement and acceleration demands.

$$A_{st}f_y = A_{sED}f_{yED} + A_{sPT}f_{yPT} \tag{5.1}$$

$$\Lambda_{\mathrm{C}} = \frac{F_{ED,o}}{P_u + F_{PT,e}} \leq 1.0 \quad \text{(a)}$$

$$\Lambda_{\mathrm{D}} = \frac{F_{ED,o}}{P_u + F_{PT,e} + F_{ED,o}} \geq 0.1 \quad \text{(b)} \tag{5.2}$$

In addition to changes in the steel reinforcement for the prototype, the bridge gradient (2%) and skew was ignored for simplicity and the number of columns was

reduced from four in the bridge to two in the prototype. The reduction in the number of columns was required to optimize the experiment for the force and displacement capabilities of the shake table while maintaining a suitable scale for the test specimen. This change required adjustments to the bent geometry, specifically the distance between columns in the prototype, to achieve similar levels of stresses in the prototype columns and the two edge columns in the bridge bent. For this purpose, a small parametric study was conducted using analytical models of the prototype and the bridge, detailed in Chapter 6.

The final prototype consisted of two hybrid re-centering columns spaced 4.2 m (58-inch) on center. Post-tensioning was provided by a 10.82 m (275-in) unbonded length of 8x4-15 mm (0.6-in) Gr 270 strands ($f_{pu} = 1860\,MPa = 270\,ksi$) with an initial prestress of 40% f_{pu} (GUTS), assumed to span from mid-depth of the foundation to mid-depth of the bent cap. The expected strength of concrete was assumed to be 46 MPa (6.7 ksi) which is equivalent to the expected concrete strength used in the analytical bridge model. Mild-steel reinforcement in each column consisted of 10 No.36 (#11) ASTM A572 Grade 60 bars which were debonded from the concrete over a height of 0.5 m at each rocking interface. For analytical purposes, the bar bond development length was assumed to be 10 bar diameters on each end of the debonded bar resulting in an effective debonded length of 1.22 m. An illustration of this concept is shown in Figure 5.1. The debonding is required to prevent early dissipator fracture, since the gap opening results in large inelastic deformations in the mild-steel reinforcement crossing the rocking interface.

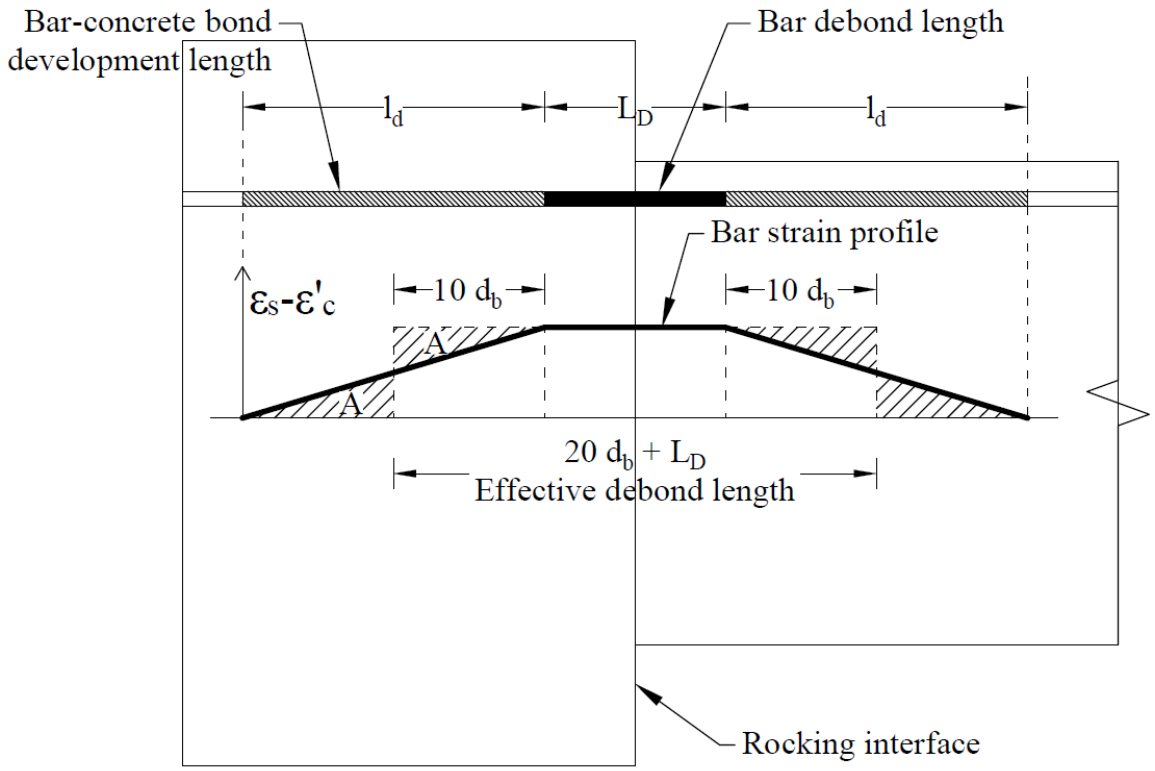

Figure 5.1 Reinforcement bar debonding at rocking interface

The dimensions of the cross-section of the foundation and the bent-cap are the same as those in the bridge. The effective inertial and gravity loads applied to the prototype bent are 2.55 MN (573 kip), estimated from the tributary length of the bridge deck corresponding to Bent 3. Table 5.1 compares the parameter values given by equations 5.2 (a) and (b) for the prototype and the test specimen in Guerrini et al. (2015).

The test specimen was obtained by scaling down the prototype by a factor of $S_l = 0.35$ to limit the expected forces and displacements within the shaking table specifications. To maintain similarity in terms of stresses between the prototype and the specimen, the inertial mass of the specimen was scaled by ${S_l}^2$ instead of ${S_l}^3$ as required

by volume scaling. This modification resulted in a scaling factor of $\sqrt{S_l}$ for the harmonic periods of the system and for the time scales associated with the test, requiring a compression in time for the ground motion histories. The scaling procedure followed for the bridge bent specimen is the same as the one presented in Chapter 3 The inertia mass was provided by the bent cap and six concrete blocks post-tensioned to the bent cap. This splitting of the inertia mass was required to have components which could be safely picked up by the indoor crane available at the shaking table.

Table 5.1 Comparison of Re-centering (Λ_C) and Energy Dissipation (Λ_D) Coefficients between Prototype and Guerrini et al. (2015)

	Mild Steel	PT Steel	Λ_C	Λ_D
Prototype	10 x No. 36	32 x 15 mm	0.84	0.46
Guerrini et al. (2015), Unit 1A	6 x 14.3 mm	4 x 35 mm	0.42	0.29
Guerrini et al. (2015), Unit 1B	6 x 12.7 mm	4 x 35 mm	0.60	0.37

The specimen was tested in the transverse direction of the bridge, i.e. along the length of the bent and the motion in the longitudinal direction was restrained. The restraint was required since the bridge girders and adjacent bents (or abutments) provide important constraints in the longitudinal direction which cannot be emulated in the testing of a single bridge bent. An overview of the specimen is presented in Figure 5.2, and the as built specimen with the restraints can be seen in Figure 5.11.

Compared to earlier studies on low-damage bridge columns where the column clear height was seated on a mortar bed, a dry-jointed socket-connection (Haraldsson et al. 2013b) to join the columns to the foundation and bent-cap was used where the column is aligned and inserted into an opening in the previously cast foundation or bent cap followed by introduction of grout to fill the gap between the two elements. This resulted

in a more robust assembly of the specimen and eliminated the need of a mortar layer at the interface which can undergo crushing, becoming a limiting factor for the optimum performance at higher drifts as was found in Guerrini et al. (2015). Details of the design and construction of the columns, foundation and bent-cap are presented below.

5.2.1. Column

The column design was based on the scaled prototype column. Each column had an external diameter of 406 mm (16 in). Ten #4 (12.7 mm dia.) A706 Grade 60 rebars provided the longitudinal reinforcement; a 6 in. length of each rebar at the rocking interface was debonded from the surrounding concrete using duct tape to prevent large strains. A #3 ($d_b = 9.5\,mm = 0.375\,inch$) A706 Grade 60 spiral was used to hold the longitudinal reinforcement together. The spiral was subdivided into three sections along the column height to prevent the transverse spirals from contributing to energy dissipation by yielding at the rocking interface. The entire reinforcement assembly was placed inside a special outer steel shell, which served as permanent formwork and provided confinement and shear strength for the column. The #3 spiral was necessary only for construction purposes, since the column outer shell provided the required shear and confining reinforcement.

Due to the difficulty in obtaining scaled down equivalents of the post-tensioning strands used in the prototype, the strands were replaced by a single 1-3/8-inch ASTM A722 Grade 150 threaded post-tensioning bar. The bar anchorage was embedded inside the column bottom before the pouring of concrete, and the PT bar itself was enclosed inside a 2-inch (50.4 mm) ID PVC sleeve over the column length to debond it from the

concrete. The PT bar was left inside the sleeve during the pouring of concrete to help keep the PVC sleeves aligned. The top end of the bar extended 4-ft (1220 mm) above the top of the column to allow for the installation of a concentric load measuring cell resting on the bent-cap. This extension also proved helpful in guiding the bent cap in place during assembly.

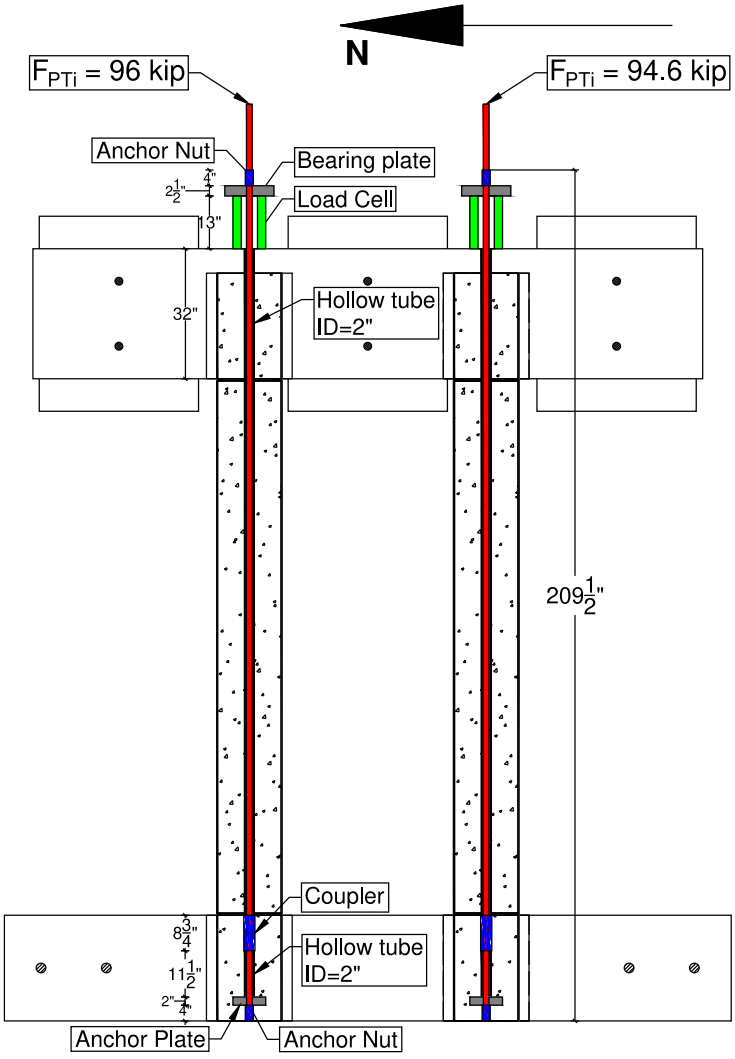

Figure 5.2 Bridge bent specimen overview

The use of a dry-socket connection to join the columns to the foundation and the bent cap allowed for an innovative construction method. Each column was formed by

inserting the reinforcement cage inside the specially built segmented steel shell, which was assembled from a 6.4 mm (0.25 inch) thick ASTM A53 Grade B pipe, followed by the casting 41.4 MPa (6 ksi) concrete inside the steel shell. The steel shell served as a permanent formwork, provided a force transfer mechanism between the column and end beams, and served as confinement to prevent crushing of concrete during rocking behavior. To allow rocking at the beam-column interface without any tensile stresses from the steel casing, the shell was segmented into five sections:

- two end sections, to be embedded inside the socket connection which were provided with weld beads outside and inside for developing composite action;
- one central section over the column clear height, and lastly
- two 12.7 mm (0.5 inch) wide, removable open strips: one strip between the central section and each of the two end sections.

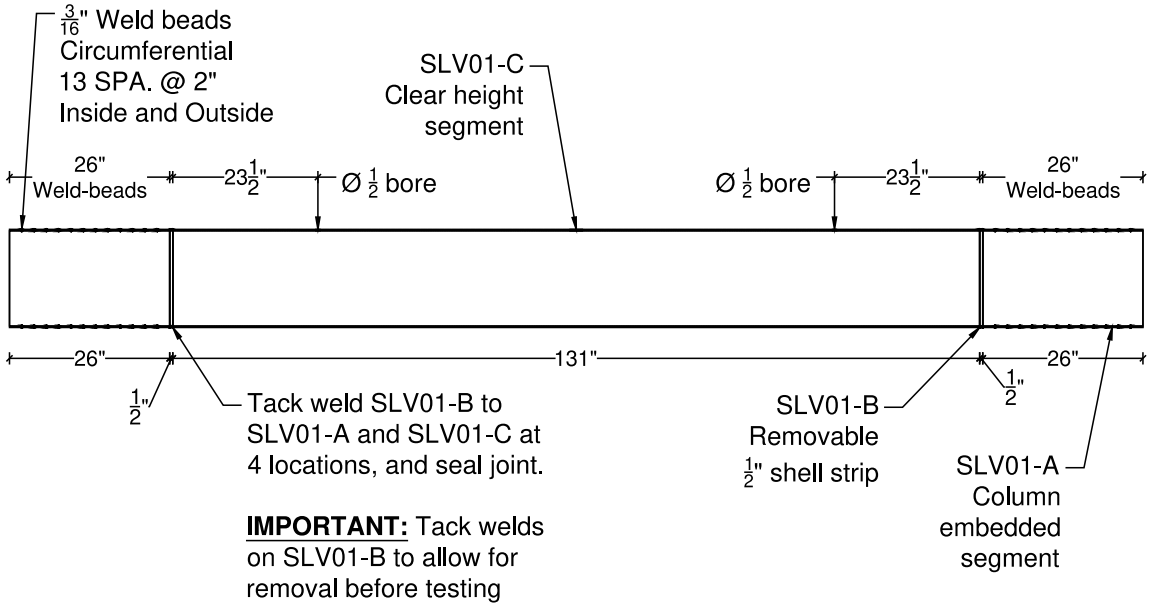

Figure 5.3 Segmented column shell

(a) Column steel shells

(b) Weld beads at column ends

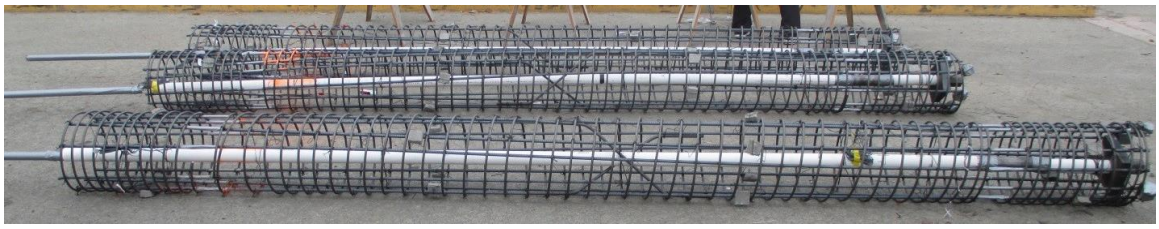

(c) Column reinforcement cages

(d) Mild steel reinforcement debonding detail and PT bar end anchorage detail

Figure 5.4 Column reinforcement details

The five segments were spot welded together at a few locations to form the single pipe unit used for casting each column. Following the curing of the concrete inside the

outer shell, the spot welds were ground off and the thin strip segments removed to form the rocking interface in the assembled specimen. The construction drawing of the segmented column shell is presented in Figure 5.3. Some photographs from the column construction process are shown in Figure 5.4 and Figure 5.5.

Figure 5.5 Column casting setup

5.2.2. Foundation

The foundation design was centered around the socket connection. The socket for each column was formed out of a 559 mm (22-inch) Inner Diameter (ID) Corrugated Metal Pipe (CMP). The foundation width was set to 965 mm (38-inch) to allow 203 mm (8-inch) of space on either side of the socket for placing reinforcement and provide cover. The foundation depth was set to 660 mm (26-inch) for bond development between the column and the foundation in the socket. Finally, a foundation length of 4521 mm (178-inch) was selected to accommodate the clamping bars for securing the foundation to the shaking table.

The primary reinforcement design was performed using the strut-and-tie method as prescribed in § 5.6.3 of AASHTO LRFD Bridge Design Specifications, 6th Edition (2012). The columns' axial loads were assumed to be transferred directly to the shaking table, while lateral loads were assumed to be transferred by lateral bearing at the top and bottom of the socket. The strut and tie model indicated that the socket-type of joint requires extra cross ties around the connection. This is to prevent splitting of the foundation in the longitudinal direction due to the bearing forces arising from the transfer of column shears to the foundation. Additional C-shaped reinforcement bars were provided around the socket to prevent any splitting due to out-of-plane forces. This reinforcement, while not necessary for the specimen, is required in actual bridge foundations to prevent socket failure due to bridge longitudinal deformations. A picture of the foundation reinforcement around the socket connection detail is shown in Figure 5.6(a).

5.2.3. Bent cap

Similar to the foundation, the bent cap design was centered on the socket connection. The socket was again formed from 559 mm (22-inch) ID, 660 mm (26-inch) deep CMP and the beam width was kept the same at 965 mm (38-inch). Unlike the foundation, vertical load transfer was also needed between the bent-cap and the columns. For this purpose, a 152 mm (6-inch) thick layer of reinforced concrete was placed on top of the column sockets for a total bent cap depth of 813 mm (32-inch). Vertical force transfer through friction between the bent cap and the ridged column shell segment inside the socket was ignored for a conservative design. The bent-cap length was set at 4166 mm (164-inch) to accommodate the six blocks needed to simulate the superstructure mass.

The reinforcement design was determined using the strut-and-tie method. The vertical load was transferred from the bent-cap to the column via bearing against the top layer of concrete, strengthened by straight- and bent-hanger-reinforcement. As in the foundation, additional cross-ties and staples were provided to prevent the beam from splitting in the longitudinal and transverse direction.

A 51 mm (2-inch) ID opening in the top layer above each socket allowed the PT bars to pass through. Smaller openings were provided near the socket periphery for the pouring of grout. Additional 51 mm (2 inch) ID horizontal sleeves were provided through the vertical faces of the bent-cap at three locations for prestressing the six inertia blocks to the bent cap. Photographs of the bent-cap reinforcement and the socket connection detail are shown in Figure 5.6(b) and (c).

(a) Socket detail in foundation

(b) Socket reinforcement detail in cap beam

(c) Completed reinforcement cage, cap beam

Figure 5.6 Foundation and cap beam reinforcement

5.2.4. Additional mass

Besides the bent cap, the required additional inertial mass was provided by six concrete blocks, each measuring 1219 mm x 1219 mm x 991 mm (48-inch x 48-inch x 39-inch). The block size was selected based on the lifting capability of the indoor crane at the shaking table. Each block had a mass of nearly 3550 kg, and blocks were installed in pairs on each side of the bent cap at three locations. Minimum reinforcement was provided for each block, distributed as skin reinforcement along each face. The blocks were installed at mid height on the bent cap to avoid introducing artificial rotational mass moment of inertia in the specimen.

5.2.5. Specimen assembly

The precast columns, foundation and bent-cap were manufactured offsite by a precast concrete fabricator and delivered to the UC Berkeley Shaking table for assembly and testing. Before starting the assembly, the 6.4 mm (0.25 inch) steel strips located at the column rocking interface were removed by grinding off the spot welds and prying apart the strips (Figure 5.7). The PT bars extending out from the columns' top were covered with a few layers of duct tape to prevent any bonding to the grout in the sockets. Simultaneously, the foundation was installed on a bed of gypsum on the shaking table and tied down with a total force of 1.33 MN (300 kip) exerted through three tie-down bars. Once the foundation was installed, the shaking table was calibrated to the input ground motions for faithful reproduction of the response spectra.

With the foundation installed and the shaking table calibrated, columns were leveled inside the foundation socket, anchored down to maintain their level (Figure 5.8a)

and non-shrink grout was poured in the gap between each column and the CMP forming the foundation socket (Figure 5.8b). The grout was then allowed to set for three days before beginning the placement of the bent cap on top. During this time, the wooden formwork supporting the bent cap was erected.

For the bent cap installation, 12.7 mm (0.5 inch) shim blocks were placed on top of the columns, and the column tops covered with wet rags to ensure proper setting of grout. The bent cap was then lifted above the columns and brought down carefully until it was lightly resting and centered on the columns (Figure 5.9). The centering of the bent cap was aided by the PT bars extending out from the top of the columns. The bent cap was leveled on top of the columns by adjusting the wooden supports, which were strengthened further by cross braces. With the bent cap in place and leveled, the bottoms of the sockets were sealed (Figure 5.10(a)) and grout was poured from the top (Figure 5.10(b)). A thin layer of grout was first poured into each socket, and allowed to harden for a day, before completely filling the sockets with grout. This measure further strengthens the seal at the bottom of the socket, preventing any leaks due to the weight of the grout.

After the grout in the bent cap set for three days, the PT bars extending out from the top were moderately tensioned, and the inertial mass blocks were post-tensioned to the bent cap with a total force of 445 kN (100 kip) for each set of two blocks, using two 25.4 mm (1 inch) PT bars passing through the blocks and the bent cap as seen in Figure 5.11(a).

Since the specimen was designed to be tested under transverse and vertical shaking only, two restraint frames were erected to limit any twisting or motion in the longitudinal (out-of-plane) direction, (see completed specimen, Figure 5.11(b)). Each frame consisted of two A-Frames connected by a diagonal and horizontal W section for lateral stability. To minimize unwanted lateral forces due to friction between the specimen and the restraint frames, the interface between them consisted of greased wooden shims, which acted as low friction bearing surfaces. The frame installation was done concurrently with the installation of the inertial mass blocks, and when the installation of the blocks and restraining frames was finished, the column PT bars were tensioned to the target stress of 40% GUTS, for a target force of 422 kN (94.8 kip) on each bar.

(a) Removal of shell strip **(b) Shell strip removed**

Figure 5.7 Preparation of column rocking interface

(a) Column placement **(b) Foundation socket grouting**

Figure 5.8 Installation of columns in the foundation

Figure 5.9 Cap beam erection

(a) Cap-beam socket seal **(b) Cap-beam socket grouting**

Figure 5.10 Cap-beam grouting

(a) Inertia block installation **(b) Completed specimen**

Figure 5.11 Final assembly

5.3. Material properties

5.3.1. Concrete

The specified strength of concrete for the foundation, bent cap and the columns was 41.4 MPa (6 ksi). The compressive strength was measured using 152 mm (6 inch) diameter and 305 mm (12-inch) high standard concrete cylinders. The foundation and bent-cap were cast from the same batch of concrete, while the columns were cast together from a different batch. Before the test, six cylinders were tested on two days to track the development of concrete strength. Additionally, on the first day of testing six cylinders from each batch of concrete were tested using a compressometer to obtain their stress-strain profile in addition to the crushing strength. The average strengths measured on each day of testing are listed in Table 5.2 and the average stress-strain response from the compressometer tests are shown in Figure 5.12.

Table 5.2 Measured strengths of cementitious materials

Material	Age	Compressive strength	
	Days	MPa	ksi
Foundation / Cap-beam concrete	14	31.1	0.46
	32	37.6	5.45
	73 (DOT)	41.9	6.08
Column concrete	7	30.5	4.42
	22	34.6	5.02
	48 (DOT)	47.5	6.89
Grout	22 (DOT)	47.4	6.87

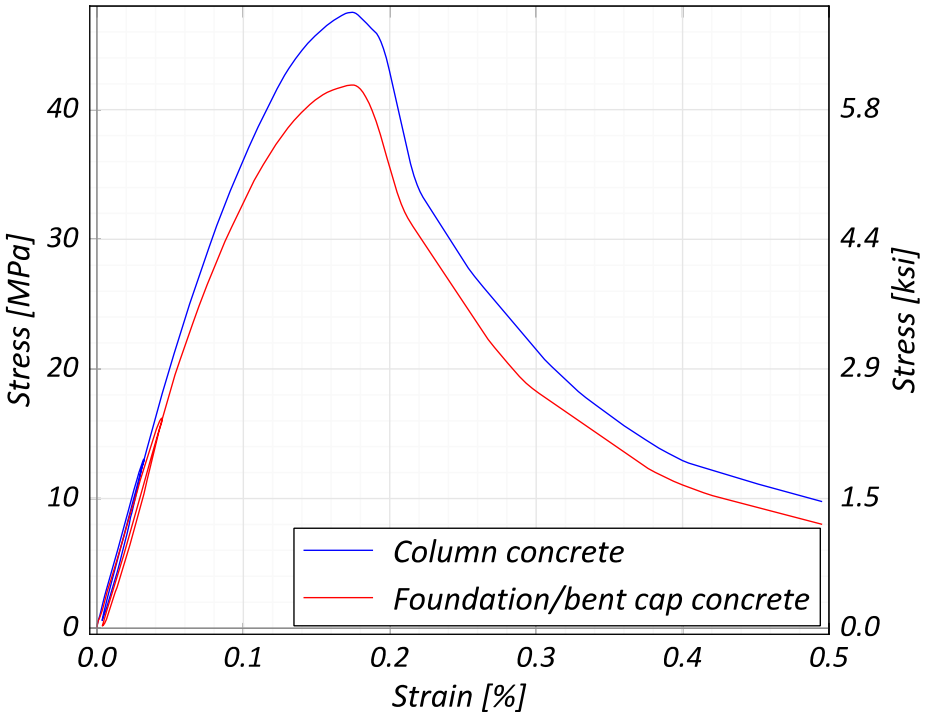

Figure 5.12 Concrete material stress strain response

5.3.2. Grout

BASF MasterFlow® 928 non-shrink grout, mixed at fluid consistency with a large percent of water (17% by weight) was used for filling the gap between the columns and the CMP socket walls. Compressive strengths were measured on the day of test on 51 mm (2 inch) diameter and 102 mm (4 inch) tall standard cylinders. The average strength from three cylinders is reported in Table 5.2.

5.3.3. Hysteretic energy dissipator

Three specimens, each 457 mm (18 inch) long, of the A706 Grade 60 #4 bars used in the column reinforcement were tested under monotonic tension to characterize the material. The average properties of the three samples are reported in Table 5.3 and the average full stress strain relation is shown in Figure 5.13. Note that the uniform strain is taken as the minimum strain at peak stress from among the three samples.

5.3.4. Prestressing steel

Three specimens, each 610 mm (24 inch) long, of the ASTM A722 Grade 150 threaded bar used for post-tensioning the columns were tested under monotonic tension to characterize the material. The average properties of the three samples are reported in Table 5.3 and the average full stress strain relation is shown in Figure 5.14.

5.3.1. Shell steel

Three samples obtained by straightening some of the 6.4 mm (0.25 inch) strips removed from the column outer steel shell at the rocking interface were tested under monotonic tension to characterize the material. The average properties of the three samples are reported in Table 5.3 and the full stress strain relation is shown in Figure 5.15. For the strips, the strain recording was stopped at 1.8% strain, and only the ultimate strength is reported beyond that point.

Table 5.3 Measured steel mechanical properties

Material	Elastic modulus		Yield stress		Yield Strain	Onset of strain hardening	Tensile strength		Uniform Strain
	GPa	ksi	MPa	ksi	(%)	(%)	MPa	ksi	(%)
A706	192	27900	489	70.9	0.45	n/a	681	98.8	10.0
A722	217	31400	939	136	0.63	1.25	1100	160	7.0
A53	188	27200	339	49.2	0.38	n/a	461	66.9	n/a

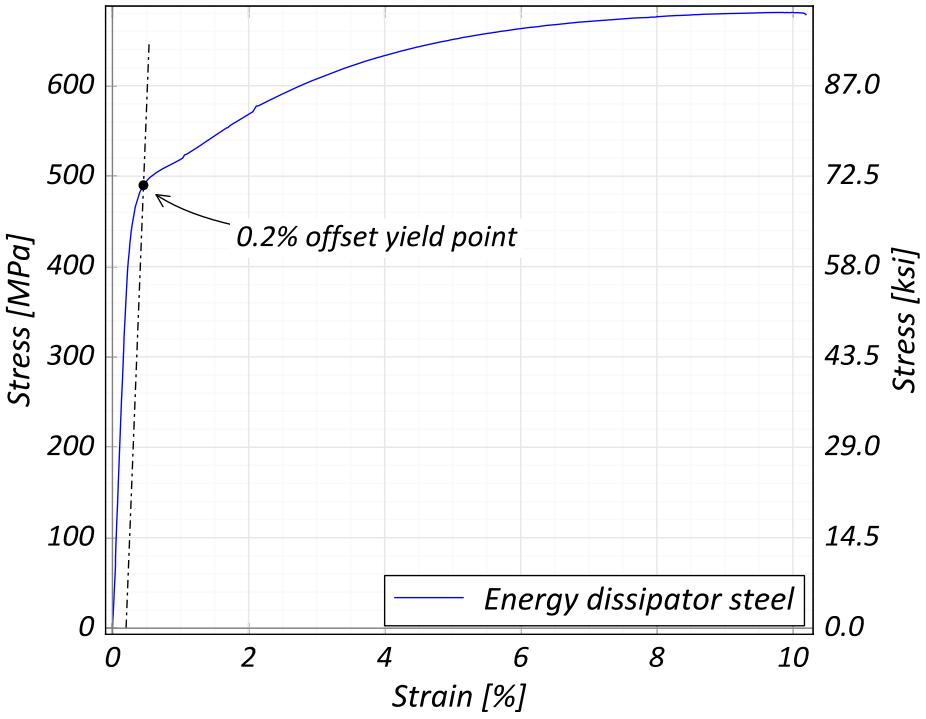

Figure 5.13 Energy dissipator steel stress-strain response

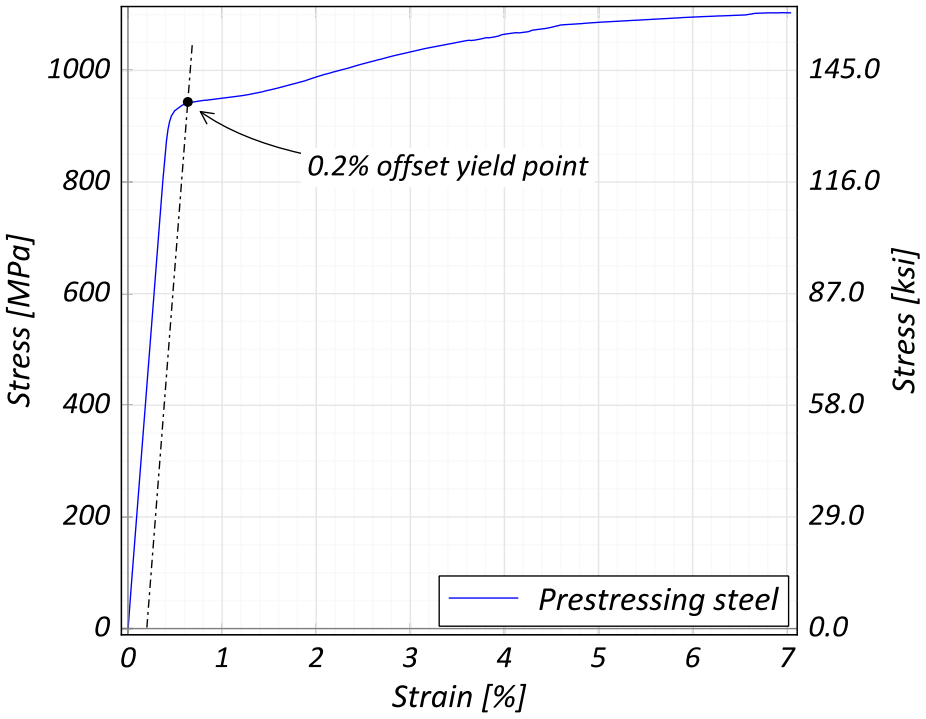

Figure 5.14 Prestressing steel stress-strain response

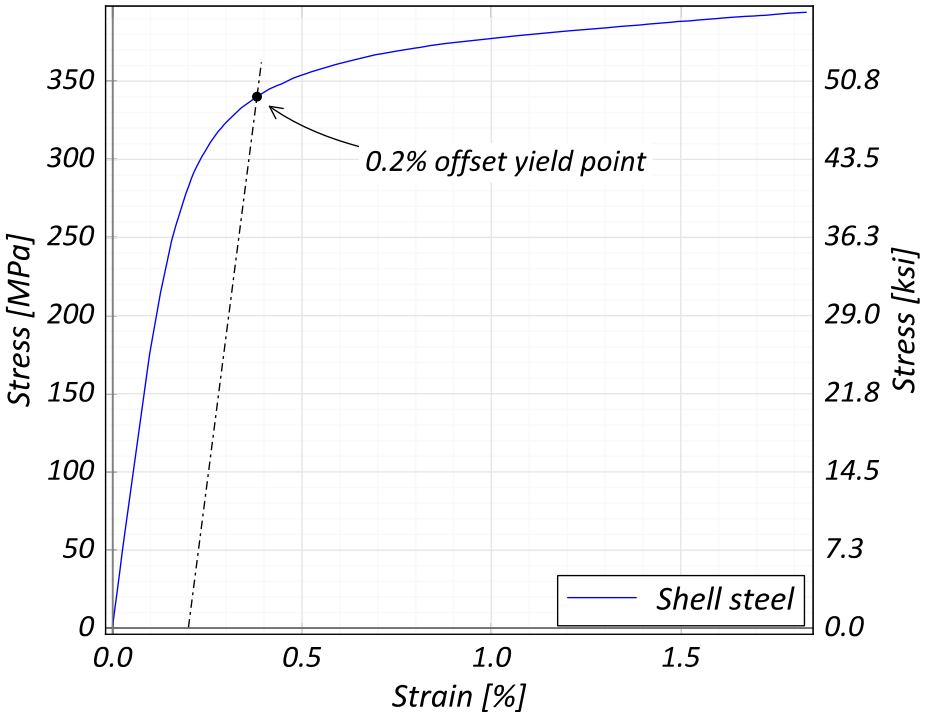

Figure 5.15 Shell steel stress-strain response

5.4. Test program

5.4.1. Instrumentation

An array of 156 instruments was installed to monitor the response of the specimen. All the sensor data was sampled at 200 Hz. Six (6) accelerometers each were installed on the shaking table and the foundation, near each end of the foundation to measure the input accelerations in three directions. Eight (8) accelerometers were installed on the bent cap and three (3) accelerometers were installed on each mass block to measure the inertial forces experienced in the specimen along all six degrees of freedom.

Nine (9) string potentiometers were anchored at one end to frames outside the table, and connected to the foundation and the bent cap at the other end to get a measure

of absolute displacements. These, coupled with two curtains of two (2) diagonal and two (2) vertical string potentiometers each, were used to provide redundant measurements of relative displacement between the foundation and the bent cap. Four (4) spring loaded linear potentiometers were installed at each rocking interface to measure the gap openings and end-rotations in the columns. One last linear potentiometer was used to monitor the shaking table vertical displacement, by suspending it from a stiff frame anchored to a location outside the table.

Ten (10), 5 mm electrical foil TML YFLA strain gauges were installed in the debonded lengths of three energy dissipators in both rocking interfaces of each column to get a measure of longitudinal strains experienced during shaking. Four (4) 5 mm long electrical foil TML FLA strain gauges were installed in the CMP in each socket, two (2) each at a location 203.2 mm (8 inch) from the top and the bottom of the socket along the direction of shaking, measuring the strains produced by transfer of axial forces between the columns and the end beams.

For the south column, the shell segments embedded inside the sockets were fitted with four (4) TML rosette gauges at each end: one gauge at each point 50.4 mm (2 inch) from the end of the embedded segment and on diametrically opposite points along the shaking direction. Additional non-yielding gauges were installed on this segment in the out-of-plane direction of the specimen at each location corresponding to the strain gauges applied on the CMP. Four (4), 5 mm electrical foil TMF FLA strain gauges, measuring circumferential strains in the steel shells, were also installed 50.8 mm (2 inch) and 101.6 mm (4-inch) above each rocking interface in the south column.

For each socket in the bent-cap, a YFLA strain gauge was installed in the 45° segments of two hanger reinforcement bars, to get a measure of the force transferred between the bent-cap and the columns through bearing instead of socket shear. Two (2) YFLA strain gauges were installed in each of the PT bars, located on the portion of the bar above the bent cap and inside the load cells, which were installed to measure the PT bar forces.

In addition to the sensors, video recordings of the specimen response during the shaking were also made from various locations. Four (4) GoPro cameras recorded high quality videos of the rocking interfaces at the foundation level for each of the two columns, while two additional GoPro cameras, and two Canon T5i DSLR cameras were used to record the specimen overall response as seen from various locations off the table. The videos were synchronized to the sensor data using a system of LEDs set to blink at the beginning and end of the tests, with the common input LED voltage being monitored at one of the data channels.

5.4.2. Test sequence

The prototype analytical model used to select the column on-center distance was modified by scaling down the member geometries and updating the material and PT properties to match the expected material properties as per Caltrans Seismic Design Criteria (2013). This model was then used to select a suite of near fault earthquakes to be imposed on the specimen for dynamic testing.

The selection was made based on expected peak drift as calculated by the numerical model, in comparison with the design drift capacity of the system defined by

the yielding of the PT bars (7% drift at the cap-beam level). The selected motions represent very mild (0.6% drift), mild (1.8% drift), moderate (4% drift) and large (>5% drift) events.

Table 5.4 Input ground motion sequence for bent-cap dynamic test

EQ #	Event Name	Station	Unscaled PGA (g)	Scale factor	Expected drift (%)
01	Landers, 1992	Lucerne	0.72	0.9	0.6
02	Landers, 1992	Lucerne	0.72	0.9	0.6
03	Tabas, 1978	Tabas	0.85	-0.9	1.8
04	Kocaeli, 1999	Yarimca	0.3	1.0	0.6
05	Northridge, 1994	RRS	0.85	0.81	4.0
06	Duzce, 1999	Duzce	0.51	1.0	1.8
07	Northridge, 1994	NFS	0.72	-1.2	4.0
08	Kobe, 1995	Takatori	0.76	-0.8	5.0
09	Kobe, 1995	Takatori	0.76	0.9	7.0
10	Tabas, 1978	Tabas	0.85	-0.9	-
11	Northridge, 1994	RRS	0.85	0.81	-
12	Kobe, 1995	Takatori	0.76	-0.8	-

Nine earthquake simulations were planned in the initial loading protocol. To investigate the effects of lower intensity aftershocks, the test sequence was not conducted with continually increasing demands; instead, a motion was followed by smaller intensity of shaking representing an aftershock until a peak drift of 4% was reached. The resulting protocol called for test with input motions capable of producing the following sequence of maximum drifts: 0.6%, 0.6%, 1.8%, 0.6%, 4%, 1.8%, 4%, 5% and 7%. For larger drifts, ground motion polarity was occasionally switched to avoid damaging the specimen in only one direction. A 120-second-long, 2.5% g RMS noise signal, bound by an upper

frequency of 75 Hz, was applied in the horizontal excitation direction after each earthquake to monitor the dynamic properties of the specimen.

Significant structural integrity remained after the initially planned sequence and the scope was expanded with three additional tests. Details of the ground motions are listed in Table 5.4 in the order they were imposed on the specimen, and the displacement response spectra for the two components are shown in Figure 5.16.

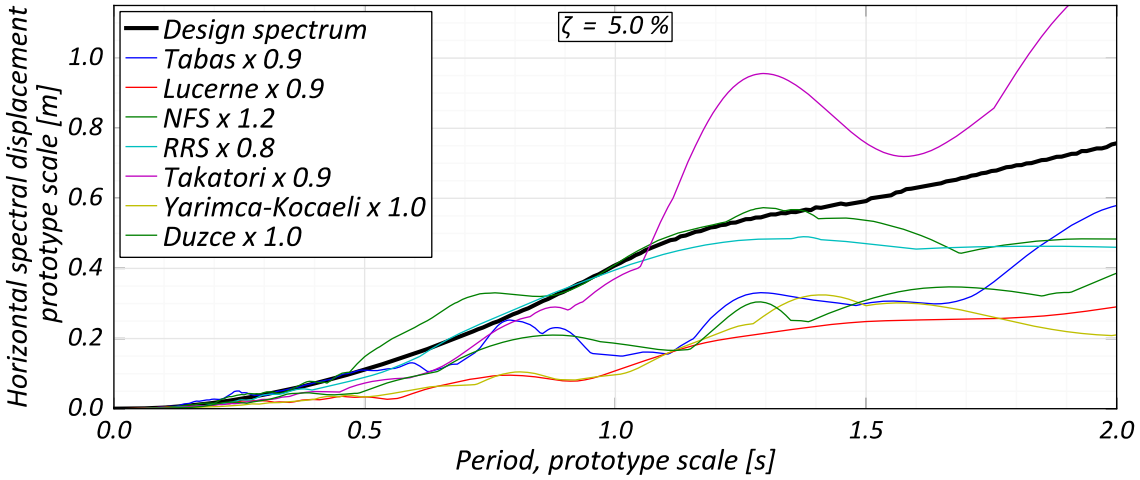

(a) Horizontal component

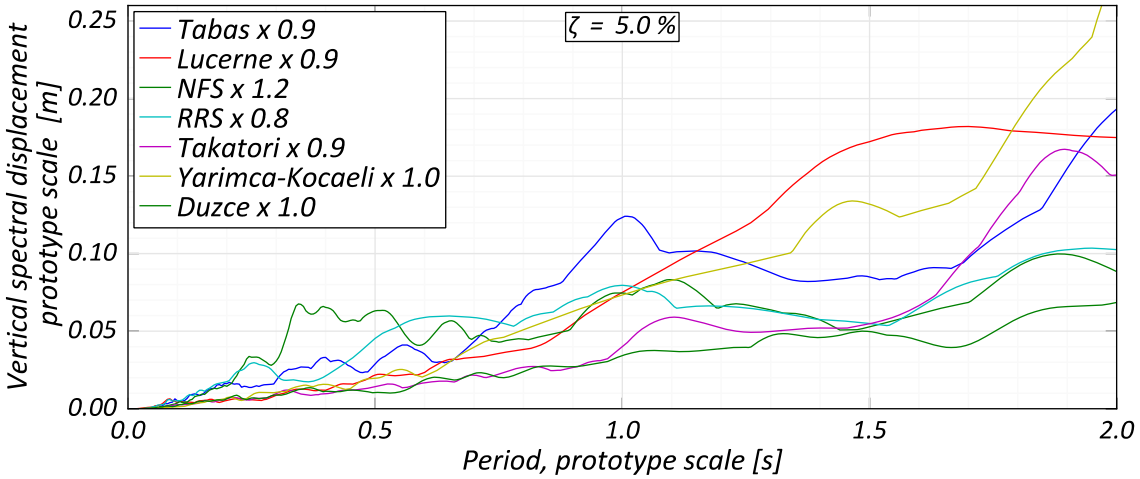

(a) Vertical component

Figure 5.16 Input motion spectral response, bridge-bent dynamic testing

5.5. Test results

In the test results presented below, lateral displacements have been normalized by the clear height of the columns and are expressed as drift ratios. Lateral forces have been normalized by the specimen inertial weight, 303 kN (68.1 kip), taken as the weight above half the column clear height and are expressed as base shear coefficients. Post tensioning forces have been normalized by the ultimate force capacity of the bars (1124 kN / 253 kip) and are expressed as percentage of the measured ultimate stress in the prestressing bars ($f_{pu} = 1100\ MPa = 160\ ksi$). Any non-normalized values have been scaled back to prototype space. Positive transverse drifts and accelerations are defined in the South direction, while positive rotations are defined along the East axis. All the results have been filtered through a high order (2000 point) low-pass filter with a cut-off frequency of 25 Hz.

5.5.1. Lateral response: hysteresis and prestress behavior

The hysteretic responses seen during the tests are shown in Figure 5.17 and Figure 5.18. In each figure, a background plot in gray represents the specimen response to all the preceding excitations, and a red dot marks the specimen base shear and drift ratio at the end of the excitation.

EQ01 and EQ02 were repetitions of the same excitation, serving as a test run to check correct behavior of the specimen and instrumentation, and to induce any settlements or cracking. This proved useful, since during EQ01 the NW inertia block was found to be not seated properly and showed twisting. Additionally, the restraint frame was found to be bearing against the specimen and providing some amount of lateral

resistance. Both these issues were corrected before EQ02, by increasing the clamping force on the inertia blocks to 890 kN (200 kip) and pushing the restraint frames slightly away from the specimen. EQ02 can be seen to have a slightly softer response as compared to EQ01.

EQ03 represented an earthquake inducing mild drift demands on the specimen, with EQ04 acting as an aftershock. The hysteresis response shows a small amount of energy dissipation, indicating possible rocking at the base. From the hysteresis response of EQ03 and EQ04, it can be seen that the specimen response has softened, indicating that the concrete at the base has cracked.

EQ05 induced moderate drift demands on the specimen, with EQ06 serving as an aftershock with mild drift demands. The pinched shape of hysteresis seen in EQ05 is characteristic behavior of hybrid re-centering systems, indicating rocking behavior under this excitation. As expected, EQ06 and EQ03 resulted in mild (~1.8%) drift demands, however, comparing the responses under the two excitations shows reduced energy dissipation and softer response under EQ06.

EQ07, EQ08 and EQ09 formed the final three motions in the initial loading protocol, with increasingly larger demands. The direction of each excitation was selected to avoid larger drifts on only one side of the specimen. From the response under EQ08 and EQ09, the specimen maintains its re-centering behavior under the large demands imposed. The peak force seen during EQ09 is slightly smaller than during EQ08, indicating a small loss in force capacity resulting from yielding of the prestressing bars. This was further verified by the data from the PT bars and can be seen in Figure 5.23.

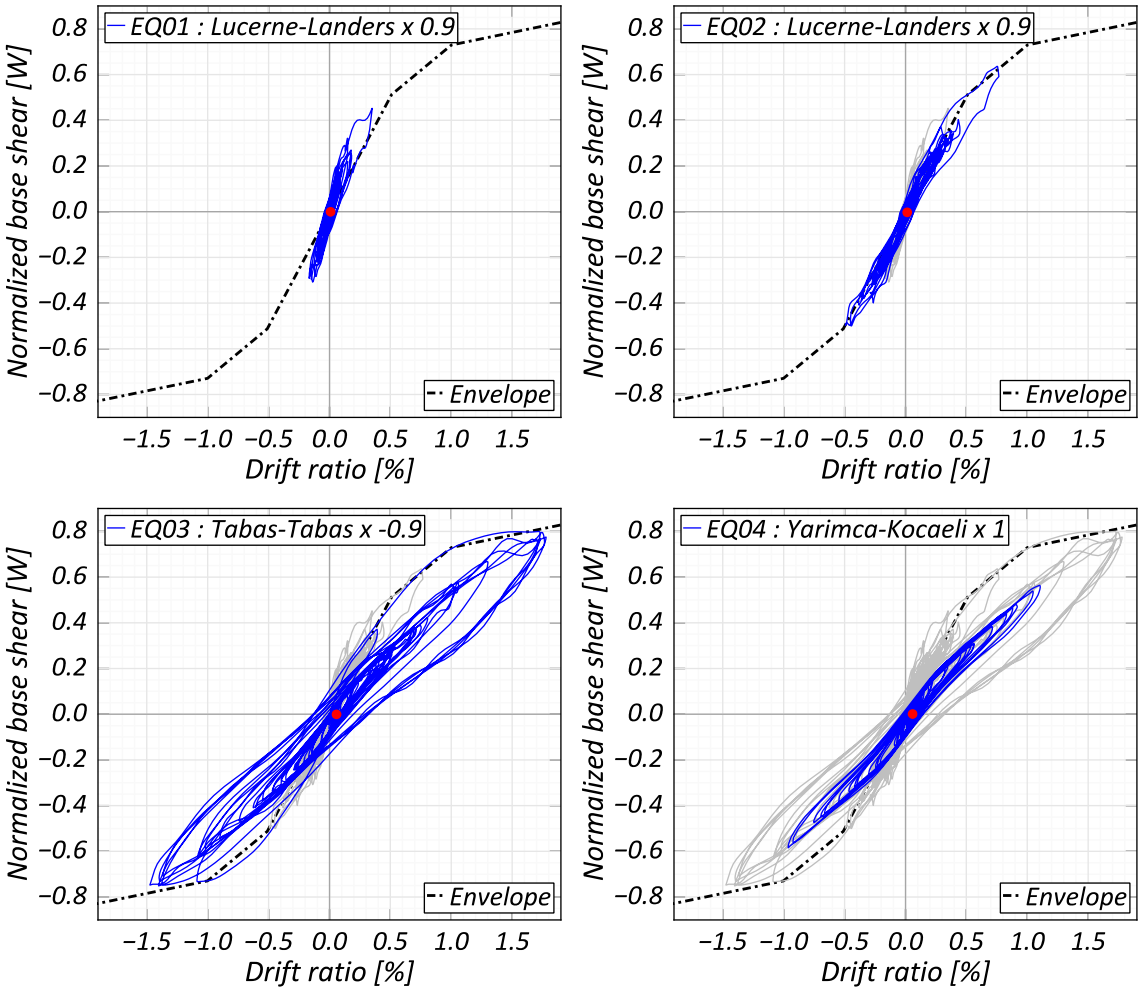

Figure 5.17 Bridge-bent hysteretic response, day 1 of testing

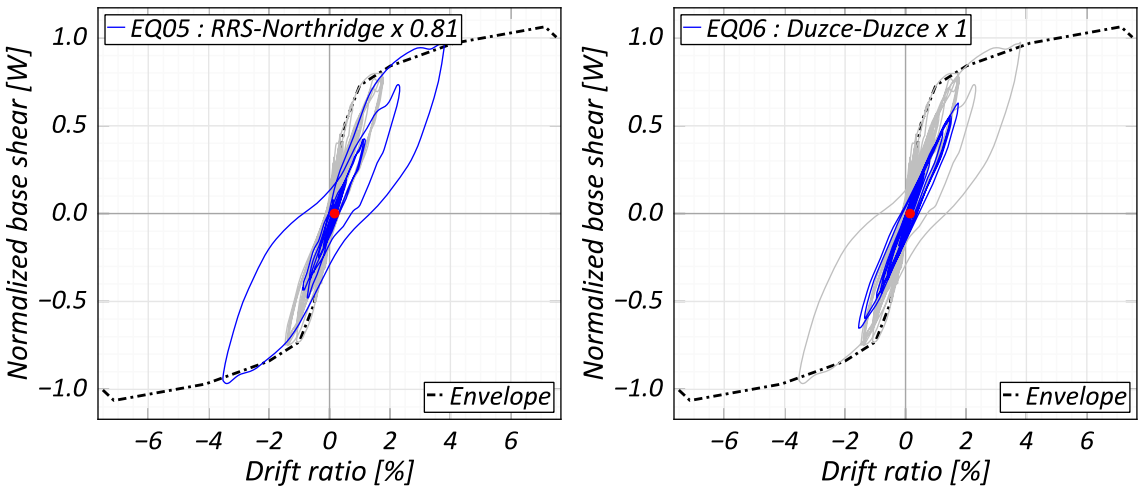

Figure 5.18 Bridge-bent hysteretic response, day 2 of testing

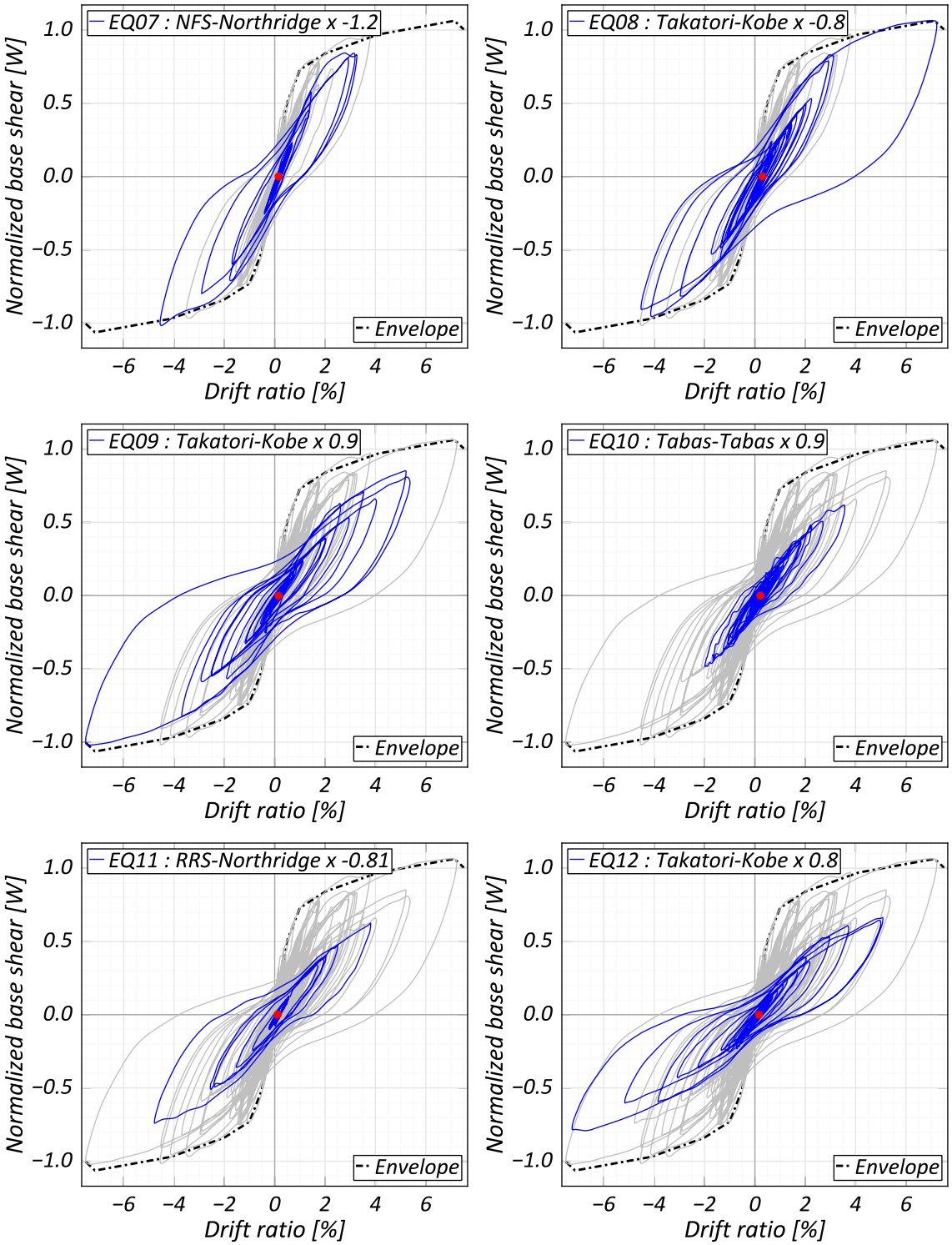

Figure 5.18 Bridge-bent hysteretic response, day 2 of testing (continued)

Since the specimen response under EQ09 suggested little damage, it was decided to impose additional ground motions, until dissipator bar fracture was observed. EQ10, EQ11 and EQ12 were repetitions of EQ03, EQ05 and EQ08 with reversed polarities. Mild-steel Bar fractures were recognized by popping sounds heard during EQ11 and EQ12. The consequence of prestress loss and bar fracture is evident in the hysteretic response: the drifts in EQ10 and EQ11 are noticeably larger than EQ03 and EQ05, and while EQ12 has similar drifts to EQ08, the base shear is considerably smaller.

A summary of peak and residual drifts seen during different excitations is presented in Table 5.5 and shown graphically in Figure 5.19. Also included in Table 5.5 are the rotations measured at the rocking interfaces of the South column, which are shown graphically in Figure 5.20(a) and (b). The re-centering behavior of the system is evident in the residual drifts and rotations seen at the end of each motion. The rotations at top of the columns are slightly smaller than at the bottom; which can be attributed to the higher shear and moment demands at the bottom due to the effect of the inertial mass of the columns. Additionally, the column base rotation time histories for EQ08 and EQ09 are shown in Figure 5.21: the rotation response closely follows the drift response, indicating that the column behaves nearly like a rigid body over the clear height.

The prestressing forces measured during the tests in each of the two bars are presented in

Table 5.6 and Figure 5.22. Additionally, the stress-strain responses measured during EQ08 and EQ09 are shown in Figure 5.23(a) and (b), which show light yielding. It is likely that the yielding is concentrated at the rocking interfaces, resulting from potential “kinks” i.e. large curvatures in the prestressing bars at these locations.

The maximum and residual gap opening at the bottom interface of the South column in the North and South faces is shown in Figure 5.32, Figure 5.33, Figure 5.34 and Figure 5.35 at the end of this chapter. These figures also show the specimen overall deformation at the instance of peak positive and negative drifts, which are listed in the sub-caption. The rocking interface naturally forms at the location where the 12.7mm wide strip was removed from the column outer shell, and the gap closes completely at the end of each excitation, with only minor spalling seen in EQ08.

Table 5.5 Summary of transverse drifts and South column rotation response

EQ #	Drift ratio (%)		Bottom rotation (100 rad)		Top rotation (100 rad)	
	Peak	Residual	Peak	Residual	Peak	Residual
EQ01	0.35	0.01	0.26	0.007	0.25	0.006
EQ02	0.77	0.01	0.66	0.026	0.59	0.005
EQ03	1.78	0.06	1.60	0.068	1.45	0.028
EQ04	1.11	0.06	0.99	0.070	0.88	0.031
EQ05	3.81	0.16	3.51	0.160	3.28	0.114
EQ06	1.74	0.15	1.60	0.139	1.44	0.094
EQ07	4.55	0.15	4.29	0.135	4.16	0.104
EQ08	7.22	0.3	6.75	0.249	6.44	0.171
EQ09	7.51	0.15	7.16	0.111	7.00	0.055
EQ10	3.57	0.22	3.28	0.178	3.09	0.118
EQ11	4.78	0.12	4.57	0.083	4.39	0.032
EQ12	7.26	0.16	6.98	0.133	6.73	0.058

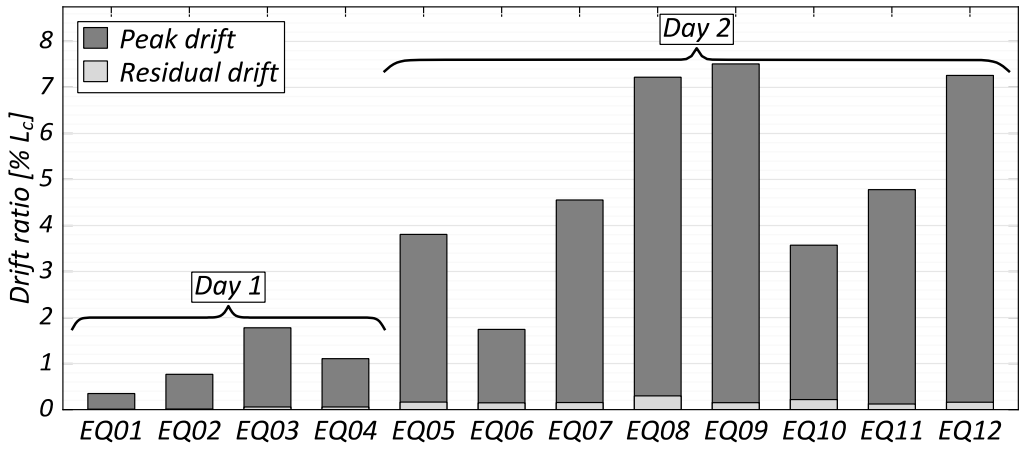

Figure 5.19 Peak and residual transverse drifts

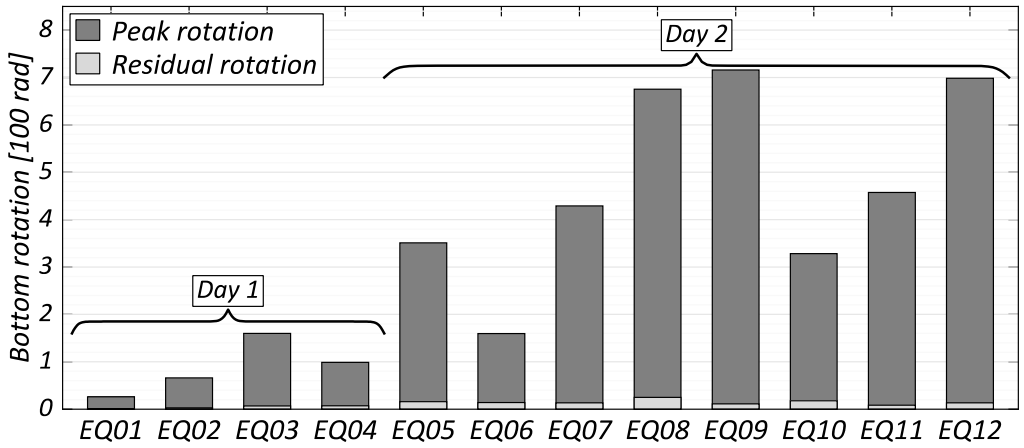

(a) South column bottom rotation

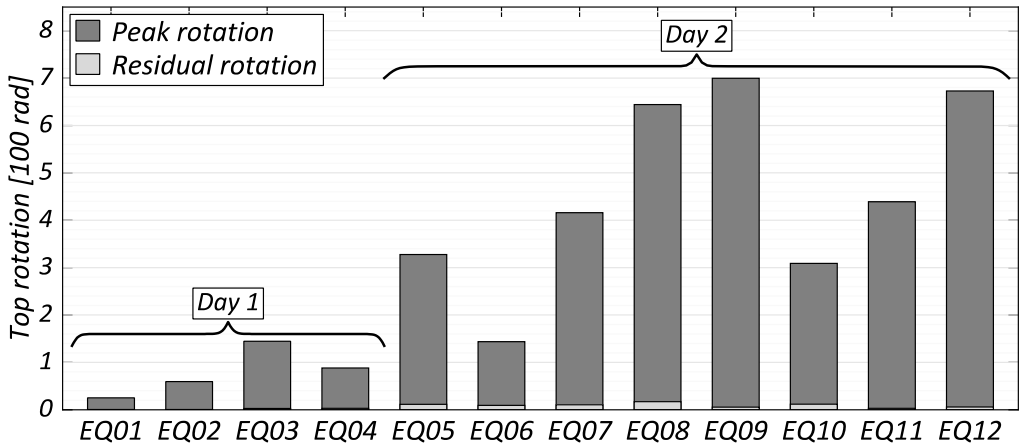

(a) South column top rotation

Figure 5.20 Peak and residual column interface rotations

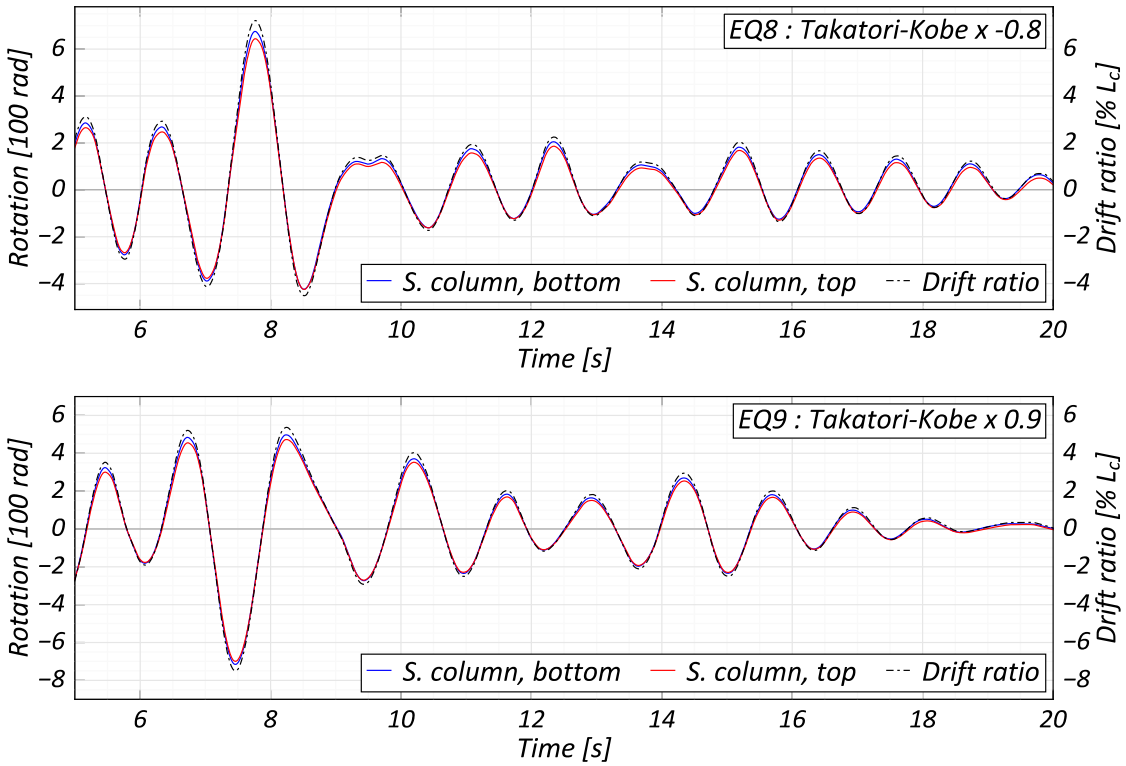

Figure 5.21 Column base rotations seen in EQ08 and EQ09

Table 5.6 Summary of peak and residual prestressing forces

EQ #	Peak stress (%f_{pu})		Residual stress (%f_{pu})	
	North bar	South bar	North bar	South bar
EQ01	0.35	0.01	0.26	0.007
EQ02	0.77	0.01	0.66	0.026
EQ03	1.78	0.06	1.60	0.068
EQ04	1.11	0.06	0.99	0.070
EQ05	3.81	0.16	3.51	0.160
EQ06	1.74	0.15	1.60	0.139
EQ07	4.55	0.15	4.29	0.135
EQ08	7.22	0.3	6.75	0.249
EQ09	7.51	0.15	7.16	0.111
EQ10	3.57	0.22	3.28	0.178
EQ11	4.78	0.12	4.57	0.083
EQ12	7.26	0.16	6.98	0.133

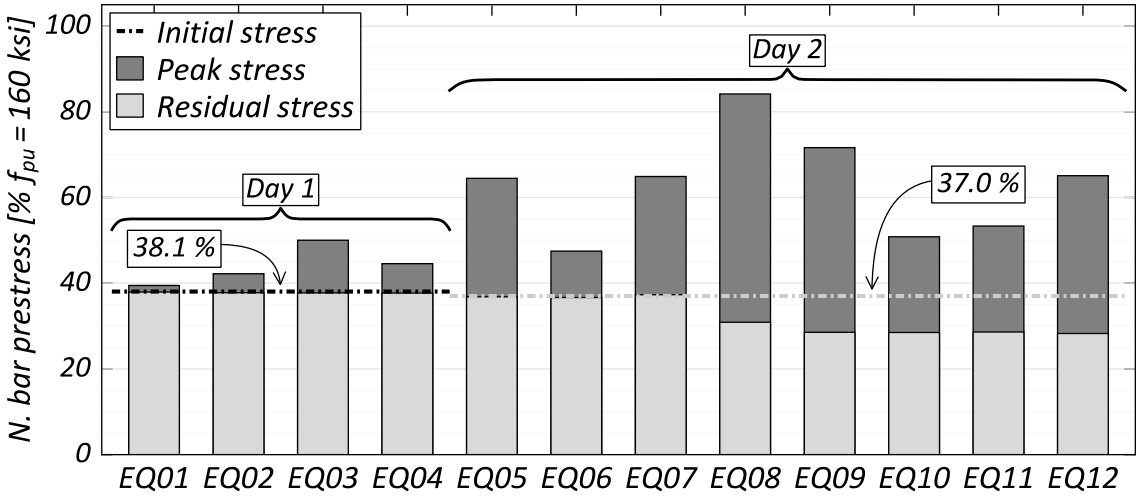

(a) North bar prestress

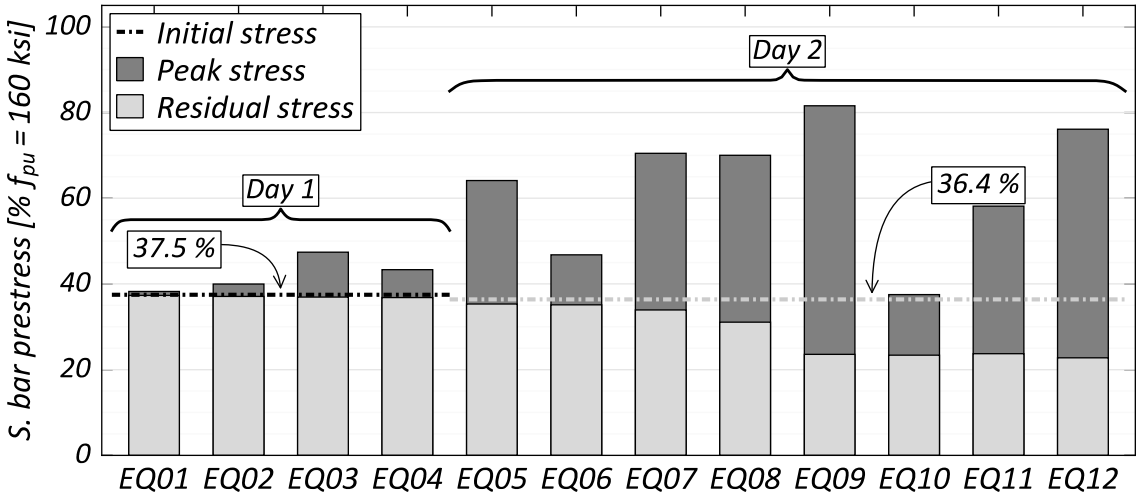

(a) North bar prestress

Figure 5.22 Peak and residual prestress ratios

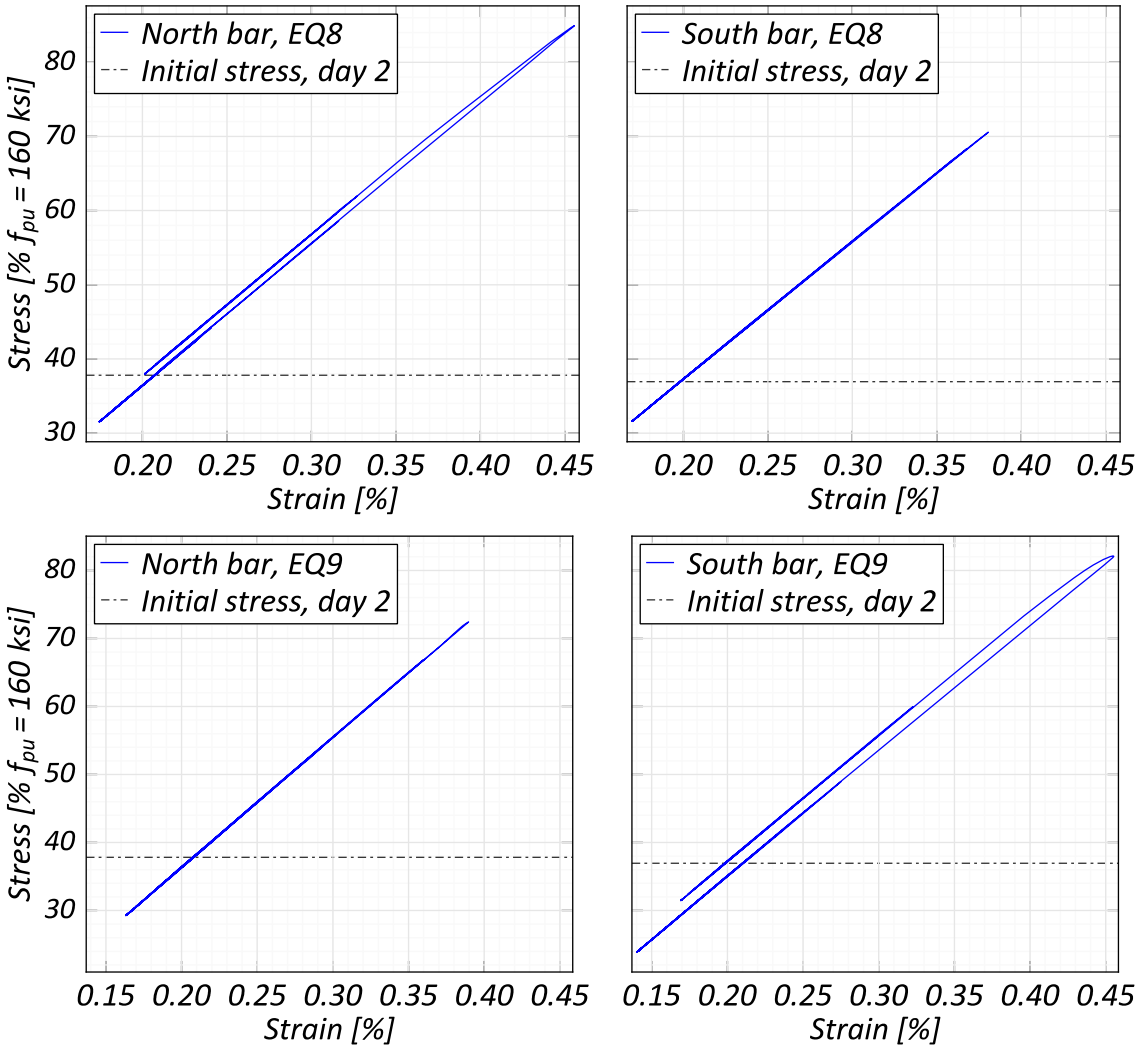

Figure 5.23 Stress-strain behavior of prestressing bars

5.5.2. Strain measurements

The strain time history measured during EQ05 from one dissipator bar in each of the two columns is shown in Figure 5.24. Also marked in the time history is the point of peak strain rate. Note the strain rate value is given in specimen time, since the strain rate plays an important role in the modeling of the specimen and will be revisited in the numerical modeling of the specimen response. Strain data from the dissipators is not available beyond EQ05, since the majority of the strain gauges installed on the dissipators

stopped working at the end of day 1 of testing, and the remaining strain gauges failed during EQ06. A similar strain history for the prestressing bars from EQ09 is presented in Figure 5.25.

The peak circumferential strains measured in the steel shell near the rocking interfaces of the South column are tabulated in Table 5.7. Comparing the values to the yield strain seen from the shell material properties, it can be seen that the shell has undergone plastic deformation under EQ08. The strain history for this earthquake is presented in Figure 5.26.

The longitudinal strain histories measured during EQ09 in the corrugated metal pipe forming the foundation socket of column 1 are shown in Figure 5.27. The measured strain values are small and predominantly in compression. The compression measurements likely result from Poisson effects caused by the circumferential elongation of the CMP under increased column compression and socket compressive stresses.

The strain history from one of the hanger reinforcement bars in the bent cap is shown in Figure 5.28. From the small strain values seen, it can be concluded that this reinforcement is not necessary, and the CMP socket connection is likely sufficient for transferring the vertical forces.

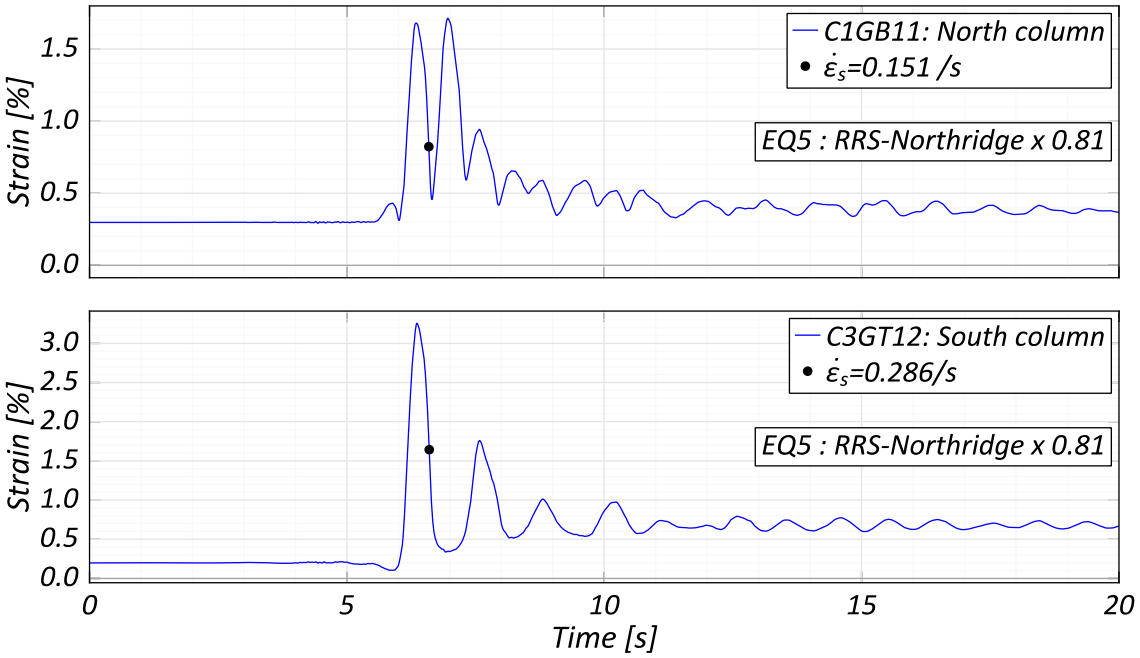

Figure 5.24 Energy dissipator strain history, EQ05

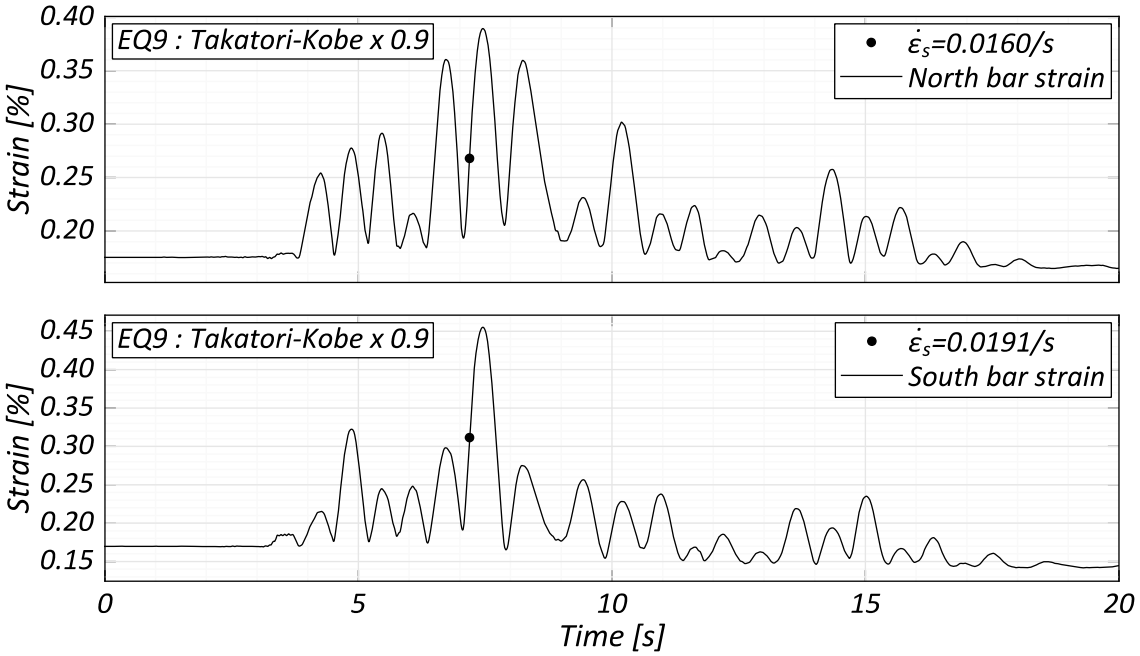

Figure 5.25 Prestressing bar strain history, EQ09

Table 5.7 South column shell circumferential strain

EQ #	North face strain (%)		South face strain (%)	
	Bottom	Top	Bottom	Top
EQ01	-0.014	0.017	-0.006	-0.017
EQ02	0.027	0.037	0.020	0.014
EQ03	0.064	0.067	0.075	-0.024
EQ04	0.056	0.041	0.054	-0.030
EQ05	0.120	0.178	0.138	-0.044
EQ06	0.081	0.115	0.085	0.023
EQ07	0.136	0.151	0.138	0.043
EQ08	0.127	0.403	0.315	0.062
EQ09	0.218	0.371	0.327	0.110
EQ10	0.135	0.322	0.276	0.078
EQ11	0.175	0.325	0.286	0.109
EQ12	0.211	0.347	0.320	0.148

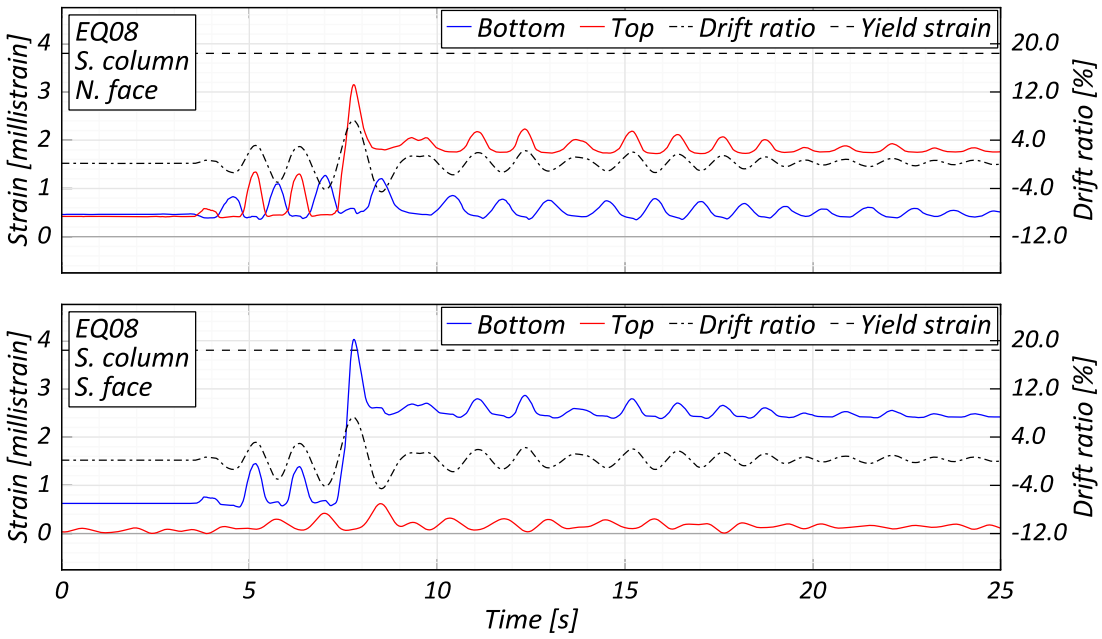

Figure 5.26 Shell circumferential strain history, South column, EQ08

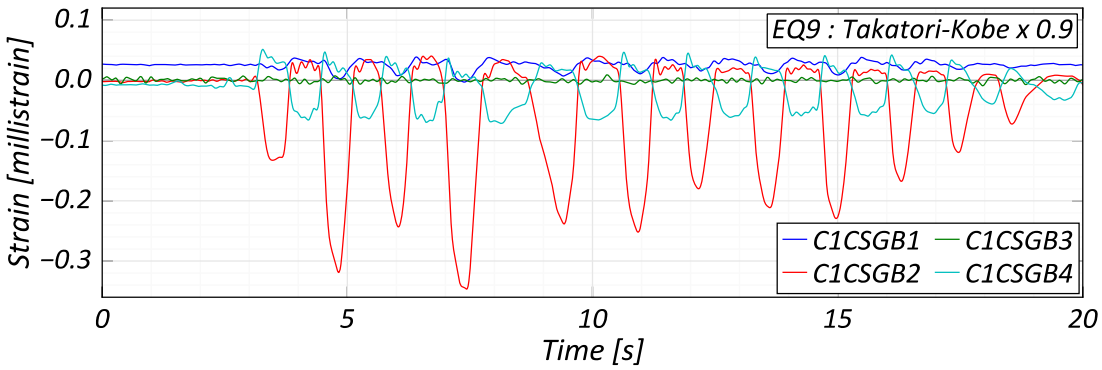

Figure 5.27 Corrugated metal pipe strain history, foundation socket, EQ09

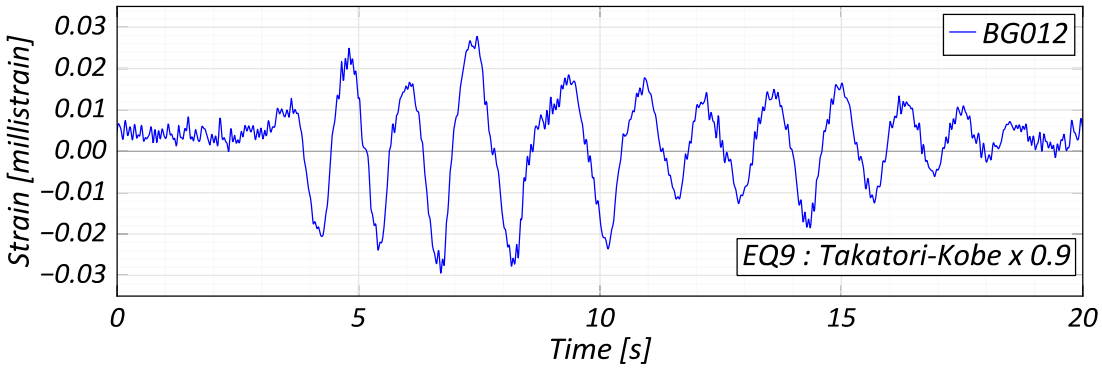

Figure 5.28 Cap-beam hanger reinforcement strain history, EQ09

5.5.3. Vertical response

A plot showing the vertical acceleration, measured positive upwards, vs drift ratio for all the excitations is shown in Figure 5.29. During rocking behavior, the interface gap opening results in vertical uplift and hence acceleration in the bent cap. Therefore, it is a reasonable assumption that there should be some correlation between vertical acceleration and column drifts during rocking motion. However, in the vertical acceleration-drift response, no such correlation is apparent, except perhaps in EQ05 and EQ07. The hysteretic response, vertical acceleration vs drift and the vertical acceleration time histories at the foundation and cap-beam for these two motions are presented in Figure 5.30 and Figure 5.31 respectively. The point of the peak vertical acceleration

during rocking in the columns is marked in all the responses for each excitation. In the vertical and horizontal responses, it can be noted that such a peak in vertical acceleration during rocking occurs simultaneously with a dip in the base shear-drift response. Looking at the time-histories of the vertical acceleration it can be seen that such a peak is not caused by the maximum input acceleration: for EQ05, the noted peak occurs at input vertical accelerations which are much smaller than the vertical Peak Ground Acceleration (PGA).

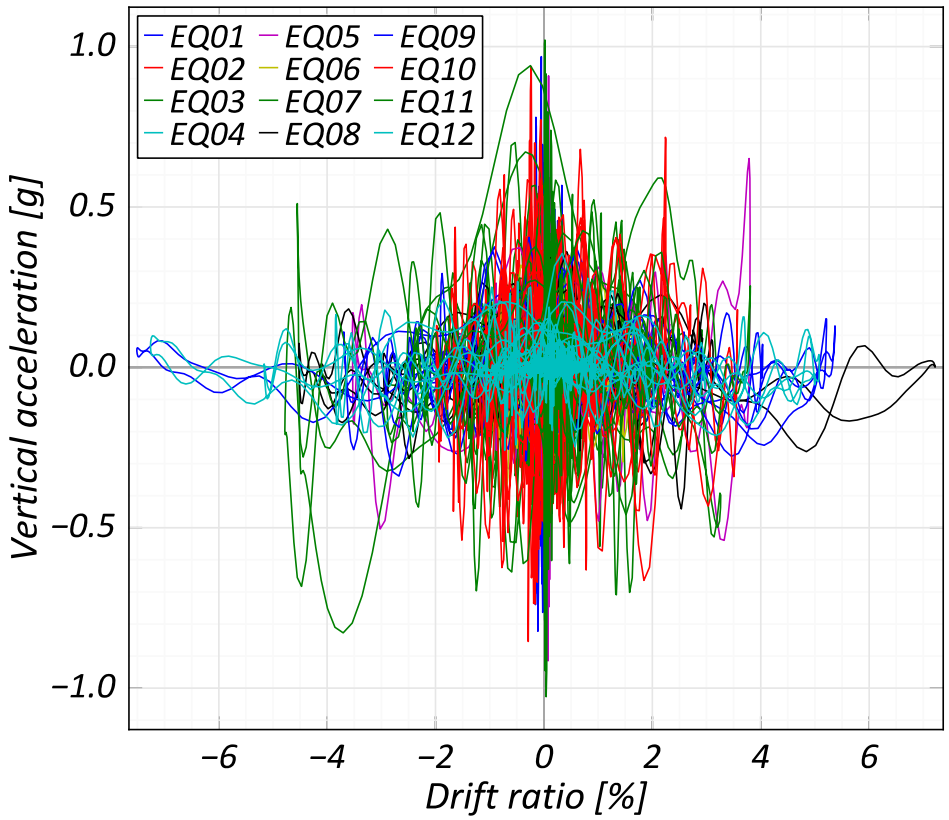

Figure 5.29 Vertical acceleration vs drift ratio

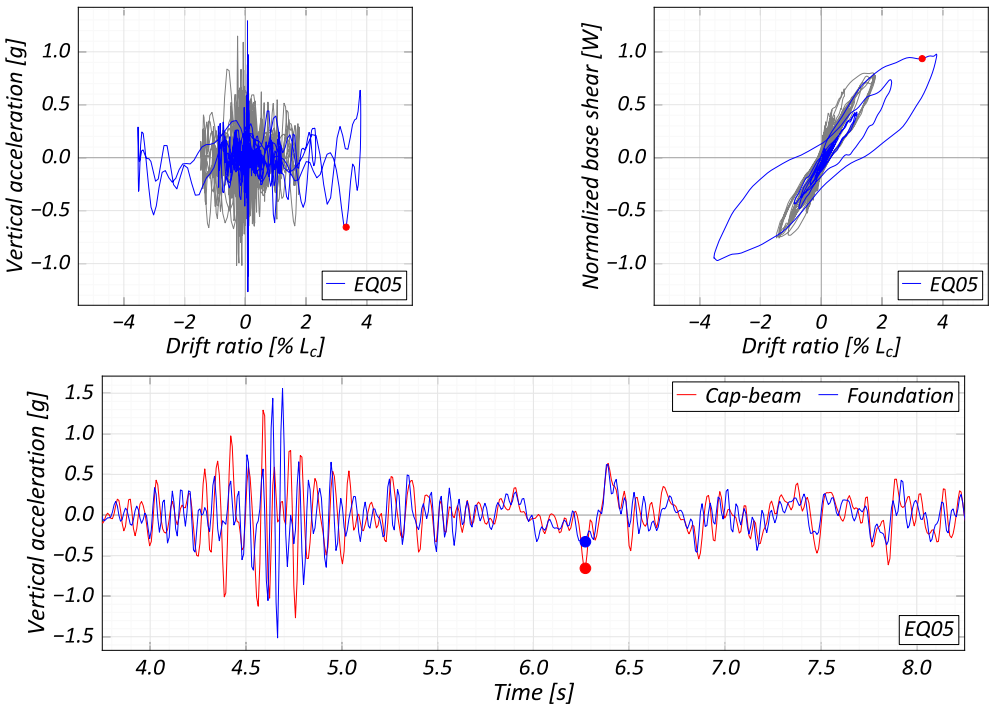

Figure 5.30 EQ05 vertical and horizontal response, and vertical acceleration time histories

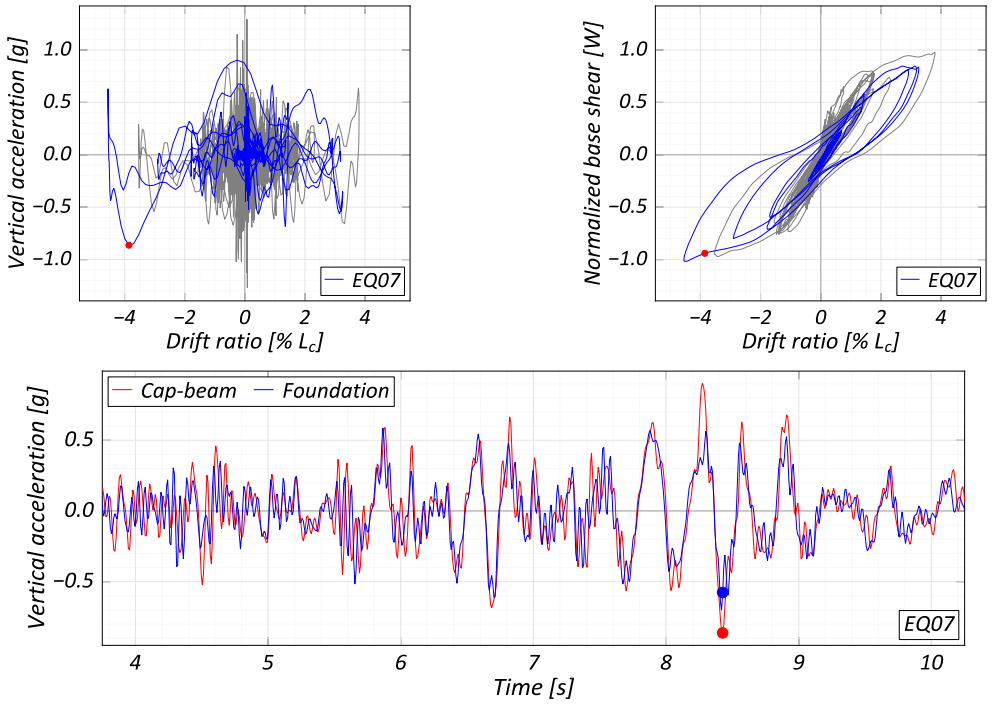

Figure 5.31 EQ07 vertical and horizontal response, and vertical acceleration time history

(a) South column interface, North face, Δ=3.8%

(b) South column interface, South face, Δ=-3.5%

(c) South column interface, North face, end of excitation

(d) South column interface, South face, end of excitation

(e) Specimen deformation, Δ=3.8%

(f) Specimen deformation, Δ=-3.5%

Figure 5.32 Specimen response at peak drifts, EQ05

(a) South column interface, North face, Δ=3.2%

(b) South column interface, South face, Δ=-4.5%

(c) South column interface, North face, end of excitation

(d) South column interface, South face, end of excitation

(e) Specimen deformation, Δ=3.2%

(f) Specimen deformation, Δ=-4.5%

Figure 5.33 Specimen response at peak drifts, EQ07

(a) South column interface, North face, Δ=7.2%

(b) South column interface, South face, Δ=-4.5%

(c) South column interface, North face, end of excitation

(d) South column interface, South face, end of excitation

(e) Specimen deformation, Δ=7.2%

(f) Specimen deformation, Δ=-4.5%

Figure 5.34 Specimen response at peak drifts, EQ08

(a) South column interface, North face, Δ=5.4%

(b) South column interface, South face, Δ=-7.5%

(c) South column interface, North face, end of excitation

(d) South column interface, South face, end of excitation

(c) Specimen deformation, Δ=5.4%

(d) Specimen deformation, Δ=-7.5%

Figure 5.35 Specimen response at peak drifts, EQ09

5.6. Acknowledgements

I would like to thank Dr. Khalid Mosalam, Dr. Selim Gunay and Yingjie Wu from University of California, Berkeley for their valuable insights into the specimen design and numerical model development for the study of the low-damage bridge specimen.

I would like to thank the technical staff at the PEER Earthquake Shaking Table at the Richmond Field Station academic facilities of the University of California, Berkeley: Clement Barthes, Robert Cerney, Lobsang Garcia and Nathaniel Knight for their enthusiasm and invaluable assistance during the testing of the low-damage bridge specimen studied in this work.

The work presented in this chapter was supported by funding from the Pacific Earthquake Engineering Research Center (PEER), University of California Berkeley. I am thankful for their contributions of time, financial support and expertise.

Chapter 5, in part, is a reprint of the material presented in *Low-damage Columns for Accelerated Bridge Construction*, PEER Research Report (in-preparation) Nema, Arpit and Restrepo, José I. The dissertation author is the primary author on the report.

Chapter 6

ANALYTICAL SIMULATION OF 4-BENT PROTOTYPE LOW-DAMAGE BRIDGE

6.1. Introduction

This chapter presents the analytical work accompanying the dynamic testing of the bridge-bent specimen presented in Chapter 5The analytical work was performed using the structural analysis program OpenSees (Mazzoni et al. 2007; McKenna et al. 2010), developed by the Pacific Earthquake Engineering Research (PEER) Center. Analytical work supporting the shake table testing included improvements to the single re-centering column model developed by Guerrini et al. (2015), and the development of an analytical model for the low-damage, multi-column bridge bent. The multi-column model was used for an analytical study to aid in the development of the shake table test prototype, in particular for selecting the column on-center distance to maintain similar levels of axial loads as compared to the prototype bridge.

After the conclusion of the dynamic testing, the model of the test specimen was calibrated to the measured material properties and specimen geometries, followed by

additional changes for improving the correlation between the test and model results. Finally, the improved model for low-damage bridge columns was incorporated into a comprehensive bridge model to study the behavior under different configurations of unbonded prestressing steel and energy dissipator steel.

6.2. Low-damage column model improvement and validation

The main elements of a hybrid rocking system are the rocking member, unbonded post-tensioned elements for improving upon the re-centering behavior provided by the axial loads and energy dissipating elements for controlling displacements. The rocking member typically has reinforced ends to withstand the large stresses arising during rocking and can be split into two subcomponents by function: the reinforced rocking interface and the central element which largely stays elastic. Typically, the elastic limit of the unbonded post-tensioned elements controls the displacement capacity of the system.

A model incorporating these elements has been developed and validated for re-centering bridge columns by Guerrini et al. (2015), hereby called Model 0, using the analysis program OpenSees, where the specific behavior of each of these elements is explicitly modeled:

- The energy dissipators are modeled individually using displacement-based beam column elements, using material models to represent the energy dissipation method.
- The post-tensioned elements are modeled using non-linear truss elements to account for any yielding, with fixity constraints to model anchorage points and an approximation of sliding constraints at the rocking interface.

- The rocking element is represented by elastic beam-column members, split into multiple segments to model the point of connection to the energy dissipators.
- The rocking interface is modeled using multiple compression-only, non-linear truss elements, with appropriate material models representing the interface material.

The truss elements forming the rocking interface are connected via rigid members, with the elastic rocking element starting at their combined center. The energy dissipators and the PT elements are modeled at their physical locations and are connected to the elastic rocking element via rigid elements. The model has been validated against experimental data obtained from two cyclic tests, details of which will be presented in the next section.

While the model shows good comparison with experimental data, the computational performance is slow. This is largely due to the modeling of individual fibers in the rocking interface: for each fiber, at least 3 DOFs are added in the model. Considering that the execution times increase exponentially with DOF count, this model is a poor choice for systems with multiple rocking interfaces, for example a whole bridge.

To improve the computational performance, as a first step, the model is simplified to use a single fiber-based beam-column element for the rocking interface and displacement-based beam-column elements to model the rocking element. This updated model, hereby called Model 1a, is again calibrated against the same tests. As a further optimization, the elements representing the individual dissipators are also combined into

a single fiber-based element. This model will be called Model 1b. A representation of the three models described above is shown in Figure 6.1.

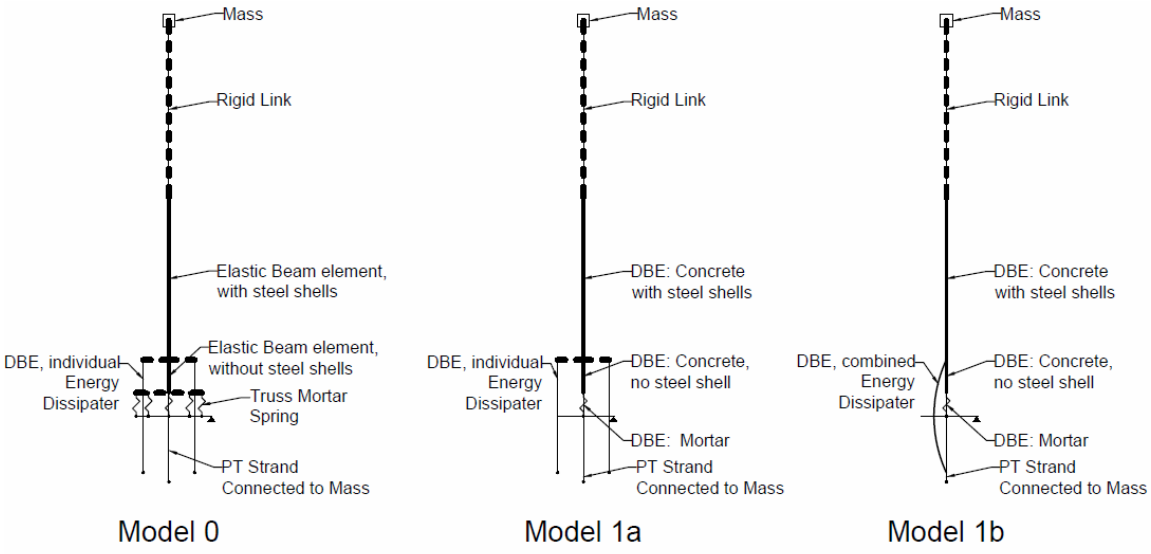

Figure 6.1 Hybrid re-centering column analytical models

The proposed models presented were validated against test results from two hybrid re-centering systems tested at the UC San Diego Powell Structural Engineering Laboratories by Guerrini et al. (2015): Unit 1A utilizing external buckling restrained energy dissipators and Unit 1B utilizing internal dowel bars. The same column was used for both the units: the column was flipped upside-down after testing Unit 1A and reused to test Unit 1B to take advantage of the fact that only the bottom region of a cantilevered hybrid column experiences large strains and damage. Some details of the test are shown in Figure 6.2.

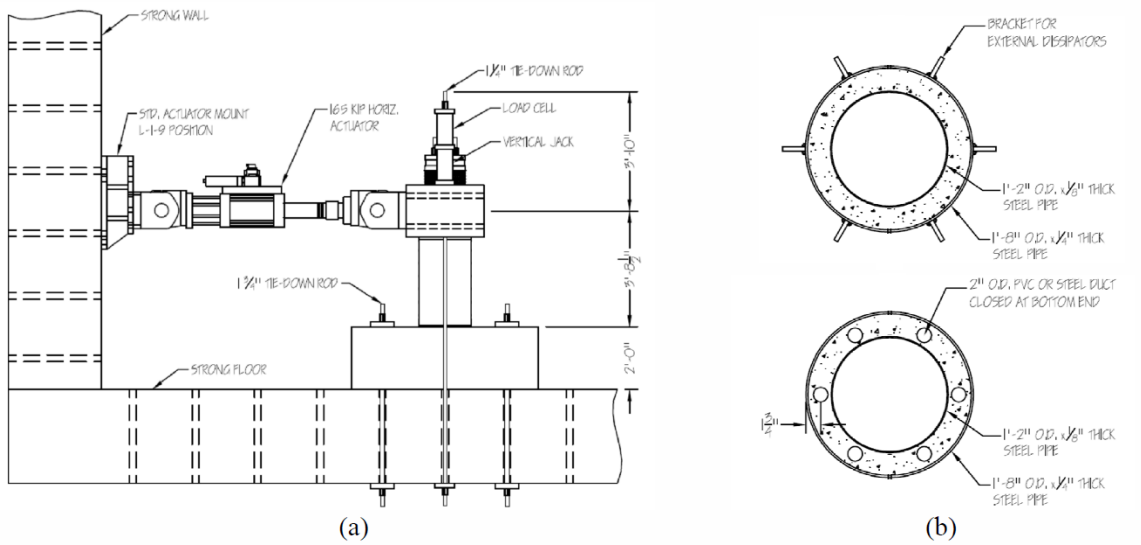

Figure 6.2 Specimen drawings: (a) Test Setup; (b) Column base cross sections for Unit 1A (top) and Unit 1B (bottom)

The tested column had an external diameter of 508 mm (20-inch) and a height of 838 mm (33-inch) The load was applied via a loading stub at an effective height of 1130 mm (44.5-inch). The column was formed by casting high strength normal weight concrete ($f'_c = 70.3\ MPa = 10.2\ ksi$) between two A572 Gr 50 steel shells: the outer shell had a diameter of 508 mm (20-inch) and thickness 6.35 mm (0.25-inch), while the internal shell diameter was 356 mm (14-inch) and thickness 3.2 mm (0.125-inch) The inside of the internal shell was left hollow to reduce the column weight and to facilitate the installation of post-tensioning steel, provided by four 35 mm (1-3/8-inch) diameter A722 Grade 150 DSI Thread bars. The threaded bars were anchored into anchorage devices prearranged in the footing and were seated on soft rubber pads on top of the loading stub. The rubber pads served to increase the displacement capacity of the column by delaying the yielding of the PT bars, their use was necessitated due by the low aspect ratio of the column. Each specimen was placed on a 12.7 mm (0.5-inch) thick high-

performance mortar layer ($f'_c = 53\ MPa = 7.7\ ksi$) created on the foundation to compensate for lack of precision and help in positioning and leveling of the specimen.

Unit 1A was provided with six radially distributed, external buckling restrained external energy dissipators, with a 6.5 in. region milled to 9/16 in. from 1 in. diameter hot rolled A576 Gr 1018 steel bars ($f_y = 331\ MPa = 48\ ksi,\ f_u = 489\ MPa = 71\ ksi$). These were welded to anchors installed in the foundation and to brackets on the column outer shell. A total effective post-tensioning force of 800 kN (180 kip) was applied, in addition to 280 kN (63 kip) of vertical load applied using two vertical jacks to simulate gravity.

Energy dissipation in Unit 1B was provided by six 316LN Gr 75 #4 internal dowels ($f_y = 745\ MPa = 108\ ksi, f_u = 889\ MPa = 129\ ksi$). The dowels were debonded over a length of 178 mm (7-inch) using duct tape and grouted inside pre-installed corrugated steel ducts inside the footing and the column, such that the middle of the debonded length was placed at the foundation level. The effective post-tensioning force and simulated gravity loads were 890 kN (200 kip) and 267 kN (60 kip) respectively.

Both units were subjected to quasi-static reversed cyclic loading in the North-South direction. The loading began with three force-controlled cycles to ±111 kN (25 kip) and three to ± 231 kN (52 kip) base shear, followed by displacement-controlled cycles: three to ±0.5% drift ratio and three to ±0.75% drift ratio. Subsequent cycles composed of two large amplitude cycles, followed by a lower one at a level

corresponding to the previous large drift level: drift ratios of ±1%, ±1.5%, ±2%, ±3%, ±5%, ±7.5%, and ±10% were targeted.

In Model 0, the mortar is modeled using two node trusses in a grid of 36 elements in the circumferential direction and 3 in the radial direction, the PT bars are modeled using truss elements, and the dual shell column is modeled using two elastic beam column elements in series to account for the anchorage location of the energy dissipators. For Unit 1A, the energy dissipators are modeled individually using three displacement-based beam column elements (DBE) per dissipator to account for their variable cross section. For Unit 1B, a single DBE per dissipator accounted for the effective unbonded length. The load is applied at the center of the load block and the PT bars' top node location accounts for the load cell height. The bar material accounts for the flexibility provided by the rubber bearing pads. Further details of the material models and fixity constraints used can be found in Guerrini (2015). It should be noted that the mortar crushing stress has been increased from 6.9 MPa (1 ksi) to 45% of peak stress (25 MPa / 3.6 ksi for Unit1A and 26 MPa / 3.8 ksi for Unit1B) to improve the model prediction at higher drifts.

For Model 1a and Model 1b, the mortar truss elements are replaced by a single two-integration point DBE, using the same mortar material and an equivalent fiber configuration and the two elastic beam column elements between the mortar and load stub are replaced by equivalent two-integration point DBE, using fiber sections made of confined concrete derived from the concrete strength in the columns. The top element also includes steel fibers representing the two enclosing steel shells. The model for the

energy dissipators remains unchanged in Model 1a, while in Model 1b, the energy dissipators for both units are modeled using a single three-integration point DBE, with an element length reflecting the total effective dissipator length. Compared to Model0, the varying section is not modeled for Unit 1A.

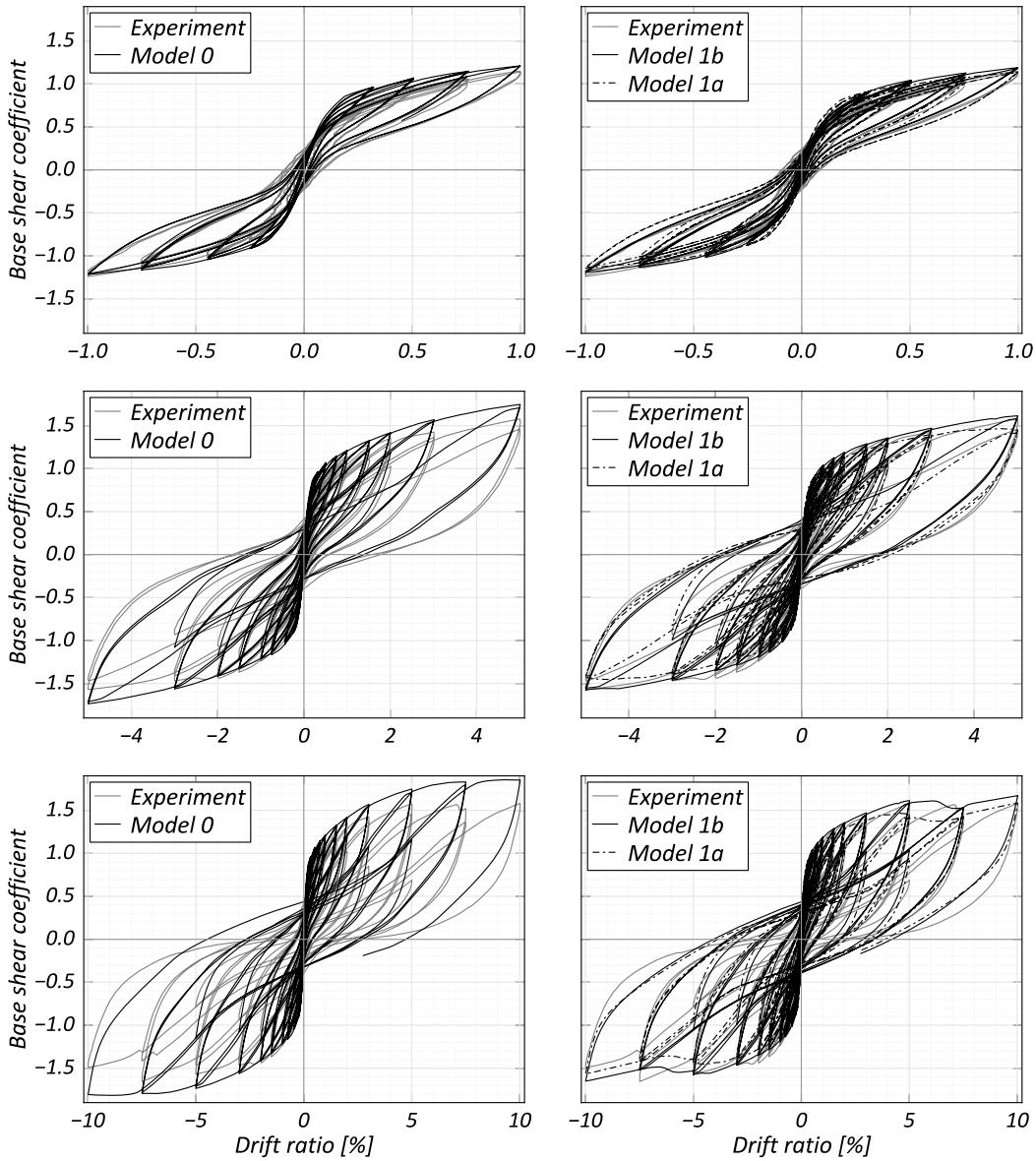

(a) Model 0: Guerrini et al. (2015) **(b) Model 1a and Model 1b**

Figure 6.3 Comparison of experimental and analytical results, Unit 1A

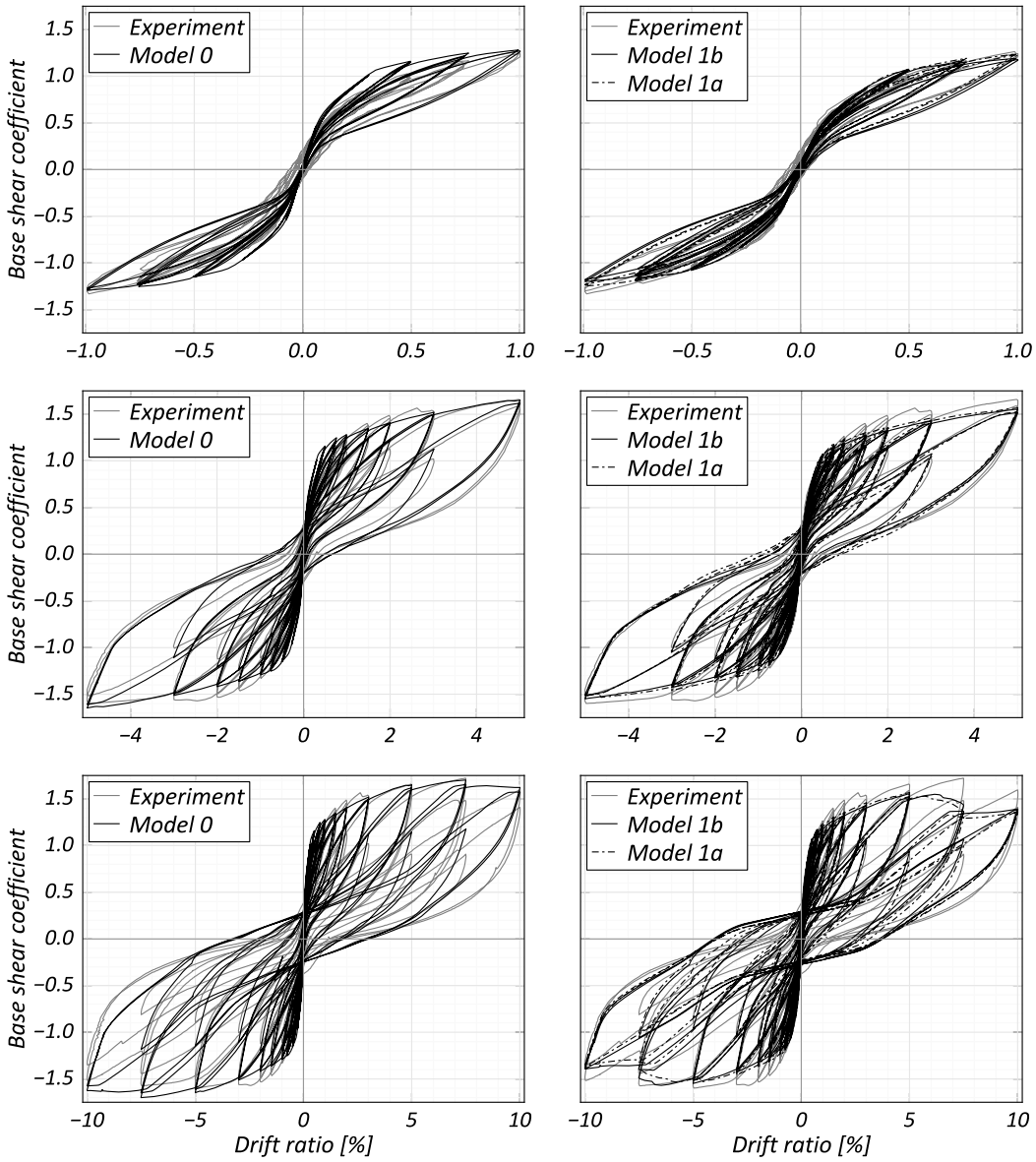

(a) Model 0: Guerrini et al. (2015) **(b) Model 1a and Model 1b**

Figure 6.4 Comparison of experimental and analytical results, Unit 1B

The results for Unit 1A from the three models are shown in Figure 6.3, while the results for Unit 1B are presented in Figure 6.4. All three models show a good agreement with the test results for Unit 1B, while for Unit 1A, Model 0 gives higher forces. Model0 also shows higher initial stiffness when compared to Model 1a and 1b; this is due to

constraints against horizontal displacement applied at the top of the mortar to ensure model stability. A lack of these constraints in Model 1a and 1b result in higher stresses and strains in the mortar, resulting in greater strength degradation at higher drifts.

The advantage of the modifications is clearly visible when comparing the execution times of the three models, as shown in Table 6.1.

Table 6.1 Execution times (in seconds) for hybrid column analytical models

	Model 0: 36x3	Model 0: 36x6	Model 0:72x6	Model 1a	Model 1b
Unit 1A	593	2894	16287	13	6
Unit 1B	1419	7535	54838	25	16

Just switching to the fiber model for the mortar results in a speed by a factor of 45 for Unit 1A and a factor of 56 for Unit 1B, while replacing the energy dissipator trusses with a single fiber-based element results in a speedup factor of 98 for Unit 1A, and a factor of 88 for Unit 1B. As stated earlier, this is due to the much larger number of degrees-of-freedom in Model 0. For models involving multiple rocking interfaces, this number should be expected to increase non-linearly. A simulation of a larger model can be made by doubling the number of mortar truss elements for two interfaces or quadrupling the number for four interfaces. The execution times for these simulations are also included in the table. From the values it can be inferred that the execution time increases with an exponent of at least 1.3, with increasing exponent with the DOF count.

6.3. Analytical model of low-damage, multi-column bridge-bent

A sketch of the main model components, overlaid on top of the prototype/specimen elevation view, is shown in Figure 6.5. The central height of each column is modeled using multiple beam-column elements in series, connected to

displacement-based beam-column elements (DBE) at each end which represent the rocking interfaces. The debonded dissipator bars are also modeled using DBE, with one element for modeling all the dissipators at each interface. Prestressing bars are modeled using non-linear truss elements with applied initial stresses as measured at the beginning of the test. The ends of the rocking interface, energy dissipators and the PT bars in the foundation are modeled as fixed ground nodes, while their ends in the bent cap are connected, using stiff elastic elements modeling the bent cap, to a central point at half the bent-cap depth and equidistant from both columns.

6.3.1. Column

Each column is modeled using three beam-column elements connected in series. The central element, modeled using a four (4) integration point force-based beam column element (FBE), represents the composite column section with the confined concrete, the bonded steel rebar and the outer steel shell. The end elements represent the concrete between the rocking interface and the effective anchorage point of the debonded energy dissipators in the specimen clear height. These elements are modeled without any steel to represent the lack of bond between the concrete and either the dissipator or shell steel, and to represent the fact that the shell does not transfer any compression at the interface (resulting from the discontinuity in the shell at the interface). DBE with two integration points are used to model these elements to ensure stable performance, since the concrete only sections were found to lead to instabilities when using FBE due to the inherent lack of tensile strength.

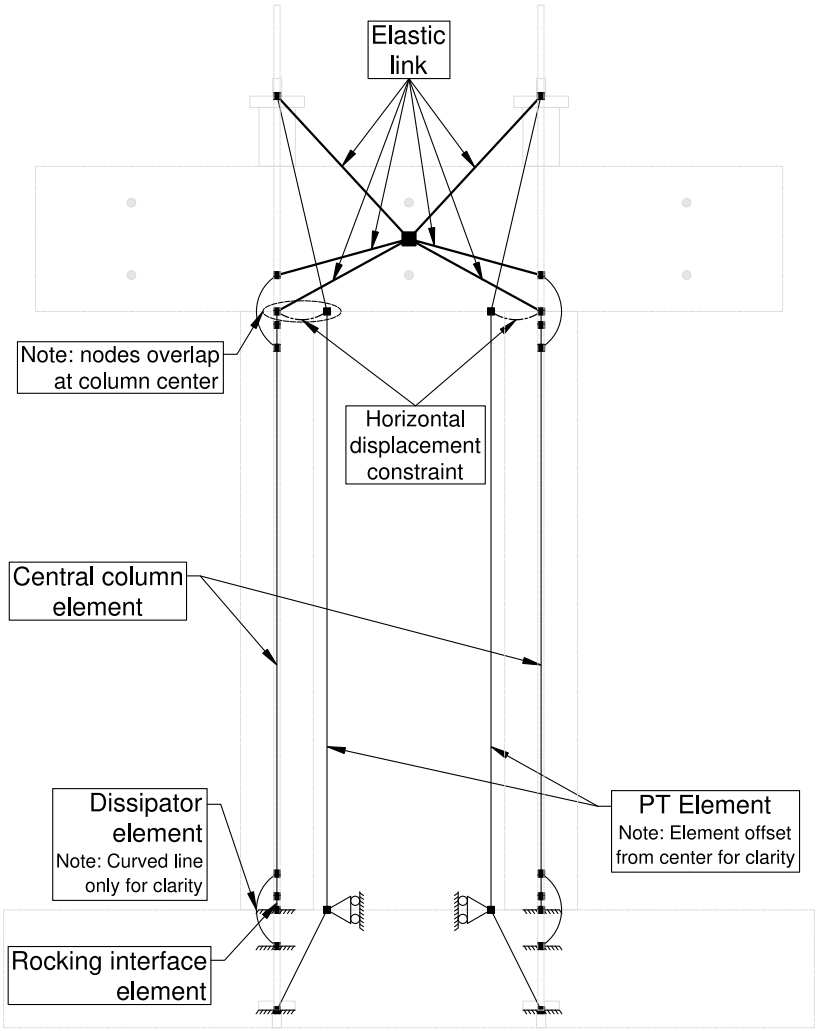

Figure 6.5 Hybrid re-centering bridge bent analytical model

The concrete is modeled using the *Concrete02* material model (Yassin 1994), with confined concrete behavior calculated from the unconfined concrete and column shell steel properties following the recommendations of Chang and Mander (1994). The steel for the fully bonded reinforcement is modeled using the *Steel02* material hysteretic rule (Filippou et al. 1983), based on Giuffré-Menegotto-Pinto model (Mengotto and Pinto 1973).

6.3.2. Rocking interface

The rocking interfaces are modeled using DBE with two integration points, in accordance with the models presented under Section 6.2. Since the rocking interface was monolithic with the rest of the column, the material model used is similar to that of the confined concrete in the columns. *Concrete02* rule is again used, with the concrete strength set to be the same as that for the column concrete. The strains, however, are amplified by twice the ratio of the theoretical neutral axis depth (assumed to be approximately 0.25 times the column diameter) to the height of the element. This transformation is done to approximately capture the spread of inelastic behavior within the column, both above and below the interface, assumed to extend uniformly for a length equal to the neutral axis depth from the interface (Restrepo and Rahman 2007).

6.3.3. Prestressing bars

The prestressing bars are modeled using non-linear corotational truss elements, connecting a point located at the anchors inside the foundation and a point at the anchor location on top of each column. The bars are split into three segments, with the end segments modeling the bars inside the foundation/bent cap, and the central segment modeling the bars inside the column. The nodes connecting the segments are restrained to have the same horizontal and rotational displacement as the closest rocking interface node, for approximately modeling the bar behavior expected at these locations.

Steel02 hysteretic rule is used to model the stress-strain behavior of the bars, and appropriate initial stresses are applied to the PT bars using the *InitStrainMaterial* to simulate the initial prestresses in the columns. While OpenSees does offer a direct

InitStressMaterial for applying initial stresses to material models, the derivative material model was found to not work accurately prompting the use of the indirect, initial-strain based derivative material model.

6.3.4. Energy dissipators

Energy dissipators are modeled using a single, two integration point DBE for the debonded reinforcement bars at each rocking interface, following Model 1b presented in Section 6.2. One end of these elements connects to the central element of the column, while the other end is either fixed to the ground or connected to the bent cap geometric center using stiff elastic element.

The length of these elements is selected to represent the debond length of the dissipators as well as the bar development length, assumed to be 10 d_b on either side of the interface to model bond-slip outside of the debonded portion of the rebars. Each element is located such that half its length is above and half below the interface. Finally, the material properties used for modeling of the bonded rebars inside the column are also used for modeling the debonded steel rebars constituting the dissipators.

6.3.5. Analysis procedure

The model analysis is performed in three stages. First, a nonlinear static analysis is performed in which the gravity loads are applied to the model. The Newton-Raphson algorithm is used to solve the equilibrium equations. At this point, the stress in the PT bars is checked to ensure correct initial conditions in the PT bars.

In the second stage, eigenvalue analysis is performed to compute the “loaded” modal properties, which are then used to set the damping properties of the structure.

Rayleigh damping, based on the initial, non-updating stiffness, is set in the model, with the coefficients calculated by assigning 1% damping to the first two calculated modal frequencies.

Dynamic, Non-Linear Time History Analysis (NL-THA) is performed in the third stage, using a time step size of 0.001 seconds and the Newmark constant average acceleration integration scheme. The foundation acceleration records in the horizontal and vertical direction as-measured during the test are used for the NL-THA. The P-Delta formulation is considered in all analyses to include nonlinear geometric effects arising due to the large drifts seen during the test.

6.4. Prototype analysis: column distance selection

As stated in Section 5.2, a small parametric study was undertaken for tuning the column distance in the prototype to maintain similar levels of column axial stresses between the two-column prototype and the two outer columns in the four-column bridge bent. For this purpose, the analytical model presented in Section 6.3 was applied to the prototype bridge-bent, and the column axial load response in the model under dynamic excitation was compared to the outer column axial load response in Bent 3 of the corresponding prototype bridge model (presented in Section 6.6).

For this study, the material properties in the prototype model were taken to be the expected values of the bridge material properties. The prototype was modeled in two-dimensions to simulate the constrained configuration of the test specimen, and to get comparable results, the bridge was modeled with zero skew and subjected to dynamic excitation in only the transverse and vertical directions.

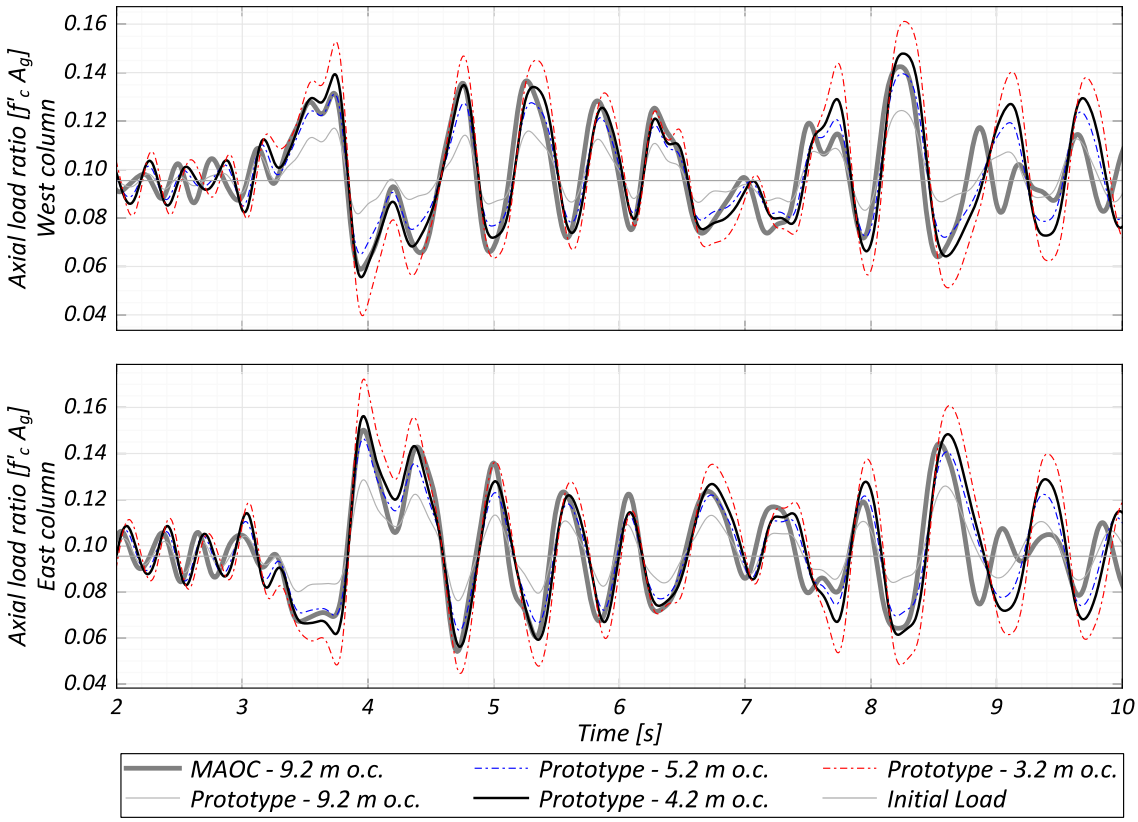

Figure 6.6 Comparison of axial loads in edge columns between MAOC and Prototype model

The parametric study on the prototype column distance utilized the fault normal and vertical components of the ground motion measured at the Sylmar - Olive View Medical Center station during the 1994 Northridge Earthquake. The column distance in the prototype was varied from 9.2 m (30-ft 2-in) to 3.2 m (10-ft 6-in) in increments of 500 mm (19.7-in). The comparison between the axial loads in the prototype columns and the outer columns of bent #3 in the prototype bridge for a select few values are shown in Figure 6.6. On the basis of these results, a column center-to-center distance of 4200 mm (13-ft 9-in) was selected for the final prototype.

6.5. Analysis of the test specimen

6.5.1. Model calibration

The preliminary analytical model for the test specimen was obtained by scaling down the geometries and applied super-structure load in the prototype model. After the completion of testing, this preliminary was modified to incorporate the as-measured material properties and geometries of the test specimen.

Incorporating the measured material properties involved updating various parameters controlling the response of the confined concrete and steel materials. The predicted confined concrete parameters were changed on the basis of measured unconfined concrete strength and stress-strain response of the column shell steel, as shown in Figure 5.12 and Figure 5.15. A comparison between the predicted and modeled confined concrete behavior is shown in Figure 6.7. Similarly, parameters controlling the behavior of energy dissipating steel bars and the prestressing steel bars were updated for a more accurate representation of these components. A comparison between the dissipator steel material model and measured material response is shown in Figure 6.8, and the material behavior used for the PT bars is compared to the measured response in Figure 6.9. In addition to updated material behavior, the initial prestresses in the PT bars were also changed to the as measured stresses of 38% GUTS and 37.6% GUTS for the North and South bars respectively.

In addition to updating the material behavior, changes were also made to some key geometries of the test specimen. The height of the rocking element was updated to 51mm (2.0 inches); this height was selected to approximately model the spread of crack

opening as seen during the test, e.g. in Figure 5.35(a) and (b). The anchor location, and hence the debonded length of the PT bars was also updated to reflect the presence of the 406 mm (16-in) tall load cells between the anchor and cap-beam.

The analytical response of the calibrated model, hereby named the Pre-test model, is presented under Section 6.5.3.

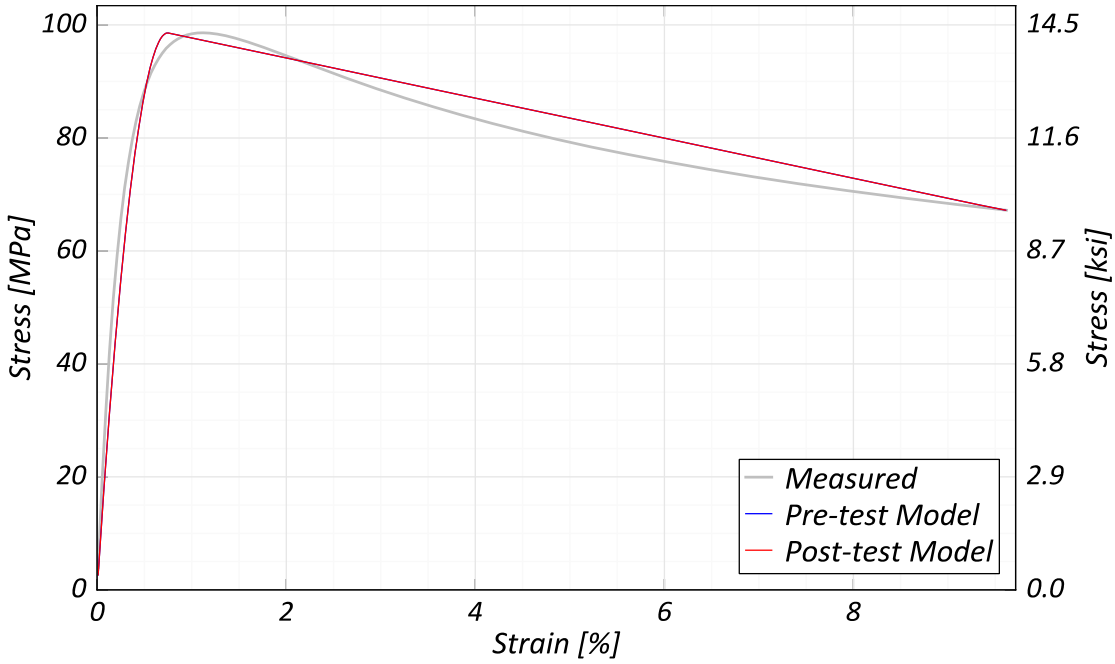

Figure 6.7 Confined concrete material properties used in analytical model

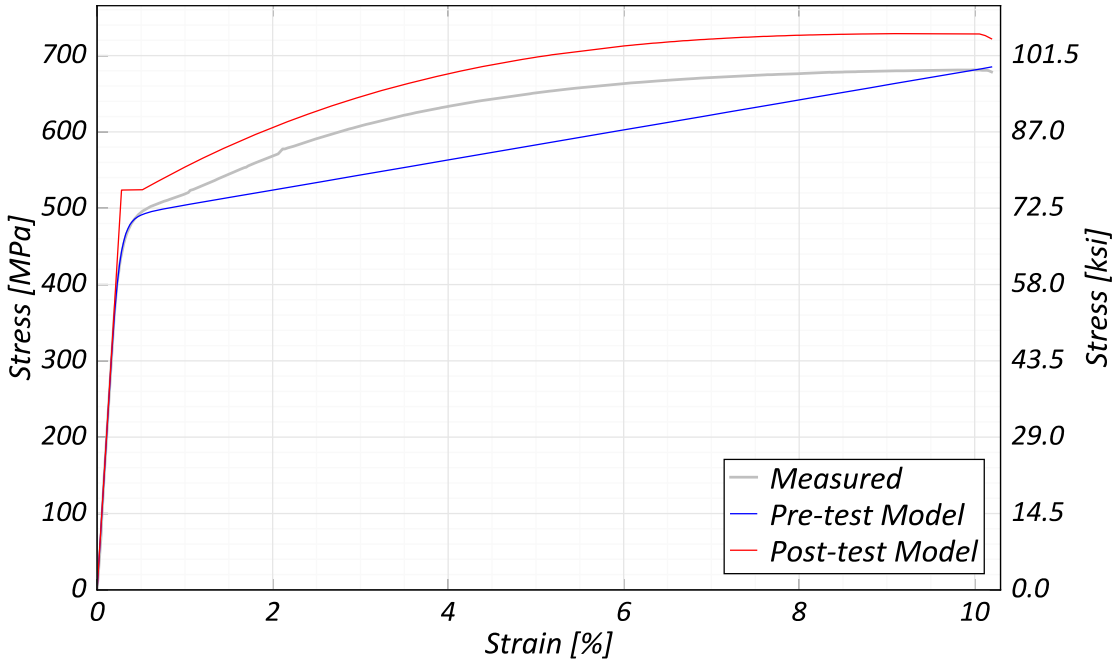

Figure 6.8 Dissipator steel material properties used in analytical model

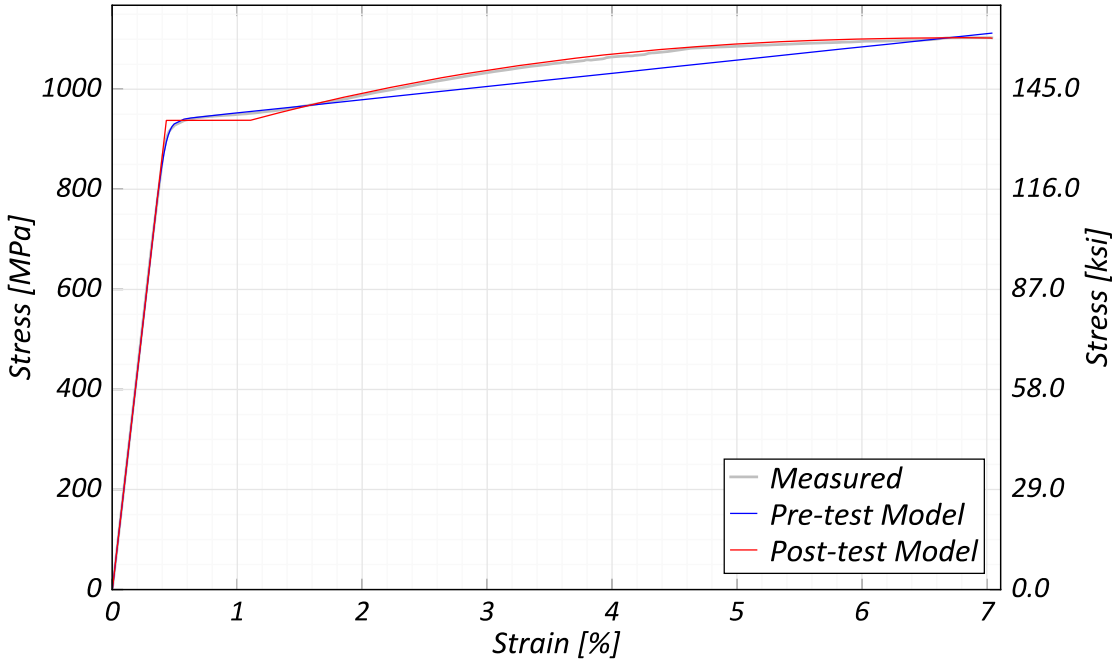

Figure 6.9 Prestressing steel material properties used in analytical model

6.5.2. Model improvement

Based on several studies done with the pre-test model as described in Section 6.5.1, several modifications were made to improve the match between the analytical model and experiment results. These changes, incorporated into the Post-test model, are listed below:

- Energy dissipators and prestressing bars are modeled using an advanced material model based on the works of Dodd, Restrepo and Carreño, which is an enhancement to the material rule presented in Dodd and Restrepo-Posada (1995).
- The prestressing bars are modeled using three force-based beam column elements, with horizontal restraints at the rocking interfaces.
- The yield and ultimate stresses of the energy dissipator steel model have been increased by 7% to account for dynamic effects, as suggested by Restrepo-Posada et al. (1994).
- The damping ratio used for calculating the Rayleigh coefficients is reduced to 0.5%. The Rayleigh damping response for the two models is compared in Figure 6.10.

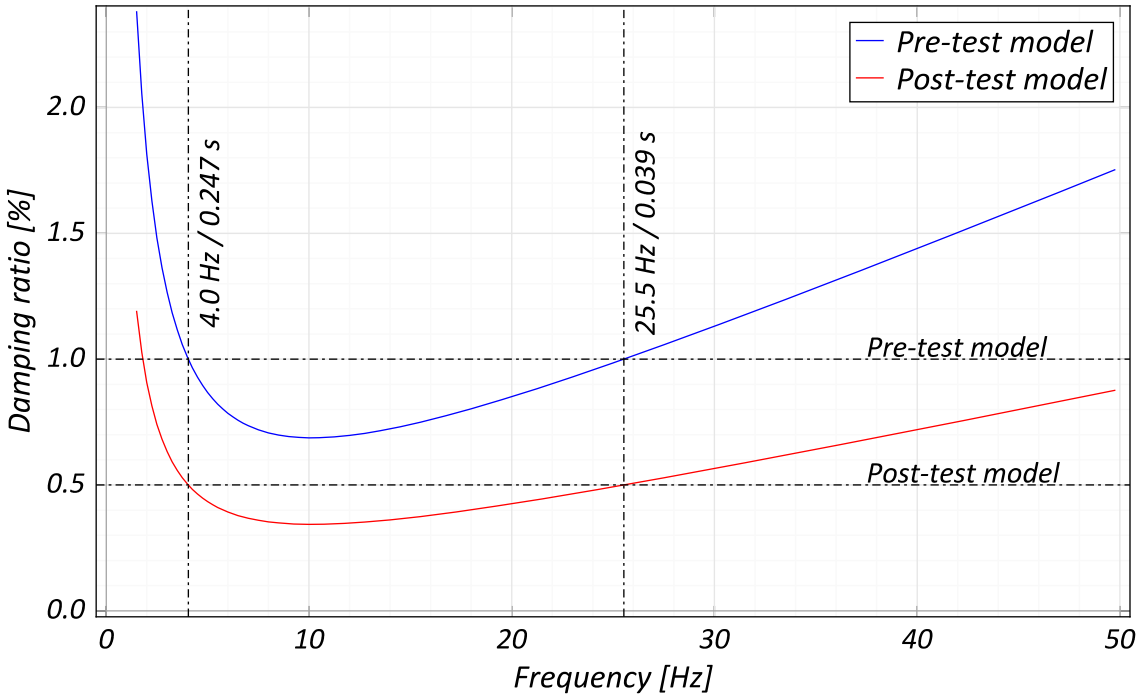

Figure 6.10 Rayleigh damping model

Among these changes, the changes in the modeling of PT bars, and the updated damping model are the most effective in improving the prediction of the analytical model. Use of FBE for modeling the PT bars helps account for the flexural yielding in the bars occurring at the rocking interfaces and prevents large losses in prestress. On the other hand, updating the damping model prevents excessive damping in large periods which are the predominant mode of response during EQ08 and EQ09 due to the yielding of the PT bars. This allows the model to reach drifts comparable to the test. A comparison of the updated material properties is included in Figure 6.8 and Figure 6.9.

6.5.3. Analytical results

The hysteretic responses of the two models are compared to the test results in Figure 6.11. For the first motion, both the models show a softer response compared to the

test: this is likely a result of the friction acting between the restraint frames and the specimen, which was eliminated before the start of EQ02. For the remaining excitations on Day 1, a reasonable match is seen between the models and the test results, although the models show slightly stiffer response for very small drifts (<0.8%). The normalized hysteretic energy (normalized by the product of the specimen weight and the clear height) for the test and the two models is listed in Table 6.2.

For day 2 of testing, results from the models typically compare well with the experiment results in terms of hysteretic behavior, except for EQ08, where the Pre-test model significantly under predicts the drifts. However, in the aftermath of EQ09, the Pre-test model shows significant softening and numerical instabilities. The reason for this becomes apparent when comparing the behavior of the prestressing bars: the Pre-test model predicts significantly larger stresses than seen in the experiment, which results in a large loss in prestressing force starting from EQ08. By the end of EQ09, the residual stresses are nearly zero, which results in the soft behavior.

Compared to the Pre-test model, the Post-test model predicts slightly smaller base shears for drifts <5%. Otherwise, the predictions from the Post-test model show a better agreement with experiment, up to the point of bar fracture in EQ11, which has not been modeled. A comparison of the peak and residual drifts between the test results and the model predictions is shown in Figure 6.12. The comparison shows that while the peak drifts are well predicted, the prediction of residual drifts is significantly optimistic when compared to the test results.

Table 6.2 Hysteretic energy comparison

Excitation	Test	Pre-test model	Post-test model
EQ01	0.0035	0.0025	0.0018
EQ02	0.0074	0.0010	0.0017
EQ03	0.0564	0.0474	0.0447
EQ04	0.0123	0.0047	0.0085
EQ05	0.0516	0.0441	0.0450
EQ06	0.0214	0.0208	0.0191
EQ07	0.0857	0.0543	0.0723
EQ08	0.1640	0.1119	0.1316
EQ09	0.2029	0.1635	0.1672
EQ10	0.0458	0.0385	0.0381
EQ11	0.0578	0.0473	0.0539
EQ12	0.1271	0.1097	0.1250

Figure 6.13 and Figure 6.14 show a comparison between the observed and predicted stresses in the two PT bars. The over prediction of PT stresses as well as the resultant early stress loss in the Pre-test model is well highlighted here. It can also be seen that the Post-test model better predicts both the peak and the residual stresses. It should be noted that the residual stresses in South bar show losses between EQ05 and EQ07; these losses, possibly caused by localized slipping during the test, are not modeled and could be a potential reason behind the remaining discrepancies with the predictions of the Post-test model.

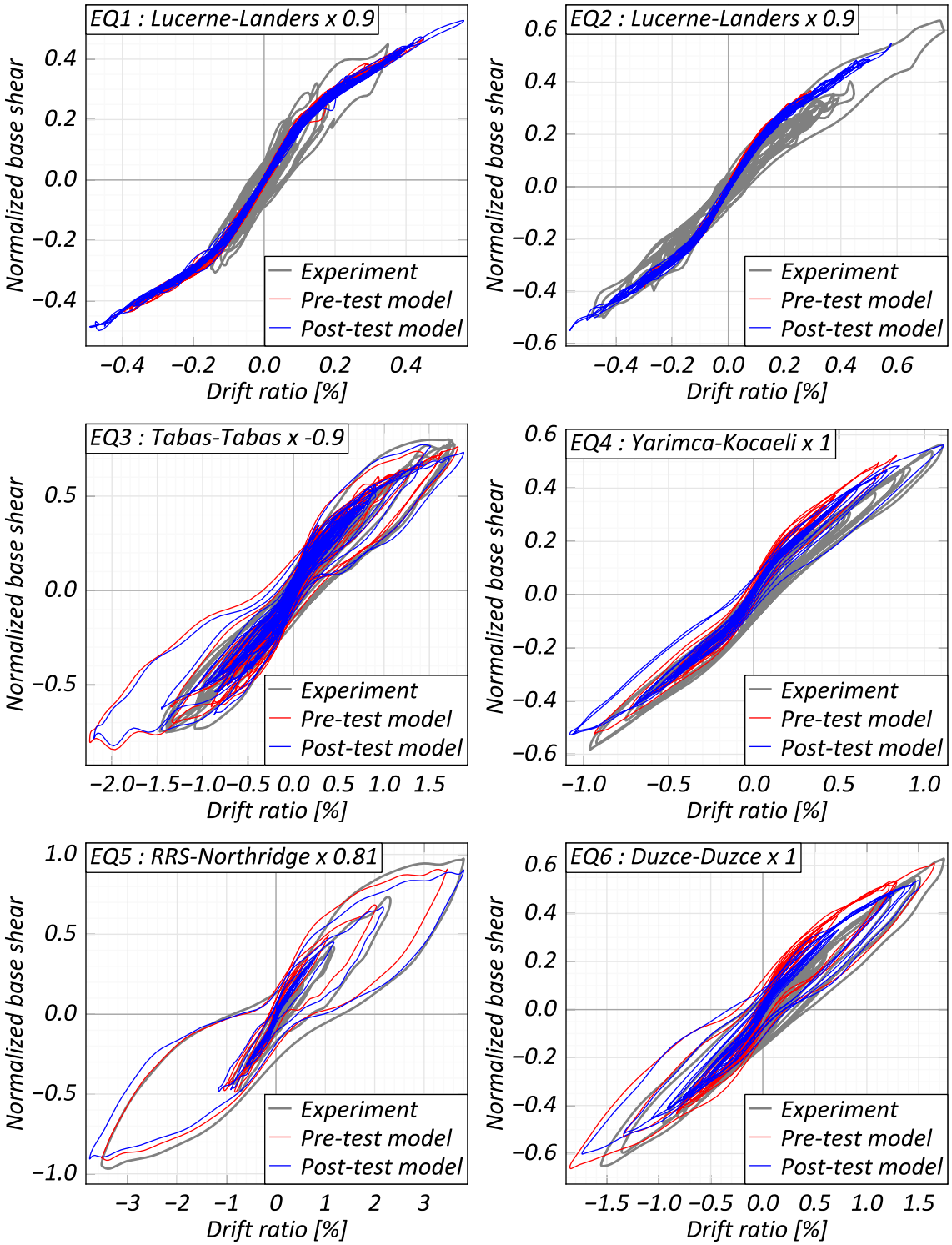

Figure 6.11 Numerical prediction of lateral force-displacement response

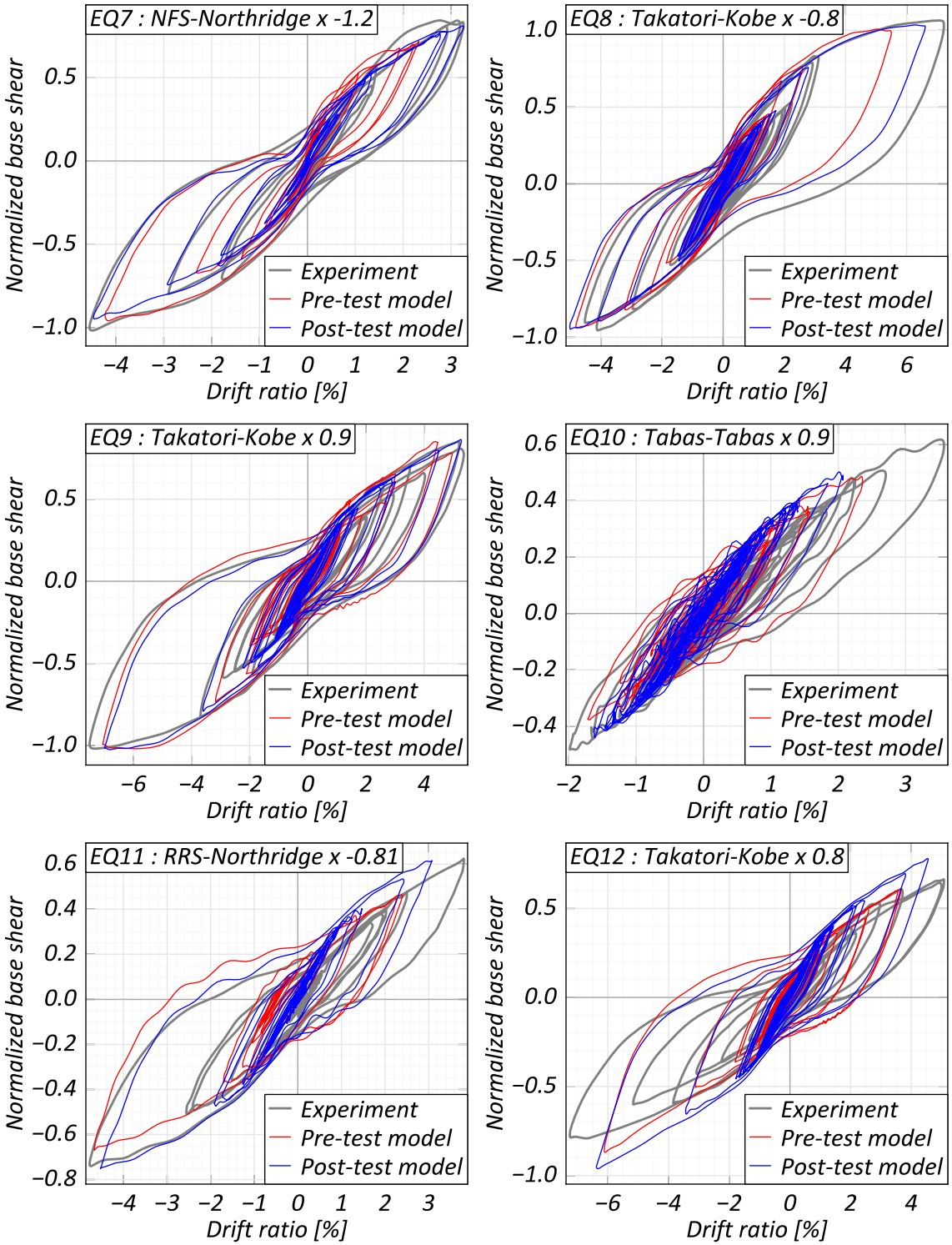

Figure 6.11 Numerical prediction of lateral force-displacement response (continued)

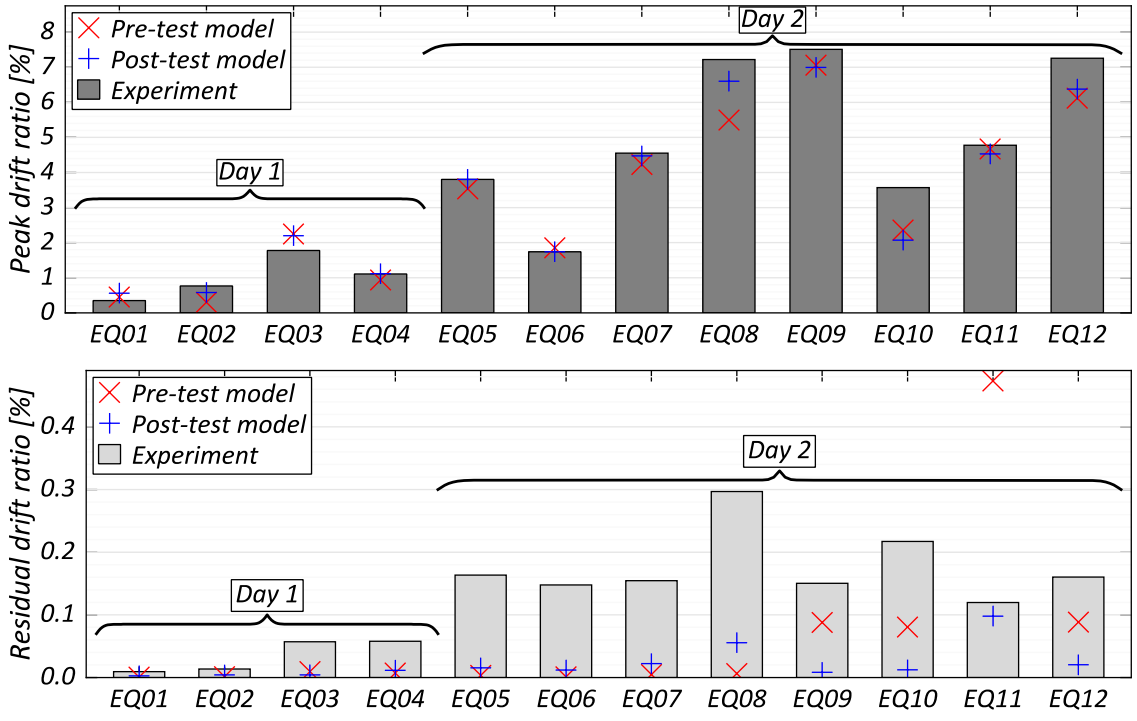

Figure 6.12 Comparison between measured and predicted drifts

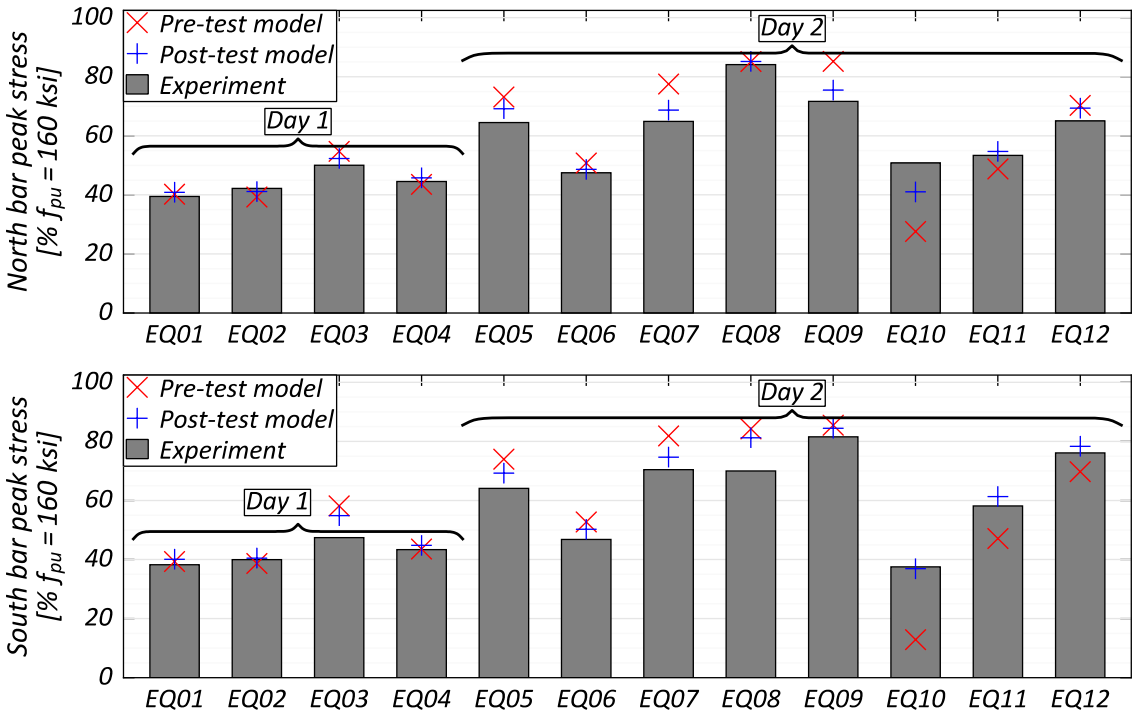

Figure 6.13 Comparison between measured and predicted peak stresses in PT bars

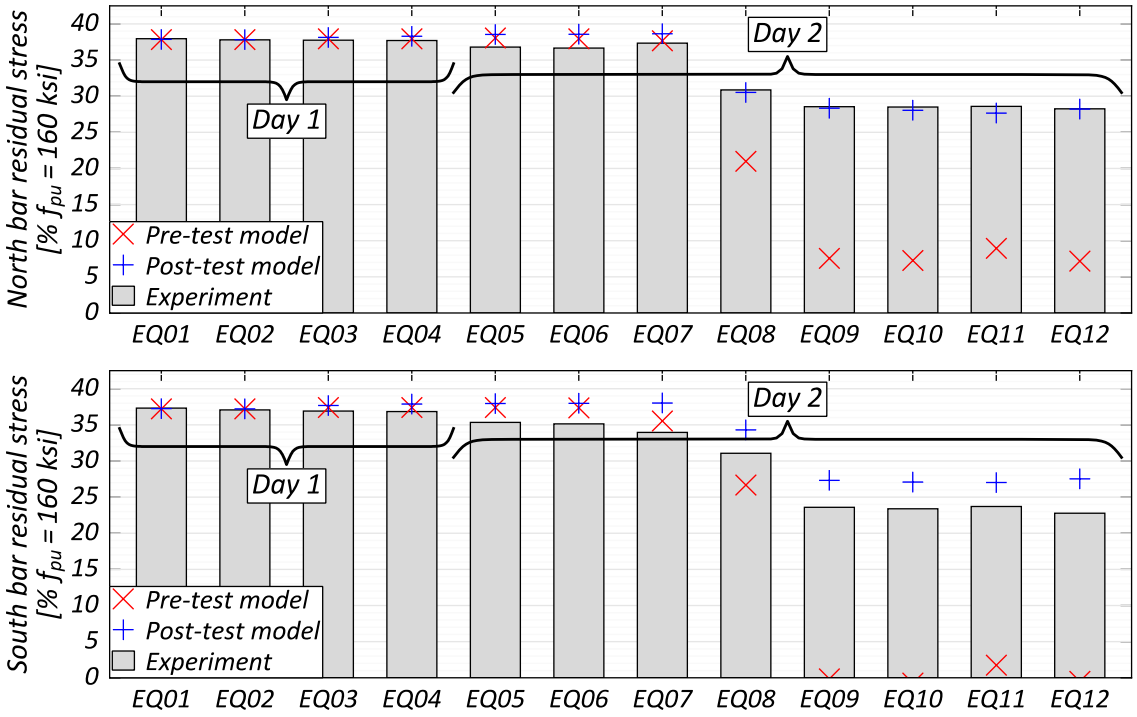

Figure 6.14 Comparison between measured and predicted residual stresses in PT bars

6.6. Low-damage prototype bridge

The hybrid bridge bent model presented in Section 6.3 was incorporated into a 3D model of the MAOC bridge and the dynamic results from this model were used to select the target behavior of the prototype, specifically the ratio of energy dissipation to re-centering capacity. The bridge model was also used for the selection of the column distance as presented in Section 6.4. The improvements in the hybrid re-centering column presented in Section 6.5 were incorporated into the bridge model and the resulting model was used for studying the advantages and disadvantages of various configurations of energy dissipators and re-centering steel. Details of the bridge model and the analytical study are presented in following sections.

6.6.1. Bridge description: monolithic and hybrid

The MAOC (Bridge No. 54-1265) located in San Bernardino and spanning Interstate 215 in the Northeast-Southwest direction, was selected for this study due to its close proximity (5.8 km / 3.6 mi) to the San Andreas Fault. The bridge, as-built, consists of five asymmetric spans of lengths 15.0 m, 28.8 m, 28.0 m, 30.4 m, 23.8 m for a total bridge length of 126 m (415 ft.). The four bent caps are skewed with respect to the bridge post-tensioned box girders to match the roadway underneath. Each bent cap is supported on four 1.22 m (48-inch) diameter circular columns with spiral ties and reinforced using 22 No.36 (#11) mild steel bars. The columns are joined monolithically with the deck and are connected to the foundation using 0.65 m (25.6 inch) diameter reduced section. The girder ends rest on seat-type abutments supported on steel piles. Each abutment consists of reinforced concrete footing, abutment backwall and stemwall, abutment wingwalls to each side of the stemwall, shear keys, bearing pads and polystyrene filler. The bridge elevation and plan are shown in Figure 6.15 while a typical bent is shown in Figure 6.16.

For the redesign of the bridge utilizing hybrid columns, two designs were initially explored. Type-1 configuration of the hybrid column follows the recommendations of Caltrans Recovery ERS Volume 1 (Bromenschenkel and Mahan 2014): it contains a higher proportion of mild steel with 12 No.36 (#11) Gr 60 bars and 4 x 4-15 mm Gr 270 strands. Additionally, the strands are stressed variably with four strands stressed at 75%, 50%, 25% and 10% of GUTS each (average initial stress of 40% GUTS). The proposed aim behind using different stress levels is to have additional stress capacities in reserve for different level events.

Type-5 configuration is based on the recommendations of Guerrini et al. (2015) presented in Equations 5.1 and 5.2, and utilizes a smaller proportion of mild steel, with 8 No.36 (#11) mild steel bars and 8 x 4-15 mm Gr 270 strands stressed at 40% GUTS. This is configuration aims to have sufficient strand force to yield the mild steel bars, a strong indicator of the re-centering ability of the column. The column section is taken to be an octagon circumscribing a 1.22m circle, from considering requirements for precast construction.

For the final prototype, a configuration with Λ_C and Λ_D values between Type-1 and Type-5 configurations is selected. This configuration, termed Type-6, consists of 10 No.36 (#11) mild steel bars and 8 x 4-15 mm Gr 270 strands stressed at 40% GUTS. The numerical value of the Λ_C and Λ_D for the three hybrid configurations is given in Table 6.3. The same gravity loading of 1.28 MN per column is used for all configurations, obtained from the tributary loads acting on the bent. A representation of the different sections is shown in Figure 6.17.

Table 6.3 Comparison of Re-centering (Λ_C) and Energy Dissipation (Λ_D) Coefficients for different prototype bridge configurations

Configuration	Mild Steel, Grade 60	PT Steel, Grade 270	Λ_C	Λ_D
Type 1	12 x No. 36	16 x 15 mm	1.34	0.57
Type 5	8 x No. 36	32 x 15 mm	0.57	0.36
Type 6	10 x No. 36	32 x 15 mm	0.71	0.42

An effective mild steel debond length of 1.22 m is used for the hybrid column configurations, obtained from 0.5 m applied debonding and additional 10 bar diameters (0.36 m) on either side of the interface to account for bar development length. The columns are confined using 12.7 mm thick steel jacket over their clear height to prevent

damage in the column toes during rocking. The jacket thickness is selected to avoid permanent deformation or damage to the shell at the column toes, for which the Guerrini et al. (2015) suggest a limit given by equation 6.1, where D_o is the outer diameter and t_o the shell thickness. The columns are assumed to be precast, and the column-foundation / column-cap-beam interface is assumed to composed of a 25.4 mm (1-inch) thick layer of well confined concrete. Finally, the effective PT strand debond is assumed to be end 0.78 m away from the column ends, which is the location of the center of gravity of the bent cap.

$$\frac{D_o}{t_o} \leq 100 \qquad 6.1$$

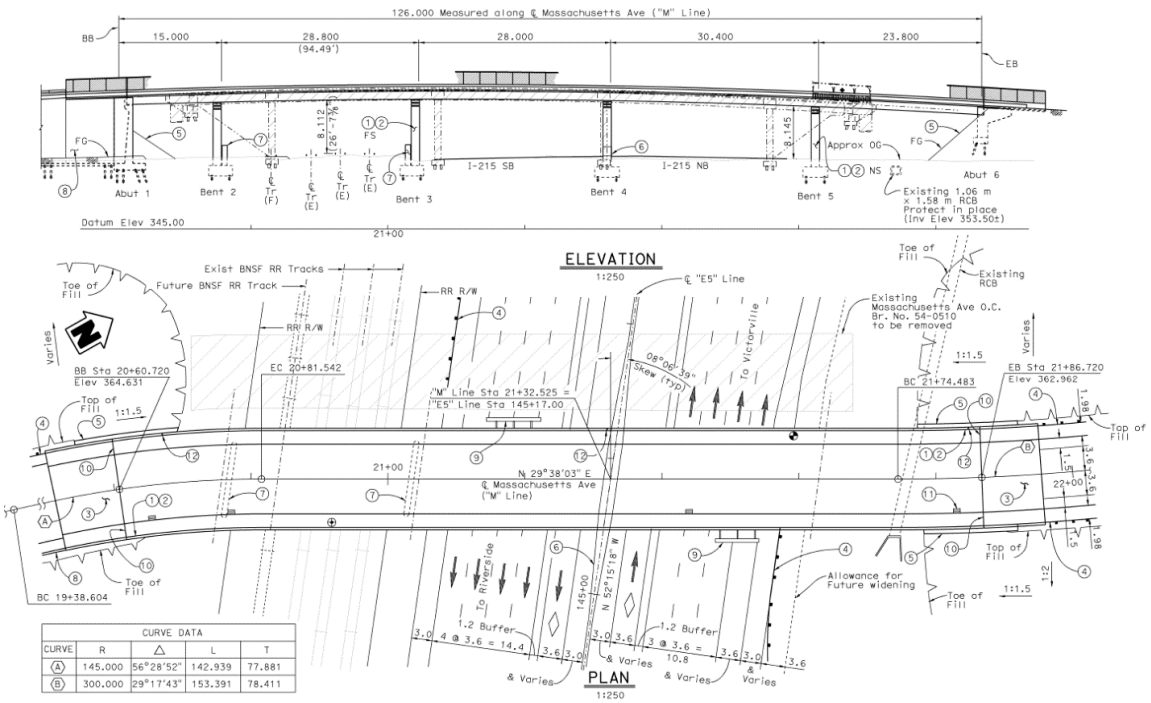

Figure 6.15 MAOC elevation and plan

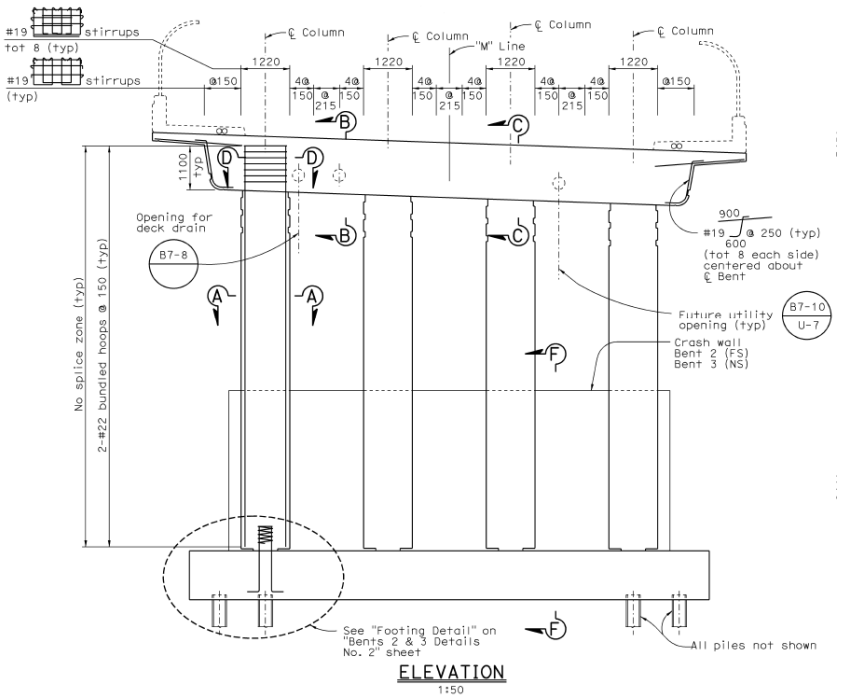

Figure 6.16 MAOC, typical bent

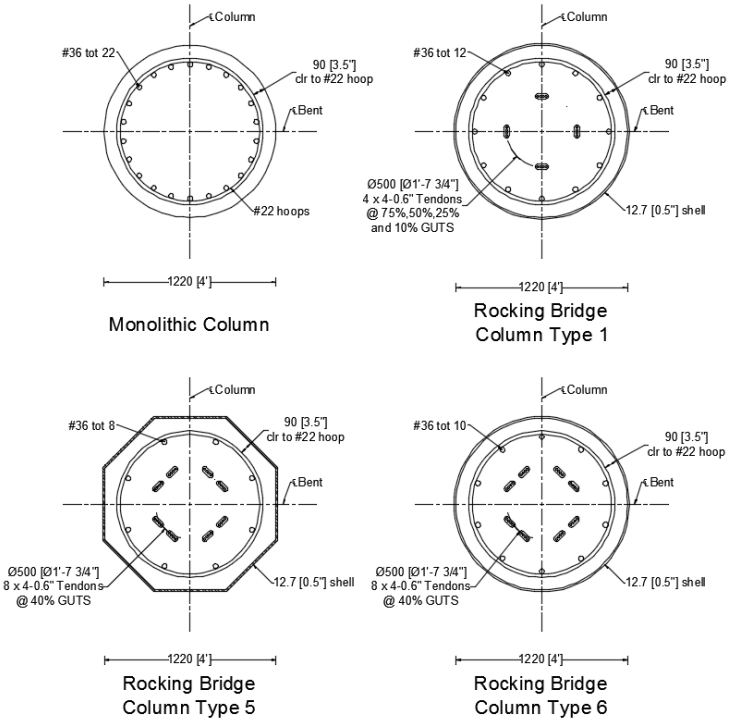

Figure 6.17 Column sections for different low-damage bridge column configurations

6.6.2. Model description

The 3D model for the as built bridge was originally developed in Beckwith (2015) for studying the seismic response with several types of shear keys. The data provided by the original model serves as benchmark result for comparing the performance of the hybrid system with a conventional cast-in-place, fixed-end system. This section focuses on the parametric studies conducted using the bridge model.

In the 3D model developed in OpenSees, the post tensioned box girder system is modeled using elastic elements along the spine of the bridge deck. Each girder is split into a number of equal length elements, with the number of elements determined such that all of them have similar lengths between different bridge spans. For the bent groups, the clear height of each bent column is modeled using a single force-based beam column element with four integration points, so that the integration weights are roughly equal to the plastic hinge recommended by Caltrans. The columns are connected to the bridge spine through rigid links with vertical offsets to model the deck height and horizontal offsets to account for the column location within the bent.

The abutment model consists of several zero-length springs modeled both in series and in parallel to approximate the behavior of the bearing pads, gaps, shear keys, soil wedge and embankment system. A representation of the bridge model is shown in Figure 6.18, and details of the abutment are shown in Figure 6.19.

Since the incorporation of re-centering columns calls for rocking at both ends, the original monolithic model is also updated by removing the shear keys at the foundations to provide a more accurate baseline. For the models utilizing hybrid columns, the single

element monolithic columns are replaced with the hybrid column model utilizing non-linear elements presented in the previous section. The strands are split into four groups, one group for each level of prestress for the Type-1 column and the prestress modeled using the *InitStrainMaterial* material in OpenSees. The strands are modeled using three-corotational elements for each strand to model the expected strand bending at each interface. It should be noted that each strand is modeled at the column center, since the strand physical location is important only for a hybrid cantilevered system and has no effect on a double-rocking system employed in the prototype bridge. Truss elements are used in lieu of beam-column elements for the strands to account for their flexible behavior when compared to prestressing bars.

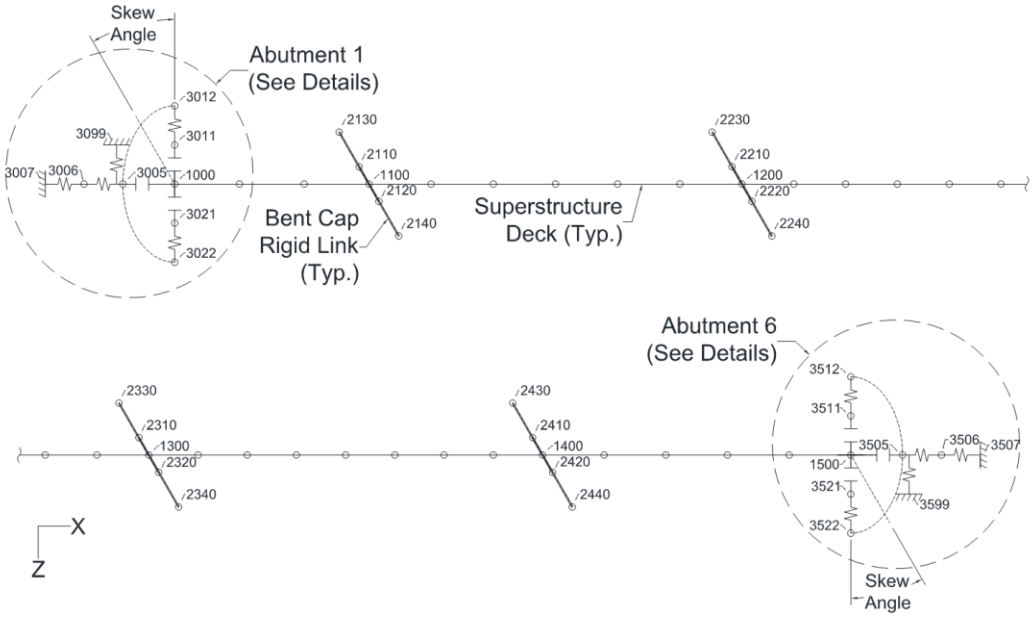

Figure 6.18 MAOC bridge analytical model, Beckwith (2015)

2% Rayleigh damping in modes 1 and 30, based on initial model stiffness, is used to model damping in all models, since in early analysis the damage-free models were found to be sensitive to damping in higher modes. Damping is modeled only in the beam

column elements, with no damping in the rocking interface elements. This is to avoid unrealistic damping forces which arise due to large velocities seen during rocking (Charney 2008).

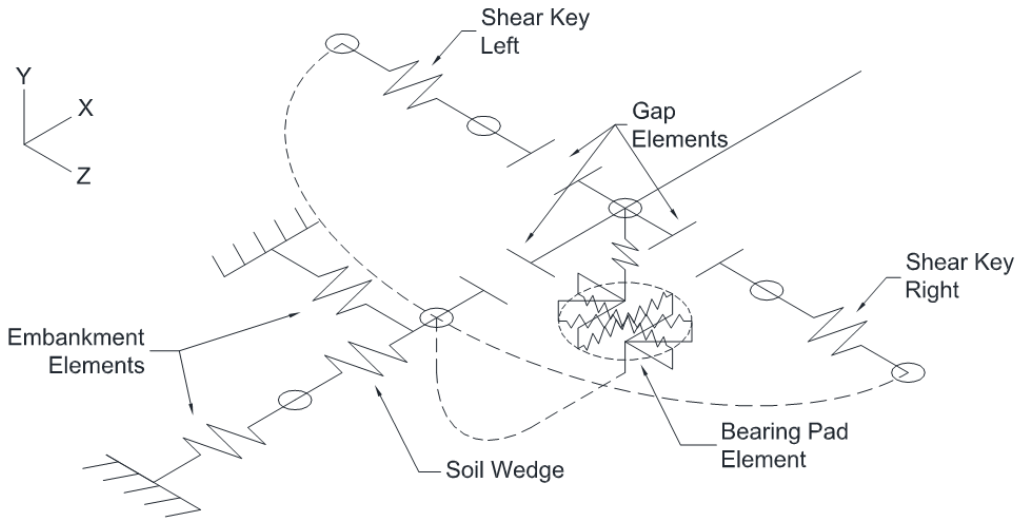

Figure 6.19 MAOC bridge abutment shear spring details, Beckwith (2015)

6.6.3. Input ground motions

For comparing the performance of different configurations listed above, the bridge model is subjected to three components of the ground motions listed in Table 6.4, with the fault normal component being applied transverse to the bridge. The unscaled horizontal ground motions have been rotated to maximize the response transverse to the bridge, and the rotated ground motion data has been obtained from the works of Lu and Panagiotou (2013). The ground motions were scaled to have a good match between the geometric mean of their fault-normal components and the SDC Acceleration Response Spectrum curve used for the original design of the bridge. The SDC ARS curve already includes modification for near fault effects, to account for the proximity of the San Andreas

Fault. The spectral responses of the three components of the ground motions can be seen in Figure 6.20.

Table 6.4 Details of ground motions used for bridge parametric study

Record ID	Earthquake	Mw	Station	Fault type+	Scale Factor	Unscaled PGA (g), Fault Normal
NZ002	Christchurch, NZ, 2011	6.3	PRPC	OT	1.55	0.73
P0927	Northridge, 1994	6.7	Newhall - Fire Station	BT	1.47	0.72
P1005	Northridge, 1994	6.7	Rinaldi Receiving Station	BT	1.07	0.89
P1023	Northridge, 1994	6.7	Sylmar - Converter Station	BT	1.46	0.59
P0934	Northridge, 1994	6.7	Sylmar - Olive View Med FF	BT	1.53	0.73
P0770	Loma Prieta, 1989	6.9	LGPC	SS	1.11	0.65
P1441	Chi-Chi, Taiwan, 1999	7.6	TCU065	T/LLS	1.51	0.83

+OT=Oblique Thrust, BT=Blind Thrust, SS=Strike-Slip, T/LLS=Thrust/Left-Lateral Slip

6.6.4. Analysis results

The average peak and residual drifts observed in the various models are presented in Figure 6.21 for the bridge transverse direction, and in Figure 6.22 for the bridge longitudinal direction. The hybrid systems show greater drifts than the monolithic systems, with the Type-6 configuration showing the smallest transverse drifts. For the bridge longitudinal direction, the drifts in all configurations are smaller, as are the discrepancies between the drifts in the different configurations. This is the result of the constraints provided by the bridge embankments.

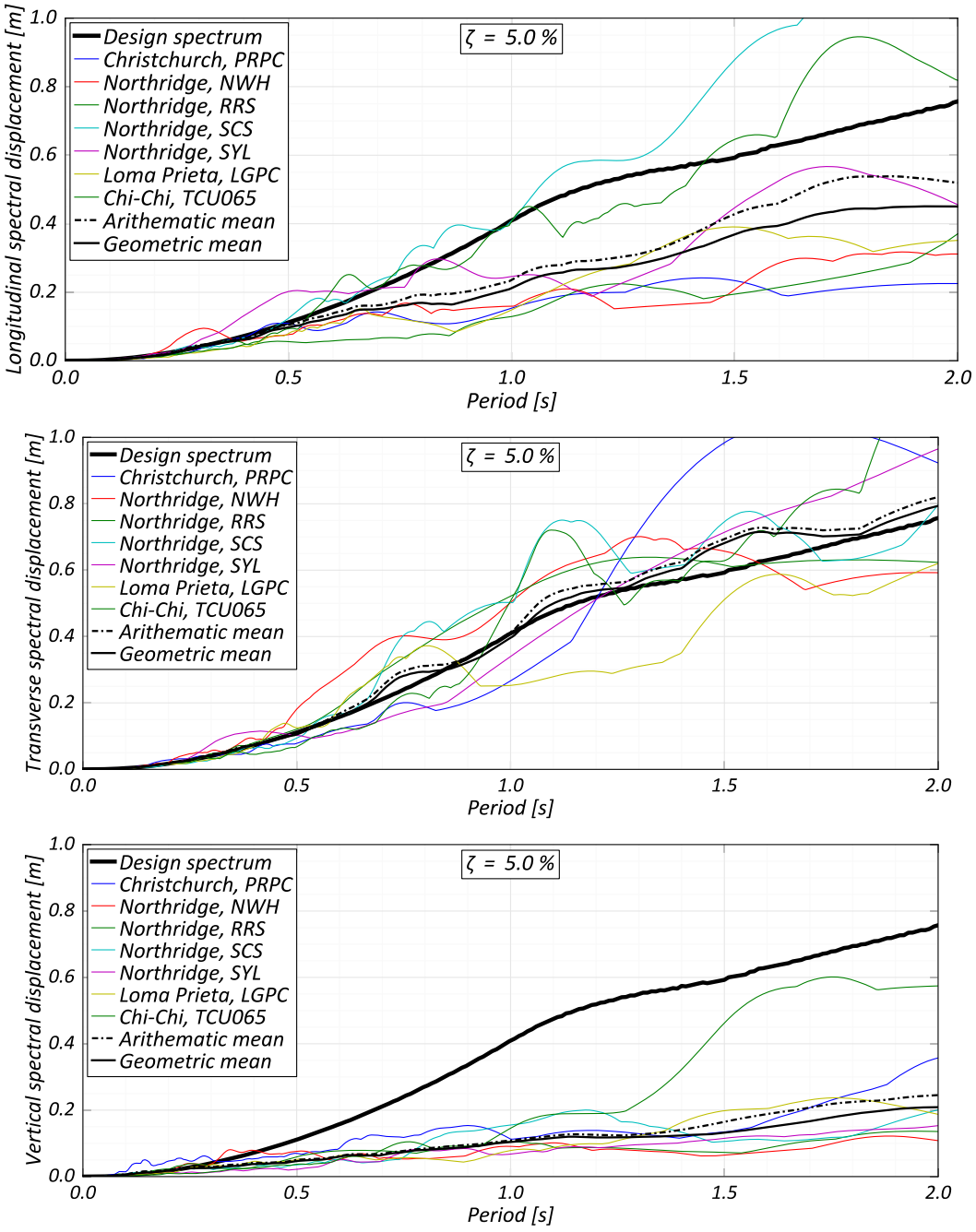

Figure 6.20 Spectral response of ground motions imposed on MAOC bridge model

The advantage of hybrid columns is clearly seen in the residual drifts, which are much lower for the hybrid columns. Comparing the different configurations of hybrid

columns, it is very clear that a high proportion of mild steel adversely affects the re-centering capacity of the hybrid columns.

The average peak strand stresses and stress losses seen in the various hybrid models are compared in Figure 6.23. Type-1 column configurations reach 90% f_{pu} under all ground motions. This is due to the highly stressed group of strands initially stressed to 75% GUTS. Consequently, these columns also show significant stress losses, which are negligible in the Type-5 and Type-6 configurations.

A typical lateral force-drift response for the different low-damage configurations and the monolithic configuration is shown in Figure 6.24. The Type-6 configuration shows the largest forces among the hybrid configurations for the same drifts which are at similar levels to the CIP, fixed-end column configuration.

The results from Figure 6.21, Figure 6.23 and Figure 6.24 strongly suggest that the optimum response of re-centering bridge column systems is achieved at balanced levels of mild- and prestressing steels, with values of the coefficient $\Lambda_C \leq 1$. Additionally, having different levels of prestresses in the same column in Type 1 configuration is found to have no beneficial effect.

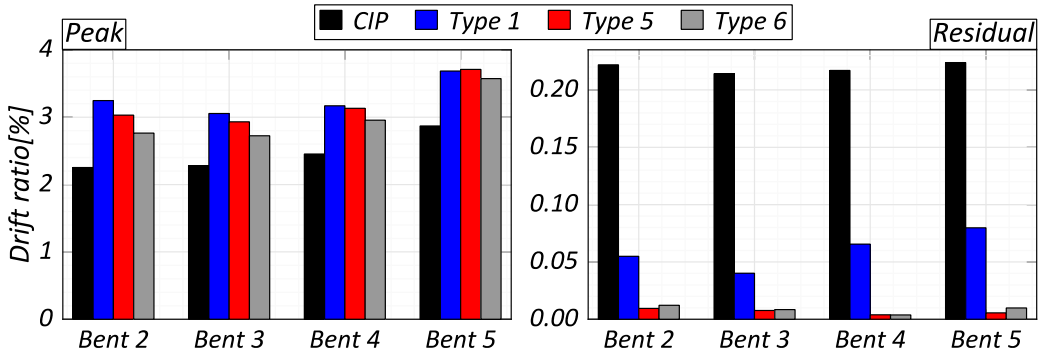

Figure 6.21 Average peak and residual transverse drifts ratios of various bridge configurations

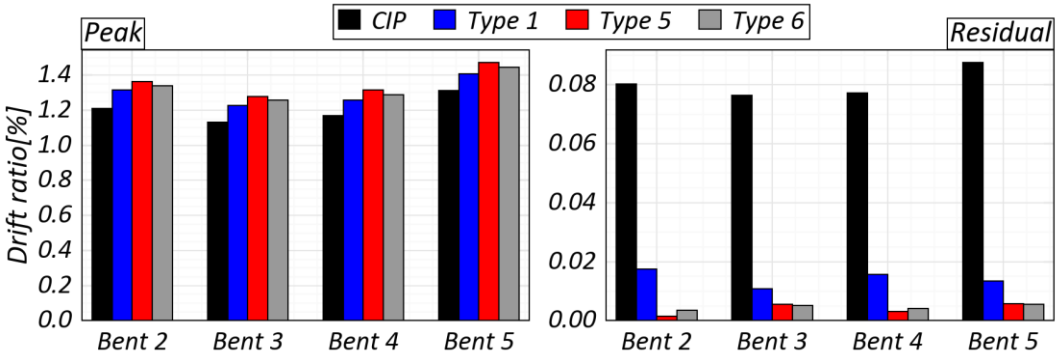

Figure 6.22 Average peak and residual longitudinal drifts ratios of various bridge configurations

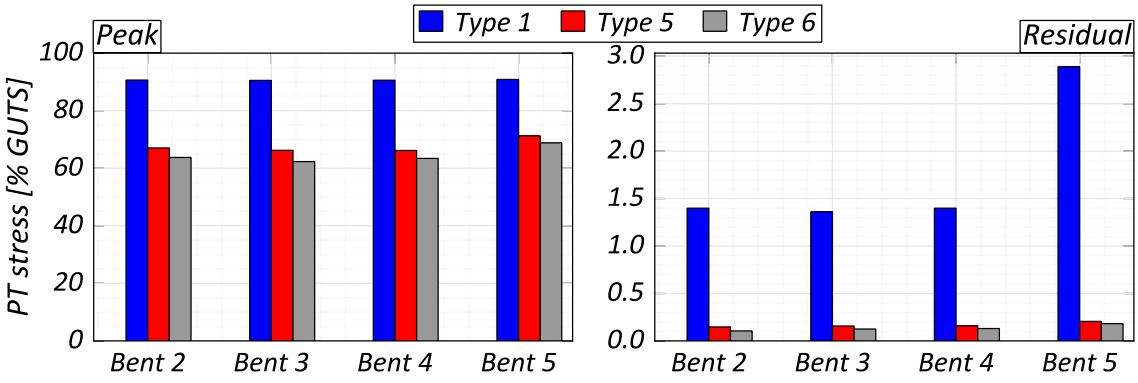

Figure 6.23 Comparison of average peak PT stress and stress losses

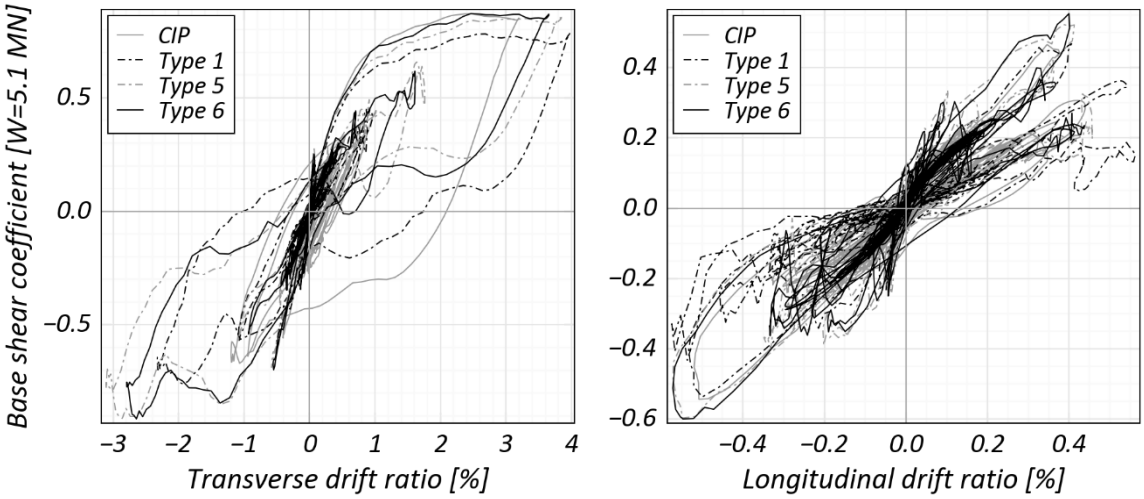

Figure 6.24 Typical hysteretic response, bent #3 in MAOC bridge model

6.7. Acknowledgements

I would like to thank Dr. Khalid Mosalam, Dr. Selim Gunay and Yingjie Wu from University of California, Berkeley for their valuable insights into model development and analytical study of the re-centering bridge systems.

I would also like to thank Frank Beckwith, Doctoral student at UC San Diego for sharing the analytical model of a 4-bent bridge which served as the base for studying low-damage bridge systems as part of this work.

The work presented in this chapter was supported by funding from the Pacific Earthquake Engineering Research Center (PEER), University of California Berkeley. I am thankful for their contributions of time, financial support and expertise.

Chapter 6, in part, is a reprint of the material presented in *Low-damage Columns for Accelerated Bridge Construction*, PEER Research Report (in-preparation) Nema, Arpit and Restrepo, José I. The dissertation author is the principal author on the report.

Chapter 7

CONCLUSIONS

7.1. Low-damage multi-story buildings

The work presented in this dissertation pertaining to low-damage multi-story buildings discussed the performance of hybrid re-centering walls and ductile gravity columns as part of a four story structure tested dynamically, and the development and performance of analytical models of hybrid re-centering structural walls and moment frames.

The following conclusions can be drawn from the experimental performance of the four-story test specimen:

- Hybrid-recentering systems undergo similar levels of maximum drifts compared to fixed-base systems.
- Re-centering systems show similar levels of maximum accelerations compared to conventional, fixed base systems.
- Compared to fixed-base systems, re-centering systems show reduced residual drifts and damage.

- Re-centering systems can bear small to moderate loss in prestress without any loss in re-centering capacity.
- Bi-directional motion has a significant effect on the deformation demands in a structure. This is particularly important for gravity or frame members at the corners of a structure.
- The proposed ductile gravity columns showed excellent performance, with only superficial damage after multiple cycles of testing. The measured strains in the central column bar remained small and within the yield strain as measured from material tests.

The experimental results were used for the calibration of a numerical model of hybrid re-centering walls. The complete test specimen was modeled using the analysis software OpenSees. The main elements of the model that required calibration include the response of the flexural energy dissipator, the FL-SC systems, the stiffness and yield of the PT bars and the response of the mortar forming the rocking interface. Key features and observations from the model are as follows:

- The model was able to capture well the characteristic flag shaped response of the test specimen, both at the structural and at the wall level.
- The region of energy dissipation through the FL-SC system was also well captured.
- The model showed good correlation to the test in terms of drifts and rotations.
- The energy dissipated in the model was smaller when compared to the test results, as seen in the form of narrower hysteretic loops.

- For the latter excitations, the moment computed from the model was lower than that from the test, particularly for larger drifts.
- As a result of calibrations, the model well captured the response of the FL-SC systems, the energy dissipators and the PT bars.
- The failure at the foundation level was not modeled, resulting in the model's failure to accurately compute the structure response during Phase III.

An analytical model for hybrid-recentering frames was developed and calibrated to test results from the works of Stanton et al. (1995). The models for the hybrid recentering walls and the hybrid re-centering frames were incorporated into an analytical model of a 13-story commercial building and the dynamic response of the structure with different combinations of wall and frame systems. Results from this study highlight some key points with regards to the response and modeling of hybrid re-centering systems:

- Hybrid systems result in reduced residual deformations indicating low damage, but at the cost of increased deformation demands.
- Hybrid re-centering walls could be detrimental to the residual response in the direction orthogonal to the plane of the wall.
- Damping needs to be modeled very carefully for rocking systems, to avoid the introduction of fictional forces in the regions of gap opening.

7.2. Low-damage bridge systems

The latter half of this dissertation has presented the design process, experimental performance and numerical simulations of the hybrid re-centering column systems for incorporation into multi-column bridge bents. The re-centering column design was

rationally derived from that of an existing monolithic bridge, and the final configuration was selected on the basis of parametric analysis performed on a 3D model of the prototype bridge. To aid in the numerical analysis, a computationally fast model was developed for hybrid recentering columns and verified against cyclic test data. The final scaled test specimen was designed to emulate the behavior of the full bridge with hybrid recentering columns as predicted by the analytical model, while maintaining the economy of the experiment.

The specimen fabrication was done following the principles of Accelerated Bridge Construction and utilized readily available technologies. The use of a socket connection allowed for the simultaneous fabrication of all the subcomponents at a dedicated precast facility, resulting in higher quality and rapid parallelized construction. The construction is further simplified by the proposed use of an external shell, specially engineered for rocking behavior, to serve as both the formwork and the transverse reinforcement in the bridge columns. As an added benefit, the proposed development using the outer steel shell eliminates the need for a separate mortar bed at the column base, required to accommodate construction tolerances in systems with precast elements, which can limit the optimal performance of the hybrid system.

The specimen was subjected to a suite of 12 seismic excitations in the horizontal (transverse to the bridge) and vertical directions, targeting increasing drift demands and representing near fault earthquakes and their aftershocks. The columns showed no external signs of damage, primarily due to the confinement provided by the outer steel shell, and the specimen maintained its strength until a drift ratio of 7%. At drifts

approaching 7%, the post-tensioning bars and the steel shells near the column toes showed signs of minor yielding. Yet repeating the excitation which caused this drift showed only a minor loss in strength and stiffness. Significant strength reduction was not seen until bar fracture in the internal mild steel, which took place under repeat imposition of drifts greater than 4%.

The tests were simulated using OpenSees for all the imposed motions, using the model developed for the design of the specimen and the measured material properties. A good match was obtained for moderate drifts, less than 4%. However, this model showed significantly larger post-tensioning bar stresses, larger prestress loss and smaller drifts for latter excitations.

An improved model, with a more realistic representation of the post-tensioning bars at the rocking interface, and using an advanced steel material model was developed to improve the computational results. This improved model, with reduced damping, was found to give improved predictions for the post-tensioning bar stresses and the specimen drifts. Neither the bar fracture in mild steel, nor the stress-relaxation in the post-tensioning bars seen during the test was modeled, which could be the cause behind the remainder of the discrepancies between the analytical prediction and the experimental results. However, considering the uncertainties in construction, the predictions from the model prove it to be an adequate tool for use in the seismic design and analysis of such systems.

With the improved and calibrated model for hybrid re-centering bridge columns, the 3D analytical model with different configurations of re-centering columns was

subjected to seven MCE_R level earthquakes. The average results suggest that a moderate value of Λ_C coefficient, larger than 0.7, is the most effective for minimizing both the residual and peak drifts. Additionally, a staggered distribution of prestresses can result in increased residual deformations if the imposed earthquake results in yielding of the PT elements with the largest initial stress.

7.3. Future work

The following work is proposed for future research on the topics presented in this dissertation:

- Dynamic experimental testing under excitations in three or more directions. This would be the most significant extension of the experimental work presented here.
- Experimental testing with more comprehensive specimens, particularly for bridges where the end conditions place important constraints on the response.
- Testing of the axial load capacity of the socket connection described for bridges. Additional information would be useful for a more economic design, with the potential of eliminating the top layer of reinforced concrete.
- Experimental and analytical work on the damping experienced in structures, particularly as a result of non-structural components.
- Analytical work for improving convergence in rocking systems. Convergence issues, while not discussed in this dissertation, were found to be the most significant source of increased computation time.

REFERENCES

AASHTO. (2012). *AASHTO LRFD Bridge Design Specifications, 6th Edition*. AASHTO, Washington, DC.

ACI 318 Committee. (2011). *ACI 318-11 Building Code Requirements for Structural Concrete and Commentary*. ACI 318, American Concrete Institute, Farmington Hills, Michigan.

Ameli, M. J., and Pantelides, C. P. (2016). "Seismic analysis of precast concrete bridge columns connected with grouted splice sleeve connectors." *Journal of Structural Engineering*, 143(2), 04016176.

Ameli, M. J., Parks, J., N. Brown, D., and Pantelides, C. P. (2015). "Seismic evaluation of grouted splice sleeve connections for reinforced precast concrete column–to–cap beam joints in accelerated bridge construction." *PCI Journal*, 60, 80–103.

ASCE. (2010). *Minimum design loads for buildings and other structures*. Amer Society of Civil Engineers.

Barbosa, A. R. (2011). "Simplified vector-valued probabilistic seismic hazard analysis and probabilistic seismic demand analysis : application to the 13-story NEHRP reinforced concrete frame-wall building design example." UC San Diego.

Barbosa, A. R., Conte, J. P., and Restrepo, J. I. (2009). *Design of a 12-story frame-wall building according to the 2003 NEHRP Provisions*. University of California San Diego.

Beckwith, F. (2015). *Nonlinear Time History Earthquake Analysis of Bridges with Varying Skew Angle to Determine the Design Parameters for Shear Keys*. Caltrans.

Belleri, A. (2009). "Displacement based design for precast concrete structures."

Belleri, A., and Riva, P. (2012). "Seismic performance and retrofit of precast concrete grouted sleeve connections." *PCI journal*, 57, 97–109.

Belleri, A., Schoettler, M. J., Restrepo, J. I., and Fleischman, R. B. (2014). "Dynamic Behavior of Rocking and Hybrid Cantilever Walls in a Precast Concrete Building (with Appendix)." *Structural Journal*, 111(3), 661–672.

Blandon, J. J., and Rodriguez, M. E. (2005). "Behavior of connections and floor diaphragms in seismic-resisting precast concrete buildings." *PCI journal*, 50(2), 56–75.

Bromenschenkel, R., and Mahan, M. (2014). *Recovery Earthquake Resisting Systems, Volume 1*. Caltrans.

Caltrans. (2013). *Seismic Design Criteria, v. 1.7*.

Center), P. (Pacific E. E. R. (2011). *PEER ground motion database*. Univ. of California Berkeley, CA.

Chang, G. A., and Mander, J. B. (1994). *Seismic Energy Based Fatigue Damage Analysis of Bridge Columns: Part I-Evaluation of Seismic Capacity*.

Chang, S. E. (2000). "Disasters and transport systems: loss, recovery and competition at the Port of Kobe after the 1995 earthquake." *Journal of transport geography*, 8(1), 53–65.

Charney, F. A. (2008). "Unintended consequences of modeling damping in structures." *Journal of structural engineering*, 134(4), 581–592.

Christopoulos, C., Filiatrault, A., Uang, C.-M., and Folz, B. (2002). "Posttensioned energy dissipating connections for moment-resisting steel frames." *Journal of Structural Engineering*, 128(9), 1111–1120.

Cormack, Lg. (1988). "The design and construction of the major bridges on the Mangaweka rail deviation." *Transactions of the Institution of Professional Engineers New Zealand: Civil Engineering Section*, 15(1), 17.

Dodd, L. L., and Restrepo-Posada, J. I. (1995). "Model for predicting cyclic behavior of reinforcing steel." *Journal of structural engineering*, 121(3), 433–445.

Eatherton, M. R., and Hajjar, J. F. (2014). "Hybrid simulation testing of a self-centering rocking steel braced frame system." *Earthquake Engineering & Structural Dynamics*, 43(11), 1725–1742.

El-Sheikh, M. T., Sause, R., Pessiki, S., and Lu, L.-W. (1999). "Seismic behavior and design of unbonded post-tensioned precast concrete frames." *PCI journal*, 44(3), 54–71.

FEMA-451. (2006). *Recommended provisions: Design examples*. Federal Emergency Management Agency, FEMA Washington.

Fernandes Canha, R. M., de Cresce El Debs, A. L. H., and El Debs, M. K. (2007). "Design model for socket base connections adjusted from experimental results." *Structural Concrete*, 8(1), 3–10.

Filippou, F. C., Bertero, V. V., and Popov, E. P. (1983). *Effects of bond deterioration on hysteretic behavior of reinforced concrete joints*. Earthquake Engineering Research

Center, University of California ; For sale by the National Technical Information Service, U.S. Dept. of Commerce, Berkeley, Calif.; Springfield, Va.

Guerrini, G., and Restrepo, J. I. (2011). "Advanced precast concrete dual-shell steel columns." *Proc., 8th Int. Conf. on Urban Earthquake Engineering*, 1125–1129.

Guerrini, G., and Restrepo, J. I. (2013). "Seismic response of composite concrete-dual steel shell columns for accelerated bridge construction." *Proc., 7th National Seismic Conf. on Bridges and Highways*, MCEER, State Univ. of New York at Buffalo Buffalo, NY.

Guerrini, G., Restrepo, J. I., Vervelidis, A., and Massari, M. (2015). *Self-centering precast concrete dual-steel-shell columns for accelerated bridge construction: seismic performance, analysis*. Pacific Earthquake Engineering Research Center.

Haber, Z. B., Saiidi, M. S., and Sanders, D. H. (2014). "Seismic Performance of Precast Columns with Mechanically Spliced Column-Footing Connections." *Structural Journal*, 111(3), 639–650.

Hall, J. F., Holmes, W. T., and Somers, P. (1994). "Northridge earthquake, January 17, 1994." *Preliminary reconnaissance report*.

Haraldsson, O. S., Janes, T. M., Eberhard, M. O., and Stanton, J. F. (2013a). "Seismic Resistance of Socket Connection between Footing and Precast Column." *Journal of Bridge Engineering*, 18(9), 910–919.

Haraldsson, O., Schoettler, M. J., Finnsson, G., Davis, P. M., Stanton, J., and Eberhard, M. (2013b). "Seismic resistance of precast concrete bridge columns made with unbonded pre-tensioning and hybrid fiber reinforced concrete." *Proceedings of the Seventh National Seismic Conference on Bridges & Highways: Bridge Resilience for Earthquakes & Other Natural Hazards. J. Kapur and T. Ostrom, eds. Buffalo, NY: University at Buffalo, State University of New York. CD Rom*.

Hewes, J. T., and Priestley, M. N. (2002). *Seismic design and performance of precast concrete segmental bridge columns*. SSRP.

Hieber, D. G., Wacker, J. M., Eberhard, M. O., and Stanton, J. F. (2005). *Precast concrete pier systems for rapid construction of bridges in seismic regions*. University of Washington Seattle, Washington, USA, Washington State Transportation Center (TRAC), 308.

Holden, T., Restrepo, J., and Mander, J. B. (2003). "Seismic performance of precast reinforced and prestressed concrete walls." *Journal of Structural Engineering*, 129(3), 286–296.

Jeong, H. I., Sakai, J., and Mahin, S. A. (2008). *Shaking table tests and numerical investigation of self-centering reinforced concrete bridge columns*. Pacific Earthquake Engineering Research Center.

Kurama, Y., Pessiki, S., Sause, R., and Lu, L.-W. (1999). "Seismic behavior and design of unbonded post-tensioned precast concrete walls." *PCI journal*, 44(3), 72–89.

Kwan, W.-P., and Billington, S. L. (2003a). "Unbonded posttensioned concrete bridge piers. I: Monotonic and cyclic analyses." *Journal of Bridge Engineering*, 8(2), 92–101.

Kwan, W.-P., and Billington, S. L. (2003b). "Unbonded posttensioned concrete bridge piers. II: Seismic analyses." *Journal of Bridge Engineering*, 8(2), 102–111.

Lau, D., and Fenwick, R. (2002). "The influence of precast prestressed flooring components on the seismic performance of reinforced concrete perimeter frames." *SESOC Journal*, 14(2), 17–26.

Leyendecker, E. V. (2008). *Java Ground Motion Calculator Version 5.0.8*. USGS.

Lu, Y., and Panagiotou, M. (2013). "Characterization and representation of near-fault ground motions using cumulative pulse extraction with wavelet analysis." *Bulletin of the Seismological Society of America*, 104(1), 410–426.

Lu, Y., and Panagiotou, M. (2014). "Three-Dimensional Cyclic Beam-Truss Model for Nonplanar Reinforced Concrete Walls." *Journal of Structural Engineering*, 140(3), 04013071.

Mander, J. B., and Cheng, C.-T. (1997). *Seismic resistance of bridge piers based on damage avoidance design*.

Marriott, D., Pampanin, S., and Palermo, A. (2009). "Quasi-static and pseudo-dynamic testing of unbonded post-tensioned rocking bridge piers with external replaceable dissipaters." *Earthquake engineering & structural dynamics*, 38(3), 331–354.

Marriott, D., Pampanin, S., and Palermo, A. (2011). "Biaxial testing of unbonded post-tensioned rocking bridge piers with external replacable dissipaters." *Earthquake Engineering & Structural Dynamics*, 40(15), 1723–1741.

Marsh, M. L., Buckle, I. G., and Kavazanjian Jr, E. (2014). *LRFD Seismic Analysis and Design of Bridges Reference Manual: NHI Course No. 130093 and 130093A*.

Mashal, M., White, S., and Palermo, A. (2013). "Quasi-static cyclic tests of emulative precast segmental bridge piers (E-PSBP)." *2013 NZSEE conference*.

Mazzoni, S., Mckenna, F., Michael H., S., and Fenves, G. L. (2007). *OpenSees command language manual*.

McBride, A., Fenwick, R. C., and Davidson, B. J. (1996). *The influence of slabs on the lateral cyclic behaviour of ductile concrete frames*. Department of Civil and Resource Engineering, University of Auckland.

McKenna, F., Michael H., S., and Gregory L., F. (2010). "Nonlinear Finite-Element Analysis Software Architecture Using Object Composition." *Journal of Computing in Civil Engineering*, 24(1), 95–107.

Mengotto, M., and Pinto, P. E. (1973). "Method of analysis for cyclically loaded RC plane frames including changes in geometry and non-elastic behavior of elements under combined normal force and bending." *Proc. of IABSE symposium on resistance and ultimate deformability of structures acted on by well defined repeated loads*, 15–22.

Nakaki, S. D., Stanton, J. F., and Sritharan, S. (1999). "An overview of the PRESSS five-story precast test building." *PCI journal*, 44(2), 26–39.

OpenSees, M. F. (2013). *Open system for earthquake engineering simulation*. Pacific Earthquake Engineering Research Center, University of California Berkeley, CA.

Osanai, Y., Watanabe, F., and Okamoto, S. (1996). "Stress Transfer Mechanism of Socket Base Connections with Precast Concrete Columns." *Structural Journal*, 93(3), 266–276.

Ou, Y.-C., Chiewanichakorn, M., Ahn, I.-S., Aref, A., Chen, S., Filiatrault, A., and Lee, G. (2006). "Cyclic performance of precast concrete segmental bridge columns: Simplified analytical and finite element studies." *Transportation Research Record: Journal of the Transportation Research Board*, (1976), 66–74.

Palermo, A., and Mashal, M. (2012). "Accelerated bridge construction (ABC) and seismic damage resistant technology: a New Zealand challenge." *Bulletin of the New Zealand Society for Earthquake Engineering*, 45(3), 123–134.

Palermo, A., and Pampanin, S. (2008). "Enhanced Seismic Performance of Hybrid Bridge Systems: Comparison with Traditional Monolithic Solutions." *Journal of Earthquake Engineering*, 12(8), 1267–1295.

Palermo, A., Pampanin, S., and Marriott, D. (2007). "Design, modeling, and experimental response of seismic resistant bridge piers with posttensioned dissipating connections." *Journal of Structural Engineering*, 133(11), 1648–1661.

Panagiotou, M., and Restrepo, J. (2006). "Model calibration for the UCSD 7-story building slice." *NEES-UCSD Workshop on the Analytical Model of Reinforced Concrete Walls*.

Pang, J. B. K., Eberhard, M. O., and Stanton, J. F. (2010). “Large-Bar Connection for Precast Bridge Bents in Seismic Regions.” *Journal of Bridge Engineering*, 15(3), 231–239.

Perez, F. J., Pessiki, S., Sause, R., and Lu, L.-W. (2003). “Lateral load tests of unbonded post-tensioned precast concrete walls.” *Special Publication*, 211, 161–182.

Priestley, M. J. N. (1991). “Overview of PRESSS research program.” *PCI journal*, 36(4), 50–57.

Priestley, M. J. N., and MacRae, G. (1994). *Precast post-tensioned ungrouted concrete beam-column subassemblage tests*. SSRP.

Priestley, M. J. N., Sritharan, S., Conley, J. R., and Pampanin, S. (1999). “Preliminary results and conclusions from the PRESSS five-story precast concrete test building.” *PCI journal*, 44(6), 42–67.

Priestley, M. J. N., and Tao, J. R. (1993). “Seismic response of precast prestressed concrete frames with partially debonded tendons.” *PCI Journal*, 38(1), 58–69.

Restrepo, J. I., and Rahman, A. (2007). “Seismic performance of self-centering structural walls incorporating energy dissipators.” *Journal of Structural Engineering*, 133(11), 1560–1570.

Restrepo, J. I., Tobolski, M. J., and Matsumoto, E. E. (2011). *Development of a precast bent cap system for seismic regions (NCHRP Report 681)*.

Restrepo-Posada, J. I., Dodd, L. L., Park, R., and Cooke, N. (1994). “Variables affecting cyclic behavior of reinforcing steel.” *Journal of Structural Engineering*, 120(11), 3178–3196.

Sakai, J., and Mahin, S. A. (2004). “Analytical investigations of new methods for reducing residual displacements of reinforced concrete bridge columns.” *PEER-2004/02*.

Saunders, J. K., Goldberg, D. E., Haase, J. S., Bock, Y., Offield, D. G., Melgar, D., Restrepo, J., Fleischman, R. B., Nema, A., and Geng, J. (2016). “Seismogeodesy using GPS and low-cost MEMS accelerometers: Perspectives for earthquake early warning and rapid response.” *Bulletin of the Seismological Society of America*, 106(6), 2469–2489.

Sharpe, R. D., and Skinner, R. I. (1983). “The seismic design of an industrial chimney with rocking base.” *Bulletin, New Zealand*.

Soesianawati, M. T. (1986). “Limited ductility design of reinforced concrete columns.”

Stanton, J., Stone, W. C., and Cheok, G. S. (1997). “A Hybrid Reinforced Precast Frame for Seismic Regions.” *PCI Journal*, 42(PCI Journal).

Stone, W. C., Cheok, G. S., and Stanton, J. F. (1995). “Performance of hybrid moment-resisting precast beam-column concrete connections subjected to cyclic loading.” *Structural Journal*, 92(2), 229–249.

Tazarv, M., and Saiidi, M. S. (2015). “UHPC-filled duct connections for accelerated bridge construction of RC columns in high seismic zones.” *Engineering Structures*, 99, 413–422.

Thonstad, T., Mantawy, I. M., Stanton, J. F., Eberhard, M. O., and Sanders, D. H. (2016). “Shaking table performance of a new bridge system with pretensioned rocking columns.” *Journal of Bridge Engineering*, 21(4), 04015079.

Toranzo, L. A., Restrepo, J. I., Mander, J. B., and Carr, A. J. (2009). “Shake-table tests of confined-masonry rocking walls with supplementary hysteretic damping.” *Journal of Earthquake Engineering*, 13(6), 882–898.

Toranzo-Dianderas, L. A. (2002). “The use of rocking walls in confined masonry structures : a performance-based approach.” PhD Thesis, University of Canterbury, Christchurch, New Zealand.

Yassin, M. H. M. (1994). “Nonlinear analysis of prestressed concrete structures under monotonic and cyclic loads.” Ph.D., University of California, Berkeley.

Zhang, Z. (2017). “Analytical Investigation of Inertial Force-Limiting Floor Anchorage System for Seismic Resistant Building Structures.” Ph.D.